THE EFFECTS OF TURBULENCE LENGTH SCALE ON HEAT TRANSFER

A thesis submitted for the degree of Doctor of Philosophy
at the University of Oxford.

January 1992.

R. W. Moss
Keble College, Oxford.

University of Oxford
Department of Engineering Science,
Parks Road,
Oxford OX1 3PJ
Tel (0865) 246561

ABSTRACT

THE EFFECTS OF TURBULENCE LENGTH SCALE ON GAS TURBINE HEAT TRANSFER by R.W.Moss.

A thesis submitted for the degree of Doctor of Philosophy, Oxford University.

Turbulence in the flow over a turbulent boundary layer increases the heat transfer above the level that would be expected for turbulent boundary layers in a low freestream turbulence environment.

This thesis describes a research programme aimed at understanding and quantifying this effect and, in particular, studying the relevance of the form of the turbulence spectrum. The purpose was to determine whether turbulence produced by the combustion chamber in a gas turbine affects the heat transfer to the high pressure turbine.

Two series of experiments have been carried out:

The first measured the turbulence levels and spectra produced at the exit plane of a variety of aircraft gas turbine combustors running at atmospheric exit pressure. A transient technique in which a pitot probe was only briefly exposed to the flow allowed uncooled, flush mounted, sub-miniature pressure transducers to be used to measure the turbulence spectra of combustor exhaust gases at temperatures up to 1500 K. It was found that the wavenumber spectrum above k = 100 m^{-1} was essentially unaffected by the combustion, being practically the same for both hot and cold cases, and was similar for all three combustors tested.

The second used a pre-heated flat plate in a transient wind tunnel to determine heat transfer rates with freestream turbulence generated by a number of parallel bar grids. Both liquid crystals and thin film gauges were used for heat-flux studies. A correlation has been derived that defines the heat transfer enhancement in terms of turbulence intensity and integral scale, as well as extending the conclusions of previous workers to apply at high intensities and with severe anisotropy.

ACKNOWLEDGEMENTS

I am indebted to all my friends and colleagues at the Osney Lab and Rolls-Royce for their help, advice and support in this work.

I would particularly like to mention my supervisor, Dr M.L.G.Oldfield, without whom it would not have been possible; Professor D.L.Schultz (in memoriam), for originally suggesting the project; and Jenny Vize, Alan Forest and Adrian White, for their support when planning the work.

I would like to thank Rolls-Royce plc and the Defence Research Agency Royal Aerospace Establishment (Pyestock) for their sponsorship and support; and in particular M.J.Oliver, Dr S.P.Harasgama and Dr R.Kingcombe for assisting with the organisation of the brochure. The combustion department at Pyestock have been most friendly and helpful, especially M.Wedlock who has spent many boring hours running the combustion rig.

Mr J. Allen painted the gauges on the flat plate by hand, a most painstaking task for which I am very grateful. The workshop staff also have done a splendid job in creating working apparatus from my drawings.

Finally, I must thank my wife Sally for her support, encouragement and (usually) patience; as she says, "Nobody could possibly want you to get this thesis *finished* more than I do".

CONTENTS

APPENDIX A.3.

TABLE OF FIGURES.

NOMENCLATURE.

A	surface area.
AFR	air: fuel ratio by mass
c	specific heat capacity (of solid) (J/kgK).
C_f	skin friction coefficient
C_{f0}	skin friction coefficient without freestream turbulence.
C_p	specific heat capacity at constant pressure (J/kgK).
d	bar or diaphragm diameter.
D	combustor diameter (m).
D_f	distance factor.
E	Young's modulus (N/m^2).
E	Output voltage from hot-wire anemometer.
E_w	Voltage across hot wire probe.
$E(f)$	Power spectral density of u'.
f	frequency (Hz).
f_n	natural (resonant) frequency.
$F(f)$	pitot probe resonant response.
h	heat transfer coefficient $\dot{q}/(T_{air} - T_{plate})$ (W/m^2K)
$G(k)$	variation in probe sensitivity with wavenumber.
k	conductivity W/m.K
k	wavenumber (1/m) $k = \dfrac{2\pi f}{\overline{U}}$
L_e^u	dissipation length scale.
m	mass flow, kg/s
M	Mach number.
$M(k, U)$	measured power spectral density $= \dfrac{d\left(\dfrac{u'}{\overline{U}}\right)^2}{dk}$

N	number of data points.
Nu	Nusselt number hx/k
Nu_0	Nusselt number with no grid.
Nu_R	Nusselt number hR/k
p	static pressure (N/m^2)
P_0	total pressure (N/m^2)
P	electrical power.
Pr	Prandtl number $Cp.\mu/k$
PSD	power spectral density.
$\dot{q}_s$, $\dot{q}_x$	heat flux at surface, and at x below surface (W/m^2)
$\dot{q}$	heat flux measured by thin film gauges (W/m^2)
R	radius of sphere.
R	resistance (Ω).
$R(\tau)$	autocorrelation of velocity fluctuations u' at time lag τ.
Re_R	Reynolds number based on radius of sphere.
Re_x	Reynolds number based on distance along plate.
Re_θ	Reynolds number based on boundary layer momentum thickness.
$S(k)$	true power spectral density.
St	Stanton number $\dfrac{h}{\rho Cp U}$
t	time.
T	temperature.
T_s, T_x	temperature at surface, and at x below surface.
T_{rec}	temperature of air resonating behind screen.
Tu	turbulence intensity $\dfrac{\sqrt{\overline{u'^2}}}{U} \times 100$ (%)
V	voltage.
U, V, W	velocity in axial and transverse directions (m/s).

u', v', w'	fluctuating components of velocity (m/s).
u^*	friction velocity $\sqrt{\frac{\tau_w}{\rho}}$
X	heat pulse penetration parameter.
X_d	correlating parameter (Equation 9.1).
X_{dr}	correlating parameter (Equation 9.2).
X_{ir}	correlating parameter (Equation 9.3).
x	distance in streamwise direction from leading edge.
x_g	distance from grid to plate leading edge.
x	depth below plate surface. (m)
y	distance above plate surface.
y^+	non-dimensional height above plate $y^+ = \frac{yu^*}{\nu}$
Z	transverse distance of gauges from the plate centre line (mm).
α	thermal diffusivity $k/\rho c$ (m^2s)
α	gauge resistance coefficient.
δ_{995}	99.5% boundary layer thickness.
θ	boundary layer momentum thickness.
θ	liquid crystal temperature ratio parameter $\frac{T_{surface,\ initial} - T_{crystal\ change}}{T_{surface,\ initial} - T_{gas}}$
λ	wavelength (m).
Λ_x	integral length scale in the streamwise direction.
μ	dynamic viscosity ($kg.m^{-1}.s^{-1}$)
ρ	density (kg/m^3)
τ	time lag in correlations.
τ_w	shear stress at wall.

ν	kinematic viscosity.
ν	Poisson's ratio.
Φ	velocity potential, such that $U = \dfrac{d\Phi}{dx}$
ω	frequency (rad/s)
ω_0	filter cut-off frequency.

Superscripts:	$\bar{}$	time-mean component,
	$'$	fluctuating component.
	$\hat{D}$	point at correlation peak.

CHAPTER 1.
BACKGROUND.

1.1 INTRODUCTION.

This chapter presents the reasons for undertaking the research described in this thesis. The aim of this research was to quantify the effects of combustor-generated turbulence on turbine heat transfer and thus enable gas turbines to be designed more accurately than hitherto. The chapter therefore starts with an general introduction to the problems facing the designers of high-pressure turbines for aircraft engines to put the work in context. This is followed by the basic objectives proposed while planning the work, and a series of questions which it was clear the research would have to answer to achieve these objectives.

The rest of the chapter presents a survey of previous experimental work in this field, subdivided into measurement techniques, combustor research and heat transfer research. Theoretical topics such as the derivation of boundary layer equations and closure techniques for the Navier-Stokes equations will not be discussed, as the research presented here has been experimentally based and has not used any finite-element type calculations; the reader is referred to **Schlichting (1979)**, **Hinze(1975)**, and **Duncan, Thom and Young (1970)** for a full description of boundary layer theory if required.

1.1.1 Requirement for heat transfer prediction in gas turbine design.

The basic gas turbine consists of a compressor that compresses air to a high pressure, a combustion chamber where fuel is added and burnt, and a turbine where it expands, thereby creating sufficient power to turn the compressor. This is usually followed by a further low pressure turbine which produces the net power output of the machine. Figures 1.1 and 1.2 show a typical arrangement of multiple "can-type" combustion chambers and turbine blading, from **Rolls-Royce**

(1986); this is the style of combustor that has been used for the experiments described here, as opposed to a fully annular combustor that would have required a much larger test facility.

It is only by running at high combustor outlet temperatures that sufficient energy can be given to the gas to provide any net power once the losses inherent in the compressor and high pressure turbine have occurred. It follows that (in general) overall engine power to weight ratio rises with combustion exit temperature. Higher compression ratios, required for greater efficiency, also lead to high exit temperatures.

In practice no materials strong enough for turbine components are available that will withstand uncooled operation at the desired gas temperatures. This problem is overcome by passing cooling air through passages inside the blades; this air is taken from the compressor exit and bypasses the combustion process.

Manufacturers are continually attempting to increase peak engine pressures and temperatures to improve the efficiency or power to weight ratio **(Miller and Bennet, 1986)**. A typical modern aircraft engine such as the Rolls-Royce RB211 will run at an overall pressure ratio of about 25.8 **(Boaden, 1990)** and experience turbine entry temperatures of up to 1688 K **(Byworth, 1986)**. Aerofoil metal temperatures can approach 1000°C in places.

At this temperature the blade material is only 250 K below its melting point and the creep strength is very dependent on the temperature. For example, **Cohen et al (1987)** show creep curves that indicate, at a constant stress of 80 MN/m^2, a reduction in creep life (to 0.2% strain) from 3900 hours to 560 hours as the temperature is raised from 1090 K to 1140 K, which corresponds to a life loss of -4%/K if one assumes that creep is the predominant failure mode.

In the above case, with a typical temperature drop between the inside and outside of the blade of about 40 K, a simplified one dimensional form of the heat balance equation that determines the blade metal temperature would be:

$$A_o h_o (T_g - T_{mo}) = A_i h_i (T_{mi} - T_c)$$

where A = surface area, h = heat transfer coefficient and the subscripts are $_i$ = internal, $_o$ = outside, $_g$ = gas, $_m$ = metal and $_c$ = coolant. Taking T_g = 1688 K and typical values of T_{mo} = 950°C and T_c = 780 K gives a worst case value of $\dfrac{A_i h_i}{A_o h_o}$ = 1.15, and the average $A_i h_i$ value will have to be even higher than this.

(It should be noted that in practice the blade life would usually be predicted using a 2- or 3-D finite element calculation of heat transfer and stress throughout the blade rather than the simplified one-dimensional equation given above.)

It can be appreciated that considerable effort is spent in designing cooling passages within the blade that have a higher surface area than the external surface and/or a higher heat transfer coefficient.

A simple calculation will show that in this example a rise in external heat transfer coefficient of 10% could be expected to raise the mean metal temperature by 20 K. Ideally one would perhaps like to predict life to within ±30% which, using the creep data mentioned above, would require the metal temperature to be known to approximately 7 K. Since the metal temperature is a function of the internal heat transfer coefficient, cooling air temperature and external gas temperature as well as the external heat transfer coefficient, and none of these can be calculated precisely, it follows that an accuracy in the prediction of h_0 of the order of ≈2-3% is desirable.

At present, although design methods for turbines are very complex and take a large number of factors into account, there are still many phenomena which influence blade heat transfer but cannot be precisely quantified. This results in blade designs that may need a certain amount of development "tuning" of the cooling system before final acceptance. Experimental development of a product as complex as a gas turbine is inevitably very expensive in comparison with changes during the design phase. This has been quantified for high pressure turbines by **Byworth (1986)**; between 1972 and 1984 improvements in design within Rolls-Royce plc reduced the ratio of development cost to design cost from 200:1 to 50:1. Further reductions in this ratio, via an improved understanding of the heat transfer process, are believed to be possible and are obviously highly desirable.

1.1.2 Effect of turbulence on heat transfer.

The heat flux into a surface from a fluid flowing over it depends on the properties of a *boundary layer* (**Prandtl, 1904**, from **Schlichting, 1979**), defined as the region in which the temperature and velocity of the fluid is modified by heat transfer and shear stresses induced by the surface; outside this region the "freestream" velocity and temperature are essentially those that would obtain in the absence of any heat transfer or friction effects.

At the point where the flow commences over the surface, the boundary layer will be in a *laminar* state; by this it is meant that the streamlines are parallel with the surface, and no mixing (apart from molecular diffusion) occurs. Typically, at some distance downstream from the starting point this smooth motion of the boundary layer fluid becomes unstable. "Turbulent spots", local regions of turbulent fluid within the laminar boundary layer, develop at random times in a *transition* region (**Schlichting, 1979**) and grow as they convect downstream. Ultimately the spots merge and the boundary layer is said to be *fully turbulent*. Fluid elements within the boundary layer then have velocity components that are no longer parallel with the surface, and convect momentum and enthalpy in a perpedicular direction much faster than the molecular processes in a laminar boundary layer. This leads to higher skin friction and heat transfer coefficients than would be obtained if the boundary layer were to remain laminar, alters the velocity profile, and makes it less prone to separation in adverse pressure gradients.

The position of the transition region depends to some extent on pressure gradients, surface curvature, roughness and heat transfer, but in practice it is very frequently determined either by freestream turbulence or by some discontinuity on the surface that generates turbulence within the boundary layer.

On turbine aerofoils the regions where heat transfer is highest are usually at the leading edge, where the boundary layer is extremely thin, and on the pressure surface where high turbulence levels and the presence of film cooling holes promote transition; on the early suction surface the flow acceleration tends to stabilise the boundary layer and delay transition and this, together with the lower pressures there, leads to rather lower heat fluxes. When the acceleration ceases on the crown of the blade, transition often gives a heat transfer peak that then decays towards the trailing edge. Since the pressure surface constitutes much more of the surface area than the leading edge, it is the prediction of the heat flux over this region that is of most importance. The relatively low velocity over the pressure surface leads to higher (fractional) freestream turbulence intensities here than elsewhere and hence it is essential that any effect of freestream turbulence on the heat transfer through a turbulent boundary layer be quantified.

Prior to the work described here, it was known that (in general) the presence of turbulence would, if levels were high enough, increase heat transfer coefficients by increasing the rate of mixing of freestream fluid into the boundary layer. It was presumed that this should depend on both the level and the frequency spectrum of the turbulence. At very low frequencies the turbulent fluctuations of the freestream would be indistinguishable from gradual changes in the velocity and mixing would not be increased, so it was believed that only those components of the turbulence with wavelengths of the same order as the boundary layer thickness would cause such an increase. On this basis one supposes that enhancement effects should be a function of both turbulence intensity and of a length-scale: boundary layer thickness ratio.

A few of the researchers (**Hancock, (1980)**; **Blair (1983)**) who had attempted to determine the effects of turbulence had measured the spectrum (and thus length scale) of the turbulence they used, and derived correlations for the increase in skin friction or heat transfer; the turbulence level and spectrum produced by gas turbine combustors, however, had never been accurately measured up to the wavelengths of interest which precluded any real use of such results.

The work described in this thesis is intended to provide some definitive data in both these areas and lead to an accurate assessment of the role of combustor-generated turbulence in turbine heat transfer.

1.1.3 Objectives of this work.

The objectives of this work are to :-

- Enable more accurate turbine heat transfer predictions.
- Provide data for the development of turbulence and transition models for Navier-Stokes and boundary layer methods used in CFD predictions of heat transfer.
- Provide an improved means of applying existing research test results to engine conditions, and allow more realistic turbulence levels to be specified for future tests.
- Establish desirable length scales from the combustor in order to minimise turbine heat transfer.

1.1.4 Experimental approach.

The experimental program was designed to answer the following general questions which were felt to be of fundamental importance -

- What is the turbulence level and spectrum in the exit flow of a typical combustion chamber?
- How much is the heat transfer to a turbulent boundary layer increased by high freestream turbulence levels and, in particular, how does this depend on the length scale?
- To what extent does movement of the transition point as turbulence changes augment or reduce the local heat transfer effects of higher turbulence levels?
- Can the increase in heat transfer be predicted from the change in skin friction - or is a length scale dependent modification to Reynolds analogy (**Reynolds, 1874,** from **Schlichting, 1979**) required as well as an accurate turbulence model?
- Are the turbulence length scales in a typical engine of such a size that they need to be considered when predicting the turbine heat transfer? - and if so, could a change in the combustor design, by changing the length scale, give a reduction in heat transfer?

Two experiments were devised to answer these questions - firstly, the measurement of the turbulence level and frequency spectrum at exit from a combustion chamber and secondly, the generation of a variety of turbulent flows (with energy at different wavelengths in each case) in a wind-tunnel to study the relative effects of differing eddy sizes on the heat transfer.

1.2 TURBULENCE MEASUREMENT TECHNIQUES IN HIGH TEMPERATURE FLOWS.

1.2.1 Introduction.

The traditional method of measuring turbulence is to use a constant temperature hot wire anemometer (**Lomas, 1986**). This consists of a fine (5 μm diameter) tungsten wire about 1.25 mm long which is suspended between a pair of sharp prongs pointing into the flow. It is electrically heated to about 540 K. The electrical resistance of the wire rises nearly linearly with temperature, and a fast response feedback circuit that senses the wire resistance is used to maintain it at a constant temperature. The instantaneous velocity is deduced from the power required to do this. Calibration in a known flow is desirable to quantify the velocity/power relationship. Signal processing of the output from the feedback circuit yields the turbulence level and spectrum; this is usually done using digital, as opposed to analogue, techniques.

Measurement of turbulence at the high temperatures in a flame is almost impossible with a hot-wire. Calibration of a hot wire for use in a hot flow would be very difficult, as the output depends on the gas temperature which would not, in general, be accurately known. Although this can be overcome by taking a number of measurements at different overheat ratios (eg **Oldfield et al, 1978**) which allows both turbulence and temperature to be derived, a very large number of measurements would be required to obtain repeatable results from a randomly fluctuating flow using this technique. The problem of wires breaking or melting is more insurmountable; the wire must be hotter than the flow, and with gas temperatures of up to 1500 K a wire temperature in excess of 2000 K would probably be required. This would lead to almost instantaneous oxidation and breakage.

Hot wires were, however, used for the measurement of turbulence in the wind tunnel (cold flow) part of the experiment, and for a limited number of cold flow combustor tests. Their use is described in Chapter 6.

Two other techniques have hitherto been used to measure turbulence in high temperature flows - laser Doppler anemometry, "*LDA*" **(McComb, 1990)** and pressure transducers.

With LDA it is very difficult to get a high enough seeding rate to accurately measure the high frequency components of the turbulence - and there may also be doubts as to whether the particles are small enough to follow small-scale turbulence reliably. The calculation of a power spectral density from the randomly occurring velocity measurements produced by a laser anemometer system is also difficult; none of the papers studied mentioned having achieved this.

These drawbacks led to the choice of pressure transducers rather than LDA for the combustor experiment.

Pitot pressure probes measure the total pressure fluctuations resulting from velocity fluctuations. In the past probes have either used a cooling jacket (which tends to be so large that there is a danger of the probe influencing the flow it is meant to measure), or have used a long supply tube to a remote transducer - which will probably either resonate (if it is large in diameter) or damp out any high frequency signals (if it is very small in diameter).

1.2.2 Relevant papers on measurement techniques.

Ebrahimini (1967) used a water-cooled condenser microphone, fed by a probe tube 90 mm long × 2 mm bore, to measure turbulence in a hydrogen flame. This had a half power cut-off frequency of about 4.5 kHz. He measured the time-mean total pressure separately with a pitot tube to obtain the dynamic head (assuming that static pressure was constant throughout the flame) and then solved

$$P_{0,\,rms}' = \frac{1}{2}(\rho(\overline{U} + u')^2 - \rho\overline{U^2}) = \frac{1}{2}\rho u'^2_{rms} + \rho\overline{U}u'$$

to find the rms u' value. This was justified on the grounds that the static pressure change on a jet centreline had been measured previously to be only 5% of the dynamic head below the external static. He did not, however, consider the implicit assumption that the static pressure does not fluctuate.

Calibration against a hot wire showed that the turbulence levels derived from his pressure measurements needed to be multiplied by a factor of about 4 at dynamic pressures above about 10 N/m^2 (and typically the flame gave about 70 N/m^2). No explanation for this was suggested, but it seems likely that it was due to a calibration error as the microphone was only calibrated at zero mean pressure.

Mizutani, Nakayama and **Yuminata (1975)** used a similar technique to measure turbulence in a premixed turbulent Bunsen-type flame. Again, they used a supply tube of 2.16 mm bore but had a smaller (0.6 mm) hole at the tip to damp out organ-pipe resonances. They also left a gap around the microphone body to increase the damping at this end. The cut-off frequency, however, was still only about 5 kHz. Turbulence intensities of about 3% were measured. Again, non-linear effects were experienced due to the pressure drop across the microphone.

Le Bot, Charpenel and **Michard (1978)** used a piezo-electric pressure transducer to measure turbulence at exit from a gas-turbine combustion chamber. The transducer diaphragm (protected by a layer of silicone rubber about 1 mm thick) was flush with the end of a water-cooled pitot probe. This avoided any organ-pipe resonance or damping problems, but required a pitot head 10 mm diameter to hold the transducer and the cooling passages. The rubber gradually charred during the test, having a useful life of about 30 minutes. This gave good results, and agreed well with hot-wire measurements in a cold flow, assuming simply that $\dfrac{P'_0}{(\bar{P}_0 - p)} = 2 \times \dfrac{u'}{\bar{U}}$ which was confirmed by calibration in a cold flow.

Figure 1.3 shows their results, with and without combustion. The hot case shows a great decrease in the turbulence below 200 Hz, but above this there is little change except for a strong combustion instability resonance at about 500 Hz that is apparently normal for this combustor.

The paper says that the probe had a frequency response of about 300 kHz, but there was no evidence to support this - and the roll off of the spectrum at about 20 kHz looks very much as if it might be a result of electronics bandwidth limitations (or perhaps the size of the probe) rather than a genuine feature. The fact that the hot and cold *frequency* spectra are so similar despite presumably having very different exit velocities supports this idea, as this implies a change in the *wavenumber* spectra which (as the results to be presented in Chapter 4 will show) is most unlikely. No details of the combustor design were given.

In a later paper from ONERA **(Charpenal et al, 1980)** optical techniques are used to determine fluctuating temperatures within a combustor flame, and the temperature spectra are compared with spectra from their cooled pressure transducer probe and from an laser anemometry system. No units are given, however, and it is not clear whether the frequency response of the system has been improved.

Mauer and Liu (1987) built a capacitative dynamic pressure probe that could be used at high temperatures without cooling. They made the diaphragm of Macor (machineable ceramic); this was coated with metal to make it electrically conducting. The transducer had a cut-off frequency of 250 Hz, and could be used up to 650 °C. Use of a material with a higher temperature capability, and large supply ports, might raise these limits to a few kHz and 1600°C. The diameter of diaphragm required to achieve a reasonable capacitance (5-10 mm) is, however, too large to measure small turbulent eddies (wavelength 1-2 mm) if mounted flush with the end of a pitot probe; and a small feed tube, as in the microphone experiments of Ebrahimini et al would reduce the frequency response considerably. Thus use of this transducer to measure small-scale turbulence would be very difficult if not impossible.

Jenkins (1987) has investigated the effect of the shape of the nose of a pitot tube on the accuracy of turbulence measurements. He found that with the Kulite transducer flush with the end of the probe the dynamic head measurement was about 4% low. He concluded that the sensing area of the diaphragm, at ⅓ of the overall diameter, was large enough to experience the radial velocities around the actual stagnation point. To avoid this he tried three different shapes of pitot tip protruding 2-6 mm beyond the kulite. He found that although the protruding tips could improve the insensitivity to incidence, they also reduced the frequency response, could lead to resonance and did not remove the original 4% error.

Nina and Pita (1985) developed a compensation technique to improve the frequency response of fine wire thermocouples. They used wires down to 15 μm diameter which gave a 5 ms time constant at a typical velocity of 13 m/s, and measured spectra up to frequencies of the order of 1 kHz. The compensating amplifier allowed compensation for time constants in the range 0 to 30 ms, and it was found that the response was very sensitive to the correct choice of time constant τ; overestimating τ by 50% led to a 50% error in the rms temperature measurement. This is a serious drawback as the time constant must be a function of the instantaneous velocity and temperature. It appears that a great deal of development and evaluation would be required before such a system could give an accurate measurement of temperature fluctuations in the flow from a combustor.

1.2.3 Conclusions.

High frequency response pressure transducers are a more practical technique than laser anemometry for measuring turbulence spectra. A small probe diameter is required for resolving details of the small-wavelength turbulence structure.

1.3 COMBUSTION CHAMBER TURBULENCE.

1.3.1 Introduction.

Experimental research into combustion chambers can be divided into three areas:-

(1) cold "model" combustors, with air or water flow, to confirm flow prediction techniques in the absence of combustion;

(2) "idealised" combustion experiments, looking at flames that are typically free-standing or stabilised over a rearward-facing step. These attempt to confirm the accuracy of combustion rate predictions, but lack the complex geometry of real combustors;

(3) tests on realistic gas turbine combustion chambers.

The latter are the most relevant when considering the nature of the turbulence that enters the turbine - but the majority of published papers belong to categories (1) and (2), as these were both easier to set up and of more fundamental benefit to people trying to study combustion processes. Most combustion researchers have attempted to validate combustor design methods against idealised flame structures, and as such have neither tested genuine combustors nor bothered to measure in any detail the turbulence structure that is passed on into the turbine.

The papers referred to here are the most relevant but the only one to give a turbulence spectrum to a usefully high frequency is that by **Le Bot et al (1978)** (§1.2), and it appears that even this suffers from limitations of instrumentation bandwidth.

1.3.2 Combustor measurements.

Dils (1973) used thermocouples protruding from the leading edge of nozzle guide vanes in a 15000 lb thrust gas turbine to investigate the flow structure from the combustor; he was primarily studying the effect of fluctuating temperatures on NGV oxidation rates. He measured large temperature fluctuations (120 K rms at take-off conditions) at frequencies of up to 300 Hz and concluded that these were due to transverse movement of dilution hole jets which had not fully mixed out; the frequencies were harmonics of organ pipe resonances within the combustor casings.

Schafer, Koch and Pfeifer (1977) used LDA to measure the turbulence from an annular SNECMA combustor. They found turbulence levels of 12% at an exit velocity of about 130 m/s. The peaks in mean velocity (presumably corresponding to hot spots) were associated with below-average turbulence levels, suggesting that most of the turbulence is generated by the mixing of the secondary cooling air rather than by the combustion process. No frequency measurements were taken.

Goldstein, Lau and Leung (1983) used LDA to measure the turbulence at exit from a pair of General Electric combustion chambers, and compared this with results from simple premixed-gas burners that were basically a straight tube with a burner at one end. No exit contractions were used.

They found that in the real combustors, combustion reduced the fractional turbulence intensity from about 30% to about 16%. They concluded that the mixing of the secondary (dilution) flow was the dominant factor in producing this turbulence.

The premixed burners showed no similarity to the real combustors in terms of turbulence level, indicating that turbulence measurements taken in "idealised" premixed combustors are unlikely to be of any value for predicting typical turbulence levels in a gas turbine; a realistic geometry is essential for this kind of measurement. No frequency spectra were taken.

Bicen and Jones (1986) have measured turbulence in a realistic model combustion chamber using LDA. This was run both cold and hot (burning propane, *AFR* = 40 giving about 1100 K temperature rise). They measured about 12% turbulence intensity (at mid-height, after an exit contraction) when cold; about 16% with *AFR* = 70; and about 21% with *AFR* = 40. There was also a notable change in the exit velocity profile, from basically flat with a central low-speed region when cold to a hot exit profile that rose from slow at the edges to fast in the centre. The large amount of exit swirl and flow non-uniformity in the cold case made the definition of turbulence difficult here, to the extent that these changes cannot really be used as an indication of any trends. No attempt was made to measure a frequency spectrum.

Heitor and Whitelaw (1986) did a similar experiment on the same combustor, but included the use of preheated air so that the same exit temperature could be achieved over a range of fuel-air ratios; they also traversed across the exit at various heights. This gave a turbulence intensity of Tu $\approx$ 26% at AFR=70 and 52 - *i.e.* it was not much affected by fuel-air ratio. The exit flow was still very non-uniform in terms of mean velocity, exit angle and turbulence intensity, presumably as a result of the swirling flow from the combustor passing through an asymmetric exit contraction.

They also measured fluctuating temperatures using a 40μm thermocouple compensated to give a frequency response up to 2 kHz; this showed temperature fluctuations of up to 12% (rms) of the temperature rise. Again, no frequency spectra were measured.

Ames and Moffat (1990) used a combustor simulation model to generate representative turbulence over a flat plate in a wind tunnel, and took comprehensive hot-wire measurements of the turbulence. Their work is discussed in Chapter 10.

1.3.3 Conclusions.

Prior measurements of turbulence spectra and length scale from a combustion chamber were not available and so were essential as part of the present study. Such tests as had been done suggested that combustion had an effect on the turbulence intensity and that this would have to be measured. It was also clear that the testing would have to be done on a realistic combustor as opposed to a bunsen-burner type flame.

1.4 HEAT TRANSFER EFFECTS OF TURBULENCE.

1.4.1 Introduction.

Facilities for the measurement of heat transfer are usually classified as being "flat plate", which approximates to an idealised situation of a constant velocity along the surface, or "cascade", which attempts to more closely simulate an engine environment by taking measurements in the varying velocity field around a series of aerofoils. The former allows easy comparison with theoretical predictions and facilitates interpretation of the results, while the latter gives a better indication of what may happen in a particular engine.

Most measurements have traditionally been taken with low (0 - 4%) freestream turbulence intensities as these are relatively easy to produce and are approximately isotropic; only a few people have investigated the effects of higher turbulence levels. Much of the original work on heat transfer was done at a time before digital processing techniques became available so very few high-frequency turbulence measurements were taken. The papers described here will give an indication of the most relevant advances to date.

1.4.2 Papers about turbulent effects on heat transfer.

One of the earliest attempts to study the effect of turbulence on heat transfer was that of **Sugawara et al (1953)**. They used a transient technique in which the temperature of a pre-heated steel plate was measured while cold air passed over it in a wind tunnel. A turbulence level of 7.3% was found to modify the boundary layer profile and increase Nusselt numbers by about 55%.

Bayley and Milligan (1977) used a rotating squirrel cage of bars to generate high levels of non-isotropic turbulence upstream of a cascade of turbine blade sections. Thermocouples on the blade surface (plus some internal cooling) were used to derive an external heat transfer coefficient. By changing the size of the bars they could vary the turbulence level, and by changing the rotational speed they could vary the frequency characteristics of the turbulence. Turbulence levels of up to 40% were produced; heat transfer coefficients were increased (above the turbulent level) by up to 50% on the leading edge and pressure surface. The large bar, high turbulence, grids that generated discrete frequencies showed a larger effect when rotated faster to give higher frequencies. This was however partly masked by changes in Reynolds number and is not a definitive result.

Later testing by **Priddy and Bayley (1985)** used a similar technique but attempted to produce lower turbulence intensities, at higher frequencies, to more closely simulate conditions in an engine; they also did a comparison with a static grid of bars. This showed that at a turbulence level of 17% the effect of rotating the cage was to increase the pressure surface and leading edge heat transfer coefficient by about 20%; the suction surface was little changed. Unfortunately the paper does not show frequency spectra for the various conditions to compare the fixed grid with the squirrel cage.

They concluded that the effects of frequency were not significant at turbulence levels below 20%, and that the aerofoil shape was more important in determining the heat transfer coefficient. In their case the pressure surface acceleration was just sufficient to keep the boundary layer transitional for much of its length, and it was thus very sensitive to disturbances.

Dils and Follansbee (1977) measured heat transfer coefficients to 6.3 mm diameter bars placed in the exhaust from a combustion chamber at a temperature of about 1300 K. The bars were uncooled and the heat transfer coefficient was determined by relating surface temperature fluctuations (using sputtered gauges) to thermocouple measurements of the local gas temperature.

Turbulence was measured by LDA, which gave Tu = 8.2% to 17.5% with a bandwidth of up to 35 kHz. Their combustor produced pulsating velocity and temperature waves; they described it as a non-linear amplifier of supply pressure fluctuations, with positive gain up to 1 kHz. By adjusting the airflows it was possible to obtain narrow- or broad-band waves, with peaks at 30, 200 and 700 Hz. The fractional temperature fluctuation was in the range 5.5% to 17.2% with a compensated fine wire thermocouple giving a 0-1 kHz bandwidth.

They found an increase in stagnation point heat transfer coefficient above the expected laminar level of about 50% at 15% Tu. Attempts to correlate the Nusselt numbers against Tu were unsuccessful, and they concluded that small-scale turbulence features, which they were unable to measure, were responsible for most of the observed enhancement.

Simonich and Bradshaw (1978) measured heat flux from a tripped boundary layer on a flat plate. Heat transfer was calculated from the plate to air temperature difference at a given (electrical) heat input. Length scales and spectra were not measured directly, but a scale was deduced from the rate of decay of the turbulence. They concluded that turbulence increases the heat transfer more than it increases skin friction; if the increase in Stanton number is described by a factor A_θ:

$$\frac{St}{St_0} = 1 + A_\theta \left(\frac{u'}{U}\right)_{rms}, \qquad A_\theta \approx 5$$

whereas the corresponding equation for Cf / Cf_0 would have $A \approx 3$. It appeared also that A_θ decreased as L_e^u / δ_{995} increased (as Hancock found for skin friction), but they could not rule out the possibility of this being a Reynolds number effect as it was only at low Reynolds numbers that large L_e^u / δ_{995} ratios had been obtained.

Hancock (1980) measured velocity profiles in a turbulent boundary layer (Re_θ < 2000) on a flat plate to determine the skin friction coefficient. This was done with a variety of grids; the distance between the plate and the grid was also varied so that some independent change in Tu and length scale could be achieved. He managed to vary the ratio of length scale to boundary layer thickness (at a constant turbulence intensity) in the range $0.74 < L_e^u / \delta_{995} < 4.9$; this was much further than previous workers, who had tested with $0.65 < L_e^u / \delta_{995} < 1.2$. From this he derived an empirical parameter combining the turbulence intensity and length scale against which the skin friction could be correlated:

$$\beta = \frac{\left(\frac{u'}{U}\right)_{rms}}{\left(\frac{L_e^u}{\delta_{995}} + 2\right)}$$

His data is shown plotted against this parameter in Figure 1.4.

Blair (1983) studied the effect of free-stream turbulence on turbulent boundary layers on a flat plate in the large scale UTRC boundary layer wind tunnel.

He used a plate mounted on one of the tunnel side walls with a boundary layer bleed to fix the origin of the boundary layer. Turbulence grids were placed a considerable distance upstream of the plate to achieve homogeneous conditions and slow decay rates along the plate; this meant that they had to be placed in front of the working section inlet contraction, which limited him to a maximum of 7% Tu.

He concluded that both skin-friction and heat transfer were increased by up to 20% by the turbulence. Attempts to correlate the change in Stanton number (relative to a low turbulence case) showed that this could not be done purely by using the turbulence intensity - but that St/St_0 could be correlated against a similar parameter to that used by Hancock with the addition of a Reynolds number term:

$$\frac{Tu}{\left(\frac{L_e^u}{\delta_{995}} + 2\right) \times \left(1 + 3e^{-\frac{Re_\theta}{400}}\right)}$$

based on data taken at Reynolds numbers in the range $1000 < Re_\theta < 7600$.

Castro (1984) did a similar study to Hancock, but looked at lower Reynolds number turbulent boundary layers ($Re_\theta < 2000$). He produced a couple of empirical correlations to relate the change in skin friction to turbulence intensity, Re_θ and length scale.

Hancock and Bradshaw (1989) used crossed hot wires to measure turbulence parameters in a large scale, low speed flat plate boundary layer while varying the freestream turbulence level and length scale. The boundary layer was heated so that a temperature sensor mounted close to the hot wires could discriminate between boundary layer and freestream measurements in the intermittent outer regions of the boundary layer. They achieved values of L_e^u / δ_{995} from 0.7 to 2.7 at turbulence levels of 2.5, 4 and 5.8%. They found that compared to the low turbulence, long length scale cases the presence of turbulence at short length scales reduced the u', v' and $u'v'$ parameters in the outer part of the boundary layer. This was explained in terms of a reduction in the velocity gradient (and a change in the velocity profile) there. The same reduction was seen when studying a conditional correlation $\overline{u'v'}$ of the heated boundary layer air which strengthens the premise that it is the velocity gradient produced by the freestream turbulence that affects the boundary layer.

They concluded that the effect of turbulence on the outer regions of the boundary layer should be a function of $e = \dfrac{u'_e \delta_{995}}{U_e L_e^u}$.

No measurements of heat transfer or skin friction were presented with these results.

Krishnamoorthy, Pai and Sukhatme (1988) used a hot gas cascade tunnel to determine the effects of combustor exit flows on cascade heat transfer. They found that a correlation for the effects of turbulence on heat transfer, if based on turbulence measured with a cold flow, gave a good approximation to the hot flow case and concluded that the turbulence produced by a combustion chamber was mainly a function of the combustor geometry.

Krishnamoorthy and Sukhatme (1989) measured the effect of turbulence on heat transfer to NGV and blade cascades in a blowdown tunnel. The aerofoils were made from a resin moulding covered with a thin, electrically heated stainless steel sheet; an array of thermocouples measured the temperature of this to allow heat transfer coefficients to be calculated.

The aerofoil suction surfaces had laminar boundary layers and showed little increase in heat transfer when subject to grid generated turbulence. The pressure surfaces were turbulent or transitional and exhibited increases in heat transfer coefficient of up to 30% at inlet turbulence levels of about 7 to 12%. They obtained correlations for the effect of local turbulence levels as follows:

Laminar boundary layers:	$h = h_0(1 + 0.04Tu)$	at $Tu < 2\%$
	$h = h_0(1 + 0.44Tu^{0.55})$	at $2\% < Tu < 12\%$
Turbulent boundary layers:	$h = h_0(1 + 0.0235\mathrm{Tu})$	at $Tu < 36\%$

Guenette et al (1988) used a rotating turbine facility to simulate every non-dimensional aspect of flow in an engine except for the combustor turbulence and radial temperature field. They found that heat transfer levels were similar to those measured in non-rotating cascade experiments and were lower than experienced in engines. This led them to conclude that turbulence and temperature profile effects were the most important areas for future study.

MacMullin et al (1989) used a wall jet to generate turbulence intensities of up to 18% over a flat plate. This gave a fixed ratio of intensity to length scale, though towards the rear of the plate they did achieve some variation in length-scale to boundary layer thickness because the b.l. thickness was increasing. Stanton number enhancement factors of up to 1.8 were measured; these were, however, relative to a predicted low turbulence datum as the tunnel could not produce a low turbulence flow. There was considerable scatter in the results, but in general they showed about 3x the enhancement seen by **Blair (1983)** at about 3x the value of his correlating parameter (similar to Hancock's). Length scale effects were not evident.

Maciejewski and Moffat (1989) used a free jet to provide very high turbulence intensities (20% - 60%) over a flat plate. They found that the heat transfer coefficient was best described by $h = 0.019 \rho\, Cp\, u'_{rms}$ and conventional boundary layer correlations were not required. This result is discussed further in Chapter 10.

1.4.3 Conclusions.

Heat transfer coefficient enhancement factors of up to 80% have been found under high freestream turbulence intensities. Most work has, however, concentrated on turbulence intensities < 7%. Some researchers have found that the enhancement can be correlated against a function of intensity, scale and boundary layer thickness (**Hancock**); the scatter in other results plotted against this parameter suggests that this may not be suitable at higher turbulence intensities.

1.5. TURBULENCE GENERATING TECHNIQUES

Gad-el-Hak and Corrsin (1974) used a grid with jet injection to modify the turbulence production. Injection in the main flow direction reduced the grid pressure drop and turbulence level, while injection upstream increased it. It would seem however that very high turbulence levels, whether from a high blockage grid or from strong upstream injection, are always associated with inhomogeneous conditions.

It was found that the decay rate was slower with injection; this could not be explained. (It had been thought that more energy at lower frequencies would be needed to give a slower decay rate, but the spectra did not seem to be significantly different here). Coflow injection gave a slightly smaller integral length scale than the zero or counterflow cases.

Tassa and Kamotani (1975) carried out a similar experiment at a slightly lower blowing rate, and found that the turbulence intensity increased with injection in either direction. The decay rate was no different to the passive case. (This may be due to small differences in the grid configuration).

Hancock (1980) used crossed bar grids in his experiment, but a parallel bar grid was also tested for comparison. He found that if the crossed bar grid was biplanar (with the bars crossing over each other, rather than like a perforated plate) there was a tendency for the flow to be unsteady - there were several possible flow patterns, and small changes to the tunnel would make it flip from one to the other. The reason why this happened with some grids but not others was unclear.

The choice of a crossed bar grid was based on it giving less anisotropy close-up, so it reaches isotropy quicker - and thus the plate can be put closer to the grid, in higher isotropic turbulence levels than would be available from a parallel bar grid.

Hancock, with **Thomas (1977)**, had previously investigated the effect of a solid wall on the turbulence. They used a belt moving at the freestream speed to avoid any turbulence generation due to boundary layer shear. They found at high Reynolds numbers that while the high frequency u' (axial) component increased near the wall, the normal component was reduced by the presence of the wall at distances from it of up to twice the integral length scale (and the low-frequency components more so). This could explain why turbulence with a much larger length scale than the boundary layer thickness does not appear to have a large effect on the skin friction - it is attenuated before it can get close enough to the wall to interact with the boundary layer.

Meier and Kreplin (1980) achieved a wide range of length scales, at apparently similar intensities, by using grids before and after a contraction. This was at an intensity of only about 0.25% however, and as they did not measure the energy of the transverse components the total turbulent energy may have been different in each case.

Pelfrey and Liburdy (1986) studied the turbulence characteristics of a free jet that curved to attach to a wall. This gave very high turbulence intensities (up to 100% on the convex side of the jet); it was very anisotropic with $\frac{u'}{v'} \approx 4$. Where the jet attached to the plate, the turbulence intensity (measured by LDA) was about 50%; this fell to about 20% further downstream as the mean velocity increased away from the stagnation point, and the flow also became roughly isotropic-so it could be used to generate high turbulence levels for a flat plate experiment.

This is not, however, ideal; the way the velocity changes with distance from the stagnation point is even less typical of the start of the boundary layer on a turbine blade than is a "conventional" flat plate experiment. Spectra were not measured.

Roach (1987) has made a comprehensive survey of grid performance with regard to both pressure drop and turbulence characteristics in a parallel duct. He studied parallel and crossed bar grids (round and square bars) and perforated plates. The very inhomogeneous region immediately downstream of the grid was avoided by only using measurements taken at more than ten bar diameters from the grid.

He found that the turbulence intensity decayed as:

$$Tu = 0.8\left(\frac{x}{d}\right)^{-\frac{5}{7}}$$, where d is the bar diameter.

Typically $u'/v' \approx 1.25$, but there was considerable scatter between experiments and he suggests that this may be due to uncertainties in the calibration of crossed hot wires used for the v' measurements, rather than genuine anisotropy.

His experiments agreed well with theoretical predictions for the shape of a isotropic turbulence spectrum (§A.1.3) up to $f = \frac{2U}{\Lambda_x}$, above which the theory overpredicts the energy; this suggested to him that (except for a small fraction of the total energy at high frequencies) the grid-generated turbulence <u>is</u> effectively isotropic without a contraction.

He derived a correlation for the turbulence intensity and spectra from bar grids, which is discussed in §6.5. The correlation is based purely on bar diameter and distance from the grid. The bar spacing (solidity) is only relevant in so far as it determines the pressure drop and the distance required for the flow to become homogeneous. Excessive solidity (> 50%) must, however, be avoided as it can cause instability in the flow.

1.6 VARIATION OF TURBULENCE LEVEL THROUGH A CONTRACTION.

1.6.1 Introduction.

An understanding of the effect of acceleration on turbulence levels and spectra is required, both to determine how it will vary through a turbine and to predict which combinations of grids and contractions would give useful turbulence conditions in a wind tunnel.

1.6.2 Papers about turbulence development.

Uberoi (1956) measured how turbulence from a bar grid was affected by contractions of 4:1, 9:1 and 16:1. He assumed that the u', v' and w' components of the turbulence could each be calculated independently by considering the effect of the contraction on the vorticity. This is a different approach to the "frozen turbulence" assumption used by **Zerkle and Lounsbury (1988)**, (and others) that takes u', v' and w' as staying constant.

On this basis a contraction ratio c ($c > 1$) would produce $\left(\frac{u_2'}{u_1'}\right)_{rms} = \frac{1}{c}$ and

$\left(\frac{v_2'}{v_1'}\right)_{rms} = \sqrt{c}$ for discrete vortices. He quotes **Ribner and Tucker (1952)** as using

this to derive formulae for a continuous vorticity distribution:

$$\frac{\overline{u_2^2}}{\overline{u_1^2}} = \frac{3c^{-2}}{4}\left(\frac{1+C}{C^{3/2}}\tanh^{-1}\sqrt{C} - \frac{1}{C}\right) \approx \frac{3c^{-2}}{4}(\log 4c^3 - 1) \quad \text{for } c >> 1$$

$$\frac{\overline{v_2^2}}{\overline{v_1^2}} = \frac{3c}{8}\left(\frac{1+C}{C} - \frac{c^{-6}\tanh^{-1}\sqrt{C}}{C^{3/2}}\right) \approx \frac{3c}{4} \quad \text{for } c >> 1$$

where $C = 1 - c^{-3}$. This "linear theory" is shown to be approximately correct for a 4:1 contraction, but to be less accurate at larger contractions.

It can be seen that these changes in u' and v' imply that the total turbulence energy $\overline{u'^2} + \overline{v'^2} + \overline{w'^2}$ is almost constant through the contraction - and so, once isotropy has been reached further downstream, the value of $\overline{u'^2}$ will be roughly the same as before the contraction if one neglects decay processes. This is the justification for the "frozen turbulence" assumption mentioned above.

Uberoi also presented measurements of turbulence spectra before and after contractions. It appears that in general the effect of a contraction c on a graph of power spectral density is as follows:

(1) the spectrum is moved *down* by the change in Tu^2 (derived from the expressions above and the change in mean velocity).

(2) the spectrum is moved to the *left* by a factor c, implying an increase in length scale.

(3) to preserve the total turbulent energy as implied by the definition of power spectral density, the reduction in wavenumber (2) above must be accompanied a *rise* in PSD by the same factor.

His results show that the transverse components v' and w' closely follow this rule; the axial spectrum is distorted, with less power at low wavelengths and more at high wavelengths which must represent a small reduction in length scale on top of the increase mentioned above.

1.6.3 Summary.

Passage area contractions change both the fractional turbulence intensity and the ratio of axial to transverse rms levels. As the turbulence decays after the contraction it tends to become isotropic again, but this may be a slow process. The effect of the contraction on the intensity and length scale can be predicted, though the accuracy of the technique is poor for high contraction ratios.

CHAPTER 2.

COMBUSTOR TESTING - EXPERIMENTAL DETAILS.

2.1 INTRODUCTION.

This chapter describes the test facility and the design of the probe and apparatus for the combustor experiments. Circuit diagrams have been included where they might be of value to anyone wishing to use the apparatus in future, together with calculations used in the preliminary design of the probe. More detailed calculations of the probe performance and calibration are included later, in Chapter 3.

2.2 COMBUSTION TEST FACILITY.

The choice of test facility (air compressor, fuel supply, pipework and combustion chamber) for the combustion turbulence measurements was based on the requirements that it should use a genuine combustion chamber and discharge nozzle, as opposed to some idealised experiment on a simple flame; it should achieve realistic fuel: air ratios, but run at atmospheric exit pressure to simplify traversing and to reduce heat transfer to the probe relative to engine conditions (which are typically at much higher pressures); and it should already exist. It was felt that the construction of a facility from scratch was out of the question in the time available, and that the difficulty of satisfying fire safety requirements on the sites available would have been prohibitive.

The Combustion Department at DRA RAE (Pyestock) has a test facility that fulfilled all of the requirements, and very kindly agreed to its use for this project. The facility consists of an electrically driven Reavel compressor that supplies air to the combustion chamber via a long pipe, which may be heated by an auxiliary combustor to increase the supply temperature up to 700 K. The pipe protrudes through the wall of the compressor building about 1.5 m above ground level and the combustor under test is mounted on the end of it. The combustor is thus outside the building, which minimises any fire risk. The combustor exhaust is a free jet from the discharge nozzle into the atmosphere, which facilitated the design of the traverse mechanism as a free standing unit could be used without any need for passing the probe into a duct or sealing it against leakage. The facility is shown in Figure 2.1.

The combustors tested were can type (as opposed to fully annular). As they are being used individually, rather than as a ring of interconnected units as in the engine, the facility uses a purpose built combustion outer casing instead of a real engine one.

The combustion part of the facility worked very well and proved well suited for the test program, though some form of weather protection would have avoided the need to store the equipment indoors overnight and set it all up again in the morning, a process which took about 3 hours each day.

2.3 TYPES OF COMBUSTION CHAMBER TESTED.

Three combustion chambers were tested; they will be denoted here as **A**, **B** and **C**. They differed mainly in the design of the burner and head region, and all were very similar in terms of overall size and appearance.

A was from a Rolls-Royce Spey engine, of the type that would have been used on a Nimrod aircraft.

B used the RAE "Pepperpot" design, as described by **Cottington, Hakluytt and Tilston (1987)**. In this the fuel flows over the inside surface of the conical "head" end of the combustor and is mixed with the primary zone air by being ingested into jets of air blowing through holes in this surface. The downstream walls were of "transply" with straight-cut dilution holes instead of the plunged holes in a standard Spey combustor.

C was from a diesel burning marine Spey engine, and used a "RAB" burner in which the flame is stabilised by an annular vortex induced by a ring of small cooling holes about one third of the way along the outer wall.

It was not possible with the time and facility available to study the turbulence in a rigorous engine environment, nor to use an annular combustor that would be typical of most large engines. Three different combustor designs were used, however, in the hope that this would show whether the turbulence was strongly dependent on the geometry of the head region and thus might be expected to vary considerably from one engine to another.

Similarly it was hoped that the use of two fuels (paraffin and diesel) burning at two different rates would show whether one could expect a very different turbulence level in a real engine with a faster burning rate because of the higher pressure there. If this was the case a subsequent test at high pressure would be an important area for further research.

2.4 DESIGN OF TRAVERSE MECHANISM.

The requirement that the probe should be briefly inserted into the flame and then removed to cool down again could be met either by inserting the probe into the flame, pausing briefly and then withdrawing it back the way it came, or by passing the probe right through the flame and out the other side. The latter technique was chosen both for ease of manufacture and because it would give a better indication of position and uniformity within the flame.

The probe was mounted on a swinging arm, with the transducers at a radius of 0.5 m from the pivot (see Figures 2.1 and 2.2). This allowed the probe to be long enough to reach to the side of the flame furthest from the mechanism without the flame touching the mechanism itself; to avoid possible vibration problems, the arm was designed to be no longer than strictly necessary.

The arm was moved by a connecting rod from a crank driven by an electric motor. A windscreen wiper motor was chosen because it included a worm reduction gear to give a usefully high torque at a low speed, and had a built-in microswitch to make it stop in one position; also, being a DC motor, the speed could easily be controlled.

This microswitch was used to park the arm in the lower position after passing down through the flame. A second microswitch was used to make the motor stop again when the probe was returned to its upper position; this both disconnects the power supply and short circuits the motor leads to make it stop quickly.

A voltage regulator circuit was built onto a commercial 14 V dc power supply, with a switch to select output voltages of 3.3, 4.6, 6.2, 8.3, 11.3 or 13.7 volts, which gave flame transit times from approximately 390 ms to 87 ms.
A "RUN/START" switch was provided to bypass the microswitches and start the motor. Once started, the switch was returned to the "RUN" position so that parking would occur automatically when the probe reached the end of its traverse. This unit was operated from within a porta-cabin about 4 m from the combustor, via 15 m cables passing out through the door in the rear of the cabin. The circuit used is shown in Figure 2.3.

The swinging arm was counter-balanced to minimise the load on the motor, and the linkage was designed so that once the motor had reached a constant speed the probe velocity would be roughly constant while it passed through the flame.

A pair of LED/photo-transistor switches were used to trigger the transient recorder as the probe entered the flame. These detected rows of holes along the edges of an aluminium quadrant.

Along the outer edge of the quadrant there was a continuous row of holes at 2.25 mm pitch. The transient recorder was triggered when the opto-switch detected the first of these; they could be covered over with insulating tape to modify the apparent position of the first hole in the row, which allowed the trigger position to be changed to suit the sampling rate and flame position. The time axis is defined in the original data such that $t = 0$ is the point at which the transient recorder was triggered (data is, however, recorded prior to this using the pre-trigger facility), and thus does not correspond to any probe position in particular. The inner edge of the quadrant had three holes in it, spaced as a single hole some distance from a close pair. The appearance of the signal from these could be used (if there was any doubt) to confirm the direction of the traverse.

Preliminary testing showed that the motor and worm gear were producing a torsional vibration of the crank, and this could affect transducers mounted on the swinging arm. This was overcome by fixing a large flywheel to the crank, and connecting the crank to the motor via a flexible coupling using a pair of small rubber grommets on drive pins at a radius of 10 mm from the shaft centreline.

Figure 2.4 shows the motion of the probe (calculated from the opto-switch signals) while driven through the combustor exit flame by the traverse mechanism. The position has been defined here as being relative to the single hole out of the row of three that indicate traverse direction, and positive upwards. The positions of the holes in the opto-switch quadrant are shown on the left of the graph.

The "upwards, time reversed" line in Figure 2.4 allows the probe speed to be compared for the upwards and downwards directions. The upwards traverse gives a speed of 0.46 m/s, and the downwards one gives 0.455 m/s ±17%. This is close enough for most time series data to be plotted against time instead of position, which is highly desirable. In all subsequent figures in which downwards and upwards traverses are compared (*eg.* Figure 2.8) the time values have been reversed for the "upwards" data so that measurements from each point in the flame can easily be compared, and adjusted by eye to allow for the arbitrary nature of the start time. This was felt to be more practical than attempting to measure the probe position accurately for each test (which would have roughly halved the data acquisition rate) and calculate a time offset, particularly as the latter would also have required frequent measurements of the combustor position. The probe tips (see below) were positioned in the centre of the flow at approximately x = -21 mm (thermocouple), 1 mm (thin film), 15 mm (kulite) and 33 mm (pitot).

The whole mechanism was mounted on a horizontal bar, along which it could be slid to vary the position of the traverses through the flame, and supported by a tripod made from 100 mm square steel tube. This could be dismantled easily for transportation by car.

2.5 DESIGN OF PROBE.

The probe had four sensing elements that were all at the same radius from the pivot point of the arm, and were spaced 20 mm apart in the direction of motion. From top to bottom in Figure 2.5 they are:

(1) a slow response pitot connected to a Sensym type LX1601D pressure transducer via 400 mm of 1 mm bore tubing to obtain a drift free measurement of total pressure through the flame,

(2) a fast response pitot probe containing a flush mounted Kulite pressure transducer,

(3) a thin film heat transfer gauge painted on the hemispherical end of a pyrex rod,

(4) a 25 μm type R Platinum/Platinum-Rhodium thermocouple.

A type XCW-062/15 Kulite pressure transducer was used for the fast response probe. The "W" (low impedance) designation was chosen to give the lowest possible electrical noise (see formulae for Johnson and shot noise, **Horowitz and Hill, 1989**), but this appears to have been unnecessary as later tests on a high impedance XCS type showed no increase in noise.

A 15 psi Kulite was chosen on the basis that this would give a reasonable signal to noise ratio without having too low a resonant frequency. A layer of silicone rubber cast on top of the diaphragm was used to protect it from particle impact and to increase its mass to avoid an excessive temperature rise while passing through the flame. Consideration of the likely effect of this on the resonant frequency led to a rubber thickness of 0.2 mm being requested from Kulite, but examination on delivery suggested that the rubber layer was actually about 0.4-0.5 mm thick.

The thickness of rubber required to protect the transducer diaphragm was chosen as follows:

Highest expected flame temperature = 1300 K.

Typical flow Mach number = 0.3 (facility data).

This gives typical values of Cp = 1242 J/kgK, μ = 4.875 $\times$ 10^{-5} kg/ms, k = 0.0866 W/mK, and Re = 1.09 $\times$ 10^{6} m^{-1}.

The Nusselt number at the stagnation point of a sphere may be predicted (**Kays and Crawford, 1980**):

$$Nu_R = \frac{hR}{k} = 0.93 Pr^{0.4} \sqrt{Re_R}$$

At these conditions, and assuming a surface temperature of 300 K, a heat flux of 1.9×10^6 W/m^2 is obtained. This prediction for a sphere may over-estimate the heat flux to a square ended cylinder, but it is probably accurate enough for design purposes.

The silicon diaphragm thickness was stated to be 0.0125 mm by the manufacturers; this was checked roughly by calculating the resonant frequency that this would give. **Harris and Crede (1961)** state that the natural frequency of a flexing plate may be calculated using:

$$f_n = B\sqrt{\frac{Et^2}{\rho d^4(1-\nu^2)}} \times \frac{1}{2\pi}$$

where B = 11.84 for the first mode of a circular plate with a clamped edge.

Taking Young's modulus $E = 1.03 \times 10^{11}$ N/m^2, Poisson's ratio $\nu = 0.345$, density $\rho = 2330$ kg/m^3 and diameter $d = 7.1 \times 10^{-4}$ m gives a resonant frequency of 335 kHz. The quoted resonant frequencies of typical transducers, which lie in the range 250 to 500 kHz, suggest that the diaphragm thickness is approximately as stated.

The heat flux level calculated above would raise the diaphragm temperature at a rate of approximately 90000 K/s, or 4500 K during a traverse lasting an estimated 50 ms. Semiconductor devices are usually limited to operation at temperatures below 110 °C, so a temperature rise of less than 90 K was chosen as a target. This requires a factor of 50 reduction in the warm-up rate.

It was felt that silicone rubber (also known as RTV, "room temperature vulcanising" rubber) would make an excellent protective coating because of its low stiffness (compared to silicon), easy castability and durability at temperatures well above the chosen limit. Calculation of the heat conduction through a rubber layer showed that the rubber and diaphragm would probably reach a uniform temperature soon after leaving the flame; the design can thus be based on a "bulk" temperature rise. Taking ρ = 1200 kg/m^3 and Cp = 1550 J/kgK for typical RTV rubber **(Schultz and Jones, 1973)** implies that a rubber layer 44 x thicker than the silicon diaphragm would be required to reduce the warm-up rate by a factor of 50.

The choice of transducer depends on a compromise between a thick diaphragm (with a high natural frequency, which will still be usefully high even after adding rubber) and a thin, more flexible diaphragm giving a higher voltage output (ie. a better signal to noise ratio). If it is assumed that the diaphragm is much stiffer than the rubber layer, the natural frequency of the diaphragm plus rubber ($f_{n,r}$) can be calculated as follows:

$$f_{n,r} \approx f_n \sqrt{\frac{\rho_{Si} d_{Si}}{\rho_r d_r + \rho_{Si} d_{Si}}}$$

The thicknesses of the diaphragms used in a variety of different Kulite transducers were estimated from their quoted resonant frequencies. An XCS062/15 transducer was chosen as best satisfying the requirements for sensitivity and resonant frequency; it has a natural resonant frequency of 250 kHz, reducing to 100 kHz when coated with a 0.15 mm thick rubber layer, and a nominal sensitivity of 13 mV/psi. This thickness of rubber was less than ideal as regards heat absorption, but it was expected that the temperature rise could be kept within reasonable limits by recessing the transducer slightly below the tip of the probe. A probe mounting that allowed the transducer to be recessed by up to 3 mm was designed and built.

The probe tip configuration is shown in Figure 2.6.
The need for a good high frequency response is illustrated by considering that eddies of 1.6 mm diameter (which is larger than a typical boundary layer thickness) would pass the probe with a frequency of 100 kHz if the velocity was 160 m/s.

Preliminary testing of the effect of recess distance showed that any recess in front of the diaphragm led to resonance problems. The rate of temperature rise was found to be acceptable without a recess so all subsequent tests were done with the diaphragm flush mounted.

The electrical resistance of the Kulite (across the bridge supply wires) rises linearly with temperature. This is used as a way of determining its temperature, to ensure that it is not in danger of overheating - the 15 V voltage regulator that powers it is supplied by a current mirror circuit that detects the current taken and gives a voltage output proportional to this (see Figure 2.7).

The Kulite, although supplied with a temperature compensation module, was found to drift severely with changing temperature - this is thought to be due to the silicon rubber layer, which is about 30x thicker than the diaphragm and will exert a force if there is a temperature gradient through it.

25 μm wire was chosen for the thermocouple because it was the finest type "R" size available. Figure 2.8 compares traverses in opposite directions, and shows that the response is fast enough to accurately measure the flame temperature.

2.6 INSTRUMENTATION.

The instrumentation layout is shown in Figure 2.9.

The Kulite signal was amplified 100x by a Fylde amplifier and passed through a Sallen and Key type anti-alias filter (ω_0 = 66 kHz). The thermocouple signal was amplified 100x by the other amplifier channel.

The output from the Sensym transducer was at about 7.5 V with no applied pressure. To reduce this to a level close to 0 V so that small changes in voltage could be resolved by the A-D converters this was passed through an OUEL CAS2 amplifier that amplified it ×2 and applied an offset. The signal from the current mirror Kulite power supply also passed through a channel on the CAS2. Here the gain and offset were adjusted to give a sensitivity of 0.1 V/°C. A digital voltmeter was used to display this continuously.

The thin film gauge was connected to an HTA1 heat transfer analogue circuit (**Oldfield et al, 1982**). Both the input and output of the analogue were recorded so that the change in heat flux as the gauge heated up could be determined. These recordings had to be taken on separate traverses to avoid electrical interference at the analogue input.

2.7 DATA ACQUISITION AND PROCESSING TECHNIQUES

A Datalab DL1208PG waveform recorder was used for all the data acquisition. This has eight channels each with a 12 bit analogue to digital converter, and is designed to be controlled either by switches on the front panel or remotely by commands sent along a GPIB interface from an IBM-compatible "PC" computer.

Initially a package called *Spiders DSP* was used for data capture and analysis. This provided a number of analysis options, but the lack of a dual sampling rate facility, limited graphics options and slow speed were a considerable handicap. To overcome this a data capture and analysis program "*DUCKS*" (described in Appendix A.2.1) was written and has proved invaluable.

Captured data is saved as files of Datalab input voltage. These are typically (if measuring turbulence) cut into a number of sections of 2048 points each; the Fast Fourier Transforms of each section are then averaged (Figure 2.10). Enough data is captured to allow between 40 and 80 FFTs to be averaged. This gives a reasonable FFT resolution (97.7 Hz at 200 kHz sampling rate) with much less random noise and smaller files than if the whole data sequence of up to 32768 points was Fourier transformed at once. The data is then scaled to convert to u'/U, and divided by files that correct for the frequency response of the anti-alias filter, amplifier, and transducer. This data is plotted as a power spectral density which is defined in terms of wavenumber rather than frequency (see §3.3). Plotting turbulence spectra against wavenumber allows results taken at different mean velocities to be compared in a meaningful way as turbulence wavenumber spectra, whether from bar grids or combustors, appear to be principally a function of the geometry of the turbulence generator and do not depend on velocity.

2.8 CALIBRATION PRIOR TO COMBUSTOR TESTS.

The first Kulite transducer (an XCW-062/15d with a silicone rubber layer over the diaphragm, but no screen) was tested in a shock tube in an attempt to measure the frequency response and the diaphragm resonant frequency. It was placed end-on in the tube on the basis that a resonant frequency of about 130 kHz was expected. If it had been placed side-on the shock would have taken 5 μs to pass the tip of the probe, and it was felt that this might make any resonance less visible.

After a few shock tests one of the wires that connect onto the diaphragm became open circuit. Kulite Ltd subsequently removed the rubber, reattached the wire with conducting adhesive, and recoated the diaphragm with rubber, but the drift rate when exposed to thermal transients was then very high. This transducer was not subsequently used for turbulence measurements. A replacement transducer was obtained and it was decided that this should be protected by both a rubber layer (with which it was supplied) and a mesh screen.

This transducer ("Kulite 2") had been built without a screen and it was not possible to fit a standard Kulite "B" or "M" screen. A brass sleeve about 3 mm long with a phosphor bronze gauze soft soldered on one end was machined to fit over the transducer body. This was slid over the diaphragm end of the kulite with a small amount of Loctite to hold it in place (see Figures 2.5 and 2.6). A small gap was left between the gauze and the rubber because the sleeve would not slide up the last fraction of a millimetre onto the kulite; at the time it was felt that this gap was acceptable, given that some gap was essential as contact might have broken this diaphragm also.

A third transducer was later obtained as a spare. This was a standard XCS-062/15 with a B-screen (and no rubber). It was not used for the combustor measurements as it was felt that the second transducer was better protected.

The second Kulite was heated in an oven to measure the change in resistance across the bridge supply lines with temperature. This gave the curve shown in Figure 2.11, using which the CAS2 amplifier and current mirror were set up to give an output of 10 °C/V.

A preliminary calibration of the probe's sensitivity to turbulence was done in the turbulent part of the (free) jet from a portable hot wire calibrator. This consisted of a small centrifugal fan feeding a plenum chamber leading to a 50 mm diameter nozzle, and was capable of velocities up to 29 m/s. It showed that the signal from the pressure transducer could easily be converted to a turbulence spectrum that closely resembled that measured by a hot wire. The low velocity meant that little could be deduced about the probe's response at high frequencies.

A more detailed calibration of the turbulence sensitivity was carried out once the flat plate working section and grid boxes had been built. This is described later in §3.3.3.

2.9 CONCLUSIONS.

An open air combustion test facility at DRA RAE (Pyestock) was chosen for the combustor turbulence measurements.

Design calculations showed that an uncooled sub-miniature pressure transducer, protected by a thin layer of silicone rubber, could be used to take measurements in a flame provided the time in the flow was limited to of order 50 ms.

A Kulite XCS-062/15 transducer was chosen as having the best combination of high natural resonant frequency (after rubber coating) and sensitivity. A recessable probe holder was built to hold this transducer flush (or almost flush) with the tip of a pitot tube.

The probe also included a fine wire thermocouple, thin film gauge and pitot tube for determining mean flow conditions.

A portable traverse mechanism, control electronics and data acquisition system were developed and worked faultlessly.

CHAPTER 3

THEORY OF PITOT PROBE MEASUREMENT OF TURBULENCE

3.1 INTRODUCTION.

This chapter will consider the theory of turbulence measurement using a pitot probe, and describe a novel probe calibration technique.

All three Kulite transducers (Figure 2.6) were calibrated; these results are presented in full in §3.4.3 (despite the fact that only Kulite 2 was used for the combustor tests) as they may be of use for future probe designs.

At low turbulence levels the probe has a linear response to velocity fluctuations which is very close to the predicted sensitivity. A reduction in sensitivity is seen as the wavenumber of the turbulence approaches the transducer diameter. At high frequencies Kulite number 2 exhibited an "organ pipe" resonance of air through the gauze in front of the transducer; the other two Kulites also resonated, though to a lesser degree.

3.2 CONVERSION OF PRESSURE FLUCTUATIONS TO VELOCITY.

It was assumed that the ideal response of a fast pitot probe would be described by the unsteady form of Bernoulli's equation **(Bradshaw, 1971)**:

$$p + \frac{1}{2}\rho(U^2 + V^2 + W^2) + \rho\frac{\partial\Phi}{\partial t} = constant \qquad (3.1)$$

This describes the effect of local velocity on static pressure along a streamline. In a turbulent flow the concept of a "streamline" is not well defined; it seems likely, however, that this equation will describe the flow field correctly for velocity components with wavelengths that are large compared to the probe tip diameter. The velocity distribution around the probe tip will then be similar to the steady-state case. The suitability of this equation at smaller wavelengths will be judged empirically from the probe calibration results.

The probe will be considered as having a flat front face, over which $U = 0$, and it will be assumed that the transverse velocity components V and W are unaffected by the presence of the probe. (U is defined here as the velocity component perpendicular to this surface). Defining P_0 as the pressure acting over this face gives:

$$P_0 + \frac{1}{2}\rho(V^2 + W^2) + \rho\frac{\partial\phi}{\partial t} = p + \frac{1}{2}\rho(U^2 + V^2 + W^2) + \rho\frac{\partial\phi}{\partial t} \tag{3.2}$$

(If one considers a *stagnation point* one has the condition $V = W = 0$ as well as $U = 0$; but it can be seen that this is not essential for the analysis. The assumption that V and W are unaffected by the probe, however, will introduce some error unless the flat face is small compared to the probe tip diameter. One can see that there must be *some* change in the radial velocity components to divert the flow around the probe, and this will lead to a pressure distribution over the front face. The accuracy of these assumptions will be apparent from the low-frequency levels of the calibration coefficients in §3.4).

Eliminating terms from Equation 3.2 gives:

$$P_0 = \bar{p} + p' + \frac{1}{2}(\bar{\rho} + \rho')(\bar{U} + u')^2 \tag{3.3}$$

Hinze (1975) suggests that the *static* pressure fluctuations resulting from turbulent velocity components can be approximately predicted by:

$$p' = 0.7\rho u'^2 = 0.7(\bar{\rho} + \rho')u'^2 \tag{3.4}$$

Substituting this into Equation 3.3 gives:

$$P_0 = \bar{p} + \frac{1}{2}(\bar{\rho} + \rho')(\overline{U^2} + 2\bar{U}u' + 2.4u'^2)$$

The time mean component of this gives the mean probe pressure:

$$\overline{P_0} = \bar{p} + \frac{1}{2}\bar{\rho}(\overline{U^2} + 2.4\overline{u'^2}) + \bar{U}\,\overline{\rho'u'} + 1.2\overline{\rho'u'^2}$$

Hence the probe pressure fluctuations $P_0' = P_0 - \overline{P_0}$ are given by:

$$P_0' = \frac{1}{2}\bar{\rho}(2\bar{U}u' + 2.4(u'^2 - \overline{u'^2})) + \frac{1}{2}\rho'(\overline{U^2} + 2\bar{U}u' + 2.4u'^2) - \bar{U}\,\overline{\rho'u'} - 1.2\overline{\rho'u'^2}$$

$$\frac{P_0'}{\frac{1}{2}\bar{\rho}\,\overline{U^2}} = 2\left(\frac{u'}{\bar{U}}\right)\left(1 + \frac{\rho'}{\bar{\rho}}\right) + \frac{\rho'}{\bar{\rho}} + 2.4\left(\frac{u'}{\bar{U}}\right)^2\left(1 + \frac{\rho'}{\bar{\rho}}\right) - 2.4\left(\overline{\left(\frac{u'}{\bar{U}}\right)^2} + \frac{\overline{\rho'u'}}{\bar{\rho}\,\bar{U}} + \frac{\overline{\rho'u'^2}}{\bar{\rho}\,\overline{U^2}}\right) \quad (3.5)$$

The measured signal depends on both $\frac{u'}{U}$ and $\frac{\rho'}{\rho}$; ρ' (which is not measured) is itself a function of p' and T'.

The equation of state $\rho = \frac{p}{RT}$ can be differentiated to give:

$$\frac{\rho'}{\bar{\rho}} = \frac{p'}{\bar{p}} - \frac{T'}{\bar{T}} \quad (3.6)$$

From Equation 3.4, assuming low M (< 0.8) and low Tu (< 20%):

$$\frac{p'}{\bar{p}} \approx \frac{0.7\rho u'^2}{\bar{p}} = \frac{1.4\,(\frac{1}{2}\rho u'^2)}{\frac{1}{2}\bar{\rho}\overline{U^2}}\,\frac{\frac{1}{2}\bar{\rho}\overline{U^2}}{\bar{p}} \approx 1.4\left(\frac{u'}{\bar{U}}\right)^2\frac{\overline{P_0} - \bar{p}}{\bar{p}}$$

At the subsonic velocities in the present experiment, $M \approx 0.25$.

$$\therefore \frac{\overline{P_0}}{\overline{p}} \approx 1.04, \qquad \frac{\overline{P_0} - \overline{p}}{\overline{p}} \approx 0.04, \qquad \frac{p'}{\overline{p}} \approx 0.06\left(\frac{u'}{\overline{U}}\right)^2 \tag{3.7}$$

In subsonic flow these *static* pressure fluctuations are very small and density fluctuations will be mostly due to embedded temperature fluctuations, *i.e.* local hot-spots resulting from the combustion or dilution processes within the combustor. Since $\frac{p'}{\overline{p}} < \frac{u'}{\overline{U}} < 1$ one can substitute (using Equation 3.6)

$\frac{\rho'}{\overline{\rho}} = -\frac{T'}{\overline{T}}$ and $\left(1 + \frac{\rho'}{\overline{\rho}}\right) = \left(1 - \frac{T'}{\overline{T}}\right)$ into Equation 3.5:

$$\frac{P_0'}{\frac{1}{2}\overline{\rho U^2}} = 2\left(\frac{u'}{\overline{U}} + 1.2\left(\frac{u'}{\overline{U}}\right)^2\right)\left(1 - \frac{T'}{\overline{T}}\right) - \frac{T'}{\overline{T}} - {P_0'}_{mean}$$

where ${P_0'}_{mean}$ is the time-mean value of the other terms on the right-hand side.

Neglecting third order terms, this may be expanded as:

$$\frac{\frac{1}{2}P_0'}{\frac{1}{2}\overline{\rho U^2}} = \frac{u'}{\overline{U}} + 1.2\left(\frac{u'^2 - \overline{u'^2}}{\overline{U}}\right) - \frac{T'}{2\overline{T}} - \left(\frac{u'T' - \overline{u'T'}}{\overline{U}\overline{T}}\right) \tag{3.8}$$

Moss and Oldfield (1990) have shown that at low levels of turbulence the u'^2 **and** $\overline{u'^2}$ terms may be ignored; the 0.7 constant in Equation 3.4 is therefore not critical. If one assumes that the T' terms are also negligible (the validity of which is discussed in §3.3) the turbulence level can be derived simply by scaling the pressure data:

$$\frac{u'}{\overline{U}} = \frac{1}{2}\frac{P_0'}{(\overline{P_0} - \overline{p})} \tag{3.9}$$

The dynamic head measured by the Sensym transducer (a low frequency response, silicon strain-gauge bridge device) and pitot probe was used to define $(\overline{P_0} - \overline{p})$; this avoided having to allow for the drift of the Kulite as it heated up.

3.3 ASSUMPTIONS ABOUT TEMPERATURE FLUCTUATIONS.

It was assumed in §3.2 that the flow is isothermal to the extent that any temperature fluctuations can be ignored in the conversion of pressure to velocity. Equation 3.5 gives:

$$\frac{P_0'}{(\overline{P_0} - \overline{p})} = \frac{2u'}{\overline{U}} - \frac{T'}{\overline{T}}$$

to first order.

The rms average of this over any frequency band can then be described in terms of the velocity and temperature fluctuations:

$$\overline{\left(\frac{P_0'}{2(\overline{P_0} - \overline{p})}\right)^2} = \overline{\left(\frac{u'}{\overline{U}}\right)^2} + \overline{\left(\frac{T'}{2\overline{T}}\right)^2} - \frac{\overline{u'T'}}{\overline{U}\,\overline{T}}$$

One cannot easily predict the level of temperature fluctuations from the velocity turbulence. Although temperature and velocity fluctuations are probably both generated by the interaction of cold, low velocity dilution air jets with a moving, hot primary zone flow, the (fractional) velocity turbulence level is then greatly reduced by the acceleration through the discharge nozzle; this will have little effect on any temperature fluctuations. One might, however, suppose that there will be a weak positive correlation $\overline{u'T'}$, for two reasons. Firstly, primary zone (hot) gas will have some axial velocity before the contraction, whereas cold air entering radially will not, and this will lead to these elements having a higher velocity after the contraction. Secondly, the pressure gradient across the nozzle will tend to accelerate hot, low density regions in the flow to a higher velocity than cold regions; this is only likely to be a significant effect at large wavelengths.

In cooler flows it is possible to extract T' (and hence ρ') using a hot wire at several overheat ratios (eg. **Oldfield et al, 1978**), but this is not possible in combustor flows as the wire would oxidise and break if heated to a temperature significantly hotter than the flame.

Attempts to measure temperature fluctuation levels using a thin-film probe (see Appendix 3) have so far been of very dubious accuracy. It will be shown in Chapter 4 that the apparent velocity spectra, if temperature effects are assumed negligible, are very similar for burning and cold combustors. It seems most unlikely that this result should be an accident, with velocity and temperature fluctuations changing in precisely such a way as to make the pressure spectrum stay at a constant level. It will instead be assumed that the probe is measuring the velocity spectrum accurately. (The small variations in spectra between different conditions may be due to either genuine turbulence level changes or some temperature fluctuation effect).

3.4 PROBE RESPONSE TO FREQUENCY AND WAVENUMBER.

3.4.1 Introduction

The DC pressure sensitivity of the Kulite transducer was determined by calibration in a dead-weight tester, and subsequently by a suck-down test in the flat-plate tunnel. It was, however, felt that a measurement of the AC response was desirable. **Jenkins (1987)** has shown that the sensitivity of a pitot probe depends slightly on the shape of the probe tip; **Le Bot et al (1978)** suffered from bandwidth problems; the sensitivity to small vortices was unknown; and shock tube testing had failed to determine the transducer resonant frequency. A calibration test process was devised to investigate these topics.

3.4.2 Theory.

The calibration as described by **Moss and Oldfield (1990)** is based on the assumption that the probe response $M(k,U)$ to turbulence having a true wavenumber spectrum $S(k)$ depends on a probe resonance factor $F(f)$ and a change in sensitivity with wavenumber $G(k)$ such that

$$M(k,\overline{U}) = S(k)F(f)G(k) \qquad \text{where } f = \frac{k\overline{U}}{2\pi}$$

If two tests are done at velocities U_1 and U_2 and the true spectrum $S(k)$ is the same in each case (which has been confirmed by hot wire measurements) then

$$F\left(\frac{k\overline{U}_1}{2\pi}\frac{\overline{U}_2}{\overline{U}_1}\right) = \frac{M(k,\overline{U}_2)}{M(k,\overline{U}_1)}F\left(\frac{k\overline{U}_1}{2\pi}\right)$$

If $U_2 >> U_1$ and it is assumed that $F(0) = 1$ the function F may be found by iteration from the two measured spectra M. This was achieved using the Matlab .M file "acalc.m" which is given in §A.2.2.2. Once $F(f)$ has been found using this technique, $G(k)$ is found from

$$G(k) = \frac{M(k,\overline{U}_1)}{S(k)F\left(\frac{k\overline{U}_1}{2\pi}\right)}$$

3.4.3 Calibration of pitot probe against a hot wire using grid generated turbulence.

Once the flat plate working section and grid boxes (see Chapters 5 and 6) had been built for the wind tunnel heat transfer testing it became possible to study the turbulence response at much higher velocities and with a more typical turbulence level and spectrum than in the preliminary low speed test described in §2.8.

Although the calibration could have been done using any turbulence spectrum that gave an adequate signal to noise ratio, a spectrum very similar to that measured in the combustion tests was chosen to avoid any sensitivity to parameters that might otherwise not have been properly simulated. It was found that a grid of 6 mm diameter parallel bars at 15 mm pitch produced the most representative turbulence spectrum. The bar size was chosen using a correlation from **Roach (1987)**, and the axial distance of 144 mm (x/d = 24) was confirmed by experiment (see Figure 4.22).

The apparent spectrum $M(k,U)$ produced by this bar grid was measured at two velocities (30 and 64 m/s) using the kulite probe; the pressure signal was converted to a velocity spectrum using the method given in §3.2. The results for Kulite 2 are shown in Figure 3.1. The spectrum was also measured by a hot wire anemometer, and it was assumed that this was the true spectrum $S(k)$. (The hot wire anemometer was a Dantec type *55M01* with a *55M10* standard bridge; it was set to filter 3, gain 5 which gives a flat response to almost 100 kHz. It was felt that the wire, being shorter than the kulite diameter, would accurately measure turbulence at all wavelengths that were of relevance to the pressure probe calibration).

Applying the technique described in §3.4.2 to the curves in Figure 3.1 (and similar spectra for the other transducers) produces the resonant responses $F(f)$

shown in Figure 3.2. Kulite 1 appears to have a broad-peaked resonance with a natural frequency of about 110 kHz, which is close to expectations based on the mass of the rubber layer (see Chapter 2). Kulite 2 has a severe resonance at about 67 kHz, with some resonance being evident at all frequencies > 13 kHz. This would appear to be due to air in the recess behind the gauze resonating, as Kulite 1 (which has a similar rubber layer but no screen) does not resonate here. Kulite 3 has a rather smaller resonance around 52 kHz, which is presumably due to the air behind the screen as the diaphragm natural frequency should be much higher than this.

The wavenumber roll-off factors $G(k)$ were then calculated and are shown in Figure 3.3. These are more similar than the resonance curves. The lower level of Kulite 1 at low wavenumbers is presumably due to errors in the DC pressure calibration. The difference in roll-off slope may be due to Kulite 3 having a central hole in the screen, whereas Kulites 1 and 2 will experience a pressure averaged over a larger area.

The wavenumber sensitivity $\sqrt{G(k)}$ has been defined to give a value of 1.0 if the steady-state transducer calibration and Equation 3.9 are correct. The apparent sensitivity of 0.9 to 0.95 at low wavenumbers ($k < 1000\ \mathrm{m}^{-1}$) could be due to errors in the steady-state calibration, or to the assumptions made in §3.2. In practice accurate steady-state calibration is difficult because the rubber coated transducer is susceptible to drift; the close agreement to the predicted sensitivity appears to justify the analysis assumptions.

All the data presented in Chapter 4 has been corrected using the calibration curves for Kulite 2, with the resonant frequency of the $F(f)$ response scaled in accordance with the calculated air temperature as described below.

3.5 CALCULATION OF AIR TEMPERATURE WITHIN TIP OF PROBE.

The resonance of Kulite 2 during the combustor tests will have been affected by the speed of sound in the resonating gas, which is a function of the gas temperature in the recess between the gauze and the silicone rubber layer.

The temperature of the air in the recess between the gauze and the silicone rubber layer (which was 292 K during the calibration test) was calculated by considering the temperature rise of the probe and the radial temperature gradient in the gauze while exposed to the flame. Figure 3.4 shows a cross section of the tip of this transducer (see also Figure 2.6).

Calculation of the rate of diffusion of heat into a stationary, semi-infinite mass of air shows that, after a time interval of 40 ms the temperature change 0.7 mm below the "surface" of the air would be 50% of the temperature change at the surface. This suggests that over a time of 80 ms (the time spent in the flame) the temperature of a pocket of air about 0.5 mm deep may, to a rough approximation, be considered in thermal equilibrium with the surrounding diaphragm, bucket and gauze.

Calculations of the gauze conductivity and mass showed that the temperature distribution across the gauze was determined mainly by conduction into the bucket, and that transient effects within the gauze would have a negligible effect. The mean temperature difference between the gauze and the bucket was calculated by solving a radial heat flux equation.

The peak metal temperature during a test was inferred from the peak temperature subsequently reached by the Kulite. It was assumed that the diaphragm did not change temperature significantly while it was in the flame, so the heat transfer into this air was only a function of the gauze and bucket temperature rises. The air temperature halfway through a traverse may then be expressed as:

$$T_{air} = T_1 + \frac{A_{gz}}{A_T}\Delta T_{gz\text{-}b} + \frac{1}{2}\left(\frac{A_{gz}+A_b}{A_T}\right)\frac{(mCp)_{gz} + (mCp)_b + (mCp)_k}{(mCp)_{gz} + (mCp)_b}\Delta T_{k,2} \qquad (3.10)$$

where T_1 is the initial probe temperature, $\Delta T_{gz\text{-}b}$ is the calculated temperature difference between the gauze and bucket and $\Delta T_{k,\,2}$ is the final kulite temperature rise; the factor of ½ is to obtain a typical temperature while in the centre of the flame from the final temperature once the traverse is completed. The diaphragm, bucket and gauze have the same surface areas exposed to the recess so $\frac{A_{gz}}{A_T} = \frac{1}{3}$

and $\frac{A_{gz}+A_b}{A_T} = \frac{2}{3}$, with A_T being the total surface area surrounding the recess.

(Typical values for the terms in Equation 3.10 are as follows:
346 K = 308 + 26 + 12 at 50:1 *AFR*).

It was assumed that there was no mixing of the flame with this air and that the resonant frequency was purely dependent on this temperature.

The correction to the wavenumber spectra was then:

$$S(k) = \frac{M(k,\overline{U})}{F(f\sqrt{\frac{292}{T_{rec}}})\,G(k)}$$

with T_{rec} = 321 K, 334 K and 346 K at 100:1, 65:1 and 50:1 AFR.

While correcting the spectra for the calibration factors $F(f)$ and $G(k)$ a correction was also made for the frequency response of the instrumentation amplifiers and anti-alias filters.

3.6 CONCLUSIONS.

The use of total pressure probes to measure turbulence has been studied both theoretically and experimentally. The probe response was found to depend on two parameters: one due to resonance effects (a function of frequency), and the other a function of wavenumber (× probe diameter, in theory; this was not varied).

Calibration showed that the transducer used for the combustor testing suffered from a resonance at approximately 70 kHz. This is thought to be due the air space behind the gauze screen, and might be minimised in future tests by reducing the depth of any recess here, or relying purely on a rubber layer for protection.

The derivation of velocity signals from total pressure measurements relies upon the assumption that the temperature fluctuation levels are not significant. The evidence for this is at present circumstantial; any future work on combustor turbulence should examine this in more detail.

CHAPTER 4.

COMBUSTOR TEST RESULTS.

4.1 INTRODUCTION.

The thermocouple, pitot and Kulite probe results from the combustor tests will now be described. A few measurements were also taken with a thin-film probe; these are described later in Appendix 3, as there is some uncertainty concerning their interpretation.

Measurements of the combustor exit flow were taken both at a slow sampling rate (10 kHz) to define the overall temperature and pressure profiles, and at a fast sampling rate (200 kHz) to study the power spectrum of the pressure fluctuations. The amount of memory and sampling rate options available did not permit both measurements to be taken simultaneously. A slow data capture would first be done to determine the overall operating conditions; then, having found a suitable trigger point, a high speed capture of the pressure signal would be taken during a number of separate traverses. The first section (§4.2) will describe the results from the slow sampling rate traverses; the high speed results will be presented in sections 4.3 and later. Figure 4.1 lists the flow conditions at which testing was carried out.

4.2 TIME-MEAN FLOW MEASUREMENTS.

4.2.1 Combustor exit total pressure traverses.

The pitot probe measurements of total pressure profile from the three combustors (using a Sensym transducer) are compared in Figure 4.2. These have been plotted against time rather than position; the relationship between time and probe position is as described in Chapter 2. The usual traverse direction is downwards, which would correspond to the radially outwards direction on an engine.

4.2.2 Temperature traverses.

Figure 4.3 shows the radial temperature traverses from the three combustors at 65:1 *AFR*. It can be seen that these are not so similar as the pressure profiles; this reflects the different fuel distribution characteristics of each burner and primary zone. It appears from the higher mean temperatures achieved using combustor *B* that this burns the fuel more efficiently than the others at this condition, with pressures much lower than would be typical in an engine; evidence for this was also seen in the colour of the flame.

Combustor *B* was able to burn diesel fuel as well as paraffin. Figure 4.4 shows that the change of fuel has little effect on the temperature distribution.
Figure 4.5 shows a number of traverses taken at different circumferential positions across the exit nozzle slot, with combustor *A* running at 100:1 *AFR*. The temperature field is reasonably uniform.

This combustor had a burner with two jets: a small "pilot" and a larger "main" jet. The main jet did not achieve very satisfactory atomization at these conditions, as can be seen from a comparison of the temperatures produced by nominally similar air:fuel ratios in Figure 4.5. The pilot jet alone was therefore used for the majority of the testing on this combustor.

4.2.3 Mean velocities.

The exit velocity profiles shown in Figure 4.6 have been calculated from the temperature and pressure traverses at *AFR* = 65, using a compressible flow calculation that properly calculates the gas properties at high temperatures (see Appendix 2). These were flat enough for the turbulence *frequency* spectra from different positions in the flame to be averaged, which is a much quicker process than averaging the wavenumber spectra (see §2.7).

4.2.4 Combustor exit flow angle.

The exit flow angle from combustor *B* was measured in the radial direction by recording traverses at two different axial planes: 12 mm and 62 mm downstream of the discharge nozzle. The angle was inferred from the change in time at which the probe entered the flow, as shown in Figure 4.7. The angle was found to be 11.6° downwards for the cold case (420 K, air), and 11.7° downwards at *AFR* = 100:1. This deviation from the axial is presumably a result of the discharge nozzle having a much greater contraction on the inner wall (top side, as mounted here) than on the outer wall; the gas leaves the nozzle almost immediately after the contraction having passed through only a very short length (of order 20 mm) of parallel duct.

Crossed hot wire measurements (combustor *A*, cold) suggested that the exit flow angle was approximately 6° downwards. This is likely to be less accurate as only three traverses were recorded and these showed considerable scatter (4.6 to 8.7°).

4.2.5 Temperature rise of kulite pressure transducer.

The temperature of the Kulite diaphragm during and after a traverse is shown in Figure 4.8. The majority of the temperature rise occurs several seconds after the transducer has left the flame *i.e.* the temperature of the diaphragm lags behind the temperature rise of the gauze and surrounding steel tube. This implies that the transducer could have tolerated a much higher heat flux while in the flame if it had passed into a cooling flow upon exit, which suggests that a test at engine conditions might be feasible.

4.3 HOT WIRE COMBUSTOR TURBULENCE MEASUREMENTS.

Measurements of the combustor exit turbulence wavenumber spectrum were taken at three velocities **without** combustion. A hot wire probe was used for these, because at this stage the full resonance calibration of the kulite probe had not been done; it was felt that a hot wire might give a definitive turbulence measurement up to higher frequencies than the kulite probe, as well as a better signal to noise ratio at low velocities.

These cold tests were done because the hot tests would produce changes in both exit temperature and velocity, and it would not be possible to attribute any change in the turbulence to the combustion process without knowing that velocity changes by themselves had little effect on the spectrum.

The results are shown in Figure 4.9; the wavenumber spectra are very similar. The combustor appears to be generating turbulence in a similar manner to a bar grid, in that the wavenumber spectrum is not a function of velocity.

A crossed hot wire measurement of the axial and radial turbulence spectra was also taken to assess the amount of anisotropy in the turbulence. Some anisotropy is to be expected if an isotropic turbulence field is suddenly accelerated through a contraction; if the anisotropy is severe, measurement of the axial component alone will be insufficient to give an accurate indication of the total turbulence energy or to predict how it will decay further downstream.

It can be seen from Figure 4.10 that the u' and v' components are very similar at $k > 300\ m^{-1}$, which implies turbulent eddy sizes small enough to easily pass through the exit nozzle. (A wavenumber of 130 m^{-1} corresponds to a wavelength equal to the 48 mm height of the discharge nozzle). At longer wavelengths the radial component is attenuated relative to the axial level, as expected.

4.4 PRESSURE TRANSDUCER MEASUREMENTS OF COMBUSTOR TURBULENCE.

The Kulite total pressure signal was sampled at 200 kHz and converted to a turbulence power spectral density (vs wavenumber) as described in Chapter 2. A typical traverse through the flame is shown in Figure 4.11. It can be seen that the transducer output drifts in one direction while in the flame, and in the opposite direction after leaving the flame, despite the fact that the diaphragm itself is still increasing in temperature at this point; it would appear that the drift is due to thermal stresses induced in the surface of the protective silicone rubber layer rather than being due to the change in temperature of the diaphragm itself.

4.4.1 Turbulence spectra for combustor A at three air-fuel ratios.

Figure 4.12 compares the wavenumber turbulence spectra from a single combustor at three different conditions. The spectra are very similar at wavenumbers greater than 250 m^{-1}. It has been shown above (4.2) that velocity changes have little effect on the spectra; it now also appears that the temperature rise and other effects due to combustion have a negligible effect on those turbulence components that are likely to be of relevance to turbine heat transfer.

Figure 4.13 displays the same data as a *frequency* spectrum, which demonstrates the concept that such data is more usefully plotted against wavenumber than frequency.

4.4.2 Turbulence spectra from combustor B at four air-fuel ratios.

Figure 4.14 is similar to 4.12 and shows that the same conclusion may be drawn from the combustor B results. This graph includes results from the hottest (*i.e.* most closely representative of an engine) traverse with a peak temperature of over 1500 K. There is a slight increase in *PSD* (≈2 dB) at the hottest condition, but this is only of slight significance to the overall turbulence intensity as will be shown below.

4.4.3 Comparison of spectra from combustors A, B and C at 65:1 AFR.

Figure 4.15 compares the spectra from all three combustors at the same nominal condition. The spectra are all very similar despite the burners and primary zones being sufficiently different to give the temperature traverses seen in Figure 4.3. This suggests that the majority of the turbulence at the exit plane is produced by the relatively large diameter "secondary" dilution jets that come through holes in the cylindrical downstream portion of the combustor, rather than from flow structures within the primary zone. This would also explain why the high heat release rate in the primary zone, which might well be expected to modify the flow there, has so little effect on the exit plane turbulence as has been seen in Figure 4.12.

4.4.4 Effect of changing fuel from paraffin to diesel.

Simulation of genuine engine pressures and temperatures was not possible using an unpressurised combustion facility. One of the effects of higher combustor inlet pressures and temperatures would be to increase the rate of burning of the fuel. An attempt was made to determine whether changes in burning rate were likely to have a significant effect by changing from paraffin to diesel fuel. Diesel fuel is much less volatile than paraffin and may be expected to burn more slowly.

It can be seen from Figure 4.16 that there is no significant effect. This does not, however, *prove* that an engine would behave in the same way; other factors, such as perhaps the change in Reynolds number, may become important.

4.4.5 Uniformity of turbulence field from combustor.

Most traverses were done along a radial line that bisected the discharge nozzle exit slot. A series of traverses were also done along 5 other planes to confirm that the exit flow field was reasonably homogeneous. This was done at just one condition (combustor A, 100:1 AFR) because it was a time consuming measurement.

The spectra shown in Figure 4.17 correspond to the temperature traverses in Figure 4.5; it can be seen that they are all very similar, and it may be concluded that the central traverse used for the other tests described above gives a good indication of the mean conditions across the whole of the exit area. A typical total pressure traverse is included to show how the positions of the spectra correspond to the flow. It can be seen that the "flat" region of the pressure traverse extends over only about half the height of the nozzle; this is presumably because the flow is leaving the combustor at an angle, with a very large separation off the upper lip of the nozzle. The spectra here have been derived from data across the whole of this "flat" region.

Figure 4.18 shows data from the same traverses, but with the spectrum from each "cut" of the time series averaged circumferentially to give mean spectra corresponding to eight uniformly spaced radial positions. Positions 1, 2 and 8 are in the shear layers on either side of the flow; the rest of the spectra are again very uniform at wavenumbers > 200 m^{-1}.

4.4.6 Cumulative power plot of turbulence spectra.

Figure 4.19 takes the same combustor A data as Figure 4.12 but displays it as a cumulative power plot (see Appendix 1), from which the turbulence components between any pair of wavenumbers may be read off directly. This illustrates that the majority of the turbulence is in the wavenumber range 50 to 1000 m^{-1}; at k = 130 m^{-1} the cumulative level for all three conditions is the same.

Figure 4.20 shows the combustor B data in the same form. The cold, 100:1 and 65:1 cases are very similar (down to k = 100 m^{-1}), but the 50:1 *AFR* case is higher.

4.4.7 Combustor turbulence length scales.

The turbulence spectrum of a perfectly isotropic and homogeneous turbulent flow can be described (except at very high wavenumbers) as a function of just two parameters - the overall energy, and the integral length scale. The length scale is therefore a useful parameter in that, if one makes the simplifying assumption that effects of anisotropy and inhomogeneity are to be ignored, the effect of the turbulence on any aspect of the flow may be correlated or modelled in terms of just the energy and length-scale. (The extent to which such assumptions about the shape of the spectra are valid must, of course, also be defined).

Integral length scales and turbulence intensities have been calculated for several of the combustor tests and are tabulated in Figure 4.21. These were calculated using a correlation derived from the power spectral density as described in §A.1.3; direct correlation of the raw data was found to give very similar results. It can be seen that the hot combustor tests gave a typical integral scale of approximately 7 mm.

The Combustor A test at *AFR* = 65:1 gave a larger length scale because of the rise in the spectrum at low wavenumbers (at higher wavenumbers it is very similar to the other spectra). This part of the spectrum, at k < 20 m^{-1}, corresponds to wavelengths > 0.3 m. It cannot be considered to be turbulence because, with a discharge nozzle height of only 0.05 m, there cannot be a significant transverse velocity component of this wavelength. This wavelength is so much larger than the chord of typical turbine aerofoils that it will not lead to any heat transfer enhancement. It therefore seems appropriate to characterise all these combustors as producing a streamwise turbulence intensity of 9% and an integral length scale of 7 mm.

It is of interest to consider what length scale, if the turbulence *were* isotropic and homogeneous, would give an ideal spectrum most similar to the measured ones. This is investigated in Figure 4.22, where an "ideal" spectrum from a bar grid has been chosen to represent the measured spectrum at wavenumbers between 80 and 1000 m^{-1}. This was measured using a grid of 6 mm bars in the flat plate wind tunnel which will be described in the next chapter. The distance to the measurement station (x/d = 24) should be sufficient for the turbulence to be reasonably isotropic.

The spectrum from this grid is compared with a typical combustor spectrum in Figure 4.22. It can be seen that, apart from the low wavenumber region mentioned above, the shapes of the two spectra are very similar. The integral length scale of the grid-generated turbulence (included in Figure 4.21) is similar to the combustor scale.

A grid turbulence correlation (**Roach, 1987**) has also been included in Figures 4.21 and 4.22 for comparison. This uses a grid of 5 mm bars to simulate as closely as possible the high wavenumber (k > 100 m^{-1}) part of the spectrum. It suggests that, as far as the high wavenumber part of the spectrum is concerned, the data could also be described in terms of a slightly shorter integral scale (4.6 mm) instead of the 5.6 to 7.6 mm typical of the combustor spectra themselves.

Attempts to calculate dissipation length scales for the combustor spectra by fitting a parabola to the correlation peak (see §A.1.3) gave values of approximately 3.5 mm. These cannot be considered accurate, however, as the probe response to wavenumber and frequency is insufficient to properly define the correlation for very small time steps.

The "Kolmogorov" theoretical spectral decay rate of -5/3 (**Kolmogorov, 1962,** from **Hinze, 1975**) is also shown in Figure 4.22 to indicate the wavenumber range in which an "inertial subrange" can be considered to exist. The shape of the spectrum over this range (approximately $500 < k < 1000$ m^{-1}) is independent of the details of the largest, most anisotropic eddies and of the viscous dissipation at higher wavenumbers; it may be considered isotropic here.

4.5 HEAT FLUX MEASUREMENTS.

A thin film gauge painted around the hemispherical end of a 2.5 mm diameter pyrex rod was used in an attempt to examine the level of gas temperature fluctuation in the combustor exit flow. This is of interest because the derivation of the turbulence spectrum from the pressure transducer measurements is based on the assumption that temperature fluctuations are negligible. The measurements were inconclusive but have been included in Appendix 3 for reference purposes.

4.6 CONCLUSIONS.

The uncooled transient probe technique has proved itself capable of taking high quality measurements of combustor exit gas temperature and velocity.

Measurements using hot wires show that combustor exit turbulence spectra at low temperatures are independent of exit velocity. Measurements using the kulite probe, assuming that temperature fluctuations are negligible, show that the same applies even in the presence of combustion.

Tests of three different combustors with different designs of burner and primary zone show that turbulence spectra are largely independent of the burner design and are thus presumably a function of the large ("secondary") dilution hole geometry, length and exit contraction ratio.

Tests with fuels burning at different rates suggest that this result is likely to hold at more realistic (engine) conditions.

The turbulence spectrum closely resembles that produced by a parallel bar grid and can usefully be defined in terms of an intensity and integral length scale. If there is a very low frequency peak in the spectrum this should be removed when calculating a representative length scale.

CHAPTER 5.

DESIGN OF WIND TUNNEL WORKING SECTION.

5.1 INTRODUCTION.

This chapter will describe the choice of wind tunnel and design of working section for the flat plate experiments, together with details of the flat plate leading edge shape. The experimental techniques will be covered later in Chapters 6 (turbulence measurement), 7 (liquid crystal technique) and 8 (thin film gauge technique) before describing the heat transfer results in Chapter 9.

5.2 CHOICE OF TUNNEL AND PLATE SIZE.

It was decided to carry out the heat transfer part of the experiment in a zero pressure gradient, low speed, flat plate tunnel because the results from this would be much easier to interpret, and useful conclusions might be reached from a smaller number of test cases, than if a more realistic facility, eg. a cascade or rotating turbine had been used. Use of completely realistic conditions such as those which occur in an engine was not practical in the time available. Even if it had been possible, the difficulty of taking accurate heat flux measurements in a high temperature environment would have made the results less credible and would have made any investigation of the enhancement mechanism impossible.

Most previous experiments on the effect of turbulence on heat transfer have only measured time-mean heat flux levels. The success of **Doorly and Oldfield (1985)** in using fast response surface mounted thin film gauges to show the movement of turbulent spots, wakes and shocks along a blade surface subjected to periodic shocks and wakes from upstream blades suggested that a similar technique, coupled with the measurement of turbulence both in the freestream and the boundary layer, might give useful information about the phenomena involved in the augmentation of turbulent heat transfer by turbulence. This meant that the plate had to be made out of some material suitable for use with thin film gauges, preferably *Macor* machineable glass ceramic. The plate was designed to be as large as possible to allow a detailed study of boundary layer phenomena subject to limitations of Macor sheet sizes, availability of a suitable wind tunnel and achieving a reasonable signal to noise ratio from the thin film gauges.

The tunnel chosen was one traditionally referred to in Oxford as the 6" × 8" high speed tunnel because of the size of the original working section. Preliminary measurements of the volume flow rate / pressure drop characteristics of this tunnel are shown in Figure 5.1. It has been assumed that the fans rotate at constant speed regardless of load, and that the pressure rise is therefore a function of the air velocity. (The volume flow rate has been defined as $Q = \frac{\dot{m}RT}{P}$ based on conditions at entry to the fans). The measurements suggested that this tunnel would achieve velocities of order 90 m/s in a 150 mm square working section with a grid upstream causing a 5% total pressure drop. Other larger tunnels were available but these were incapable of velocities over 30 m/s, which would have required a very large plate made from several pieces of Macor to achieve a suitable Reynolds number. The difficulty of fabricating such a large plate, plus the need for inconveniently large grids and heaters and the absence of an easy control system for these tunnels led to the smaller one being chosen.

The largest Macor sheet available was 330 × 340 mm × 1/2" thick. It was decided that the working section should have a square cross section to allow grids to be rotated through 90° and to allow the plate to be rotated to allow easier viewing of liquid crystals. While estimation of the pressure drop along the tunnel suggested that usefully high Reynolds numbers (up to 1.3×10^{6}) could be achieved with a cross section of up to 200 mm square it was felt that the desirability of keeping the existing inlet bellmouth and of being able to make two plates from the material if required merited a reduction of this to 150 mm wide. Calculation of side-wall boundary layer thickness showed that a 150 mm width was possible without gauges on the plate centre-line being affected by these boundary layers at up to 330 mm downstream from the leading edge.

5.3 DESIGN OF WORKING SECTION.

The measurement of heat transfer using thin film gauges requires a transient test in which the surface is suddenly subjected to heat transfer, as it is only from the change in gauge voltage that the heat flux can be determined. The heat flux may be produced either using a test surface at ambient temperature and a hot flow, or with ambient temperature air flowing over a pre-heated plate. Sub-atmospheric temperatures may of course be used instead but are difficult to produce and risk problems with condensation. At the flow rates that were expected (of order 5 kg/s) the generation of a constant temperature flow of hot air would have required a prohibitively large heater so the second option was chosen, with ambient air passing over a pre-heated plate. The fact that this generates a heat flux out of the plate, i.e. in the opposite sense to the engine situation where heat flows into the blade, is not of any great importance as the effect of gas to wall temperature ratio on Nusselt numbers is small at low Mach numbers and low gas to wall temperature ratios.

Several ways of suddenly starting the flow were considered. The obvious technique of simply starting all the tunnel fans at once was not feasible; apart from the fact that they take a few seconds to reach a reasonably stable speed, there is a risk of blowing the main 150 amp fuse if all the motors are started simultaneously.

The first was to have a plate that was heated outside the working section and then rapidly slid (by some spring loaded mechanism) into the working section, through which the air would already be flowing. It was felt that it would be difficult to make this process happen fast enough to give a sensibly instantaneous start, given that overall test times of under two seconds were expected, and it would be difficult to have hot wires positioned close to the surface while this was happening. Potential problems with sealing around the moving plate, and the unacceptable risk of plate breakage, led to this being rejected.

A second proposal was to have a dummy working section and plate beside the real one, and to make the whole assembly able to slide sideways. The plate would be heated while it was "out" of the tunnel and, after starting the fans, the assembly would be slid across so that the air went through the real working section instead of the dummy one. It was felt that this would be difficult to seal however, and that the inertia of the working section would be too large to allow a rapid start.

The final solution was to have a fast-acting bypass "flap" valve and a secondary air inlet to the tunnel just downstream of the working section. This is shown in Figure 5.2. The plate is heated by hot air, typically at 95°C from a domestic hair dryer, which enters though one of the side walls, passes forwards underneath the plate, around the leading edge, rearwards over the upper surface, and exits though the other side wall. This air is prevented from passing rearwards along the tunnel by the flap valve being closed, and forwards by a sliding door across the front of the working section.

The latter is necessary not only to enhance the heating effect, but also to prevent the air from heating the grid; if the grid bars were hot the wake from each bar would be hotter than the rest of the air, which would make the interpretation of hot wire and gauge signals almost impossible. The flap valve is pulled into the open position by six elastic car roof-rack straps. These are sufficiently long to allow the valve to be rotated to the closed position, while in the open position applying enough force to prevent the difference in static pressure between the inside and outside of the tunnel from forcing it open. In the closed position the valve is held by a latch that will suddenly release it when pulled.

The plate temperature is monitored by a thermocouple (perspex plate) or gauge resistance (Macor plate). Once this has reached a suitable overheat, typically between 40 and 70 K, the heater is removed and the heating intake/exit holes blocked; the sliding door is opened; the plate temperature is recorded; the tunnel fans are started; and, once they have reached a stable speed, the flap valve is opened. The transient recorder is triggered by the change in dynamic head in the working section, which is detected by a Sensym pressure transducer, coupled to an amplifier and Schmidt trigger; the trigger signal also lights an LED that is visible while video recording liquid crystal tests.

Photographs of the tunnel and working section are shown in Figures 5.3 and 5.4.

5.4 CHOICE OF LEADING EDGE PROFILE.

The leading edge profile was chosen very carefully to minimise the risk of any turbulence vortices causing transient separation. This would have led to a heat transfer effect that was not of any significance in understanding gas turbine heat transfer, as in a turbine the flow acceleration around the leading edge is likely to be high enough to prevent any form of turbulence induced separation. Four designs of leading edge profile were proposed: circular (obviously not a good choice, but useful as a benchmark to show that separation could be seen), elliptical, involute and Rankine oval.

These were machined onto small perspex plates with both 4:1 and 8:1 aspect ratios, in each case blending smoothly into a flat, parallel surface, and were mounted on a rod that allowed them to be rotated to set the angle of incidence.

The various profiles are shown in Figure 5.5. Initially they were tested in a low speed flow visualisation tunnel using both a titanium dioxide and paraffin mixture painted on the surface, and a smoke wand. At very low velocities the buoyancy of the smoke meant that the angle of incidence could not be well defined, and at high velocities one could not easily see whether there was a separation or not. The titanium dioxide fluid failed to give a clear indication of separation at the velocities achievable in this tunnel. Thermochromic liquid crystals (**Ireland and Jones, 1985**) were then used to see whether the reduction in heat transfer rate in separated regions would enable them to be identified visually. The plates were heated outside the tunnel in a makeshift oven; they were then quickly inserted into a large working section and the tunnel was started before they could cool down significantly. This gave better results, but it was still difficult to distinguish between regions that had separated and those that were merely close to separation.

Shear sensitive liquid crystals (**Bonnet at al, 1989**) were subsequently found to give a very good indication of separation. If the flow has separated, there is usually a reattachment point, at which some of the crystal can be seen flowing rearwards, and some can be seen flowing forwards into the separated region; ultimately this collects at the point of separation. In contrast, in an attached region, even if the shear stress is very low, the crystal will eventually flow through from front to rear. If the surface is mounted vertically the angle of the sheared streaks of crystal (which will move both in the flow direction and downwards under gravity) can be used as an indication of the rate of shear there.

Figure 5.6 shows the critical tests that identified the 8:1 involute as the best of the profiles tested. At 4° incidence both the ellipse and involute are unseparated; at 4.5° the ellipse has separated; and at 5° they have both separated. The circular and Rankine oval leading edges, and the 4:1 shapes, were all inferior to this. The involute profile is defined with a linear variation of curvature with surface distance such that

$$\frac{d\theta}{ds} = \frac{\pi}{S_0}\left(1 - \frac{s}{S_0}\right)$$

so that at the point where $\theta = \frac{\pi}{2}$ the curve has become flat to allow a smooth blend onto the flat surface and minimise the risk of separation here. A series of points calculated along this curve were scaled to achieve the desired length and width. Note that, as slightly different scaling factors have been used in each direction the curve is strictly speaking no longer an involute; by the above definition a proper involute must have an aspect ratio of 1.7794:1 at this point. The method used is, however, felt to give a curve that has a satisfactory shape - for convenience, the term "involute" will continue to be used. Figure 5.7 lists the coordinates of the leading edge profile.

5.5 SCALE OF PLATE BOUNDARY LAYER RELATIVE TO TYPICAL ENGINE CONDITIONS.

This experiment was designed to produce a much thicker boundary layer than is usual on engine components to facilitate measurements within the boundary layer. This was achieved (as described above) by using the combination of a longer surface and lower speed than engine conditions to generate realistic Reynolds numbers. Figure 5.8 compares the momentum thickness θ around a typical nozzle guide vane with that predicted along the plate using a correlation for turbulent flow on a flat plate (**Schlichting, 1979**):

$$\theta = 0.036\, x\, Re_x^{-0.2}$$

The ratio of the plate to engine boundary layer thicknesses is not constant; the large variations in velocity along both surfaces of the nozzle guide vane have a considerable effect on the rate of boundary layer growth. The turbulence levels and length scales along the aerofoil surfaces will also be affected by the changes in freestream velocity. This means that one cannot define a universal scale factor to relate flat plate results, in their simplest form, to effects at the same chordal position on an aerofoil.

It will be shown in Chapter 9 that the effects of the turbulence *can* be described non-dimensionally (in terms of intensity, length scale and boundary layer thickness) to enable their application to engine components.

5.6 CONCLUSION.

A new working section was designed for an existing wind tunnel. It was built of perspex, with a 150 × 150 mm square cross section and a centrally mounted flat plate 332 mm long. Plates were manufactured both in perspex, for liquid crystal testing, and in Macor for thin film gauge measurements. An involute profile that was particularly resistant to separation was chosen for the leading edge.

A fast acting flap valve was used so that transient heat transfer tests could be performed after hot air heating of the plate in situ.

CHAPTER 6.

MEASUREMENT AND GENERATION OF TURBULENCE USING GRIDS.

6.1 INTRODUCTION.

This chapter describes aerodynamic measurement techniques used in the wind tunnel tests (heat transfer techniques are described later in Chapters 7 and 8). It covers practical details of using hot wires, together with the methods used to derive turbulence power spectral density and length scales and the performance of the turbulence grids chosen for the heat transfer tests.

6.2 HOT WIRE CALIBRATION

The hot wires used for measuring air velocity needed frequent calibration to ensure that up to date calibration coefficients were always available. To avoid errors in extrapolation it is essential that the calibration includes velocities higher than those expected during use; this also allows one to check that resonance does not occur at such velocities. Calibration was performed in situ in the tunnel, both because no other calibration facility was available for velocities up to 100 m/s and because this allowed the electronics and data acquisition system to be used for the calibration without any modification.

The procedure was as follows:

(1) remove the grid, if any, and ensure the flap valve is held open

(2) measure the wire resistance, and set the anemometer to 80% overheat

(3) run all 4 fans, to achieve the highest possible velocity, and check with an oscilloscope and a square wave generator that the "Q" and "L" settings give a response with the minimum of resonance. Turn off the square wave.

(4) start recording the voltage, temperature, dynamic head and total pressure (using a pair of Sensym transducers) at the slowest Datalab sampling rate.

(5) turn off fans 4, 3, 2, and 1 at intervals of a few seconds so that the velocity slowly drops, and finally falls almost to zero after 73 seconds when the Datalab finishes recording.

Typical traces of anemometer output voltage, dynamic head and total pressure loss at tunnel inlet are shown in Figures 6.1 to 6.3. A Matlab ".m" file (*wcal.m*, see Appendix 2) was then used to convert the pressure readings to velocities and do a least squares fit of the parameters A, B, and C in the equation $E^2 = A + B\sqrt{U} + CU$ **(Siddall and Davies, 1972,** from **Lomas, 1986).**

Initial attempts to use King's Law ($E^2 = A + BU^n$) had shown that this did not give a satisfactory fit over the full range of velocities; the addition of the CU term (C is relatively small) gives a much better agreement. Figure 6.4 compares the resulting correlation with the measurements; it can be seen that the agreement is very good. "*wcal.m*" calculates about 20 pairs of voltages and velocities from this curve fit and files them as an ASCII format "linearisation" file that is used by DUCKS in a linear interpolation process to convert the recorded voltage signals to velocity.

The air total temperature and pressure is also recorded in the file to allow the voltage and velocity columns to be scaled for use at different ambient conditions. This was used to correct for the pressure drop (typically $0.06 \times P_0$) across the grid. The scaling assumes that the electrical power dissipated in the wire is proportional to the heat transfer coefficient and temperature difference:

$$\frac{E_w^2}{R} = \frac{kNu}{d}(T_{wire} - T_{air}) \quad \text{and} \quad Nu = f(Re, Pr)$$

where E_w is the voltage across the wire, R is the anemometer resistance setting, k is conductivity and d is wire diameter. Since the Prandtl number is constant the Nusselt number can be described as a function of the Reynolds number. d is constant and Mach numbers are low and nearly constant at each calibration point, which allows total pressure and temperature to be used to approximate the Reynolds number.

The Dantec 55M10 standard bridge **(DISA, 1976)** has a 50 Ω ratio resistor in the probe arm, so the ratio of wire voltage to anemometer output voltage is

$$E_w = \left(\frac{R}{50 + R}\right) E$$

where E is the bridge supply voltage that provides the output signal from the anemometer. In practice this factor is constant as R is not usually adjusted after calibration.

The calibration function f can then be redefined as f_1 or f_2 to allow scaling of the voltages and velocities:

$$\left(\frac{R}{R + 50}\right)^2 \frac{E^2}{R k \Delta T} = f_1(Re) = f_2\left(\frac{P U}{\mu T}\right)$$

Scaling for changes in P, T, R, k, ΔT and μ is thus possible without making any assumptions about the (King's law or otherwise) form of the function f_2.

6.3 MEASUREMENT OF POWER SPECTRAL DENSITY.

Turbulence spectra were measured by recording the AC component of the hot wire voltage using a 55M series Dantec hot wire anemometer and the Datalab transient recorder. A simple R-C network (2.2 ms time constant) and an anti-alias filter (ω_0 = 66 kHz) were connected between the anemometer and the recorder. Filter and gain settings of 3 and 5 respectively were used on the anemometer as they gave the highest possible frequency response without risking resonance. The response using these settings is quoted in the Dantec manual as being almost flat up to about 100 kHz.

The data was captured as 32768 point files at a sampling rate of 200 kHz. Measurements of the DC component of the voltage and the air temperature were also taken at frequent intervals. The velocity derived from the hot wire voltage is very sensitive to changes in air temperature, which varied over about ±1 K from one minute to the next. The data files were processed as follows:

- add the DC voltage
- linearise, allowing for local air temperature and pressure
- "cut" data into 16 segments of 2048 points each
- FFT these and average the FFT results.
- divide by mean velocity.
- correct for anti-alias filter response.
- scale values for plotting as a power spectral density against wavenumber.

About 4 files (64 FFT's) were typically used for each turbulence measurement.

6.4 EFFECT OF DIRT ON HOT WIRES.

The presence of welding, gas cutting, grinding, spray painting, bead blasting and laser anemometry seeding in the laboratory, plus a very dusty scrapyard within a few hundred metres, meant that hot wire contamination was a serious problem for an open circuit wind tunnel. After prolonged use the wire appeared under a microscope as if covered by a layer of paint, and polystyrene microballoons could be seen sticking to the prongs. The frequency response was seriously impaired; replacing the dirty wire with a new one (Figure 6.5) showed that the measurements were affected at all frequencies above 3 kHz, and at frequencies above 40 kHz the error in the turbulence PSD could be as large as 8 dB.

Various attempts were made to clean wires and filter the air entering the tunnel which were only partially effective. No satisfactory way was found of measuring the amount of dirt on the wire except by comparing the measured spectrum with one taken using a newly replaced wire, which is too time consuming a method to be of any great use. The change in frequency response could not be reliably detected from the anemometer square-wave setup test, which is a measure of the response time of the electronics as well as the thermal time constant of the wire.

It was finally decided that the best solution was to replace the wire every few days under normal circumstances, or every day if the air appeared particularly dirty. A gauze filter over the bellmouth inlet was slightly beneficial, but not enough to cure the problem.

6.5 AVOIDANCE OF WIRE RESONANCE

It was frequently found that the grid turbulence spectra exhibited a resonance somewhere between 40 kHz and 100 kHz. This appeared to be a strain gauge effect due to vibration of the prongs (or the wire itself) leading to changes in wire tension. It was initially reduced by sticking a drop of RTV rubber between the prongs to damp out vibration there; this extended from the ceramic stem to within about 1.5 mm of the wire, and was smoothed to minimise any flow disturbance. It appeared that any remaining vibration was (with luck, if the wire was fairly tight) above 100 kHz and therefore not visible on the spectrum or, if not, could be reduced in amplitude by bending the prongs together slightly which reduced the change in tension from small prong movements. If this failed the wire would be removed and a new one welded in place.

To avoid the inconvenience of calibrating a wire and then finding that it resonated, new wires were checked for resonance by measuring and examining the spectrum from a grid (using a "typical" linearisation file) before proceeding with the calibration. Typical "good" and "bad" spectra are shown in Figure 6.6.

6.6 NOISE AND GRID-OUT TURBULENCE LEVELS.

Figure 6.7 shows the turbulence spectrum in the tunnel with no upstream grids, at a speed of 85.5 m/s. The measurement was taken 37 mm above the plate at 150 mm from the leading edge. The signal is less than the noise level (with no flow, but converted to velocity as if it was a turbulence signal) for wavenumbers

> 290 m^{-1}, which corresponds to wavelengths < 20 mm. Over larger wavelengths than this the grid-out turbulence level is 0.07%. It can be seen from the spectrum for grid A (the lowest turbulence grid-in case) which is also included in the figure that the signal to noise ratio for turbulence measurements was very good.

6.7 COMPARISON OF GRID TURBULENCE SPECTRA WITH PREDICTIONS

Roach (1987) has compiled data from a large number of researchers on the turbulence levels, length scales and spectra produced by bar grids. From these he chose the following correlations to define the spectra from parallel bar grids:

$$Tu = 0.8\left(\frac{x}{d}\right)^{-\frac{5}{7}}$$

$$\Lambda_x = 0.2\,d\sqrt{\left(\frac{x}{d}\right)}$$

(Tu is the turbulence intensity (in "%"); d is the bar diameter and x is the distance from the bar centreline to the measuring station. Λ_x is the integral length scale (see Appendix 1 for definition)).

Having correlated the intensity and scale, he then defined the shape of the turbulence power spectral density (PSD):

$$PSD = \frac{\mathrm{d}\left(\frac{u'}{\overline{U}}\right)^2}{\mathrm{d}k} = \frac{2\,Tu^2\,\Lambda}{\pi(1 + \Lambda^2 k^2)} \quad \text{for} \quad k\Lambda < 8.17,$$

$$PSD = \frac{\mathrm{d}\left(\frac{u'}{\overline{U}}\right)^2}{\mathrm{d}k} = \frac{147.55\,\Lambda\,Tu^2}{(\Lambda k)^{4.6}} \quad \text{for} \quad k\Lambda > 8.17.$$

These correlations are independent of the bar spacing, which is only of importance in so far as it affects the pressure drop and rate at which isotropy is reached. Grid solidities of much over 40% are not advisable both because of the high pressure drop incurred and because low-frequency flow instabilities may result.

Figure 6.8 compares the measured spectrum from a grid of 10 bars of 6 mm diameter at x/d=60 with the prediction using this correlation (see *roach.m* in Appendix A.2.2). The agreement was good enough for the correlation to be used while choosing the grid configurations for the heat transfer tests, although the single bar grids at small x/d values were not expected to be modelled with any great accuracy because this correlation is based on grids designed to produce essentially isotropic turbulence.

6.8 CHOICE OF GRID CONFIGURATIONS FOR FLAT PLATE TESTS.

The choice of grids for the flat plate experiment was intended to satisfy two criteria: firstly, measurements of the effect of length scale on heat transfer should be performed over the widest possible range of length scales and secondly, this range should include some conditions of relevance to heat transfer in a gas turbine HP stage.

The first criterion may easily be quantified. The largest possible length-scale will be generated by the greatest possible bar diameter, which is restricted to the largest single bar that can be fitted into the duct upstream of the working section. A 60 mm diameter bar (across a 150 mm square working section) was chosen as the largest that could be used without producing an excessively non-uniform flow downstream; this was based on previous workers who had adopted a maximum of 40% solidity as a "rule of thumb" for grid design.

Similarly, the smallest possible length-scale will be produced by the finest grid that can be used. The limitation here is that small bars have to be placed very close to the plate to generate a usefully high turbulence intensity, and that the turbulence spectrum will then decay very rapidly along the plate. This would lead to difficulty in interpreting the result, as one could not (without taking much more detailed measurements) say whether any enhancement was due to the local turbulence or to some result of the higher turbulence level further upstream. This led to a grid of 10 bars of 6 mm diameter (*i.e.* 15 mm pitch) being chosen as the smallest practical.

It was initially intended to produce a variety of turbulence length scales at a constant turbulence intensity. This proved impossible to achieve within the existing constraints of tunnel length and cross-section. As an alternative to this a number of grids were chosen that would, in the progression from one to another, give successive steps in the energy at the high or low wavenumber ends of the spectrum, while at the other end of the spectrum keeping the same characteristics as the previous grid. It was felt that this would be the best way of distinguishing between the effects of turbulence at high and low wavenumbers, and then inferring a length-scale effect for turbulence of a fixed intensity.

Four grids (A, B, C and D) were initially designed to do this, using a correlation by **Roach (1987)**. Subsequent measurements of the spectra, which decay at different rates along the plate because of the differences in x/d, led to a fifth grid (E, 4 bars, 15 mm diameter) being built for the thin film tests in an attempt to achieve this situation at more than one position on the plate.

The freestream turbulence spectrum from each grid was measured mid-way between the plate and the upper wall of the working section at three positions along the plate. These spectra are shown in Figures 6.9, 6.10 and 6.11.

The second criterion, that the test results should be of relevance to a gas turbine, was more difficult to achieve because of the very wide range of turbulence intensities and ratios of length-scale to boundary layer thickness that are produced around different parts of an aerofoil by the freestream velocity distribution. (The boundary layer thickness around a typical HP nozzle guide vane has been compared with that on the plate in Chapter 5). The solution was to use the widest possible variation in turbulence parameters to derive a correlation which would be applicable to engine conditions.

6.9 CALCULATION OF TURBULENCE LENGTH SCALES.

(See Appendix A.1.3 for definitions of length scale).

6.9.1 Integral length scale Λ_x

Integral length scales were calculated from the autocorrelation of the streamwise velocity fluctuations. A typical autocorrelation is shown in Figure 6.12; this is a mean of several 32768 point correlations. The traditional technique, of integrating the area under the autocorrelation curve to infinite time (or as far as is practical) was, however, found to yield scales that tended to zero. This is illustrated in Figure 6.13, which shows the value of the integral as the integration limit increases. It can be shown to be inevitable if the correlation is derived from a finite, zero mean time-series, as follows:

$$R(\tau) = \int_0^T u(t)\, u(t+\tau)\, \mathrm{d}t$$

$$\Lambda_x = \int_0^T R(\tau)\, \mathrm{d}\tau = \int_0^T\!\!\int_0^T u(t)\, u(t+\tau)\, \mathrm{d}t\, \mathrm{d}\tau = \int_0^T u(t) \int_0^T u(t+\tau)\mathrm{d}\tau\, \mathrm{d}t$$

where $R(\tau)$ is the correlation coefficient at a time lag τ and T is the time over which the data has been recorded. The mean level of the data is zero, *i.e.*

$$\int_0^T u(t+\tau)\mathrm{d}\tau \quad = \quad 0 \text{ and so } \Lambda_x \quad = \quad 0.$$

Hinze (1975) has noted that a similar effect must occur when attempting to integrate transverse correlations, and that some (arbitrary) integration limit must be chosen.

The correlation was therefore integrated as far as the first zero point (*i.e.* while $R(\tau) > 0$), which corresponds to the first peak in Figure 6.13:

$$\Lambda_x = \bar{U}\int_0^{R(\tau)=0} R(\tau)\, d\tau$$

6.9.2 Dissipation length scale L_e^u.

There are two methods which can be used to calculate the dissipation length scale. The first method **(Hinze, 1975)** assumes $R(\tau)$ is parabolic near $\tau = 0$, and L_e^u is taken as the point where a fitted parabola intersects the $R(\tau) = 0$ line. In the present work, $R(\tau)$ is characteristically sharply peaked near $\tau = 0$ (Figure 6.12) and fitted parabolas underestimate L_e^u, with $L_e^u \approx 0.25 \times \Lambda_x$.

The second method is to obtain L_e^u from the streamwise decay of turbulence level by fitting the line **(Castro, 1984)**

$$\left(\frac{Tu}{100}\right)^{-1.6} = \left(\frac{\overline{u'^2}}{U^2}\right)^{-0.8} = A\left(\frac{x + x_g}{d}\right) + B$$

as shown in Figure 6.14. Castro used mesh pitch rather than bar diameter when fitting this line, but in this case (*i.e.* with a single bar in some cases) the diameter d is a more appropriate parameter; this has no effect on the resulting length scale value.

The dissipation length scale is then obtained using:

$$L_u^\epsilon = \frac{\overline{u'^2}^{3/2}}{-U\left(\dfrac{\partial \overline{u'^2}}{\partial x}\right)} = 0.8\left(\frac{d}{A}\right)\left(\frac{Tu}{100}\right)^{-0.6}$$

by differentiating the fitted curve. This definition was more useful than the parabola fitting technique.

The grid dimensions, turbulence intensities and length scales are tabulated in Figure 6.15. Integral length scales for the combustor data were similarly calculated and are discussed in Chapters 4 and 10; dissipation length scales could not be deduced as the spreading of the jet made measurements of the decay rate impracticable. Turbulent boundary layer thicknesses along the plate are also shown in Figure 6.15 for comparison with the length scales; these are predicted using the equations given in §5.5 and §9.6, with Reynolds number based on the distance x from the leading edge.

Figure 6.16 shows the position of the grids relative to the plate. In all tests where the plate was present the bars were perpendicular to the surface of the plate.

6.10. USE OF HOT WIRE ANEMOMETER IN BOUNDARY LAYER.

The hot wire probe holder allowed the wire to be placed at any height from 0.4 mm to 40 mm above the plate surface. The wire height above the surface was related to the micrometer reading by placing a metal block of known thickness on the plate when the wire was inserted into its holder. The wire was set level with the block by eye using a small telescope, and the micrometer reading and block thickness were noted.

Measurements of the boundary layer profile were taken by manually setting the wire height using the depth micrometer, capturing 16384 data points and recording the mean (DC) voltage. The mean of three such readings was taken to minimise the effect of slow tunnel fluctuations; air temperature readings were also taken at frequent intervals. The mean voltages were entered into Matlab as a table, and the velocities were calculated using the wire calibration coefficients.

Figure 6.17 compares three measurements of the boundary layer profile at x = 300 mm, tripped (see §7.7), with no grid. Two of these were done using a wire with RTV damping; the third was done with a clean wire, to investigate whether interference effects between the rubber lump and the surface would lead to errors. The repeatability is excellent, and justified the use of RTV damping in subsequent measurements of spectra within the boundary layer.

Turbulent boundary layer profiles may be characterised in terms of a viscous sub-layer, a "log-law" region and a "velocity-defect" region. Theory predicts that within the log-law region the velocity distribution should be of the form (**Duncan et al, 1970**):

$$\frac{U}{u^*} = A \ln\left(\frac{yu^*}{\nu}\right) + B$$

where $u^* = \sqrt{\frac{\tau_w}{\rho}}$ is known as the "friction velocity" and y is the height above the surface. The constants A and B have been measured by many researchers; typical values (**Clauser, 1956, from Hinze, 1975**) give:

$$\frac{U}{u^*} = 2.44 \ln(y^+) + 4.9, \quad \text{with} \quad y^+ = \frac{yu^*}{\nu}.$$

u^* can be estimated using an empirical correlation for the local turbulent skin friction coefficient cf' (**Schlichting, 1979**):

$$cf' = (2\log_{10} Re_x - 0.65)^{-2.3}$$

In this case $u^* = 3.326$ m/s is predicted. This does not place the measured data exactly on the log-law line, as can be seen from Figure 6.18; this might be due to errors in u^* or y. A small adjustment to these values ($u^* = 3.193$ m/s, $y = y - 0.11\ \mathrm{mm}$) puts the innermost two points of this measured profile on the log-law line.

The form of the velocity distribution in the outer regions of the boundary layer might also be expected to follow a logarithmic law:

$$\frac{U_\infty - U}{u^*} = -2.44 \ln\left(\frac{y}{\delta_{100}}\right) + 2.5$$

(**Schlichting**). In practice it is usually found that it can be better described by an empirical correlation (**Clauser**, from **Hinze**):

$$\frac{(U_\infty - U)}{u^*} = 9.6\left(1 - \frac{y}{\delta_{100}}\right)^2$$

Figure 6.19 shows that the parameters chosen for plotting the innermost data points against the log law equation also produce a good agreement between the remaining points and this velocity-defect correlation. The assumption that the probe may have moved 0.11 mm closer to the surface when the flow started is quite believable, and to have only a 4% "error" in predicting u^* from a skin friction correlation is remarkably good. The close fit to predicted values for this boundary layer suggest that the design intent, of producing a well-developed turbulent boundary layer, has been achieved.

6.11. CONCLUSIONS.

A hot wire calibration technique was developed that allowed rapid calibration; this allowed the wire to be replaced frequently to minimise the build-up of dirt, which was found to have a significant effect on the frequency response.

Wire vibration was found to affect the measured turbulence spectra; this problem was largely cured by moulding a drop of RTV rubber between the prongs and examining the response before calibration.

Five grid configurations were chosen for the heat transfer tests. A correlation by **Roach** was found to be useful for the initial design.

Integral length scales were measured for these grids at three positions along the plate. The conventional definition of length scale had to be adapted for use with a finite-length signal.

Dissipation length scales were calculated from the intensity decay rate as the spectra from these grids were sharp-tipped and unsuitable for the theoretical technique of parabola fitting.

The hot wire probe holder proved capable of producing accurate and repeatable boundary layer traverses. Boundary layer parameters inferred from these were close to predicted values.

CHAPTER 7.

EXPERIMENTAL DETAILS OF LIQUID CRYSTAL TESTING.

7.1 INTRODUCTION.

7.1.1 Liquid crystal techniques.

The use of thermochromic liquid crystals to measure heat flux has been pioneered by **Ireland and Jones (1985)**. A chiral nematic liquid crystal is encapsulated in microscopic spheres that can be painted onto a surface if mixed with a suitable binding agent. Each crystal typically exhibits a *change temperature* at which it develops a bright colour; the colour is visible over a very narrow temperature band, typically 0.1°C wide, and the crystal is clear outside this range. If these crystals are painted onto a surface, and a temperature gradient is generated in it such that some parts are hotter and some cooler than this change temperature, coloured lines will be seen along the "contour lines" that are at the change temperature. By tracking the movement of these lines (using a video camera) one may determine the time at which any part of the plate reaches this temperature. A black substrate under the liquid crystal layer is used to enhance visibility; typically this consists of matt black paint sprayed onto a perspex base.

This allows liquid crystals to be used in the measurement of heat transfer coefficient. The technique requires that a step change in heat transfer coefficient (preferably from an initial zero heat flux case) be applied to the surface. The diffusion of heat is described by:

$$\frac{\partial T}{\partial t} = \alpha \frac{\partial^2 T}{\partial x^2} \tag{7.1}$$

where $\alpha = \dfrac{k}{\rho Cp}$.

This may be solved for the semi-infinite case where the solid is sufficiently thick and the surface sufficiently flat that the heat flux may be considered one-dimensional with no effects due to heat flux into the other side of the solid (**Schultz and Jones, 1973**). A heat flux pulse then propagates into the surface; for the constant heat flux case the shape of this pulse is given by

$$\frac{\dot{q}_x}{\dot{q}_s} = \mathrm{erfc}(X), \qquad \frac{T_x}{T_s} = e^{-X^2} - \sqrt{\pi}\, X \mathrm{erfc}(X), \qquad X = \frac{x}{2\sqrt{\alpha t}} \tag{7.2}$$

This is plotted in Figure 7.1.

The surface temperature change after a step change to a uniform heat transfer coefficient may be derived in the semi-infinite case to give:

$$\theta = 1 - e^{\beta^2} \mathrm{erfc}\, \beta \tag{7.3}$$

where $\theta = \dfrac{T_i - T_{LQ}}{T_i - T_g} = \dfrac{\Delta T_{surface,\ start\ to\ colour\ change}}{\Delta T_{initial,\ surface}}$

and $\beta = \dfrac{h\sqrt{t}}{\sqrt{\rho c k}}$

This allows the heat transfer coefficient h to be determined from the time to the colour change (t), the thermal properties of the substrate ($\sqrt{\rho c k}$), and the start, gas and change temperatures. The surface temperature change with time resulting from this equation is shown in Figure 7.2. (This has been plotted with ($1-\theta$) as the y-parameter to illustrate the situation where the plate is cooling down).

7.1.2 Purpose of experiment.

A liquid crystal test was done on a perspex plate in the wind tunnel to study the heat transfer enhancement due to turbulence. This was intended to be a quick and easy experiment to confirm that a uniform flow was achieved, and that the heating arrangements gave a reasonably uniform temperature over the whole plate; and to identify those grid configurations that gave noticeable increases in heat transfer as being suitable for more detailed study using thin film gauges.

Experience with the crystals showed, however, that results of the accuracy and reproducibility required for this kind of study were very difficult to achieve using this technique; it would have saved a great deal of time (with hindsight) to use the crystals purely for flow visualisation and to have relied on the thin film gauges for the heat transfer measurements.

7.1.3 Double crystal technique.

Equation 7.2 above defines the heat transfer coefficient using just one liquid crystal change temperature. If a mixture of crystals is used, giving two or more change temperatures and change times, another parameter (such as the initial plate temperature) may also be found **(Ireland and Jones, 1987; Jones and Hippensteele 1988)**. Details of the experimental and analysis techniques involved are described in §7.6.

7.2 APPARATUS.

The flat plate working section in the high speed tunnel (described in Chapter 5) was used for the liquid crystal experiment. A perspex plate with an 8:1 involute leading edge shape (see §5.4) was made for this; the Macor plate subsequently used for thin film tests was an exact copy of this.

The upper surface of the plate was painted black; a grid of lines at 40 mm pitch were painted with a metallic aluminium finish paint over this to provide reference points on the video recording. After thorough drying, this was coated with liquid crystals; a mirror at 45% above the working section was used to allow a video camera (Panasonic F10) standing to one side to film the surface. The recording was done on a Panasonic G45 video recorder.

Obtaining a suitable contrast level proved difficult, but was partially overcome by placing a black box around the camera to minimise reflections of itself in the perspex, and illuminating the plate with a fluorescent tube type "anglepoise" lamp positioned as close as possible to the rear working section window. Careful setting of the brightness and contrast levels on the monitor (a Panasonic television), and manual aperture setting on the camera, were also essential.

The heat transfer testing, both liquid crystal and using thin film gauges, was done using a pre-heated plate and unheated, ambient temperature air. The effect of temperature ratio on the heat transfer coefficient has previously been shown to be small, and quantifiable (**Kays and Crawford, 1980**). This technique has the advantage over a heated air test that there is little danger of a drift in air temperature during the run which would make the analysis much more complex.

7.3 CHOICE OF LIQUID CRYSTALS.

The choice of crystal change temperature should ideally take account of the following criteria:

- plate start temperature is determined in part by the heating apparatus. While in theory any plate temperature can be achieved by turning off the heater when this temperature is reached, in practice a more uniform start temperature can be produced by leaving the plate to bake for 30-40 minutes at a hot air temperature close to the desired plate temperature. The hair dryer chosen as a heater allowed this for temperatures of about 40°C and 60°C above ambient.
- plate start temperatures may not be >100°C to avoid softening the perspex, and to avoid damaging the liquid crystals themselves.

- the time taken for the first crystal to change, in the highest heat flux area of interest, should not be so small that it is either difficult to estimate from a video recording with a frame every 40 ms, or might lead to excessive sensitivity to the speed of flow start-up in the tunnel. A minimum time of at least 2 seconds might be reasonable.

- the time taken for the last crystal to change, in the lowest heat flux region, should not be so long that the semi-infinite conduction assumption becomes invalid. If one considers constant heat flux conduction from the far side of the plate (uncoated with crystals) into an infinitely thick plate, the temperature change at a distance x into it will be 1% of the surface temperature change at $x = 3.16\sqrt{\alpha t}$ (from **Schultz and Jones, 1973**). Taking $\alpha \approx 10^{-7}$ m^2/s for perspex, and a plate thickness x = 0.01 m, this condition will be met after t = 100 seconds. It can be seen from Figure 7.1 that the heat flux in a semi-infinite solid beyond this point is very small, so this result may be assumed to apply equally to the case of a plate that is only this thick and not actually semi-infinite.

- if using the double crystal technique (see §7.6 for details) to determine the start temperature as well as the heat transfer coefficient, the ratio between the change times and the difference between the crystal change temperatures must be sufficient to avoid excessive sensitivity to experimental errors in testing or calibration.

The effect of the difference between the two crystals used in the double crystal technique is shown in Figure 7.3. It can be seen that the plate temperature (from θ) will be very sensitive to any error in the time ratio t_2/t_1 or in the temperature ratio $\frac{(T_{air} - T_{crys1})}{(T_{air} - T_{crys2})}$ if this temperature ratio is small, *eg.* 1.077.

This graph also shows that high values of θ (*eg.* >0.8) will lead to the equation being so ill-conditioned that reliable results will be almost impossible to achieve, and that low values of θ may, depending on the difference between the crystal change points, give a time ratio so large that one or other of the time criteria above is infringed.

It was decided that, because the liquid crystal testing was only intended to give a quick and preliminary indication of the heat transfer effects, the plate would if possible be painted with crystals that were available in the laboratory rather than ordering an new batch with change temperatures chosen specifically for this project. Crystals with nominal change temperatures of 30, 35 and 40°C were available.

Testing started in June with air temperatures in the laboratory ranging from 20°C up to 31°C, which ruled out use of the 30°C change point material.

A plate start temperature of 65°C and an ambient temperature of 20°C, with change points at 40 and 35°C, would give $\theta_{mean} \approx 0.61$ and $\dfrac{(T_{air} - T_{crys1})}{(T_{air} - T_{crys2})} = 1.33$,

which implies a time ratio of about 2.5 from Figure 7.3. The slope of the curve at this point suggested that the double crystal technique, though rather sensitive to experimental errors, should be feasible with these two crystals.

7.4 CRYSTAL CALIBRATION.

A thin foil thermocouple was glued to the plate before spraying it with the black paint and crystals. The thermocouple position was 97 mm from the leading edge and 46 mm from the centreline; it was placed well to one side of the plate so that any disruption of the boundary layer by unevenness here would not affect heat transfer measurements taken on the centreline. The thermocouple was connected, via a cold junction and Fylde amplifier, to a digital voltmeter.

For calibration the plate was placed in the tunnel, heated to above the change temperatures, and allowed to cool slowly. Both the plate surface around the thermocouple and the DVM display were recorded on video; colour contours passing the tip of the thermocouple could be seen in great detail. The video recording was subsequently examined to identify the temperature range over which the crystals changed colour.

7.5 DETERMINATION OF TIME INTERVAL TO CRYSTAL CHANGE POINT.

A WV-KB12F character generator was fitted to the video camera to allow an introductory screen (giving run number, configuration and date) to be recorded prior to each run. This unit includes a timer that displays a stop-watch on the screen, counting in steps of 0.1 second. This is not ideal because the characters change once every 2½ frames on average, but in practice it was possible to count frames from the last character change and infer the frame time to 0.04 second steps (±about .02 second as the video frames and stop-watch were not necessarily in step).

The stop-watch was started manually before a run, so some way of identifying the time when the flap valve opened and the flow started was also required. A Sensym pressure transducer connected between a pitot tube and a static tapping at the rear of the working section detected the sudden increase in dynamic head when the flow started. The signal from this was both recorded on the transient recorder and passed through a CAS2 amplifier with a high gain, such that the amplifier was usually saturated and acted as a switch that would be triggered by a small change in dynamic head. This switching signal, at ±18 V, was passed to a Schmidt trigger circuit that provided some hysteresis, sharpened the switching, and reduced it to TTL voltage levels, and then to the external trigger connection on the Datalab transient recorder and a light-emitting diode (LED) which was visible on the video. As the flow started the LED went out, and the Datalab dynamic head signal proved that the flow actually started at this time, *i.e.* that it was not a false trigger. Figure 7.4 shows a typical pressure signal at the start of a test.

This measurement of the tunnel start-up transient allowed the heat transfer effect of the finite start-up time to be estimated. The boundary layer was predominantly turbulent, which implies that $Nu_x \propto Re_x^{0.8}$. Figure 7.5 shows how the parameter $\upsilon^{0.8}$ varies during the starting transient, and allows an effective "start delay" relative to the trigger point to be defined in terms of the mean value of this parameter over (say) the first 0.1 second of the test. The stop-watch time seen on the video recording as the LED went out was then corrected by this delay, which was generally of order 0.015 second.

The change time at each grid point was determined from the video recording by eye. This is an exceedingly tedious business (and not to be recommended if you are colour-blind), but it was felt that automatic digitisation methods would probably not save any time for the limited number of runs and points required.

7.6 DERIVATION OF INITIAL TEMPERATURE AND HEAT FLUX.

The plate temperature before a run was measured at one point using the surface thermocouple. It was felt that spatial variations in plate temperature might have a severe effect on the heat transfer measurements, so attempts were made to determine the starting temperature at each grid point using the double-crystal technique.

This involves using two liquid crystals that change at different temperatures. If both the change times are known at any particular point one may determine a start temperature and heat transfer coefficient that satisfy Equation 7.3 for both pairs of change time and change temperature.

This was done iteratively in Matlab using the macro file *lqht.m* (see Appendix 2), which works by alternately estimating the start temperature from the upper crystal change time/temperature and an (approximate) heat transfer coefficient, then revising the heat transfer coefficient using this start temperature and the lower crystal change time/temperature.

A matrix containing start temperatures and heat transfer coefficients for all the data points is generated. At some points the start temperature prediction would fail to converge (or give unreasonably high values), and there was then the option of specifying a mean start temperature for the whole plate and recalculating the heat transfer coefficients using this. This will be discussed more fully below.

7.7 COMMISSIONING TESTS.

A number of commissioning tests were done to:-

- show that separation did not occur at the blend point from the leading edge to the flat surface,
- demonstrate the repeatability of the technique,
- confirm that suitable start temperatures were being achieved,
- test that the flap valve and working section operated as intended,
- confirm that the trip strip caused transition without increasing the Nusselt numbers above turbulent levels.

Successful use of the double-crystal technique proved very difficult to achieve with the crystals and ambient temperatures available. The fact that the plate showed typical heat transfer coefficients somewhat below the level expected from a turbulent flat-plate correlation also cast doubts on the quality of the measurements, and it was decided to persevere with an investigation of possible sources of error until at least one of these was resolved.

The (nominally) 35°C and 40°C change-point crystals proved on calibration to be 36.36°C and 38.44°C, which was much too close to allow any accuracy in the determination of the start temperature. These were replaced with crystals from a different batch (also nominally 35 and 40°C) which gave 36.9 and 41.1°C when calibrated. This also proved too close to allow an accurate start temperature estimate to be made. Successive runs showed larger and larger discrepancies between the thermocouple and the temperature inferred using the double crystal method. Recalibration showed that the change temperatures had drifted to 35.36 and 39.37°C, and (later) 35.76 and 39.59°C. It appears that ultra-violet light from the fluorescent tube (and perhaps from sunlight) was penetrating the perspex and degrading the liquid crystals. The detrimental effects of UV light on crystals are well known, but perspex had been thought to be so opaque to UV as to offer complete protection. This appears not to be the case under the test conditions, which had a fluorescent tube 20 cm from the plate shining through a 30 mm thickness of perspex for hours while the plate was being heated before each run. Once this was realised the light was turned on only a few seconds before each test, and a screen was built to prevent daylight hitting the working section directly. This seemed to have a very beneficial effect.

While attempting to obtain believable start temperatures it was gradually realised that the ambient air temperature changed during each run by typically ±1°C, and was generally slightly lower than the temperature of the air in the inlet duct before the flow started. It was also found that the velocity in the tunnel varied from run to run, which can only be attributed to variations in the mains supply voltage. This meant that use of the Datalab transient recorder was

essential to monitor air temperature and velocity throughout the run, as well as to accurately determine the start time.

By October the ambient air temperature had fallen to about 17°C and use of a 30°C change point crystal became possible. This was simply sprayed on top of the existing two crystals, which continued to be visible. This gave a much more believable prediction of the start temperature, as shown by Figure 7.6, and indicated that the plate heating arrangements gave a reasonably uniform temperature over the whole plate. (The peaks at about x = 40 mm are due to the trip strip and are not believed to be genuine). Having thus confirmed that the heat conduction process was properly understood, the thermocouple temperature was in fact used as the start temperature over the whole plate for subsequent tests, which reduced the sensitivity to any drift in crystal calibration (it should be noted that the double crystal technique is very sensitive to the difference in crystal change temperatures, whereas the heat transfer coefficient calculation is only dependant on the absolute change temperature, and so is much less sensitive to drift).

Figure 7.7 shows the repeatability of this technique for two tests with grid A and for two with grid B. Typically two runs were done at each condition, and the results (if close) were averaged; if the results were noticeably different the test would be repeated until it became clear which runs were valid and which one was a rogue measurement.

The trip strip consisted of a double layer of glass-fibre tape (0.34 mm thick overall) which extended from 21 to 25 mm axial chord; this corresponds to a Reynolds number of approximately 100000. Figure 7.8 shows that this worked well in that it caused immediate transition in the grid-out case, without increasing the Nusselt numbers when subject to 4% turbulence from grid A above the level seen after (rapid) natural transition.

7.8 CONCLUSIONS.

Thermochromic liquid crystal measurements are often presented as being a "quick and easy" way of determining heat transfer coefficients. This is not entirely the case. They **are** particularly suitable for taking measurements over complex surfaces, where one wants complete surface coverage to show (for instance) secondary flow features, and they **can** give quick results if one is not looking for any great accuracy; but achieving repeatability accurate to a few percent is very difficult, and is unlikely to be possible without very careful monitoring of air temperature, velocity and initial temperatures, and frequent crystal recalibration. If this level of accuracy is required, and the equipment is available, thin-film heat transfer gauges are a much easier technique (see Chapters 8 and 9).

CHAPTER 8.

EXPERIMENTAL DETAILS OF THIN FILM GAUGE TESTS.

8.1 INTRODUCTION.

The liquid crystal flat plate tests were followed by tests using thin-film heat flux gauges on a Macor plate. The construction, calibration and commissioning of this plate will now be described so that the results from both the liquid crystal and thin film tests may be discussed together in Chapter 9.

8.2 GAUGE LAYOUT ON PLATE.

The gauge layout on the flat plate was chosen both to give a measurement of the heat transfer coefficient along the plate centreline, at a number of uniformly spaced positions, and to allow a detailed study of the heat transfer process over a small region. The former was achieved by a series of gauges at a uniform 20 mm spacing from $x = 0$ to $x = 300$ mm, and the latter by two clusters of gauges, with one around $x = 150$ mm and the other around $x = 300$ mm. The reason for having two such clusters was that the one at 150 mm would be close enough to the grid boxes to allow a usefully high turbulence intensity to be generated even with a fine bar grid, whereas the one at 300 mm would allow tests to be done at a higher Reynolds number if desired.

For ease of manufacture (with a reasonable yield and sensitivity) the gauges were made 4 mm long $\times$ 0.25 mm wide, with 5 mm wide leadouts. A photograph of the plate is shown in Figure 8.1, and the gauges are numbered in Figure 8.2.

8.3 GAUGE CALIBRATION.

Figure 8.3 lists the gauge coordinates, resistances and resistance change with temperature. The resistances were measured in a temperature controlled water bath to ensure uniform temperatures. The properties of the Macor substrate were not measured, as this has been done thoroughly in the past by **Doorly (1985).**

8.4 THEORY OF HTA1 "ANALOGUE" CIRCUITS AND THEIR CALIBRATION.

The heat conduction equation $\frac{\partial^2 T}{\partial x^2} = \frac{\rho c}{k}\frac{\partial T}{\partial t}$ which was discussed in Chapter 7

with respect to mean heat transfer coefficient levels over a extended period will now be considered with regard to the frequency response of surface temperature to heat flux. The Laplace transform solution to this at the surface is (**Schultz and Jones, 1973**)

$\bar{T} = \frac{\bar{\dot{q}}}{\sqrt{\rho c k}\sqrt{s}}$, which may be described in the frequency domain as

$$\dot{q}(\omega) = T(\omega)\sqrt{\rho c k}\sqrt{\mathrm{j}\omega} \tag{8.1}$$

The gauge resistance is a function of temperature,

$R = R_{20}(1 + \alpha(T - 20))$ where $\alpha = \frac{1}{R_{20}}\frac{\mathrm{d}R}{\mathrm{d}T}$ is the gauge resistance change/°C as

usually defined. For determining heat flux, this resistance is best measured by connecting it to a constant current generator and recording the voltage across it.

In theory one could digitise this gauge voltage and calculate the heat flux signal from it. In practice the change in surface temperature due to a high-frequency component of the heat flux is so small relative to the low-frequency components (because of the $\sqrt{\omega}$ term in Equation 8.1) that an impractically high resolution analogue to digital converter would be needed to avoid loosing any high frequency signal amid the digitisation noise. The solution to this problem is to convert the gauge voltage into a heat flux signal electrically **before** digitisation. This may be done using an amplifier with a voltage gain proportional to $\sqrt{\omega}$. Such an amplifier is described by **Oldfield et al (1982)**; it uses a resistor-capacitor transmission line to achieve the desired frequency response. A block diagram of the circuit is shown in Figure 8.4.

This has the response $\dfrac{V_2}{V_1} = \dfrac{-R_f}{Z_A}$ where V_1 is the voltage across the gauge and V_2 is the analogue output voltage; R_f is the feedback resistor and Z_A is the impedance of the transmission line. An 8-channel amplifier of this design (known as an "HTA1") was used to convert the gauge voltages to heat flux signals. Putting $V_1(\omega) = i_g R_{20} \alpha T(\omega)$ allows $\dot{q}$ to be specified in terms of V_2:

$$\dot{q}(\omega) = \left(\frac{\sqrt{j\omega}}{\frac{V_2}{V_1}}\right) \frac{\sqrt{\rho c k}}{i_g R_{20} \alpha} V_2(\omega)$$

Calibration is needed to measure V_2/V_1 for each channel. This could be done using a signal generator and measuring the response at a large number of different frequencies, but is much easier with an "anti-analogue" circuit, as shown schematically in Figure 8.5 (**Carlini, 1984**). This uses the fact that a step change in heat flux would produce a parabolic rise in surface temperature with time. A step in voltage, passed through the anti-analogue, creates an output voltage $\propto \sqrt{t}$ as shown in Figure 8.6. This is passed into the analogue amplifiers, which should then produce a step in output voltage.

Calibration is thus reduced to two steps:

1) calibrate the anti-analogue,
2) compare the output step heights of each HTA1 channel when fed with the

anti-analogue output against the height of the input pulse to the anti-analogue.

The anti-analogue was calibrated by recording both the input pulse and the resulting parabolic output waveform. A least squares curve fit to this parabola then gave an anti-analogue calibration coefficient of:

$$\frac{V_{AAo}}{V_{AAi}} = \frac{0.3217}{\sqrt{j\omega}}$$

where V_{AAi} and V_{AAo} are the anti-analogue input (pulse) and output voltages. Calibration of all eight HTA1 channels gave:

$$\frac{V_2}{V_1} = \left(\frac{0.9667}{0.3217}\right)\sqrt{j\omega} \quad \pm 1\%$$

8.5 TUNNEL INSTRUMENTATION.

The same Datalab DL1200 waveform recorder was used for both the combustor and flat plate experiments. Figure 8.7 shows the instrumentation for this tunnel; with the exception of the hot wire, gauges and analogues, the liquid crystal tests used the same configuration. A Sensym transducer (measuring dynamic head) coupled to a CAS2 amplifier was used both to determine the flow velocity and to trigger the Datalab as the flap valve opened; for the latter, a high gain was used so that the amplifier output was always saturated to the positive or negative limit and gave a rapid swing as the flow started.

8.6 EFFECT OF GAUGE CURRENT ON LOCAL TEMPERATURE AND NOISE.

The HTA1 analogues allow the gauge current to be set at any level up to 40 mA. The current must be high enough to give an adequate signal to noise ratio, but not so high that the power dissipated in the gauge raises its temperature enough to produce errors in the derived heat transfer coefficient or to invalidate the definition of heat transfer coefficient that implies a nearly isothermal wall temperature.

The formulae for Johnson and shot noise (**Horowitz and Hill, 1989**) suggest that, at typical temperatures and resistances (350 K, 50 Ω), $V_n \propto \sqrt{I_g}$. Measurements of the noise spectrum at the analogue output (Figure 8.8) show that the noise level is actually almost independent of the gauge current, which suggests that most of the noise is produced by the electronics rather than by the gauge itself. The noise signals have been converted to an effective $\frac{\dot{q}}{Q}$ using a scale factor based on the same current (37 mA) as used for the grid D measurement shown here.

The local heating effect of the current passing through the gauges was determined by simultaneously measuring the current through and voltage across a gauge at various currents. This allowed the gauge resistance, and thus its temperature, to be calculated. In each case the current was maintained for several minutes until the voltage became practically constant. It was found that the temperature rise could be correlated by $\Delta T = 96.5P^{0.8} - 0.7$, where P is the power dissipated in watts (Figure 8.9).

It was felt that a temperature rise of 3 K would probably give negligible errors in the heat transfer coefficient (with T_s - $T_a \approx 50$ K), particularly as it was principally the changes in heat transfer coefficient with the various grids, rather than the absolute level, that were of interest. This temperature rise implies a gauge current of ≈20 mA. It can be seen from Figure 8.8 that this gives a signal to noise ratio of over 10 dB at wavelengths greater than the length of the thin film gauges, which is more than adequate for measurement of the mean heat flux and a preliminary examination of the boundary layer state. A higher current was used later for a more detailed study of high-frequency effects and correlations between gauge and hot-wire signals, for which the signal to noise ratio was more important than absolute levels.

8.7 ANALYSIS TECHNIQUE.

Mean heat flux tests were done with a sample rate of 2000 Hz for 5% pre-trigger to 15% post-trigger, followed by sampling at 10 kHz for the remainder of the 4096 points. This allowed the tunnel flow to stabilise before starting to record at high frequency. The mean heat transfer coefficients were derived from the recorded signals as follows:

- read off the voltage of the inlet thermocouple, and convert to temperature
- read off the dynamic head, and convert to velocity
- for each channel, offset the data so that pre-trigger points have a zero mean level, multiply by the scale factor (see 8.3), and read off the mean value from the change in sampling rate onwards. Create a Matlab matrix q with rows for each gauge and columns for each run.
- create a similar Matlab variables *dt* giving the initial plate to air temperature difference for each of these columns, x giving the perimeter to each gauge, and *Re* with the Reynolds number at each gauge.
- run the *QTT* calculation (see §8.8) in *DUCKS* for one gauge to find the mean fall in plate temperature to the centre of the fast sampling rate period. Generate a Matlab matrix *dtqtt* of a temperature change value for each element of q by scaling this.

- create a similar matrix *dtvi* of the gauge temperature rise due to ohmic heating, and calculate (in Matlab language):

```
h = q ./ (dt + dtvi - dtqtt);
Nu = h .* x / k;
```

- plot *Nu* vs *Re*.

This allowed tests at slightly different initial temperatures and velocities to be compared; "rogue" results could then be eliminated, further tests could be done if required if there was any uncertainty in the result, and finally they would be averaged to produce a single result for comparison with other configurations. The change in surface temperature during the test was sufficiently small that the surface could be regarded as isothermal; there was therefore no need to extrapolate the heat flux trace back to $t = 0$ to obtain an isothermal value as has been done by previous workers using thin-film gauges.

8.8 COMMISSIONING TESTS.

Figure 8.10 shows the run to run repeatability of thin film measurements. This is close enough for a highly repeatable result to be obtained from a small number of tests; in practice, because the tests were not particularly time consuming once set up, the results from 4 or 5 runs were averaged at each condition. This level of repeatability was much easier to achieve with thin film gauges than with liquid crystal techniques. Averaging over $t = 0.3$ to 0.6 seconds was required to avoid scatter due to flow unsteadiness over shorter periods.

Figure 8.11 compares the measured fall in temperature during the first 0.7 seconds of the test with that calculated using the "QTT" subroutine mentioned above. (This result was obtained by sampling both the analogue input and output voltages simultaneously, a practice that is not possible during a proper test because it introduces too much noise at the analogue input).

The algorithm is based on **Oldfield et al (1978)**:

$$T(t) = \frac{1}{\sqrt{\rho c k}} \sum_n a_n \left(\frac{4}{3\sqrt{\pi}} \right) (t - t_n)^{1.5} H(t - t_n)$$

where $T(t)$ is the change in surface temperature at time t resulting from the applied heat flux $\dot{q}$, H is a step function and a_n is a derivative parameter evaluated at each data point n (time spacing τ_n) as follows:

$$a_n = \frac{(q_{n+1} - q_n)}{\tau_n +} - \frac{(q_n - q_{n-1})}{\tau_{n-}} \quad \text{and} \quad q_0 = q_1 = 0$$

It can be seen that this gives a good agreement with the measured temperature change. The small difference between the measured and predicted curves here is not due to an error in the calculation, which has been shown to give a perfect (parabolic) response for the idealised case of a simple step in heat transfer. It seems likely that the difference is instead due to an earth loop caused by connecting both the analogue input and output to the transient recorder; variations in resistance around this loop could have caused the heat flux channel to suffer offset voltages not experienced by the temperature channel.

Figure 8.12 shows heat flux signals during natural transition, with gauges at x = 40 (gauge 7), 80, 140, 180, 220 and 300 mm (gauge 33) from the leading edge. The sampling rate is 20 kHz, and the unit Reynolds number 5.15×10^6 /m. The appearance of the signals is exactly as expected, with intermittency gradually increasing from 0% (gauge 7) to 100% (gauge 33). One can see that the boundary layer reaches a "steady state" after t = 0.1 seconds, and that there is no sign of any flow separation.

8.9 CONCLUSIONS.

A Macor plate was machined and instrumented with 33 thin film gauges for measuring heat flux. These were found to give excellent signal to noise ratios and run to run repeatability. The gauges were calibrated during manufacture, and the "analogue" circuits were calibrated using an "anti-analogue" circuit.

The changes in gauge temperature before a test due to electrical power dissipation were measured, and a program was written to allow the change in temperature during a tests to be calculated from the heat flux signal. This allowed heat transfer coefficients to be accurately calculated from the measured heat flux signals.

CHAPTER 9.

FLAT PLATE TESTING - RESULTS.

9.1 INTRODUCTION.

This chapter describes the results from both the liquid crystal tests and the thin-film heat flux gauge tests. The thin-film measurements are more reliable than the liquid crystal ones, both because the surface temperature is almost uniform throughout the test and because they do not suffer from calibration drift to the same extent as liquid crystals. The correlation of the results against freestream turbulence intensity and length scale has therefore been based on the thin-film data alone. The liquid crystal results are, however, described here (before moving on to the thin-film data) to show that an alternative measurement technique does give a similar result.

Measurements of turbulence spectra in the boundary layer, heat flux spectra, correlations between these signals and changes to the boundary layer profile are also included, with explanations of the heat transfer phenomena in terms of these parameters where possible.

9.2 LIQUID CRYSTAL RESULTS.

Figure 9.1 shows Nusselt numbers derived from the liquid crystal tests using grids A, B, C and D (tripped), and compares them with the grid-out tripped and untripped cases. All the tests were done with unit Reynolds numbers of about 5.26×10^6 /m. Crystal change times were measured at 13 points along the plate; these have been plotted against Reynolds number to minimise the effect of slight changes in velocity from test to test and to allow comparison with heat transfer correlations. All results shown are for a tripped boundary layer unless otherwise stated.

The turbulent Nusselt number after natural transition is very similar to the tripped, grid-out level. This is unexpected as the (thin) laminar boundary layer over the front of the plate should, after transition, lead to a thinner turbulent boundary layer and higher heat fluxes than when the boundary layer grows as a turbulent layer over the whole plate. The apparent similarity of the levels when measured using liquid crystals may be due to the large changes in surface temperature that occur during the test - the laminar region will cool more slowly than the turbulent parts of the surface, and so the boundary layer will become hotter, and heat transfer downstream will be less, than if the plate was isothermal. A similar phenomenon will of course occur even if the whole boundary layer is turbulent, as the change times are quicker at the front of the plate. This suggests that one would need to use a small value of θ if an absolute value was required for the heat transfer coefficient. In the present study, though, absolute values were not required; the main purpose of these tests was to prove that heat transfer enhancement effects could be detected on the plate using the grids available and that the boundary layer was behaving as expected prior to machining and instrumenting the Macor (thin-film) plate.

Figure 9.2 compares the tripped, no grid Nusselt number with that predicted using a turbulent boundary layer prediction from **Schlichting (1979)**, which is given in Appendix 2. The measured level is typically 20% less than predicted. This could be due to errors in the value of $\sqrt{\rho c k}$ used, which was a standard value for perspex (569 W/mK), but the fact that the thin film tests (included in Figure 9.2 for comparison) gave a similar result makes this most unlikely. One possibility is that it is a result of the pressure gradients around the leading edge thickening the boundary layer; it may simply indicate that a "flat plate" correlation is not ideal for this configuration.

Figure 9.3 shows the effect of the various grids as a Nusselt number enhancement factor relative to a "base" tripped, low turbulence Nusselt number at the same Reynolds number. The initial very high enhancement "spike" is of no relevance, as it merely represents transition over the region in front of the trip strip which has a laminar boundary layer in the low turbulence case. Enhancement factors as high as 28% are reached towards the rear of the plate with the highest turbulence level (grid D).

The initial fall in enhancement factor behind the trip strip (over the $Re = 0.12$ to 0.6×10^6 range with grid A) is difficult to explain; comparison with the thin-film results in Figure 9.5 suggests that there is an error in the datum measurement, and that all grids should actually give a positive enhancement level.

9.3 THIN FILM MEAN HEAT TRANSFER LEVELS.

9.3.1 Results.

The thin film gauge results are similar to those from the liquid crystal tests. The repeatability of the thin film measurements was much better than the liquid crystal results, and the surface temperature change during the tests was small so the above discussion about the effects of surface temperature distribution will have very little effect on the thin-film tests. For these reasons the correlation of heat transfer effects against turbulence parameters will be based exclusively on the thin-film gauge data.

Figure 9.4 shows the Nusselt numbers from six gauges along the plate with grids A, B, C, D and E (tripped), plus the grid-out tripped and untripped cases. The data is plotted against Reynolds number at each gauge and so is comparable with the liquid crystal results in Figure 9.1. The results are broadly similar, though it may be seen that in this case there is some enhancement even with the low (3-4%) turbulence level produced by grid A. The natural transition test now gives the expected result of a higher Nusselt number after transition than the tripped case.

Comparison of the thin film results with the liquid crystal data in Figure 9.2 shows that the thin film gauges gave Nusselt numbers for a tripped boundary layer that were on average 1.2% higher than the equivalent liquid crystal results, with a standard error between the results of 4.5%.

9.3.2 Correlation of Nusselt number enhancement.

Figure 9.5 shows enhancement coefficients calculated from the thin film gauge data shown in Figure 9.4; these coefficients were generated using Nusselt numbers interpolated from the straight lines between the data points in Figure 9.4 at 15 Reynolds numbers in the range 3.2×10^5 to 1.5×10^6.

Figure 9.6 tabulates the enhancement coefficients shown in Figure 9.5 at Re = 526000, 947000 and 1513000, corresponding roughly to gauge positions of x = 100, 180 and 288 mm. (The corresponding flow parameters are given in Figure 6.15). The enhancement factors are plotted against local turbulence level in Figure 9.7, and it can be seen that these points could not be accurately correlated using the intensity alone. (If a best fit straight line were to be fitted to these points, the standard error would be about 6.8%).

In attempting to correlate the enhancement against some function of the length scale, the most obviously relevant parameter is the ratio of length scale: boundary layer thickness (see §6.8 and Appendix 1 for definitions of length scale). This is plausible on the basis that the turbulence will be attenuated near the wall, out to a distance of order one length scale from the surface; the level of turbulence that affects the boundary layer is therefore a function of the ratio of boundary layer thickness to length scale **(Hancock and Bradshaw, 1989)**.

Figure 9.8 shows the range of test conditions in terms of turbulence intensity and Λ_x/δ_{995} achieved at three positions along the plate; δ_{995} is predicted using the correlation in §9.6. The Nusselt number enhancement factors, expressed as percentages, are shown beside each point. It can be seen that there is a trend of enhancement increasing at high intensities and small length scales.

Hancock (1980) found that his skin friction measurements could be collapsed onto an empirical curve by plotting enhancement factors C_f/C_{f0} against a parameter which combines turbulence intensity and dissipation length scale:

$$X_d = \frac{Tu}{\left(\frac{L_e^u}{\delta_{995}} + 2\right)} \qquad (9.1)$$

and **Blair (1983)** found that the same correlation, adjusted in accordance with Reynolds' analogy, gave a good approximation to his heat transfer data. Figure 9.9 examines the suitability of this parameter for correlating the present data. There is a considerable amount of scatter; it appears that this parameter could correlate the 6 mm and 15 mm bar data, or the 60 mm bar data, but not both at once.

Examination of the table of integral (Λ_x) and dissipation (L_e^u) length scales for each grid (Figure 6.15) shows that the 60 mm bar grids (B and D) have $L_e^u \approx 3.5\Lambda_x$, whereas the other grids have more normal values of $L_e^u \approx$ 1 to $1.45\Lambda_x$. One may suppose from this (given that the use of Hancock's parameter based on dissipation scale has not given a particularly good fit) that the dissipation scales for grids B and D are anomalous and that the decay rate for these does not give a useful indication of the distribution of turbulence wavelengths. This is probably because the working section is too small relative to the bar diameter to allow the low wavenumber part of the spectrum to develop properly.

It will be shown below that the integral scale Λ_x is a better correlating parameter than the dissipation scale for these grids.

Blair (1983) found that dissipation length scales could be well described by

$$L_\epsilon^u \approx 1.5\,\Lambda_x$$

Although this is not valid for the present data, the factor of 1.5 has been retained to allow comparison with published correlations and measurements; the agreement of the correlations with the data is not strongly dependent on the precise value of this factor.

Figure 9.10 shows the present data plotted against a modified form of Hancock's parameter based on the *integral* length scale:

$$X_i = \frac{Tu}{\left(\frac{1.5\Lambda_x}{\delta_{995}} + 2\right)} \tag{9.2}$$

The data points now collapse satisfactorily onto a curve.

Unfortunately the functional form of Hancock's correlation was not published. Measurements from Figure 2(a) in **Hancock and Bradshaw (1983)** suggest that the power law curve

$$\frac{\Delta C_f}{C_{f0}} = A X_d^{\,n}$$

fits well for A = 1.139, n = 0.136.

If a similar power law curve is fitted to the present data as plotted in Figure 9.10 the standard error of the data points from the line would be 2.4% in terms of enhancement factor.

Figure 9.11 shows the data from Figure 9.10 plotted against a new combined parameter:

$$X_{ir} = \frac{Tu}{\left(\frac{1.5\Lambda_x}{\delta_{995}} + 2\right)\left(1 + 3e^{\frac{-Re_\theta}{400}}\right)} \tag{9.3}$$

which applies Blair's correction for low Reynolds number effects to the parameter in equation 9.2. An empirical power law curve

$$\frac{Nu}{Nu_0} = 1.185(X_{ir})^{0.222} \tag{9.4}$$

has been fitted and gives a standard error of 2.1%. This curve is, of course, not valid for $X_{ir} < 0.46$, for which $Nu/Nu_0 \approx 1$. The agreement with the data points is slightly better than in Figure 9.10, and the errors are small enough to be insignificant if used for turbine design.

Hancock's and Blair's data is compared with these results in Chapter 10.

9.4 EFFECT OF FREESTREAM TURBULENCE ON HEAT FLUX SIGNALS.

Figure 9.12 compares the signal from gauge 22 (x = 150 mm, $Re = 7.5\times10^5$) at Tu = 15% (grid D) with the low turbulence grid-out case. The signals have been non-dimensionalised by scaling to $\frac{Nu}{Re^{0.8}}$ to remove effects due to run-to-run variations in the velocity and plate temperature. This assumes that the boundary layer obeys turbulent boundary layer correlations to the extent that $Nu \propto Re^{0.8}$ if the turbulence parameters are unchanged.

The high-turbulence signal shows Nusselt number fluctuations between a "low" level which is very similar to that seen in a turbulent boundary layer with no freestream turbulence, and a "high" level which can be up to 100% higher. The transition between these levels occurs at a lower frequency than the turbulent fluctuations within them, and one may imagine that the large features are due to large freestream turbulence vortices acting on the boundary layer while the smaller fluctuations may be a result of the turbulence within the boundary layer.

9.5 BOUNDARY LAYER TRAVERSES.

Figure 9.13 compares boundary layer velocity profiles under four different freestream turbulence levels. These were measured using a hot wire (see Chapter 6); the kinks in the grid-out line are due to small changes in air temperature, and were avoided in later measurements by taking more frequent temperature readings.

The presence of freestream turbulence has changed the velocity profile by increasing the mixing in the outer part of the boundary layer (and giving a higher velocity gradient across the log-law region). The boundary layer has also increased in thickness from (approximately) 3.2 mm to 6 mm. Even grid A (Tu = 4%) produces this effect; the difference between the three grids, in terms of the velocity profile, is surprisingly small.

9.6 TURBULENCE LEVELS AND VELOCITY SPECTRA THROUGH THE BOUNDARY LAYER.

Figure 9.14 compares measurements of turbulence spectra in the boundary layer with no grid and with grid D. These are velocity measurements, taken using a hot wire in a continuous (cold plate) test, and they have been plotted against wavenumber defined using the freestream (as opposed to local) velocity.

The grid-out case shows turbulence levels that are highest close to the surface and fall to zero as one approaches the freestream. Grid D, however, produces turbulence spectra that are almost identical, whether measured in the freestream or 0.5 mm above the surface. Only at low wavenumbers (k < 80 m^{-1}) is there any noticeable variation with height; a slight increase in the (streamwise) velocity component is seen close to the surface, and is presumably associated with the attenuation of any vertical component here. The similarity of the spectra throughout the boundary layer is remarkable; it suggests that freestream turbulent eddies are penetrating right through the velocity-defect part of the boundary layer.

Figure 9.15 shows similar measurements using grid A. In this case the freestream turbulence level is less than that produced at the bottom of the boundary layer in the grid-out case; the spectrum within the boundary layer is not raised by the presence of the freestream turbulence except at low wavenumbers. This suggests that the change in the velocity distribution (Figure 9.13) and the increase in Nusselt number are a result of changes to the low wavenumber structure of the boundary layer; it may, however, only reflect that fact that the grid-out case has relatively little turbulence at low wavenumbers.

Measurements of boundary layer spectra were also taken using grid E. These (Figure 9.16) are similar to the grid D result except that the increase in PSD near the surface at low wavenumbers is not apparent.

Figure 9.17 shows autocorrelations of the velocity signal from a wire close to the surface. The integral length scales and turbulence intensities are given in Table 9.1, and have been defined using the freestream velocity. (Freestream length scales have been interpolated from Figure 6.15). Positions within the boundary layer can be seen from the measured velocity profiles in Figure 9.13; the predicted boundary layer thickness is **(Schlichting, 1979)**

$$\delta_{995} = 0.37\,x\,Re_x^{-0.2} = 3.67 \text{ mm.}$$

where x is distance from the leading edge.

Table 9.1.

Integral length scales and turbulence intensities within the boundary layer at x = 150 mm, Re = 7.89 × 10^5.

	y = 0.6 mm	y = 3 mm	Freestream
No grid	3.3 mm, 5.4%	2.0 mm, 2.5%	64 mm, 0.07%
Grid A	8.2 mm, 6.4%	14.2 mm, 5.9%	9.1 mm, 3.5%
Grid D	12.0 mm, 15%	15.9 mm, 15.4%	15.0 mm, 14.5%
Grid E	10.4 mm, 10.5%	9.5 mm, 11.3%	9.3 mm, 11.7%

It can be seen that even as little as 3.5% Tu in the freestream makes a large difference to the integral scale within the boundary layer, and that the boundary layer length scale is similar to that in the freestream when the latter is turbulent.

9.7 COMPARISON OF HEAT FLUX AND VELOCITY SIGNALS.

The measurements of mean heat transfer level used a low (≈ 16 mA) gauge current to avoid gauge heating errors and a fairly low (10 kHz) sampling rate to give sufficient test time to average the turbulent fluctuations and achieve repeatable results. Once these had been finished a number of runs were done to determine spectra and show high-speed phenomena. These used a 200 kHz sampling rate and a slightly higher gauge current (typically 23 mA) to give a better signal to noise ratio. Data was taken from five gauges (10, 12, 19, 20, and 22, at x = 80, 120, 140 145 and 150 mm), and from a hot wire positioned fractionally behind and above gauge 22.

Figures 9.18, 9.19 and 9.20 compare the velocity signal 0.5 mm above the plate with the heat flux signal from gauge 22. The grid A and D heat flux measurements show much larger fluctuations than the grid-out case (as expected from Figure 9.12) and one can see that these correspond to the larger (low wavenumber) events in the velocity signal.

Figures 9.21, 9.22 and 9.23 show cross-correlations between the velocity and heat flux signals at 0.6, 3 and 10 mm above the surface. These have been plotted against "lag distance" $U\tau$ instead of lag time, which should make the correlation shape independent of velocity for turbulence structures with a constant wavenumber spectrum.

The grid-out case gives a lower correlation coefficient than the cases with freestream turbulence, implying that in the absence of freestream turbulence an appreciable proportion of the fluctuations in heat flux must be due to very small turbulence structures of wavelength < 1 mm.

The results for grids A, D and E are similar at 0.6 mm and 3 mm above the surface, with peak correlation coefficients of approximately 0.5. At y = 10 mm grids D and E still give a weak correlation (0.16); grid A, which produces a smaller integral scale, does not give a noticeable correlation here.

9.8 HEAT FLUX SPECTRA.

Heat flux spectra from gauge 22 are shown in Figure 9.24. All three turbulence conditions produce the same spectrum at wavenumbers > 1400 m^{-1}, but at lower wavenumbers the spectrum increases with increasing freestream turbulence.

Comparison with Figure 9.25 (grid A) and 9.26 (grid D) suggests that the spectra might be broadly described in terms of three regions - the high wavenumber region mentioned above where the spectrum is independent of the velocity spectrum at y = 0.6 mm, a low wavenumber region (k < 90 m^{-1}) where the velocity and heat flux spectra have the same PSD (though grid A is anomalous on this basis) and a medium wavenumber range (approximately 200 < k < 1400 m^{-1}) where the heat flux PSD is approximately 3 dB higher than the velocity PSD.

9.9 CROSS-CORRELATION OF GAUGE SIGNALS.

Figure 9.27 shows cross-correlations between gauges 10, 12, 19 20 and gauge 22, plotted against "lag distance" defined as the freestream velocity × the time lag used when correlating. The order of correlation was chosen for ease of interpretation, such that peaks would appear at negative lag values with the leftmost peak on the graph corresponding to a correlation (of gauge 22) with the gauge closest to the leading edge. These curves are the averages of correlations from 15 tests; the data is the same as that discussed in §9.7 and §9.8.

As expected, the gauges that are close together (5 and 10 mm spacings) give appreciable correlation peaks, while the 30 mm and 70 mm spacings give rather smaller peaks. The lag distance at which peaks occur is roughly proportional to the gauge spacing.

These correlations may be used to infer a propagation velocity for heat flux events. This could be useful in showing whether, for instance, the periods of high Nusselt number seen in Figure 9.12 are the immediate (local) effect of turbulence structures moving at freestream velocity, or are due to the effect of the turbulence on the boundary layer at some point upstream producing boundary layer events that then propagate over the gauges at a lower than freestream velocity.

Figure 9.28 shows the same data as Figure 9.27 replotted against a "Distance factor" defined as the distance that freestream fluid would have moved during the correlation time lag, divided by the spacing of the two gauges, *i.e.*:

$$\text{Distance factor} \quad D_f = \frac{-\overline{U}\tau}{\Delta x}$$

The propagation velocity ratio, V_e, of the events causing the correlation peak can then be calculated:

$$V_e = -\frac{1}{\hat{D}_f}$$ where $\hat{D}_f$ is the distance factor at which the peak occurs.

It can be seen that, with no grid, the 5 mm gauge separation gives a distance factor of 1.5, which falls to 1.3 as the spacing increases. Figures 9.29 and 9.30 show grid A and grid D data correlations for comparison; the peak correlation coefficient increases as the freestream turbulence level is raised, and a correlation peak is easily seen even for a spacing of 70 mm.

The velocity ratios defined by these correlation peaks have been plotted in Figure 9.31. The low turbulence case tends to a velocity ratio of 0.78 for large gauge spacings, which must be due to structures within the boundary layer moving at less than the freestream velocity. (It is commonly believed that boundary layer events, *e.g.* turbulent spots, propagate at about $0.8 \times U_\infty$).

As the turbulence level is increased this value rises to approximately 1.0 which suggests that the peaks seen in Figure 9.12 are produced by freestream turbulence having an immediate effect on the boundary layer that is much more severe than effects due to turbulence structures developing within the boundary layer.

At small gauge spacings (5 and 10 mm) the velocity ratio is less than the asymptotic value for large spacings. This suggests that the correlation here consists partly of the correlation produced by freestream effects, and partly of a correlation of the boundary layer turbulence which will be propagating at a lower speed.

An attempt has been made to identify the wavenumber regions which lead to the "freestream velocity" and "boundary layer velocity" correlations, by digitally filtering the signals before correlation. Two filters were chosen: a low pass (Filter 1) which passed frequencies corresponding to wavelengths greater than 10 mm and a high pass (Filter 2) which corresponded to wavelengths less than 10 mm. 300 point "fir" filters **(Little and Shure, 1988)** were used to achieve a high rejection ratio and rapid roll-off. Their effect on the heat flux spectrum is shown in Figure 9.32. Filter 2 was also designed to reject frequency components above 80 kHz which were largely noise.

Figure 9.33 shows some typical cross-correlations of the filtered data. The low-pass filtered data produces a correlation similar to the unfiltered data but the high pass produces very small correlation coefficients, implying that the signals at these frequencies are almost mutually random. The 30 and 70 mm spacing correlations were too low to allow a velocity ratio to be inferred for the high-pass filter case.
(Ideally one would like a gauge length of less than the present 4 mm to study phenomena at very short wavelengths, but this would lead to practical difficulties in achieving an adequate signal to noise ratio).

Figure 9.34 shows the velocity ratio values derived from correlations after filtering with filters 1 and 2. Filter 1 gives velocities that are similar to the unfiltered case shown in Figure 9.31, which is to be expected since most of the turbulence power is within this wavenumber band. Filter 2 gave velocities that were slightly lower than the unfiltered case at a 5 mm spacing, but were actually higher at the 10 mm spacing. This is unexpected; it had been hoped that the higher frequencies would show a velocity difference more clearly. The explanation is probably that at wavelengths of the order of 10 mm the turbulent fluctuations are still associated with the freestream flow, and that a higher cut-off frequency would be required to remove the effect of these on the correlation. This is impractical with the present data as the effect of a rapid roll-off in the spectrum at high frequencies and a high pass filter is to produce a signal that resembles a single frequency and gives a repeating correlation on which any genuine peak is difficult to discern.

The fall in velocity ratio at small gauge spacing is still apparent even when using the low-pass filter which filters out all wavenumbers corresponding to structures smaller than the boundary layer thickness. This suggests that there is some (albeit short-lived) "history" effect of boundary layer events convecting downstream for distances of, perhaps, 20 mm before dissipating and that these events are longer than the boundary layer thickness.

9.10 CONCLUSIONS

Nusselt number enhancement factors of up to 42% were found at the highest turbulence intensity of 16%. The liquid crystal and the thin film gauge tests both gave similar results, with a mean difference in level of only 1.2%.

These enhancement factors could not be correlated accurately against turbulence intensity alone. A useful correlation giving a standard error of only 2.1% was achieved using a parameter derived from the turbulence intensity, length scale and boundary layer thickness. This parameter is similar to parameters derived by **Hancock (1980)** and **Blair (1983)** except that it uses the integral scale instead of the dissipation scale; the integral scale appears to be a better correlating parameter in the present case where the turbulence is likely to be anisotropic and not fully developed.

The heat flux signal showed that the enhancement was due to periods of high heat transfer that lasted for 1 to 2 ms before dropping back to the undisturbed level typical of a turbulent boundary layer under a low turbulence freestream. The "high" level was approximately 60% higher than this datum level.

Measurements of the boundary layer profile showed that freestream turbulence results in a higher velocity gradient close to the wall and an increase in overall thickness.

The streamwise velocity spectrum from grids D and E ($Tu > 9\%$) exists unchanged down to 0.5 mm above the surface. The velocity signals at this height show similar features to the heat flux signals; correlation coefficients between the two signals can be as high as 50%. In general, at low ($k < 100$ m^{-1}) wavenumbers the heat flux spectra are similar to the velocity spectra, but at higher wavenumbers ($k > 1500$ m^{-1}) the heat flux spectrum is unaffected by freestream turbulence.

It appears in this case that the enhancement is produced mainly by turbulence structures that are larger than the boundary layer thickness. The enhancement is caused by fluid being carried down into the boundary layer by large freestream turbulence vortices; this is conceptually different to the alternative explanation of a simple increase in mixing within the boundary layer.

This hypothesis was tested by determining the propagation velocity of heat flux events by cross-correlating signals from gauges spaced along the plate centreline. At high turbulence levels the propagation and freestream velocities were equal; as the turbulence intensity was lowered to 4% the velocity ratio fell to 0.8. Subsequent correlation after digitally filtering the signals to include only structures of wavelengths > 10 mm or < 10 mm in the hope of resolving freestream and boundary layer phenomena did not show any more detail.

CHAPTER 10.

DISCUSSION.

10.1 INTRODUCTION.

This chapter will first attempt to compare the present experimental results with any relevant measurements by other workers. The aim of the comparison is to either strengthen the conclusions already drawn and demonstrate their generality, or to indicate areas in which the current level of understanding is still inadequate. Some possible consequences of this work will then be discussed, and suggestions will be made regarding its application.

10.2 COMBUSTOR RESULTS.

10.2.1 Comparison with previous results.

Ames and Moffat (1991) used a simulated combustion chamber (Figure 10.1) to generate turbulence in a wind tunnel. The "combustor" was a box, of square cross-section, with two rows of holes in each of the upper and lower walls (to simulate a sector of an annular combustor) and four slots through a panel across the upstream end to simulate primary zone flows. A 2:1 contraction led into the parallel-sided working section, which was 0.254 m high. They measured $Tu \approx 16\%$, $L_e^u \approx 0.15$ m and $\Lambda_x = 0.043$ m.

The measurements presented in Chapter 4 were taken on a combustor with an geometric area contraction ratio of 2.3. It was, however, exhausting to atmosphere without any outer wall to constrain the flame to flow axially, and this led to a separation off the inner discharge nozzle. Examination of the duration of the pitot pressure traverses suggests that the effective height of the flow was only 29 mm, giving a contraction ratio of 3.5:1.

If it is assumed that u' is constant through the contraction, the measurements from combustor A can be scaled to Ames and Moffat's dimensions as follows:

$$Tu = 8.6\left(\frac{3.5}{2}\right) = 15\%$$

A more detailed analysis using the "linear theory" as described by **Uberoi** (§1.6.2) predicts that Tu = 21% after a 2:1 contraction. One may conclude from the (approximate) agreement of this prediction with the measured value of 16% that similar levels of turbulence intensity occur inside both the real "can" type and simulated annular combustors. This is analogous to the performance of a bar grid, which generates similar turbulence levels whether parallel or crossed bars are used (though the latter will generally give a higher pressure drop and more rapid approach to isotropy).

By analogy to a bar grid, one would expect the scale of the turbulence within the combustor to be proportional to the dilution hole diameter. As the flow passes through a rapid contraction the turbulence will be "stretched" axially and to a first approximation the length scale should increase in proportion to the contraction ratio. On this basis, using a mean hole diameter of 17 mm for combustor A (and 62.5 mm for Ames and Moffat's combustor) one would predict:

$$\Lambda_x = 7.6\left(\frac{62.5 \times 2}{17 \times 3.5}\right) = 16 \text{ mm}$$

This is smaller than their measured value of 43 mm. There are several possible explanations for this, which future research should aim to resolve:

- the annular combustor model is producing larger length scales than would be expected from tests on a cylindrical can-type combustor (possibly as a result of swirl or the asymmetry of the exit contraction in the latter),
- there are gross flow differences because their measurements were taken within a duct, whereas the present measurements were taken in a free jet,
- the effect of the contraction on length scale has not been properly calculated by this simple technique.

Figure 10.2 compares the shape of the measured combustor A turbulence spectrum with that measured by Ames and Moffat. The data has been plotted on non-dimensional axes as used by Ames and Moffat to allow comparison; in terms of the wavenumber spectra presented earlier, the dimensionless wavenumber is $\frac{k\Lambda_x}{2\pi}$ and the dimensionless power spectral density is $\left(\frac{2\pi}{Tu^2\Lambda_x}\right)\left(\frac{\mathrm{d}\overline{\left(\frac{u'}{U}\right)^2}}{\mathrm{d}k}\right)$, which implies that the area under each spectrum = 1.0. It seems likely that the differences in spectral distribution between the two sets of data are mainly due to combustor A having a higher contraction ratio and smaller exit height to combustor diameter ratio than the simulated combustor.

10.2.2 Limitations of data.

The present combustor data was measured, as mentioned above, in a free jet which had separated from the discharge nozzle to form a "vena contracta" and thus had effectively experienced a slightly higher contraction ratio than would be the case in an engine at this axial position. This would have made the turbulence highly anisotropic and as such the measurement of only the streamwise component may underestimate the total turbulence energy. Ames and Moffat measured all three components of the turbulence; the three-dimensional intensity was 1.2x higher than would have been predicted for an isotropic flow based on the axial intensity. This does not, however, detract from the value of the present measurements, as this level of acceleration will actually occur in a real engine as the flow passes through the nozzle guide vanes.

One obvious criticism of the present experiment is that it used a "can" type combustor instead of a fully annular one of the type now typical on almost all large civil engines. Such combustors generally have less of a contraction at exit; it would appear from a casual examination of engine drawings that an area ratio ≤2:1 is typical. The differences in length scale between the present data and that of **Ames and Moffat** show that further investigation of the effects of contraction (and of other combustor geometries) are desirable. The fact that combustion has been shown to have very little effect on the turbulence production means that cold measurements on a more representative (annular) combustor, possibly using a hot wire within an enclosed annulus, could be done relatively easily and would give valuable results.

10.2.3 Implications for the design and testing of combustors and heat transfer experiments.

If, as the present work indicates, combustor generated turbulence is not significantly affected by the combustion process and its wavenumber spectrum is insensitive to velocity then the intensity and length scale will be purely a function of the combustor geometry. Combustors A, B and C all gave very similar results, suggesting that the turbulence parameters depend mainly on gross aspects of the design (hole diameter, overall size) rather than on the intricacies of the primary zone and burner. One might suppose that the intensity and length scale would be primarily a function of three parameters: hole diameter (equivalent to bar diameter in a turbulence generating grid), contraction ratio through the nozzle guide vanes, and combustor length. By analogy with a bar grid again, the larger holes would be effectively at a smaller x/d ratio from the turbine than small holes and would therefore be responsible for the majority of the turbulence spectrum. Hole spacing may have an effect, but in practice the spacing and diameter will be related by the need for a particular total hole area, and effects due to hole diameter are likely to be of greater importance.

It is perhaps appropriate to ask whether changes in combustor design practice could lead to different turbine heat transfer levels.

There are two aspects to turbulence effects on heat transfer - transition and turbulent enhancement. As regards the former, the turbulence levels expected in present designs (see below) are likely to cause rapid transition on any area not experiencing rapid acceleration, and it seems unlikely that the turbulence intensity could be reduced sufficiently by combustor design changes to avoid this as even the 4% turbulence intensity generated by grid A caused almost immediate transition on the flat plate.

It will be shown below (§10.3.2) that typical levels of turbulent enhancement are small. The length scale is much larger than the boundary layer and, with the exception of a small region on the pressure surface where the turbulence intensity will be high, there is likely to be no enhancement above the nominal turbulent level.

There is thus little opportunity for reducing the overall aerofoil cooling burden by small changes in the combustor design. Combustors *need* turbulence to dilute the primary zone gases within a reasonably compact volume and to avoid an excessively peaky temperature traverse or hot streaks at exit. The dilution holes need to be relatively large (compared to, say, film cooling holes) so that the jet from them can reach the combustor centreline. There are two conflicting effects here - small holes produce smaller length scales which will increase X_{tr} for a given Tu, while large holes will produce higher intensities but at a larger length scale.

It can be seen that if **Roach**'s correlation (§6.6) for the effect of diameter and distance on turbulence from a bar grid applied to combustors, the combination of a (radially) enlarged combustion chamber giving a higher contraction ratio, and larger diameter holes, would lead to a smaller X_{ir} parameter and less heat transfer enhancement. If the combustor was also lengthened a further reduction would be possible. The benefits, however, would be very slight for current designs and the drawbacks, of greater diameter and weight, would be prohibitive.

It is likely that the present work will be of greater benefit in this respect in assessing the likely effects of future, highly innovative combustors. It might be desirable, as regards engine length and weight, to design a very short combustor using higher turbulence levels than at present to achieve more rapid mixing; and a reduction in cross-section area (*i.e.* contraction ratio) might be attractive to allow a smaller outer diameter or more room for shafts and bearings. The benefits of such changes would have to be quantified against the increase in turbulence that they would produce, which might then lead to significant heat transfer effects. The present work has shown that the turbulence characteristics of such designs could be measured at an early stage using a cold flow perspex model, and that such measurements could give a useful indication of whether increased heat transfer was likely to occur.

If rig tests are being done to study the cooling requirements and performance of aerofoils it is highly desirable that they should be subject to realistic turbulence levels and scales. Although the case described below only experiences an increase in heat transfer over a small region of the pressure surface, other designs might well show more severe effects. Realistic turbulence levels are also required to produce transition at the correct point.

It has been shown that at the nozzle guide vane entry plane (*i.e.* downstream of the combustor exit contraction) the spectrum from a combustion chamber closely resembles the spectrum from a bar grid and so could easily be simulated by extending a parallel annulus forwards from the nozzle guide vanes and fitting a bar grid. If, however, the annulus is made to follow a realistic path with a contraction before the NGVs the choice of grid could be difficult; the desired position as regards x/d would typically put it in front of the contraction, but it would have to generate a very high intensity there to achieve a sufficient level further downstream. It might be possible to achieve this by putting the grid part-way through the contraction and choosing a suitable bar size by trial and error, but a more certain method would be to design a simulated combustion chamber using a shell with radial holes (as Ames and Moffat).

10.2.4 Conclusions.

Measurements on a crude annular combustor model by Ames and Moffat gave (after correction for geometry changes) a similar turbulence intensity to the present results but a length scale that was nearly 3x larger than expected. It would appear that length scales are specific to a particular combustor geometry. Further investigations into the effects of contraction ratio and combustor geometry on length scale are therefore required.

All future turbine external heat transfer tests should include a means of generating a realistic turbulence intensity and scale. Depending on the upstream annulus shape, this would require either a bar grid or a simulated combustor shell.

10.3 FLAT PLATE RESULTS.

10.3.1 Comparison with previous results.

Figure 9.11 showed that a parameter X_{ir}:

$$X_{ir} = \frac{Tu}{\left(\frac{1.5\Lambda_x}{\delta_{995}} + 2\right)\left(1 + 3e^{\frac{-Re_\theta}{400}}\right)}$$

could be used to correlate the Nusselt number enhancement.

Data from **Hancock (1980)** and **Blair (1983)** has been plotted against this parameter in Figure 10.3 for comparison with the correlation devised in Chapter 9. Within the scatter, the similarity of these sets of results is gratifying, and supports the use of the correlating parameter $X_{i,r}$ based on Λ_x rather than L_e^u in the present work which includes highly anisotropic turbulence. It can be seen by comparison with Figure 9.9 that there is less overall scatter when plotted against $X_{i,r}$ than if the present data were to be plotted against the dissipation scale parameter X_d.

Ames and Moffat (1990) measured heat transfer to a plate which was built into a sidewall of their combustor simulation facility (Figure 10.1). The heat flux was measured using an electrical heating technique and they found that the increase in Stanton number (relative to a datum Stanton number at the same Re_h) could be predicted by a correlation similar to that used by Hancock but using a parameter $XB = \dfrac{Tu}{(\dfrac{L_e^u}{\delta_{h,995}} + 2)}$ where $\delta_{h,995}$ is the thermal boundary layer thickness.

Their data has been converted to $X_{i,r}$ and enhancement factor and is shown in Figure 10.4 for comparison with the present Nusselt number enhancement correlation. The conversion used correlations to predict values for δ_{995} and θ:

$$\delta_{995} = \frac{0.37x}{Re_x^{0.2}}, \qquad \theta = \frac{0.036x}{Re_x^{0.2}}$$

(Schlichting, 1979) based on a boundary layer virtual origin 19 cm in front of the heated section as assumed by Ames and Moffat. A datum low turbulence Stanton number based on distance from the start of the heated section was calculated using

$$St = 0.03\, Pr^{-0.4}\, Re_x^{-0.2}$$

(**Kays and Crawford, 1980**, as Ames and Moffat).

The points that are furthest from the correlation line are those from the front half of their plate, over which the ratio of thermal to velocity boundary layer thickness will be very different to that in the present experiment. The curve fit in Ames and Moffat (1990) against *XB* showed much less scatter than this, which suggests that the present work could be extended to cover configurations with an unheated starting length by correlating against a parameter $X_{i,r,t}$ using the predicted thermal instead of velocity boundary layer thicknesses. Adiabatic surfaces are, however, unusual in gas turbines and for most purposes the correlation given in Chapter 9 should be adequate.

Maciejewski and Moffat (1989) used a turbulent free jet to generate high (20-60%) turbulence intensities over a flat plate. They found that the best correlation for heat transfer coefficient at these turbulence levels was

$$\frac{h}{\rho\, Cp\, u'_{rms}} = 0.019$$

i.e. it was insensitive to Reynolds number, position or length scale. Figure 10.5 compares the present flat plate data with their correlation. (It should be noted that, at a typical mean velocity of 80 m/s, their correlation is not expected to hold for $u' < 16$ m/s. A dotted line is used here to show this correlation extrapolated to lower turbulence intensities).

A good agreement is not expected since the turbulence intensity in the current work is less than 20%, but the correlation can be seen to give approximately the right level for the high turbulence grids D and E. Turbulence levels in the range

20 to 60% are much higher than would usually be produced by a combustion chamber but they may occur on aerofoil pressure surfaces due to the low velocities there, and are also likely to occur within the combustor itself.

10.3.2 Prediction of effect on turbine heat transfer of typical combustor turbulence levels and spectra.

The question of whether these enhancement mechanisms are important in turbines will now be considered. A typical Mach number distribution around a high-pressure nozzle guide vane is shown in Figure 10.6. The techniques described by **Uberoi (1956)**(see §1.6.2) have been used to predict the effect of this acceleration on the turbulence intensity and length scale from the Combustor A measurements. The values presented will be approximate, as a number of assumptions have been made concerning the ratio of combustor exit velocity to NGV inlet velocity, but should be sufficient to indicate general trends.

Figure 10.7 shows the predicted streamwise intensity Tu around the aerofoil pressure and suction surfaces. The intensity is, of course, high around the stagnation point. On the suction surface Tu falls rapidly to around 2%, which may assist transition but is unlikely to lead to higher heat fluxes within the turbulent region. On the front half of the pressure surface Tu is higher (at 25% in places) than the combustor exit level, and then falls towards 3% at the trailing edge.

Figure 10.8 shows the ratio of integral length scale to boundary layer thickness. This is very high on the suction surface; it is only over a small part of the pressure surface that the ratio falls enough for some boundary layer interaction to be credible. Calculations of X_{ir} (Figure 10.9) show that X_{ir} > 0.5, which is the required condition for enhancement, occurs over about 8% of the pressure surface perimeter, with a peak X_{ir} = 0.78. Comparison of this with Figure 10.3 shows that this should lead to a peak Nusselt number enhancement of approximately 12%. Other aerofoil shapes, with lower pressure surface velocities, could experience higher turbulence levels and more enhancement here.

It is often found that aerofoil pressure surfaces are difficult to cool and run hotter than predicted. This may be partly due to the film cooling effectiveness being less than expected, but it is tempting to see whether it can be explained in any other way. Figure 10.10 compares a typical prediction from a boundary layer code with the heat transfer coefficients that would be expected using **Maciejewski and Moffat's (1989)** "non-boundary layer" correlation.

This has firstly been done using the axial velocity fluctuations as they recommend. Noting that the turbulence will be highly anisotropic, however, a similar calculation has also been done using the transverse component v'. (This was predicted assuming that the measured anisotropy of **Ames and Moffat** applied at a station where the contraction ratio was 2:1).

It can be seen that there is a small region on the pressure surface where this approach predicts an enhancement of up to about 20%. This is clearly a crude approximation based on a large number of assumptions and no experimental evidence is available to show that this correlation is actually correct here, but it does suggest that the technique could be useful in some circumstances. It is interesting to note that this enhancement is similar in terms of both position and order of magnitude to the prediction using Figure 10.9.

10.3.3 Conclusions.

Turbulence intensities over the first quarter of the pressure surface on a nozzle guide vane are likely to be 25% or more; this will then fall to about 3% at the trailing edge. Suction surface levels are typically 2 to 3%.

The ratio of integral length scale to boundary layer thickness is generally so large (7 to 140:1) that Nusselt number enhancement of the type described in Chapter 9 would only occur over a small region on the pressure surface.

Measurements of turbulence parameters around an aerofoil subjected to realistic turbulence levels and scales (*e.g.* from a simulated combustor) would enable these approximate calculations to be repeated to a more useful accuracy.

The turbulence levels over the front of the pressure surface are sufficiently high that a "non-boundary layer" correlation, as described by Maciejewski and Moffat, may give a useful indication of regions where a traditional boundary layer code would not give accurate predictions. This deserves further study.

CHAPTER 11.

PROPOSALS FOR FUTURE WORK.

11.1 COMBUSTOR RESEARCH.

11.1.1 Measurements within an enclosed annulus.

The tests described in Chapter 4 used a probe traversing through a free jet that had just separated from the lips of the combustor discharge nozzle. The traverse plane was close enough to the nozzle that the shear layers on each side would not have affected the turbulence structure. The height of the vena contracta is not accurately known, however, and this has the effect of an uncertainty in the contraction ratio between the combustion chamber and the measurement plane. It is important that this ratio be accurately known as the measured level of turbulence intensity will depend on it. A cold test with a fixed hot wire within simulated nozzle guide vane endwalls would solve this question; for future hot tests it is recommended that a sliding probe be inserted through a hole in a sidewall rather than traversing a free jet as here.

11.1.2. Turbulence measurements around aerofoils.

The prediction of changes in turbulence level and scale due to flow acceleration is not yet an exact science. Future cascade tests should use a grid or simulated combustor model to produce representative turbulence parameters. Detailed measurements of intensity and scale around the aerofoils could then improve confidence in methods to predict the effects of acceleration on turbulence.

High frequency response pitot probes would be used to measure turbulence in the transonic regions of the blade passage flow, for which they are better suited than hot wires.

11.1.3. Measurements of fluctuating temperature.

Attempts to measure temperature fluctuations in the combustor exhaust gases were inconclusive. Any future hot combustor turbulence measurements using pressure probes should also attempt to prove that temperature effects are (as suspected) negligible.

11.1.4. Effects of pressure.

All the present measurements were undertaken at atmospheric pressure. The conclusion that combustion does not significantly affect the turbulence spectrum is, therefore, only strictly true at low pressure. A high pressure test, if a suitable facility was available, would confirm this conclusion applied at actual engine operating conditions.

11.1.5 Annular combustors.

Simple models of an annular combustor sector (Ames and Moffat) produced integral length scales nearly 3x larger than would be expected from the present work. A test on a proper, burning annular combustor is required to more accurately determine the turbine entry conditions for large civil engines.

11.1.6 Instrumentation development.

The use of uncooled, miniature probes to measure combustor exhaust gases could usefully be extended to provide a rapid technique for mapping the exit flow characteristics (temperature, velocity) of combustion chambers. A compact traverse mechanism that could insert the probe through a small access hole (and then withdraw it again into a cooled chamber) would be required.

11.2 HEAT TRANSFER RESEARCH.

11.2.1 Pressure surface heat transfer.

It appears from the predicted level of turbulence around a nozzle guide vane aerofoil that turbulence intensities of 25% or more are found on the pressure surface. **Moffat and Maciejewski (1989)** have shown that on a flat plate at similar turbulence levels the heat transfer coefficient is better correlated against turbulent Stanton number than by using a boundary layer calculation. The accuracy of such predictions with what must be highly anisotropic turbulence is uncertain. A measurement of heat transfer enhancement on a concave surface under realistic turbulence (following §11.1.2 above) would be most useful.

It has been shown that for the anisotropic turbulence produced by a single large bar the integral length scale is a better correlating parameter than the dissipation scale. The velocity power spectrum from a combustor, however, also contains a significant component at low wavenumbers which may be considered as streamtubes of different velocities rather than as genuine turbulence. Typically 50% of the spectral energy will be at wavelengths greater than the discharge nozzle height, and even the "genuine" turbulence will be very anisotropic once it has accelerated into the nozzle guide vanes. One would expect that heat transfer effects are dependent mainly on the transverse velocity components, which must be attenuated at low wavenumbers. Further work is required in this area to measure the heat transfer effects of anisotropy and to decide on appropriate definitions of length scale to allow correlation for these types of flow.

11.2.2 Effects on film cooling.

It is well known that film cooling has the effect of raising heat transfer coefficients in addition to the desired effect of reducing the local gas temperature. Most film cooling experiments have used low (4% or less) turbulence intensities which are certainly not typical of the pressure surfaces on which film cooling is often required, and the effects of higher turbulence levels on both the film effectiveness and this increase in heat transfer coefficient remain to be studied.

11.2.3 Effects of very large length scale.

The present work has been limited to ratios of $\Lambda_x/\delta_{995} \leq 5.51$. This is smaller than typical turbine values and it is dangerous to extrapolate conclusions from this work up to length scale ratios of order 20 to 300. The current correlation predicts zero enhancement at 25% *Tu* for high length scale ratios on the basis of small length scale effects which in the present experiment were never sufficient to totally prevent enhancement, and there is no reason to believe that such effects can be extrapolated linearly. It is therefore essential that measurements of the effects of longer length scales should be undertaken. Intuitively, however, one must suppose that length scales longer than the turbine blade chord would have the same effect as changes in freestream velocity.

CHAPTER 12.

CONCLUSIONS.

12.1 INSTRUMENTATION.

12.1.1 Kulite probe.

The use of uncooled, sub-miniature pressure transducers has been shown to be the most practical way of measuring turbulence in hot flows. A *Kulite XCS062* transducer survived traverses through a flame at up to 1500 K, during which diaphragm temperatures as high as 130°C were experienced.

The response of a pressure probe to turbulence has been investigated both theoretically and experimentally. It was found that, at turbulence intensities of order 9%, the velocity fluctuations could be accurately described as a linear function of the pressure fluctuations provided that temperature fluctuations were assumed to be negligible.

A technique was devised for calibrating the pitot probe's response in a known turbulence field. This determined the response in terms of two parameters: firstly a sensitivity to wavenumber and, secondly, a resonance at a frequency dependent on the size of recess in front of the transducer diaphragm.

12.1.2 Hot wire anemometry.

A three term expression for the response of a hot wire **(Siddall and Davies, 1972)** was found to give a much better correlation between velocity and voltage than the conventional King's Law. A transient calibration technique was developed that allowed wires to be rapidly calibrated in situ in the tunnel. This rapid calibration technique was required because of the rate of dirt accumulation on the wires, which spoilt the frequency response and necessitated frequent wire replacement. The response was also found to be very sensitive to air temperature, which could vary over a few minutes. Wire vibration problems were cured by placing RTV rubber between the prongs.

12.1.3 Design of flat plate leading edge.

An 8:1 aspect ratio involute was chosen as the best (most resistant to transient separation) leading edge shape for the flat plate. A flow visualisation test showed that this could withstand 4.5° incidence before separating. Shear-sensitive liquid crystals were found to be much easier to understand than other visualisation techniques.

12.1.4 Heat transfer measurement techniques.

Thermochromic liquid crystals were used to demonstrate that the flat plate could be heated to a uniform temperature and to take preliminary heat transfer measurements. Repeatable results were initially very hard to achieve; enough ultra-violet light was penetrating the 30 mm thick working section walls to make the crystal change-point temperatures drift. Use of a transient recorder to monitor the start point and air temperature was found to be essential.

The use of thin-film heat flux gauges was, by comparison, relatively straightforward. The gauges were nominally 4 mm long × 0.25 mm wide with a resistance of 50Ω, and at a typical current of 20 mA gave an adequate signal to noise ratio up to approximately 40 kHz.

12.2 COMBUSTOR MEASUREMENTS.

12.2.1 Effect of velocity.

Cold flow measurements at three different velocities showed that the turbulence wavenumber spectrum from a given combustor geometry is independent of velocity. The velocity changes were achieved by varying the supply pressure; the turbulence spectrum will, of course, depend on velocity changes that are produced by the combustor geometry, *e.g.* changes in the discharge nozzle contraction ratio.

12.2.2 Effect of combustion.

Pitot probe turbulence measurements at three different air: fuel ratios showed that the presence of combustion does not significantly change the turbulence spectrum.

12.2.3 Insensitivity to burner design and fuel.

Turbulence measurements downstream of three combustors which were similar in shape and size but had different burner and primary zone configurations shows that these changes had no significant effect on the spectrum. One must therefore conclude that the turbulence spectrum is only a function of the geometry of the combustor, and it seems likely that the principal factors affecting it are the contraction ratio, dilution hole sizes and combustor length.

Experiments using diesel fuel instead of paraffin showed that the slower burning rate achieved in this way had no effect on the turbulence spectrum.

12.2.4 Assumptions about temperature fluctuation levels.

The assumption that temperature fluctuations may be ignored in the conversion of measured pressure fluctuations to turbulence is still unproven. Attempts to measure high-frequency gas temperature fluctuations using a thin film probe were inconclusive (see Appendix 3). It does, however, seem unlikely that temperature fluctuations could have a significant effect without changing the similarity of hot and cold spectra mentioned above.

12.3 FLAT PLATE MEASUREMENTS.

12.3.1 Liquid crystal results.

Preliminary liquid crystal measurements showed Nusselt number enhancement factors of up to 28% at 16% Tu.

12.3.2 Thin film gauge results.

Nusselt number enhancement factors of up to 42% were found at the highest turbulence intensity of 16%. The liquid crystal and thin film tests both gave similar results, with a mean difference in level of only 1.2%.

The heat flux signal showed that the enhancement was due to periods of high heat transfer (approximately 60% higher than the datum level) that lasted for 1 to 2 ms before dropping back to the datum turbulent boundary layer (low freestream turbulence) level.

12.3.3 Correlation of heat transfer enhancement.

The Nusselt number enhancement factor could not be correlated accurately against turbulence intensity alone. A useful correlation giving a standard error of only 2.1% was, however, achieved using a parameter derived from the turbulence intensity, length scale and boundary layer thickness. In the present case where the turbulence is likely to be anisotropic the integral scale appears to be a better correlating parameter than the dissipation scale used by **Hancock (1980)** and **Blair (1983).**

12.3.4 Effect on boundary layer profile.

Measurements of the boundary layer profile showed that freestream turbulence results in a higher velocity gradient close to the wall and an increase in overall thickness.

12.3.5 Turbulence spectra within boundary layer.

The freestream velocity spectrum of u' from grids D and E ($Tu > 9\%$) exists unchanged down to 0.5 mm above the surface. The velocity signals at this height show similar features to the heat flux signals; correlation coefficients between the two signals can be as high as 50%. This suggests that freestream vortices are penetrating the boundary layer and that this is responsible for the increases in heat flux. The turbulence structures that do this are generally larger than the boundary layer thickness.

12.3.6 Propagation speed of heat flux events.

The propagation velocity of heat flux events was measured by cross-correlating signals from gauges spaced along the plate centreline.

At high turbulence levels the propagation and freestream velocities were equal; as the turbulence intensity was lowered to 4% the velocity ratio fell to 0.8. This adds credence to the suggestion that large elements of freestream fluid entering the boundary layer (as opposed to merely increased mixing) are responsible for the increases in heat flux.

12.4 EFFECTS AT ENGINE CONDITIONS.

12.4.1 Typical turbulence levels.

Turbulence intensities over the first quarter of the pressure surface on a nozzle guide vane are likely to be 25% or more; this will then fall to about 3% at the trailing edge. Suction surface levels are typically 2 to 3%.

12.4.2 Enhancement levels on nozzle guide vanes.

The ratio of integral length scale to boundary layer thickness using the can-type combustors tested in Chapter 4 is so large (7 to 140:1) that Nusselt number enhancement of the type described in Chapter 9 would only occur over a small region on the pressure surface - and the peak enhancement factor would be 1.12.

12.4.3 Enhancement levels on turbine blades.

Wakes from the nozzle guide vanes will contain turbulence. This will be at smaller length scales than the turbulence from the combustion chamber, and might thus be expected to increase blade heat transfer coefficients during wake passing periods. Further work is required to quantify the increase.

12.5 RECOMMENDATIONS FOR DESIGN.

There is, as yet, no general correlation for turbulence levels from combustors. The best approach is probably to assume that all combustors have a similar turbulence intensity internally and scale the intensities and length scales discussed in Chapter 10 to allow for changes in contraction ratio, NGV velocity distribution and dilution hole size. Alternatively, cold flow combustor model tests can provide turbulence length scales and intensities.

These turbulence intensities and levels can then be used to see if any heat transfer enhancement is predicted, either by the correlation developed in §9.3 or using the correlation by Maciejewski and Moffat (§10.3).

12.6 RECOMMENDATIONS FOR FUTURE RESEARCH.

12.6.1 Cold flow turbulence measurements.

Further measurements are needed to determine the variation of turbulence parameters around an aerofoil. This should ideally be done with a model combustor upstream to produce realistic turbulence spectra; an annular combustor instead of the can-type used here would be more representative of large civil engines.

12.6.2 Hot flow turbulence measurements.

A high pressure annular combustor test with both a pressure transducer to measure turbulence and a probe to quantify temperature fluctuation levels would answer all the outstanding questions about the turbulence levels entering the high pressure turbine in a typical engine. The current work has developed the required turbulence measurement techniques for such a test.

12.6.3 Heat transfer effects of large length scale and anisotropy.

The present work has been limited by the tunnel dimensions to $\Lambda_x/\delta_{995} < 5.5$, and it seems unwise to extrapolate to typical nozzle guide vane pressure surface values which are much higher than this. Further testing at more typical levels is therefore desirable. This should also attempt to generate representative levels of anisotropy; at present the effects of anisotropy are unknown.

12.6.4 Effects of turbulence on film cooling.

Aerofoil pressure surfaces, which often rely upon film cooling, are subject to turbulence intensities as high as 25%. Past film cooling tests have only provided low levels of freestream turbulence; it is therefore essential that measurements at more typical turbulence levels are now undertaken.

REFERENCES.

Ames, F.E., and Moffat, R.J., 1990, Effects of Simulated Combustor Turbulence on Boundary Layer Heat Transfer. ASME HTD 138 "Heat Transfer in Turbulent Flows".

Bayley, E.J., and Milligan, R.W., 1977, The Effect of Freestream Turbulence upon Heat Transfer to Turbine Blading. AGARD CP229.

Bicen, A.F., and Jones, W.P., 1986, Velocity Characteristics of Isothermal and Combusting Flows in a Model Combustor. Combustion Science and Technology, Vol 49, pp1-15.

Bonnet, P., Jones, T.V., and McDonnell, D.G., 1989, Shear Stress Measurements in Aerodynamic Testing using Cholesteric Liquid Crystals. Liquid Crystals, Vol 6, No. 3.

Blair, M.F., 1983, Influence of Free-stream Turbulence on Turbulent Boundary Layer Heat Transfer and Mean Profile Development (Parts 1&2). Journal of Heat Transfer, Vol 105, pp33-47.

Boaden, B., 1990, Future development of the 535E4 engine. Rolls-Royce Magazine Number 44, March 1990.

Bradshaw, P., 1985, An Introduction to Turbulence and its Measurement. Pergamon Press.

Byworth, S., 1986, Design and development of high-temperature turbines. Rolls-Royce Magazine Number 29, June 1986.

Carlini, A, 1984, Development of a Calibration Method for High Speed Analogues. Third year project report, Oxford University Dept. of Engineering Science.

Castro, I.P., 1984, Effects of Free-stream Turbulence on Low Reynolds Number Boundary Layers. J. of Fluids Engineering, Vol 106 pp298-306

Charpenel, M., Le Bot, Y., Magre, P., Labbé, J., and Moreau, P., 1980, Méthodes de mesure a court réponse pour la détermination des fluctuations de vitesse et température dans les écoulements a température élévée. AGARD CP281 "Testing and Measurement Techniques in Heat Transfer and Combustion".

Clauser, F.H., 1956, Advances in Applied Mechanics, 4, 1.

Cohen, H., Rogers, G.F.C., and Saravanamuttoo, H.I.H., 1987, Gas Turbine Theory. 3rd edition. Longman Scientific and Technical.

Cottington, R.V., Hakluytt, J.P.D., and Tilston, J.R., 1987, The Development of a Diesel - Burning Combustion Chamber with a Multiple Jet Primary Zone. 87-GT-140.

Dils, R.R., 1973, Dynamic Gas temperature Measurements in a Gas Turbine Transition Duct Exit. ASME 73-GT-9.

Dils, R.R. and Follansbee, P.S., 1977, Heat Transfer Coefficients Around Cylinders in Crossflow. J. of Engineering for Power 77-GT-9.

DISA, 1976, Description of the DISA CTA System. Published by DISA Information Department (now called Dantec).

Doorly, D.J., and Oldfield, M.L.G., 1985, Simulation of Shock Wave Passing on a Turbine Rotor Blade. 85-GT-112.

Doorly, J. E., 1985, The Development of a Heat Transfer Measurement Technique for Application to Rotating Turbine Blades. D.Phil Thesis, University of Oxford.

Duncan, W.J., Thom, A.S., and Young, A.D., 1970, Mechanics of Fluids. Arnold.

Ebrahimini, I., 1967, A Method for the Measurement of the Local Distribution ofTurbulence Intensity in Jet Flames. Combustion and Flame 11, 255.

Gad-el-Hak, M., and Corrsin, S., 1974, Measurements of the Nearly Isotropic Turbulence behind a Uniform Jet Grid. J. of Fluid Mechanics, Vol 62 Part 1 pp115-147.

Goldstein, R.J., Lau, K.Y., and Leung, C.C., 1983, Velocity and Turbulence Measurements in Combusting Systems. Experiments in Fluids 1, 93-99 (1983).

Guenette, G.R., Epstein, A.H., Giles, M.B., Haimes, R., and Norton, R.J.G., 1988, Fully Scaled Transonic Turbine Rotor Heat Transfer Measurements. ASME 88-GT-171.

Hancock P.E., 1980, The Effect of Free-stream Turbulence on Turbulent Boundary Layers. Thesis, University of London.

Hancock, P.E., and Bradshaw, P., 1983, The Effect of Free-Stream Turbulence on Turbulent Boundary Layers. ASME J. Fluids Eng, Vol 105, Sept 1983.

Hancock, P.E., and Bradshaw, P., 1989, Turbulence structure of a boundary layer beneath a turbulent free stream. J. Fluid Mech, Vol 205 pp45-76.

Harris, C.M., and Crede, C.E. (Editors), 1961, Shock and vibration handbook, Volume 1. McGraw-Hill Book Company.

Heitor, M.V., and Whitelaw, J.H., 1986, Velocity, Temperature and Species Characteristics of the Flow in a Gas-Turbine Combustor. Combustion and Flame 64, pp1-32.

Hinze, J.O., 1975, Turbulence. McGraw-Hill, p.309.

Horowitz, P., and Hill, W., 1989, The Art of Electronics. Cambridge University Press, pp431-432.

Ireland, P.T., and Jones, T.V, 1985, The Measurement of Local Heat Transfer Coefficients in Blade Cooling Geometries. AGARD Conference on Heat Transfer and Cooling in Gas Turbines, CP390 Paper 28, Bergen 1985.

Ireland, P.T., and Jones, T.V., 1987, Note on the Double Crystal Method of measuring heat transfer coefficient. Oxford University Engineering Laboratory Report No. 1710/87.

Jenkins, R.C., 1987, Effect of Pitot Probe Shape on Measurement of Flow Turbulence. AIAA Vol 25 No 6 p.889

Jones, T.V., and Hippensteele, S.A., 1988, High-Resolution Heat-Transfer-Coefficient Maps applicable to Compound-Curve Surfaces using Liquid Crystals in a Transient Wind Tunnel. NASA TM 89855.

Kays, W.M., and Crawford, M.E., 1980, Convective Heat and Mass Transfer. McGraw-Hill Book Company.

Kolmogorov, A.N., 1962, J. Fluid Mech, 13, 82.

Koutmos, P., McGuirk, J.J., and Vafidis, C., 1984, Internal Flow Field Measurements in a Model Can-type Gas-turbine Combustor. Second Intl. Symp. on Appl. Laser Anem. to Fluid Mech., Lisbon.

Krishnamoorthy, V., Pai, B. R., and Sukhatme, S. P., 1988, Influence of Upstream Flow Conditions on the Heat Transfer to Nozzle Guide Vanes. J. of Turbomachinery Vol 110 pp412-416, July 1988.

Krishnamoorthy, V., and Sukhatme, S. P., 1989, The Effect of Free Stream Turbulence on Gas Turbine Blade Heat Transfer. ASME J. of Turbomachinery Vol 111 pp497-501.

Le Bot, Y., Charpenel, M., and Michard, P-J., 1978, Techniques de Measure dans les Turbines a Hautes Temperatures. AGARD CP229 pp33.1-33.11

Little, J.N., and Shure, L., 1988, Signal Processing Toolbox for use with Matlab. The MathWorks Inc, 21 Eliot St, South Natick, MA 01760.

Lomas, C.G., 1986, Fundamentals of Hot Wire Anemometry. Cambridge University Press.

Maciejewski, P.K., and Moffat, R.J, 1989, Effects of Very High Turbulence on Heat Transfer. 7th Symposium on Turbulent Shear Flows, Stanford University, August 1989.

MacMullin, R., Elrod, W., and Rivir, R., 1989, Free-Stream Turbulence From a Circular Wall Jet on a Flat Plate Heat Transfer and Boundary Layer Flow. ASME 88-GT-183.

Mauer, G.F., and Liu, H-T., 1987 A Capacitative Dynamic Pressure Probe for High Temperature Flow Measurement. Proc. ASME/JSME Thermal Engineering Joint Conference (Hawaii) pp91-96.

McComb, W.D., 1990, The Physics of Fluid Turbulence. Clarendon Press.

Meier, H.U., and Kreplin, H-P., 1980, Influence of Freestream Turbulence on Boundary Layer Development. AIAA Journal Vol 18 No 1 Art 78-800R.

Mikaye, Y., Kajishima, T., and Obana, S., 1987, Direct Numerical Simulation of Plane Couette Flow at a Transitional Reynolds Number. JSME Int. J. Vol 30 No 259 pp57-65.

Miller, S.C., and Bennet, H.W., 1986, Future Trends in Propulsion. Proc 15th ICAS Congress, London, 1986.

Mizutani, Y., Nakayama, T., and Yuminata, T., 1975 A Study on the Structure of Premixed Turbulent Flames by the Microphone Probe

Technique. Combustion and Flame 25, 5-14.

Moss, R.W., 1990, DUCKS User Guide. Private publication.

Moss, R.W., and Oldfield, M.L.G., 1990, Comparisons between turbulence spectra measured with fast response pressure transducers and hot wires. Symposium on Aerodynamic Measuring Techniques for Transonic and Supersonic Flow in Cascades and Turbomachines, Von Karman Institute, Brussels, September 1990.

Moss, R.W., and Oldfield, M.L.G., 1991, Measurements of Hot Combustor Turbulence Spectra. ASME 91-GT-351.

Navier, M., 1827, Memoire sur les lois du mouvement des fluides. Mem. de l'Acad. de Sci. 6, 389-416.

Nina, M.N.R., and Pita, G.P., 1985, Measurements of fluctuating gas temperatures using compensated fine wire thermocouples. AGARD CP390 "Heat Transfer and Cooling in Gas Turbines".

Oldfield, M.L.G., Bird, H.J., and Doe, N.G., 1982, Design of Wide-Bandwidth Analogue Circuits for Heat Transfer Instrumentation in Transient Tunnels. 16th Symposium of the International Centre for Heat and Mass Transfer, Dubrovnik, Sept. 1982, (papers edited by Metzger, D.E., and Afghan, N.H.).

Oldfield, M.L.G., Jones, T.V., and Schultz, D.L., 1978, On Line Computer for Transient Cascade Instrumentation, IEEE Vol AES-14 No. 5.

Pelfrey, J.R.R., and Liburdy, J.A., 1986, Effect of Curvature on the Turbulence of a Two Dimensional Jet. Experiments in Fluids 4, 143-149.

Prandtl, L., 1904, Proc III Intern. Math. Congr., Heidelberg.

Prandtl, L., 1925, Bericht uber Untersuchingen zur ausgebildeten Turbulenz. Z. ang. Math. Mech. 5, 136-7.

Priddy, W.J., and Bayley, F.J., 1985, Effects of Free-stream Turbulence on the Distribution of Heat Transfer around Turbine Blade Sections. International Journal of Heat and Fluid Flow, Vol 6, No.3.

Reynolds, O., 1874, On the extent and action of the heating surface for steam boilers. Proc. Manchester Lit. Phil. Soc. 14, 7-12.

Ribner, H.S. and Tucker, M., 1953, Spectrum of Turbulence in a Contracting Stream NACA TR1113.

Roach, P.E., 1987, The Generation of Nearly Isotropic Turbulence by means of Grids. J. of Heat and Fluid Flow, Vol 8, No.2.

Rolls-Royce plc., 1986, The Jet Engine.

Schafer, H.J., Koch, B., and Pfeifer, H.J., 1977, Application of LDV Techniques to High Speed Combusting Flows. ICIASF '77 Record pp31-39.

Schlichting, H., 1979, Boundary Layer Theory. Fourth Edition. McGraw-Hill.

Schultz, D.L., and Jones, T.V., 1973, Heat transfer Measurements in Short duration Hypersonic Facilities. NATO Advisory Group for Aeronautical Research and Development AGARDOGRAPH 165.

Siddal, R.G., and Davies, T.W., 1972, An improved response equation for hot wire anemometry. Int J. Heat and Mass Transfer 15, pp367-368.

Simonich, J.C., and Bradshaw, P., 1978, Effect of Free-stream Turbulence on Heat Transfer through a Turbulent Boundary Layer. J. of Heat Transfer Vol 100 pp671-677.

Sugawara, S., Sato, T., Komatsu, H., and Osaka, H., 1953, Trans. Japan Soc. Mech. Engrs 19(80), 18 25; translated into English and republished in 1988, Effect of free stream turbulence on flat plate heat transfer. Int. J. Heat Mass Transfer Vol 31 No. 1 pp5-12.

Tassa, Y., and Kamotani, Y., 1975, Experiments on Turbulence behind a Grid with Jet Injection in Downstream and Upstream Direction. The Physics of Fluids, Vol 18 No 4.

The MathWorks Inc, 1989, 386 Matlab Users Guide. The MathWorks Inc, 21 Eliot St, South Natick, MA 01760.

Thomas, N.H., and Hancock, P.E., 1977, Grid Turbulence near a Moving Wall. J. of Fluid Mechanics Vol 82 Part 3 pp481-496.

Uberoi, M.S., 1956, Effect of Wind Tunnel Contraction on Free-stream Turbulence J. of Aero. Science 23, 754.

Zerkle, R.D., and Lounsbury, R.J., 1988, Freestream Turbulence Effect on Turbine Aerofoil Heat Transfer. J. of Propulsion Vol.5 No.1 pp82-88.

APPENDIX 1.

DEFINITION OF TURBULENCE PARAMETERS.

A.1.1 DEFINITION OF POWER SPECTRAL DENSITY.

Frequency information is usually extracted from a set of N time-series data points using a *Fast Fourier Transform* ("*FFT*"). This is a rapid computational algorithm that assumes that the time series repeats itself every N points, and produces a sequence of complex coefficients such that

$$x(n+1) \;=\; \frac{1}{N}\sum_{k=0}^{N-1} X(k+1)e^{-j(\frac{2\pi kn}{N})}$$

where $x(n)$ are the time series points and $X(k)$ are the frequency series points (**The MathWorks, 1989**).

It is not usually convenient to plot the FFT values directly, both because these are complex numbers and because the interpretation of the graph would depend on the number of points used for the FFT. A *Power Spectral Density* (*PSD*) is derived from the FFT points in such a way that it *can* be meaningfully plotted and interpreted without a knowledge of the number of points. In its simplest form (as used here) this is done by scaling the values of the FFT points and plotting the magnitude squared (R^2+I^2), for a complex point R+jI). The scaling factor is usually defined such that the area under the graph between any two frequencies, if plotted on linear axes, would equal the turbulence power ratio $\dfrac{\frac{1}{2}\overline{u'^2}}{\frac{1}{2}U^2}$ over this frequency range. (The absolute power is of course strictly defined as $\frac{1}{2}\overline{u'^2}$ per unit mass flow, but it is usually more useful to consider the power ratio. For convenience the term "power" will be taken as applying to the power ratio).

The same definition of spectral density may also be used when plotting against some function of frequency (*eg.* wavenumber); the definition is then

$$PSD = \frac{\mathrm{d}\overline{\left(\frac{u'}{U}\right)^2}}{\mathrm{d}k}$$

It is usual to plot power spectral densities as a loglog plot because of the wide range of values obtained. The PSD (y) axis is plotted here with dB values, defined as

$$PSD_{dB} = 10\log_{10}\left(\frac{\mathrm{d}\overline{\left(\frac{u'}{U}\right)^2}}{\mathrm{d}k}\right)$$

A.1.2 USE OF CUMULATIVE POWER PLOT.

Turbulence power spectral densities may also usefully be plotted as a *cumulative power plot* instead of a direct log-log plot. The cumulative power is defined as

$$P_{cum}(K) = \int_{k=K}^{\infty} PSD\,\mathrm{d}k$$

This allows the turbulence power (as defined above) over any wavenumber range to be read directly off the graph as the difference between the two corresponding y-values.

A.1.3 CALCULATION OF TURBULENCE LENGTH SCALE.

It is desirable to be able to characterise turbulence spectra by a turbulence level:

$$Tu(\%) = \frac{\sqrt{\overline{u'^2}}}{U} \times 100 = 100\sqrt{\int_0^{\infty} PSD\, dk}$$

and a length scale, representing the "average" size of the eddies, which can then be compared to the boundary layer thickness when analysing heat transfer enhancement.

A number of turbulent length scales are in use:

(a) Integral length scale **(Hinze, 1975)**

This is a measure of the size of the largest structures in the flow; it is derived from the area under the central peak of the autocorrelation of the streamwise velocity fluctuation:

$$R(\tau) = \frac{\overline{u'(t).u'(t+\tau)}}{\overline{u'^2}}$$

$R(\tau)$ can also be derived from the energy spectrum as follows:-

$$R(\tau) = \frac{1}{\overline{u'^2}} \int_0^{\infty} E(\omega)\cos(\omega\tau)d\omega$$

The autocorrelation of a typical turbulence velocity signal is shown in Figure 6.12.

The integral length scale is traditionally defined as $\Lambda_x = \bar{U}\int_0^{\infty} R(\tau)\, d\tau$.

This is based on the assumption that the signal can be considered to be composed of two parts: a random part, which at long time intervals will give a roughly zero correlation (plus a unit spike at zero time lag), and a component that has a positive correlation over some finite time interval; the scale is then the area under the correlation of this signal. It assumes that measurements of velocity at a single point at two times (t and $(t+\tau)$) are equivalent to simultaneous measurements at two positions, x and $x+U\tau$. (Taylor's hypothesis). The latter could be done by recording the correlation between signals from two hot wires as the x-spacing between them is varied - but it is much simpler in practice to autocorrelate a single wire signal.

In practice one cannot integrate a finite correlation to infinite time and an arbitrary limit has to be imposed - see discussion in §6.7.1.

Another technique comes from the equation for the shape of an ideal spectrum if the turbulence is assumed to be perfectly homogeneous and isotropic (**Hinze, 1975**),

$$\frac{4\overline{u'^2}\Lambda_x}{E(f)\,U} = 1 + \left(\frac{2\pi f \Lambda_x}{U}\right)^2$$

from which $\Lambda_x = \left(\frac{E(f)\overline{U}}{4\overline{u'^2}}\right)_{f\to 0}$.

Λ_x is a useful parameter for non-dimensionalising spectra; except at very high wavenumbers, the shape of an isotropic turbulence spectrum is a function purely of the intensity and length scale.

(b) Dissipation length scale L^u_e.

The dissipation scale (also known as a micro-scale) is a measure of the size of the smallest vortices in the flow, which are responsible for the decay process. There are two methods used to calculate the dissipation length scale. The first method (**Hinze, 1975**) assumes $R(\tau)$ is parabolic near $\tau = 0$, and L^u_e is taken as the point where a fitted parabola intersects the $R(\tau) = 0$ line, *i.e.*

$$\frac{1}{\lambda_x^2} = \frac{-1}{2\overline{U}^2}\left(\frac{\partial^2 R(\tau)}{\partial \tau^2}\right)_{\tau \to 0}$$

In the present work, $R(\tau)$ is characteristically sharply peaked near $\tau = 0$ (Figure 6.12) and fitted parabolas underestimate L_e^u, with $L_e^u \approx 0.25 \times \Lambda_x$.

The second method is to obtain L_e^u from the streamwise decay of turbulence level. The dissipation length scale is then obtained using

$$L_u^e = \frac{\overline{u'^2}^{\,3/2}}{-U\left(\dfrac{\partial \overline{u'^2}}{\partial x}\right)}$$

(This can be evaluated by fitting a power law correlation to the turbulence intensity measured at several distances from the grid, and differentiating). This definition was more useful.

Although the integral and dissipation scales are proportional to the size of the largest and smallest structures in the flow, the constants of proportionality differ for the two definitions (and are in general not known). In practice integral and dissipation length scales for reasonably isotropic turbulence are of the same order of magnitude.

APPENDIX 2.

SOFTWARE.

A.2.1 "DUCKS" DATA CAPTURE AND ANALYSIS SOFTWARE.

"DUCKS" is a suite of programs for the PC that are designed to remotely control a Datalab DL1200 waveform recorder, download and file data captured on it, and perform routine data analysis.

There are two main programs - DUCKS itself and DUCKS2. The former uses a spreadsheet style of display to show the configuration (sampling rate, amplifier sensitivity etc.) of up to four transient recorders at once. Once these are armed the program waits for recording to finish and then downloads the captured data, plots it, and files it if required. A highly accurate calibration file facility that automatically corrects each channel for offset and gain errors is available. The captured data file format used is an extension of that from *Pafec's "Spiders DSP"* package, so that files captured by Spiders can be used in DUCKS and (with some restrictions) vice-versa.

DUCKS2 uses the same plotting options as DUCKS, which recognise time, frequency, power spectrum and event marker data types, but includes an analysis module instead of the data capture module. This allows a sequence of "processes" to be applied to the test data. The data may be held in memory and processed interactively, or a specified number of files may be read from disk and processed automatically. The data may then be refiled in the native DUCKS format, Matlab binary format or ascii.

There are 31 process options, including (for instance):

Add value,

Multiply by a value,

Linear interpolation using a table of measured and derived values,

Fast Fourier Transform,

Smooth,

Set points to a specified value,

Select subsets of the data.

Graphs may be printed either directly to a 24 pin dot matrix printer, or via a dump of the data to Matlab to use the Matlab printer drivers. The DUCKS suite is described in more detail in **Moss (1990)**.

A.2.2 MATLAB .m FILES.

Matlab is a numerical calculation program that is available for a number of computer types including PC's. Unlike a spreadsheet, it allows variables to be described by name and calculations to be done using a BASIC-like macro language. While this is very powerful it is not as user-friendly as DUCKS, so Matlab was used mainly for its laser printer plotting facilities and for "one-off" analysis tasks while DUCKS was used for all the routine data reduction. Matlab processing can be facilitated by executing a batch file containing a sequence of commands; these are ASCII files with a "**.m**" extension. A brief description of the more generally useful **.m** files written for this project is included here.

A.2.2.1 List of matlab .m Files.

acalc.m

Derives transducer resonant response from apparent spectra measured at two different velocities (see §3.4 and §A.2.2.2).

addcal.m

Puts results from successive runs of **wcal.m** into a matrix as part of a crossed hot wire calibration prior to use of **xhfile.m**.

arrow.m

Uses the mouse to draw an arrow on a graph. If text labels have been used it will align the end of the arrow vertically with any label that is at roughly the arrow y-coordinate. **Newplot.m** is used to reset the list of text coordinates.

box.m

Draws a box on the graph; the coordinates of two points at opposite corners must be specified, or may be chosen using **mouse(2)**.

comment.m

Reads lines of text and adds them to a string variable *com* which can then be saved in a *.mat* file with the data. *NB*. each ASCII character is saved as a 8-byte real number, so this will make the data files rather larger than expected.

comv.m

Calculates viscosity μ, conductivity k, specific heat Cp, R and γ for combustor exhaust gases, using digitised carpet plots and correlations, and then calculates (compressible) flow velocities at given temperature and pressure ratio.

corr.m

Performs auto and cross-correlation using Fast Fourier Transforms. Used for correlating flat plate gauge and hot wire signals.

duckfft.m

Applies a Hamming window to each column in a matrix (after subtracting the mean level), calculates the Fast Fourier Transform, averages the result and discards the components above the Nyquist frequency (similar to the "FFT" option in Ducks).

findel.m

Uses the mouse to define a point on a graph, and then determines the nearest (in terms of x-coordinate) point to this in the plotted data.

fit.m

Calculates a curve fit (of a specified order) to plotted data, plots the curve, and returns the correlation expression.

fmaxel.m

Finds which element of a matrix has the maximum value.

gethtr.m and **gettheta.m**

Calculates $\frac{h\sqrt{t}}{\sqrt{\rho c k}}$ from θ and vice-versa using a look-up table (from **thetdata.mat**) at low $\frac{h\sqrt{t}}{\sqrt{\rho c k}}$ and a correlation (**hitheta.m**) above this, for liquid crystal analysis.

hline.m and **vline.m**

Draws horizontal or vertical lines right across the graph. The line positions may be specified as coordinates or using **mouse(N)**.

holctime.m

Takes a time vector and a Datalab event marker signal (pulses of level 0 or 1, such as are generated by an opto-switch passing a row of holes), and returns the times corresponding to the centre of each pulse.

lam.m

Returns a laminar Nusselt number as a function of Reynolds number, using $Nu_x = 0.332 \sqrt[3]{0.7}\sqrt{Re_x}$ (from **Schlichting, 1979**).

lineform.m

Plots a line with a given formula in terms of y = f(x) to facilitate manual curve fitting.

logx.m, logy.m

These put log-spaced tick marks on a linear plot to overcome the limitation of not being able to use non-integer axis limits for a loglog plot. Axis values must then be converted to powers of 10 by editing the postscript file.

lqht.m

Solves the semi-infinite heat transfer equation for a pair of liquid crystal change times and temperatures, iterating (using **sttemp.m**) to calculate the plate start temperature at each point, and then calculating heat transfer coefficients and Nusselt numbers.

meantemp.m

Estimates a mean plate start temperature, using a series of point temperatures derived from the double crystal technique and discarding dubious values.

merge.m

Uses the MS-DOS copy command to merge a large number of small Matlab format binary data files into one large file for ease of handling and documentation.

mmean.m

Calculates the mean level of a plotted signal between two positions indicated using the mouse.

mouse.m

Returns the x and y-coordinates of the mouse as a single matrix that may be accepted by the INPUT command.

name.m

Performs a string handling operation which can be called within a loop to facilitate the use of variables and file names that are sequentially numbered.

newh.m

Recalculates heat transfer part of liquid crystal calculation using a new (manually specified) start temperature.

psd.m

Converts a Fast Fourier Transform signal (eg. from "duckfft") into a matrix of wavenumbers and power spectral density (similar to Ducks "PSD" option).

roach.m

Calculates the turbulence power spectral density from a parallel bar grid of a specified diameter and *x/d* using the correlation from **Roach**. Plots the *PSD*, using lines of successively different colour or type if initialised with line format lists **coline.m** or **dashline.m**.

spbit.m

Takes *Spiders DSP* (as opposed to *DUCKS*) Datalab event marker data and extracts the signal for each event line. The data may be input to Matlab as a Spiders ASCII file if the header is removed first.

sttemp.m

Iterates using **gethtr.m** and **gettheta.m** to find a plate start temperature that satisfies the two liquid crystal change times and change temperatures.

smo.m

A simple smoothing procedure, similar to "SMO" in Ducks.

tmv.m

Converts output from a type T thermocouple (in mV) to °C.

turatio.m

Predicts effect of passage contraction on turbulence intensities.

turb.m

Returns a turbulent Nusselt number as a function of Reynolds number, using $Nu_x = 0.0296\sqrt[3]{0.7}\,Re_x^{0.8}$ (from **Schlichting, 1979**), where x is distance from the leading edge.

wcal.m

Takes tunnel run-down hot wire voltage (name *eV*), dynamic head (name *dh*, in N/m^2), and total pressure deficit (dp_0), calculates velocity at each point, fits $E^2 = A + B\sqrt{U} + CU$, and writes a DUCKS linearisation file.

whol.m

Generates a string variable *wholist* containing the variables listed by the "who" command. (*wholist* may then be used by other **m**-files for batch processing of a large number of variable names or, in conjunction with **whof.m**, to ensure current data is not overwritten when loading new data from file).

whof.m

A function which returns the names and sizes of variables held in a binary file. This helps to identify files, and reduces the chance of overwriting existing data when loading new files. Comments in the data file can also be displayed without loading it.

xhfile.m

Writes a DUCKS crossed hot wire linearisation file using the matrix created by **addcal** and **wcal.m**.

A.2.2.2 Calculation of kulite resonant response.

The Matlab program "acalc.m" (see §3.4) is given here, both to explain the technique for deriving transducer resonant response and as an example of the Matlab programming language.

The variables are defined as follows:

$M(k,U)$ = measured wavenumber spectrum at velocity U

$c(:,1)$ = wavenumber k $\qquad$ $c(1,1) = 0$

$$c(:,2) = \frac{M(k,U_1)}{M(k,U_2)} \qquad c(1,2) = 1$$

$$R = \frac{U_1}{U_2} \qquad (U_2 >> U_1)$$

$$f = \frac{U_2\, c(:,1)}{2\pi}$$

The program **acalc.m** is:

```
[N n] = size(c);
a(1) = 1;
for i = 2: N
  PR = ((c(i,1)/R) - c(i-1,1)) / (c(i,1) - c(i-1,1));
  if PR > 0,
    a(i) = c(i,2) x a(i-1) x (1-PR) / (1 - (c(i,2) x PR));
  else
    a(i) = c(i,2) x table1([c(1:i-1,1) a(1:i-1,1)],(c(i,1)/R));
  end
end
plot(f, sqrt(a))
% a is a power factor, take sqrt for amplitude.
xlabel('Frequency Hz'); ylabel('Amplitude of resonance')
```

A.2.3 GRAPH PRINTING.

Most of the figures in this thesis were plotted in Matlab and saved as *Postscript* files. A Postscript editing program "POSTED.EXE" was written to automatically change the font sizes, line widths and box size so that these files could be imported into WordPerfect v5.1 without suffering from tiny text sizes. The numbers and labels are repositioned to allow for the change in font size, and additional line types (long-dash, dot-dot-dot-dash) are provided. All arrows and labelling (except for the figure captions themselves) were applied in Matlab.

APPENDIX 3.

COMBUSTOR MEASUREMENTS USING A THIN-FILM HEAT FLUX PROBE.

A.3.1 INTRODUCTION.

A thin film gauge, painted around the hemispherical end of a 2.5 mm diameter pyrex rod, was used in an attempt to examine the level of gas temperature fluctuation in the combustor exit flow. This is of interest because the derivation of the turbulence spectrum from the pressure transducer measurements is based on the assumption that temperature fluctuations are negligible. The entry of the cold gauge into the flame provided the transient temperature change that is required for thin-film gauge measurements.

These measurements have been included as an appendix because only a very limited amount of data could be captured in the time available. The results are inconclusive, and further work in this area is necessary to reach a proper understanding of them.

A.3.2 GAUGE TEMPERATURE RISE.

The gauge temperature change during a wind-tunnel test would normally be determined by calculation from the heat transfer signal from the analogue. At the time of the combustor tests a *PC* version of the code for this calculation had not been developed and so the heat flux signal (analogue output) and temperature signal (analogue input) were recorded independently. (These had to be taken on two separate traverses to avoid interference at the analogue input). The agreement with the calculated temperature rise was subsequently found to be excellent.

The measured temperature signal during a traverse is shown in Figure A.3.1. It had initially been intended that traverses in opposite directions would allow the effects of temperature and velocity fluctuations to be discriminated by examining the change in rms signal level as the driving temperature changed due to the gauge temperature rise. The level of gauge heating however was insufficient for this to be done reliably.

A.3.3. HEAT FLUX SIGNAL.

Figure A.3.2 shows a typical heat flux signal. No correction has been made for the fact that the gauge is on a 1.23 mm radius hemisphere rather than on a semi-infinite surface, which will lead to errors in the low frequency components, but conclusions may still be drawn from the high frequency part of the signal. The heat flux has been calculated by scaling the analogue output voltage using the same factor as for a gauge on a flat, semi-infinite substrate, and taking $\sqrt{\rho c k}$ to be the instantaneous value at the surface temperature. The properties of pyrex were taken from **Schultz and Jones (1973)**, and applied using an empirical line fit:

$$\frac{\sqrt{\rho c k_T}}{\sqrt{\rho c k_{300}}} = 0.02298(T-73)^{0.6997}, \qquad \sqrt{\rho c k_{300}} = 1530 \text{ W/m}^2\text{K}$$

The time for which the semi-infinite approximation may be expected to give a reasonable prediction can be estimated from the equation describing the heat flux q_x at a distance x below the surface:

$$\frac{\dot{q}_x}{\dot{q}_s} = \operatorname{erfc}\left(\frac{x}{2\sqrt{\alpha t}}\right)$$

(from **Schultz and Jones**).

Taking $\alpha = 7.9 \times 10^{-7}$ m²/s gives (for instance) $\frac{\dot{q}_x}{\dot{q}_s} \approx \mathbf{0.5}$ at $x = 0.25$ mm below the surface after $t = 85$ ms. Three-dimensional conduction effects can therefore be expected to lead to errors in the DC heat flux level over the time of a typical traverse.

Figure A.3.3 compares the measured heat flux (as above but smoothed) with a prediction for laminar flow over a spherical stagnation point (**Kays and Crawford, 1980**). The effect of gas property variations over the large freestream to surface temperature ratio has been estimated using

$$\frac{Nu}{Nu_0} = \left(\frac{T_s}{T_{gas}}\right)^{0.07}$$

where Nu_0 is calculated using freestream values of viscosity and conductivity (**Kays and Crawford, 1980**). The temperature difference on which the predicted heat flux is based is also shown. The measured values agree well with the prediction up to about 35 ms after the start of the heat flux, after which the measured value falls to approximately half the predicted value.

It seems likely that the high heat flux levels at the edges of the flame are due to the high unsteadiness here. The mean heat flux has been calculated from the time-mean pressure and temperature profiles; a prediction based on the instantaneous temperatures and heat transfer coefficients, if this were possible, would be expected to give a higher mean heat flux if it is assumed that the high velocity components consist of high temperature gas from the flame.

The low level of measured heat flux in the centre of the flame is difficult to explain. It does not appear likely that it is due to the spherical substrate being treated as a flat semi-infinite surface, as this would lead to measured values that were higher than expected. It is not due to a fault in the HTA1 analogue, as tests with two different units gave similar results (and subsequent calibration of one of these has shown it to work perfectly).

It is also unlikely to be due to the angle of incidence (≈11.5°), as the heat transfer coefficient around the stagnation point should be practically constant to larger angles than this (**Kays and Crawford, 1980**). One possibility is that thermal expansion of the pyrex substrate affected the gauge resistance, but this seems unlikely as the measured heat flux falls to the expected level as the probe leaves the flame.

It is possible that the flame generated electrical noise as a plasma, and the analogue responded to this rather than to a change in gauge resistance. These suggestions cannot be proven without a considerable amount of further testing, so the results from this probe will have to be treated as being unexplained at present.

If the apparent discrepancy is due to a genuine flow feature one would expect that a calculation of the heat transfer coefficient would give the same values for both downwards and upwards traverses. Figure A.3.4 compares the heat transfer coefficients calculated from the measured heat fluxes; there is an appreciable difference between them, which suggests that the phenomenon is at least partly due to the gauge rather than the flow.

If the discrepancy is assumed to be due to some change in the thin film gauge, it will probably affect the low-frequency (< 30 Hz) components of the heat flux output, but should not have a significant effect on higher frequency components. Figure 4.19 shows that the majority of the turbulence is at wavenumbers > 50 m^{-1}, which at 153 m/s corresponds to frequencies of > 1200 Hz. It will be assumed that the heat flux spectrum over this range is accurate.

A.3.4. HEAT FLUX SPECTRA.

Figure A.3.5 compares the heat flux spectrum from the thin film gauge with the turbulence spectrum from the kulite probe. Heat flux spectra were measured at 12 radial positions through the flame, traversing both downwards and upwards; the spectra were all similar, and have been averaged to produce the spectrum here. The spectra have been non-dimensionalised by dividing by the measured mean heat flux; if the predicted value had been used the level of the spectrum would be lower.

The heat flux spectrum will be a function of the velocity spectrum, temperature fluctuations and transient incidence changes; without a detailed calibration of the probe, and further testing to determine the source of the discrepancy between measured and expected DC levels, it will not be possible to accurately infer the temperature spectrum from these measurements. A rough estimate will, however, be attempted based on rms levels from the 24 spectra mentioned above.

A.3.5 ESTIMATES OF TEMPERATURE FLUCTUATION LEVELS.

The measured turbulence spectrum contains both "turbulence" components, at high wavenumbers, and "quasi-steady" low wavenumber components. Any component with k < 130 m^{-1} must be severely attenuated in the transverse direction as previously described. The ratio of the heat flux and turbulence levels will be arbitrarily defined for the calculations that follow as being derived from the spectra at k > 200 m^{-1} (*i.e.* vortices of wavelength about 2/3 of the discharge nozzle height) up to $k \approx$ 1200 m^{-1}, which is the limit for believing the Kulite spectrum at high velocities due to uncertainties in the correction for resonance.

The rms levels of the spectra over this range, measured at 12 positions from both upwards and downwards traverses, are shown in Figure A.3.6. The fact that these *absolute* spectra do not have a central "dip" as is seen in the mean data adds some weight to the proposal that the mean data may be exhibiting some kind of drift rather than illustrating a genuine flow feature; but as this is still uncertain, the data has been normalised by the *measured* mean level, instead of adopting the predicted value, for the calculation that follows.

If it is assumed that the flow over the gauge is laminar and that gas properties are effectively constant, the heat flux to the gauge may be described as follows:

$$q = h\Delta T = Nu\left(\frac{k}{d}\right)\Delta T = 0.93\sqrt{Re_R}Pr^{0.4}\left(\frac{k}{d}\right)(T_{gas} - T_{tfg})$$

(from **Kays and Crawford, 1980**). Putting $T_D = \overline{T_{gas}} - T_{tfg}$ and abbreviating non-fluctuating terms to a constant K gives

$$q = \bar{q} + q' = K\sqrt{(\bar{U} + u')}(T_D + T_g')$$

$$\bar{q} = K\sqrt{\bar{U}}\,T_D \quad \text{if } T_g' \text{ and } u' \text{ are uncorrelated.}$$

Putting $\sqrt{\bar{U} + u'} \approx \sqrt{\bar{U}}\left(1 + \frac{1}{2}\left(\frac{u'}{\bar{U}}\right)\right)$ gives

$$q' = q - \bar{q} = KT_D\sqrt{\bar{U}}\left(\left(1 + \frac{1}{2}\frac{u'}{\bar{U}}\right)\left(1 + \frac{T_g'}{T_D}\right) - 1\right)$$

$$\left(\frac{q'}{\bar{q}}\right) = \frac{1}{2}\left(\frac{u'}{\bar{U}}\right)\left(1 + \frac{T_g'}{T_D}\right) + \frac{T_g'}{T_D}$$

If third-order and higher terms are ignored, the mean-squared levels can be expressed as $\overline{\left(\frac{q'}{\bar{q}}\right)^2} = \overline{\left(\frac{T_g'}{T_D}\right)^2} + \frac{1}{4}\overline{\left(\frac{u'}{\bar{U}}\right)^2} + \frac{\overline{u'T_g'}}{\bar{U}\,T_D}$.

Fluctuations in viscosity and conductivity will only lead to small errors (of order 6%)

in this analysis. Assuming again that u' and T_g' are uncorrelated, the temperature fluctuations may be calculated as

$$\overline{\left(\frac{T_g'}{T_D}\right)^2} = \overline{\left(\frac{q'}{\bar{q}}\right)^2} - \frac{1}{4}\overline{\left(\frac{u'}{\bar{U}}\right)^2} \qquad \text{(A.3.1)}$$

Figure A.3.7 shows the rms temperature fluctuation levels that this analysis produces, with the gas temperature superimposed to show the position in the flame. The temperature fluctuations have been normalised with respect to gas temperature to allow comparison of the upwards and downwards traverses, using

$$\left(\frac{T'_{gas}}{T_{gas}}\right)_{rms} = \left(\frac{T'_{gas}}{T_D}\right)_{rms}\left(\frac{T_D}{T_{gas}}\right)$$

The rms levels are high compared to the turbulence intensity, which is 4% over this wavenumber range.

This suggests that temperature fluctuations (implying density changes) should have a significant effect on the Kulite probe measurements. The similarity of the hot and cold turbulence spectra, however, is very difficult to explain if this is true. It seems more likely that there is some other reason for the observed heat flux signal, particularly as the DC level is at present inexplicable and the scatter in Figure A.3.7 is considerable.

If the heat flux spectrum *is* largely due to temperature fluctuations (the T' terms in Equation A.3.1 are much larger than the u' ones) one would expect to find that

$$\left(\frac{q'}{\bar{q}}\right)_{rms} \propto \frac{1}{T_D}$$

for each pair of upwards and downwards traverse points, as $\bar{\dot{q}} \approx \bar{h}\, T_D$, $\dot{q}' \approx \bar{h}\, T'_{gas}$ and T'_{up} and T'_{down} should be identical.

Figure A.3.8 tests this by plotting q'/q against $1/T_D$, with lines to show which points are upwards/downwards pairs. The fact that the lines do not on the whole point towards the origin (as does the fitted straight line included for reference) indicates that some of the assumptions used in the calculation technique above must be invalid, or that the gauge is responding to other variables as well as heat flux. (It can be seen that the rms levels would actually be better correlated against T_D instead of $1/T_D$). Calibration in a turbulent, constant temperature flow, and in a high temperature, low turbulence flow might enable a more accurate analysis at some future date.

A.3.6 CONCLUSIONS.

Attempts to infer levels of gas temperature fluctuation using a thin-film heat flux gauge were inconclusive; they suggested that temperature fluctuations are significant, but unexplained aspects of the measurements cast doubt on their credibility. Further experimental investigations would be very useful in this area.

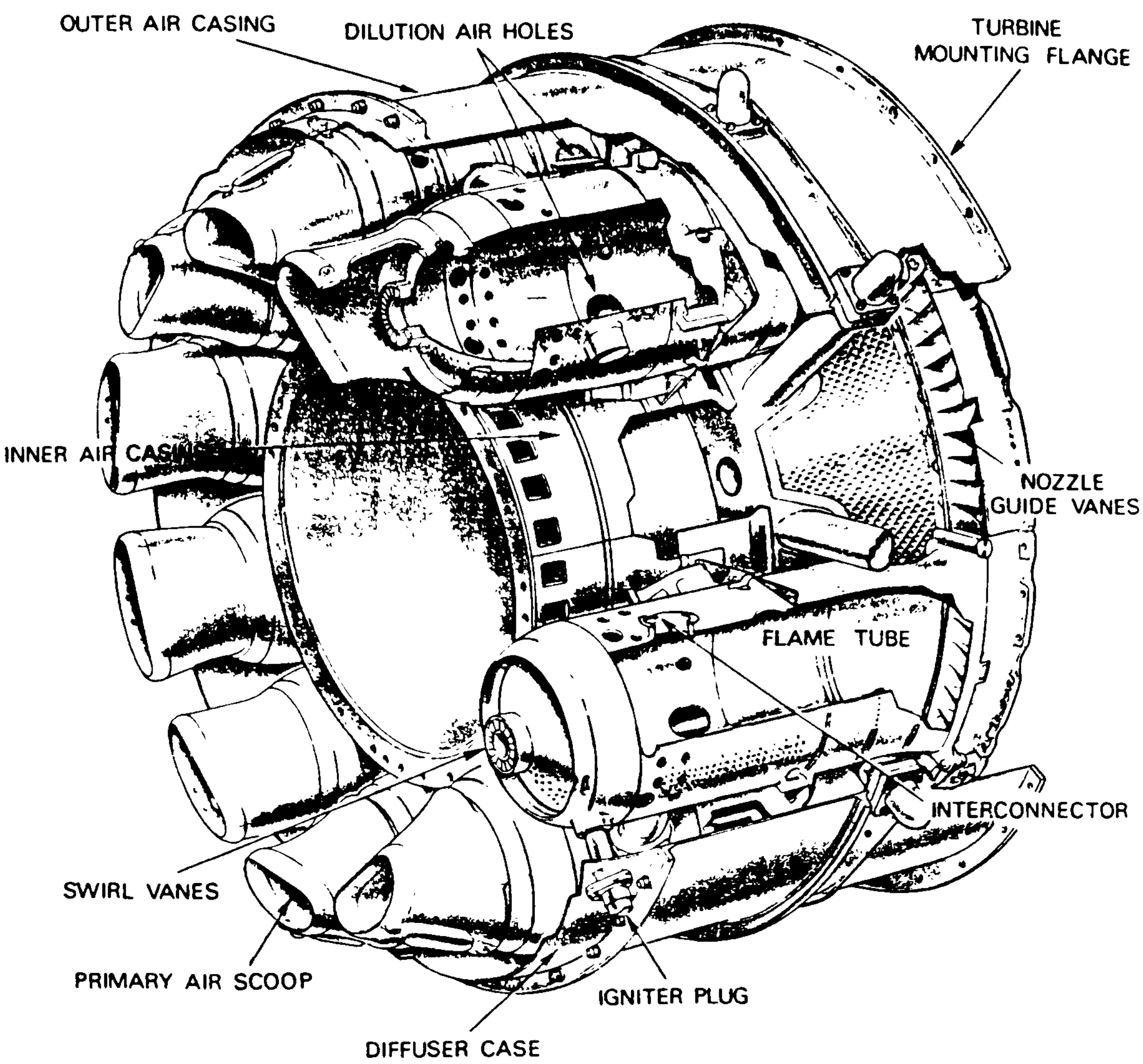

Figure 1.1.
Typical arrangement of can-type combustion chambers in an engine.

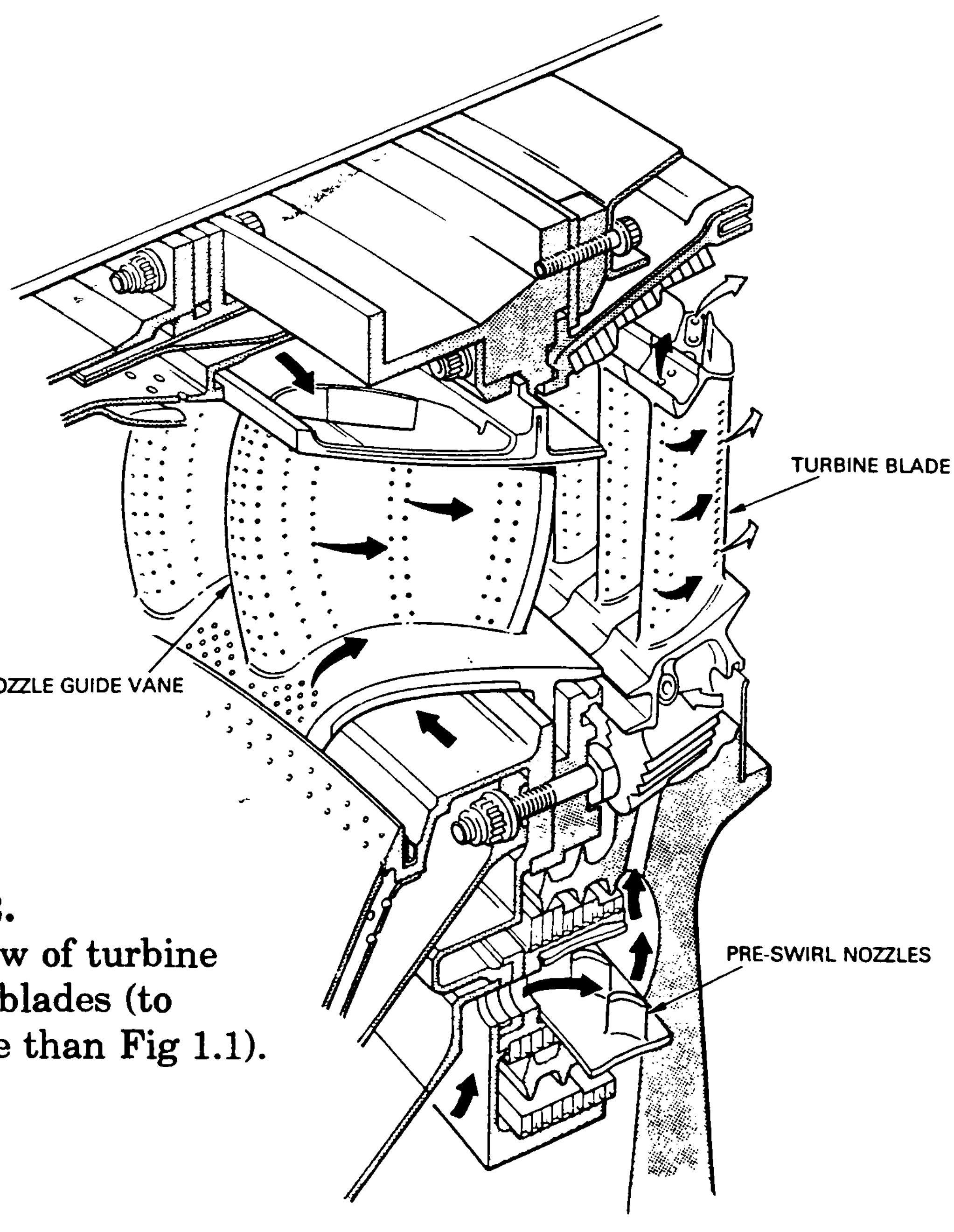

Figure 1.2.
Typical view of turbine vanes and blades (to larger scale than Fig 1.1).

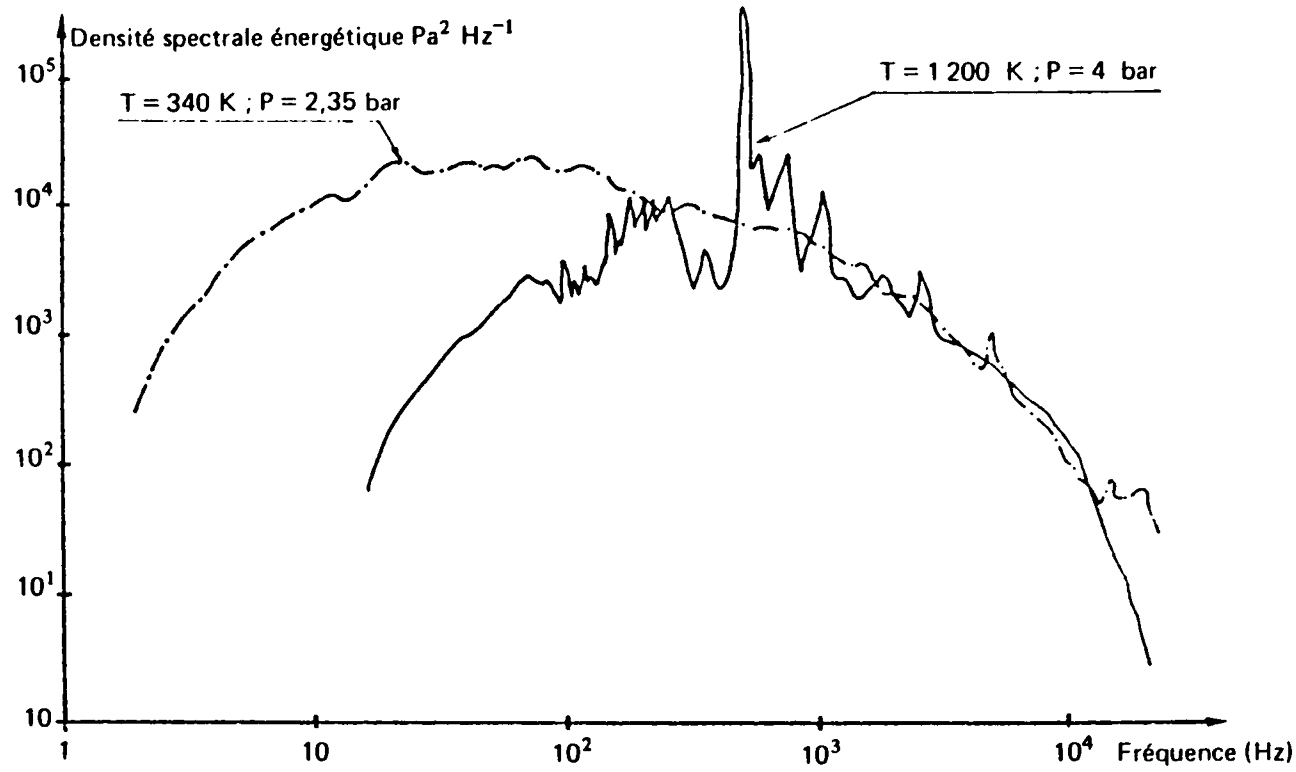

Fig. 3 — Spectres de fluctuations de pression d'arrêt dans un banc thermique.

Figure 1.3. Combustor turbulence power spectral density measured by **Le Bot et al (1978)** using a pressure probe.

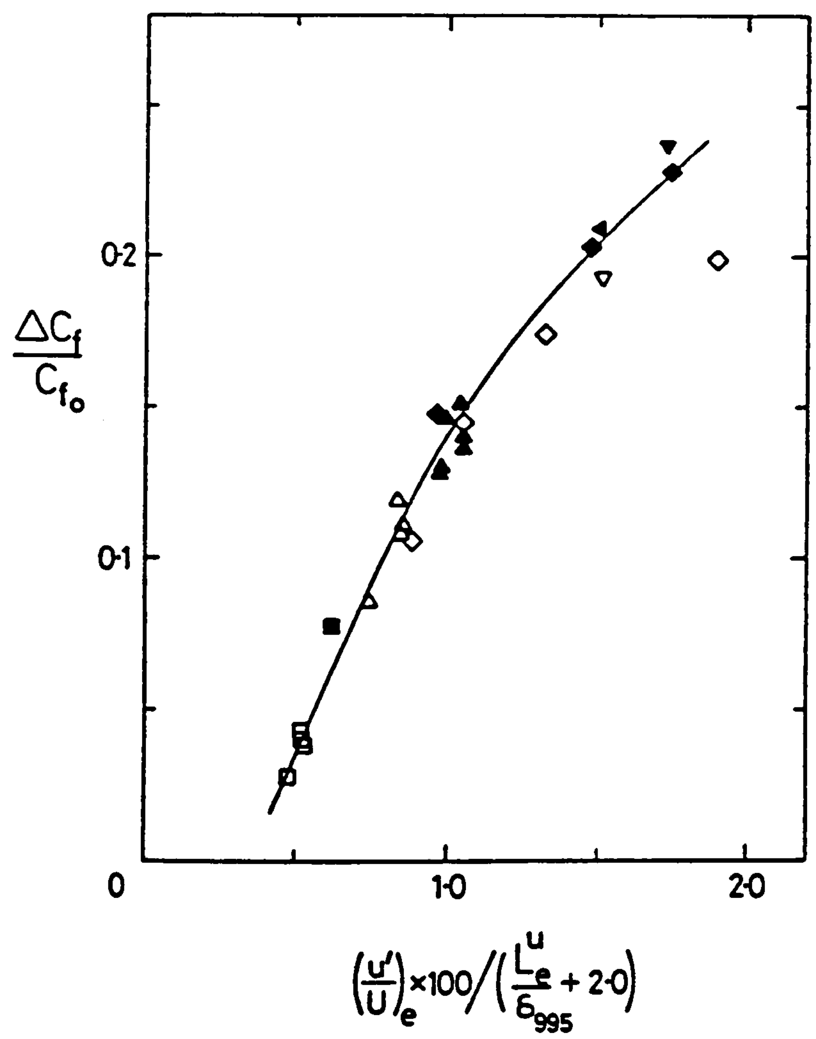

Figure 1.4. Correlation of skin friction enhancement due to freestream turbulence, from **Hancock (1980)**.

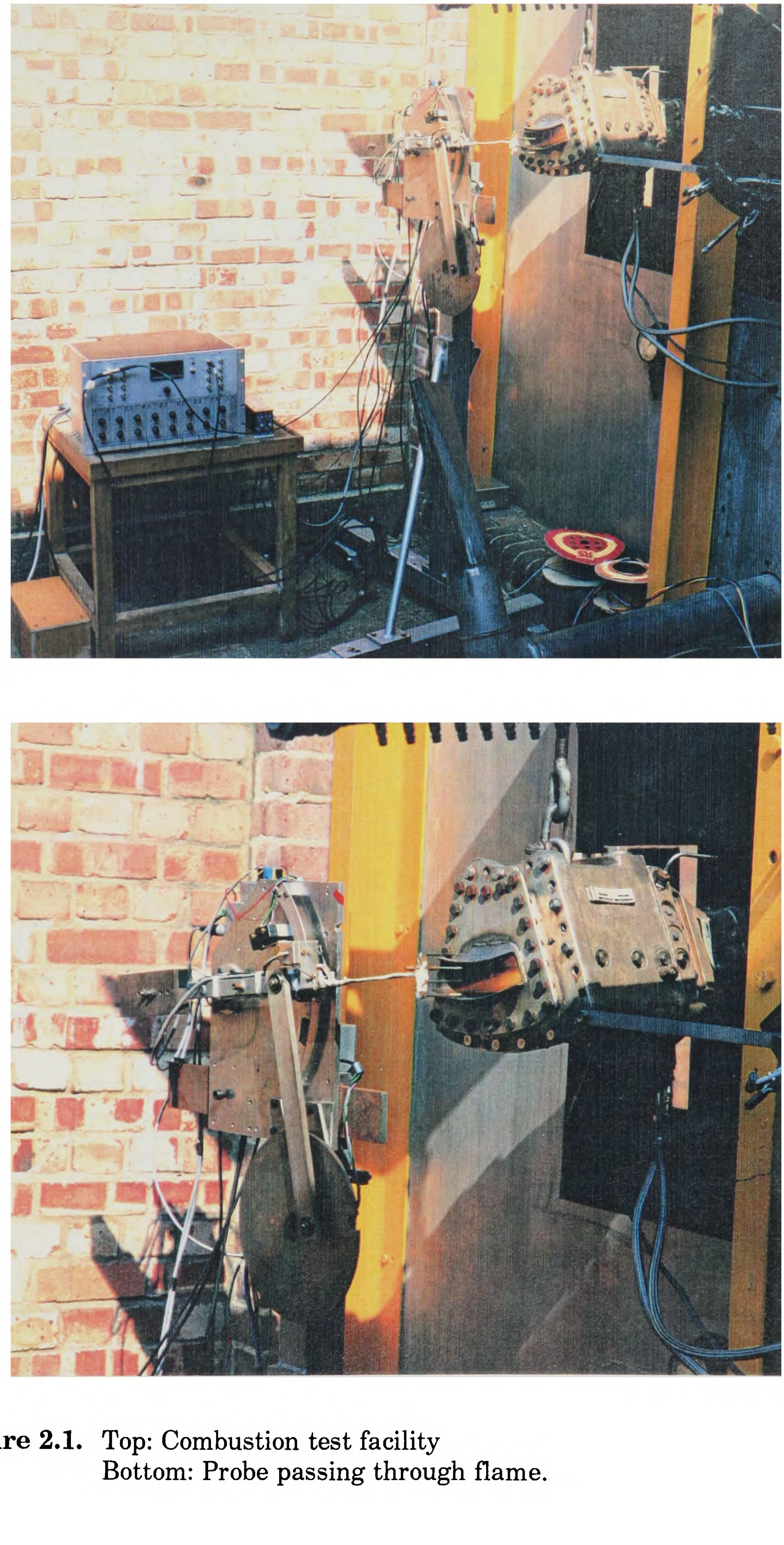

Figure 2.1. Top: Combustion test facility
Bottom: Probe passing through flame.

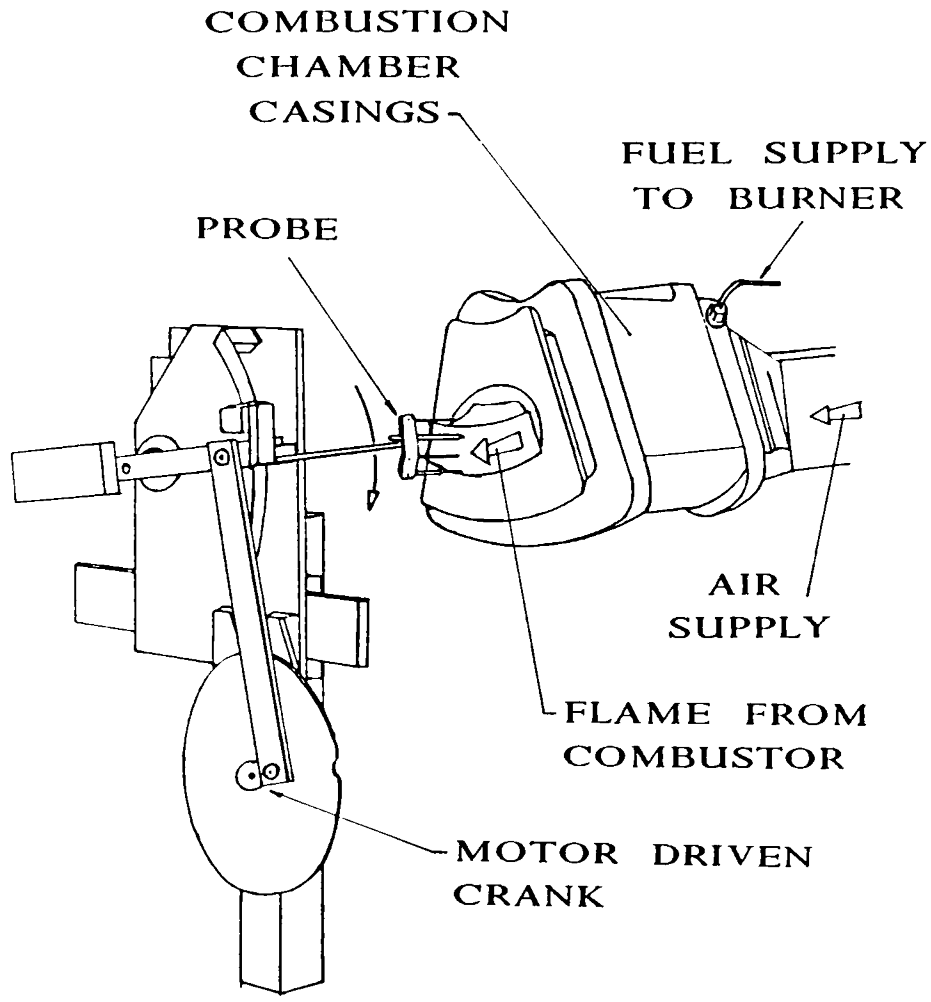

Figure 2.2. Probe traverse mechanism for combustor testing.

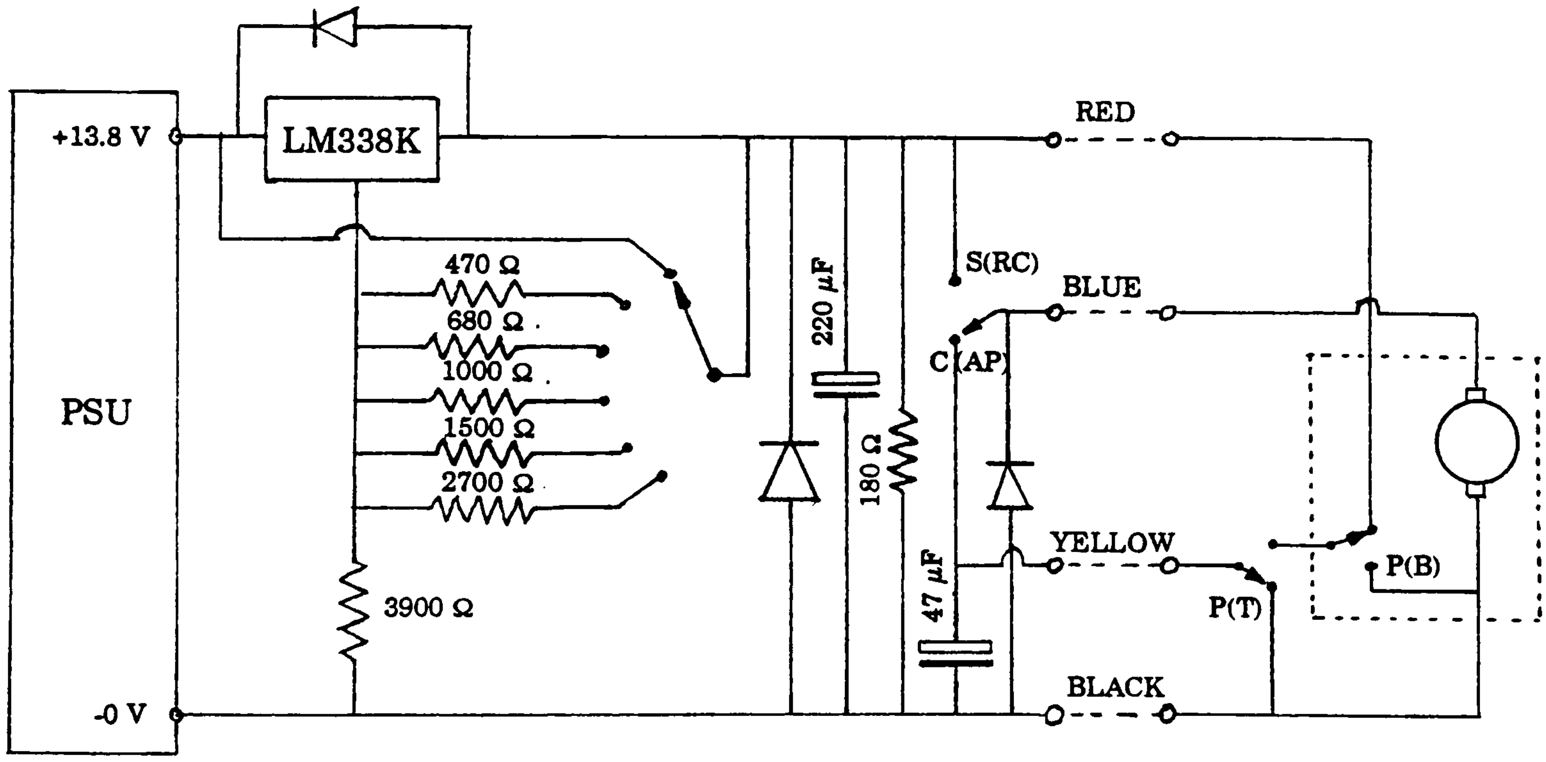

Figure 2.3. Traverse mechanism motor power supply. Switches: S(RC): start (run continuously); C(AP): continue (auto-park); P(T), P(B): parked, top & bottom.

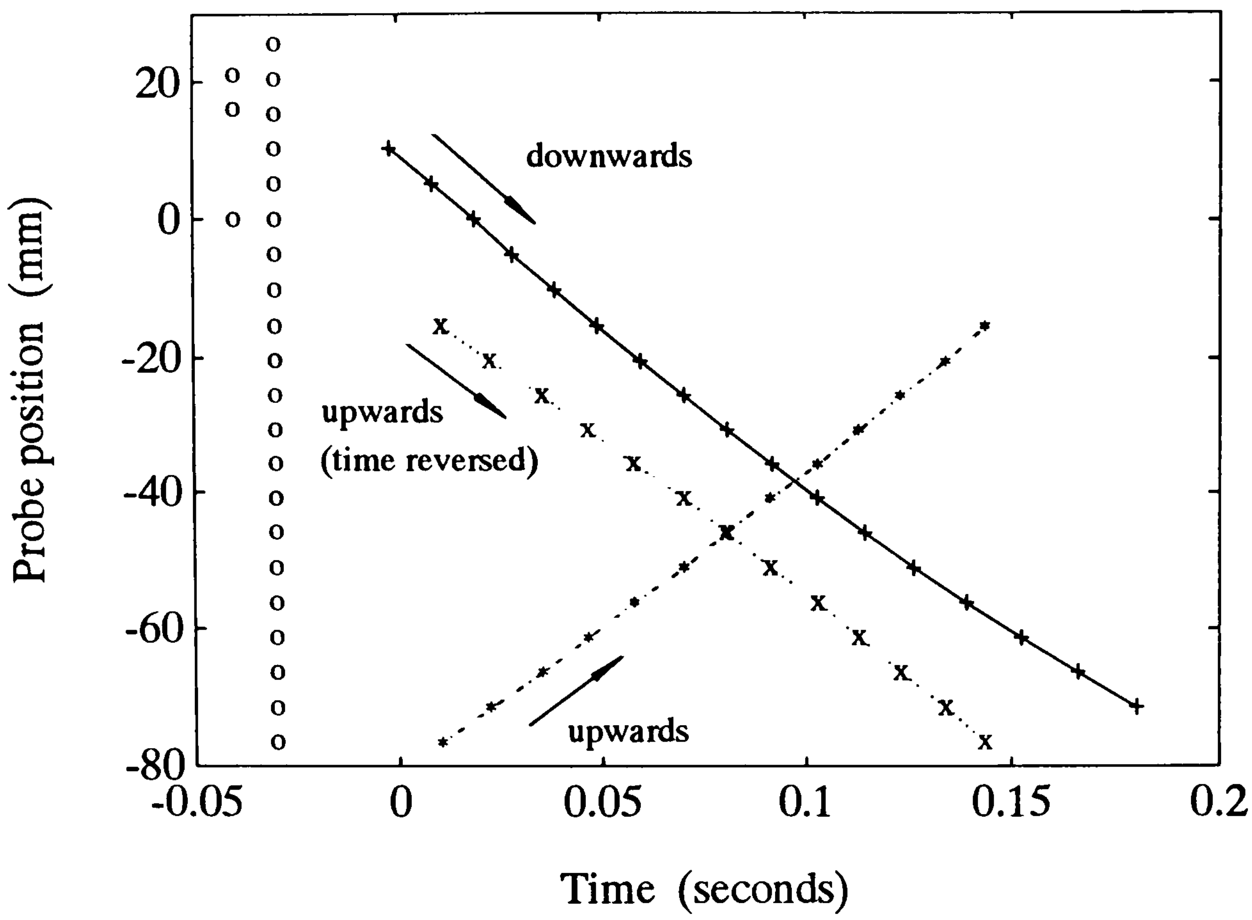

Figure 2.4. Motion of probe while driven in upwards and downwards directions by traverse mechanism. "Time reversed" line shows that velocities in each direction are very similar.

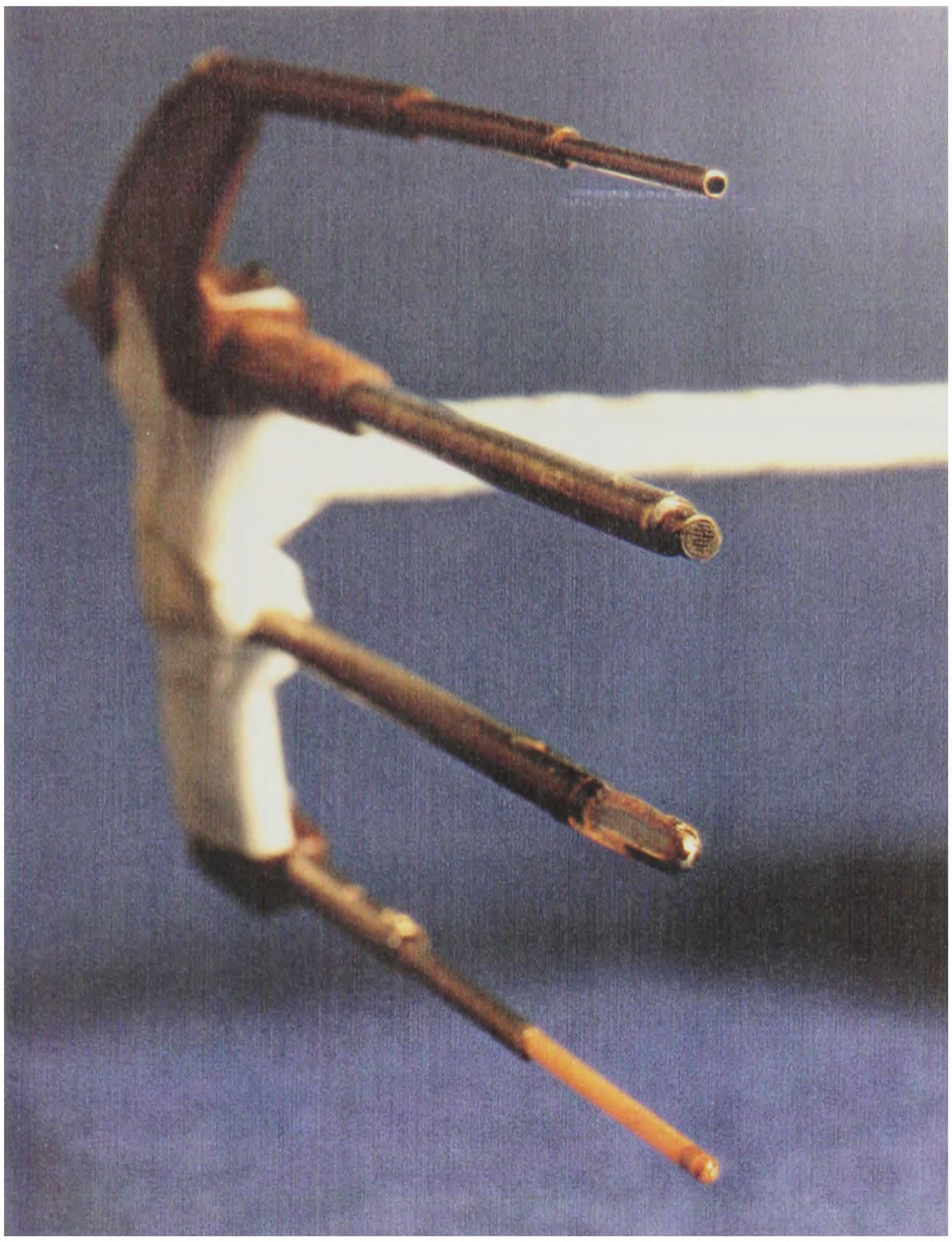

Figure 2.5.
Photograph of probe.

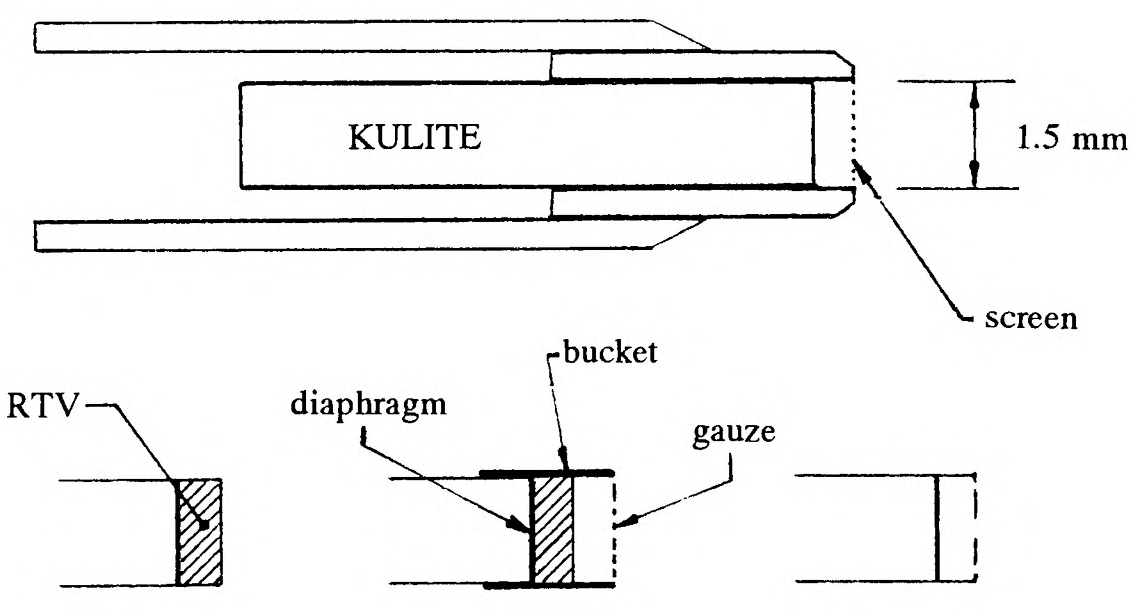

KULITE 1
*XCW*062-15 transducer. 0.5 mm of RTV rubber over diaphragm

KULITE 2
*XCW*062-15 transducer. 0.5 mm of RTV rubber plus screen of bronze gauze (0.1 mm wires at 0.25 mm pitch, 22 holes open).

KULITE 3
Standard *XCS*062-15 transducer with "B" screen.

Figure 2.6. Cross section of tip of Kulite probe showing support details, protective gauze and silicone rubber.

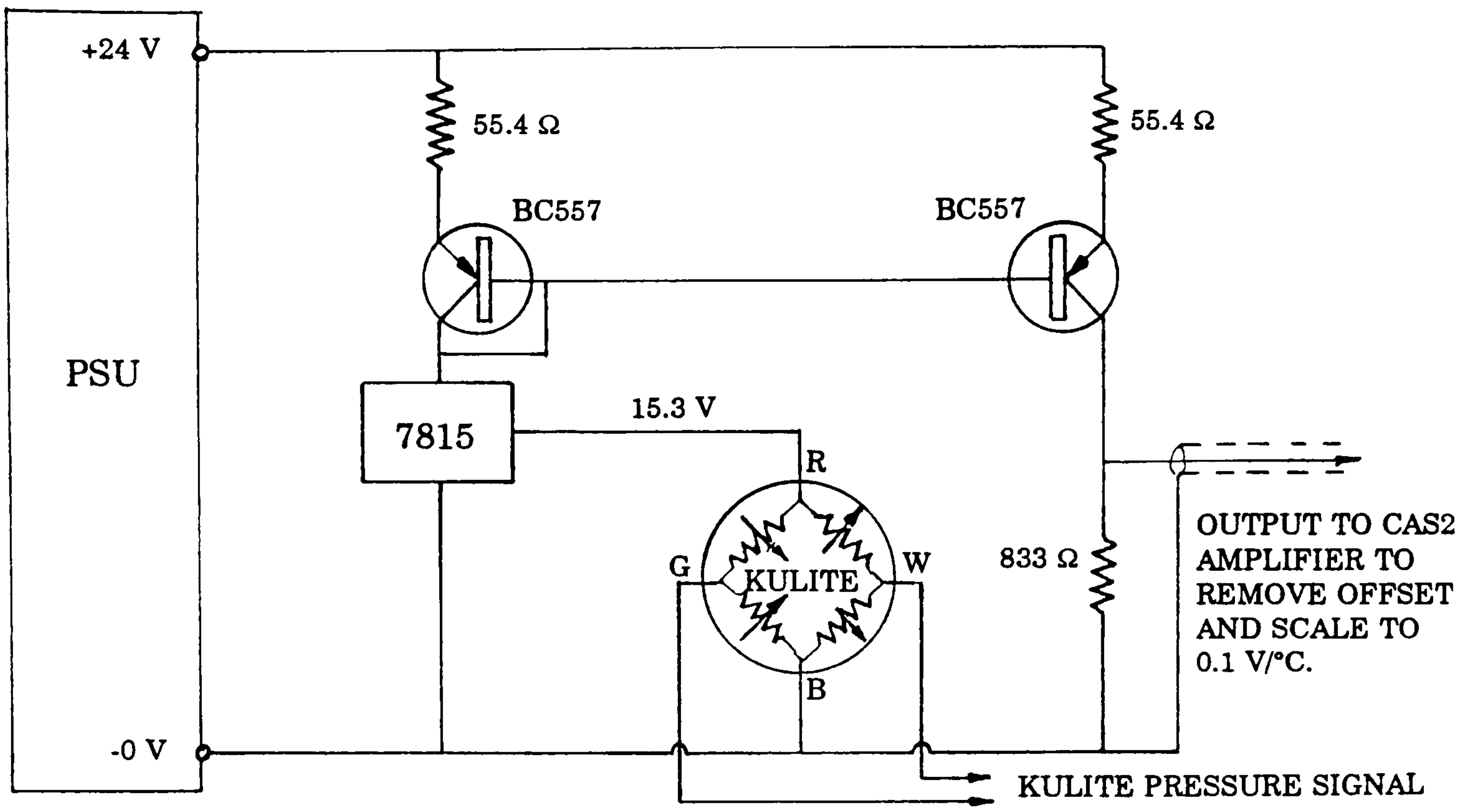

Figure 2.7. Current mirror circuit for sensing Kulite diaphragm temperature.

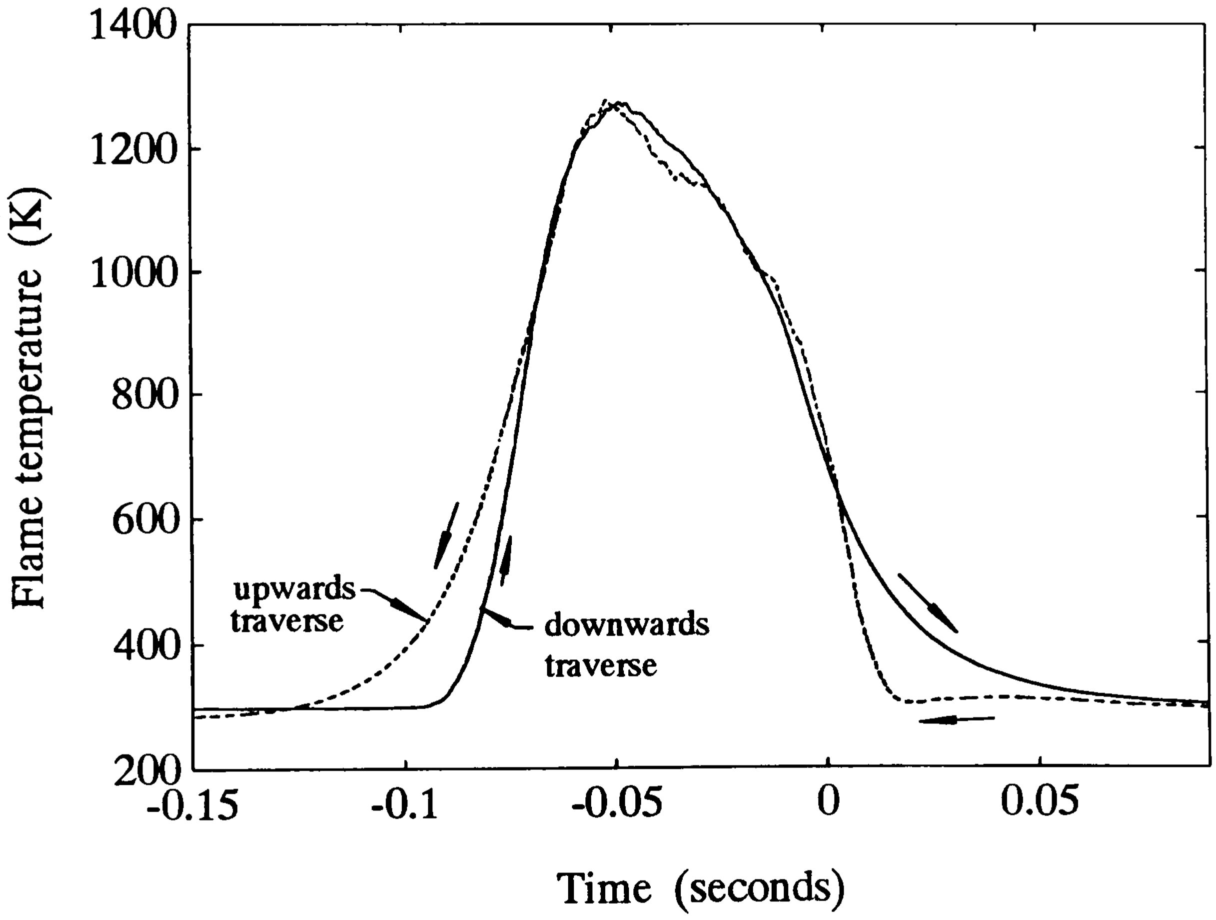

Figure 2.8. Thermocouple response demonstrated by traversing in opposite directions. "Down" is the normal traverse direction, corresponding to radially outwards in an engine. (Combustor B, 65:1 AFR, paraffin).

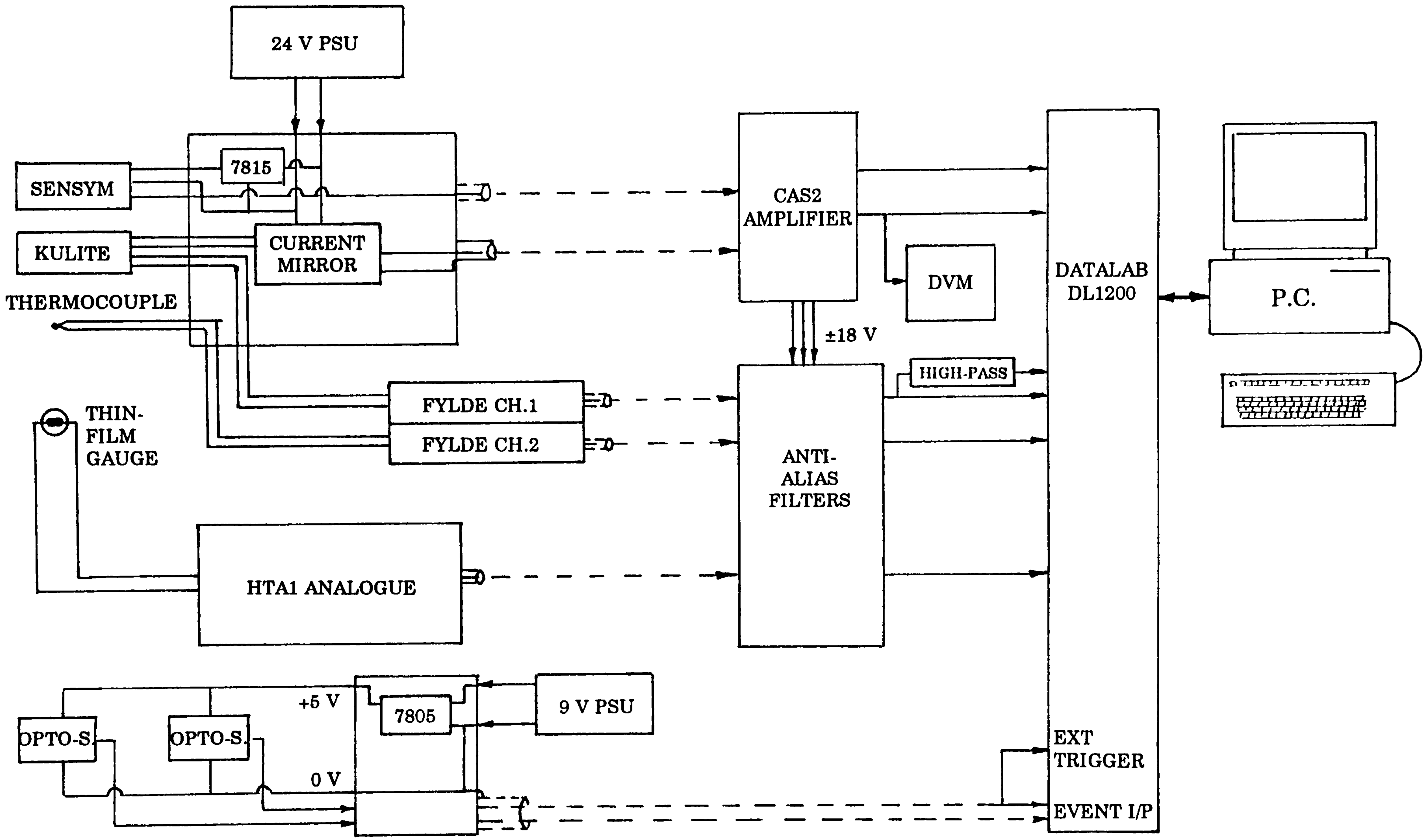

Figure 2.9. Instrumentation diagram for combustor tests.

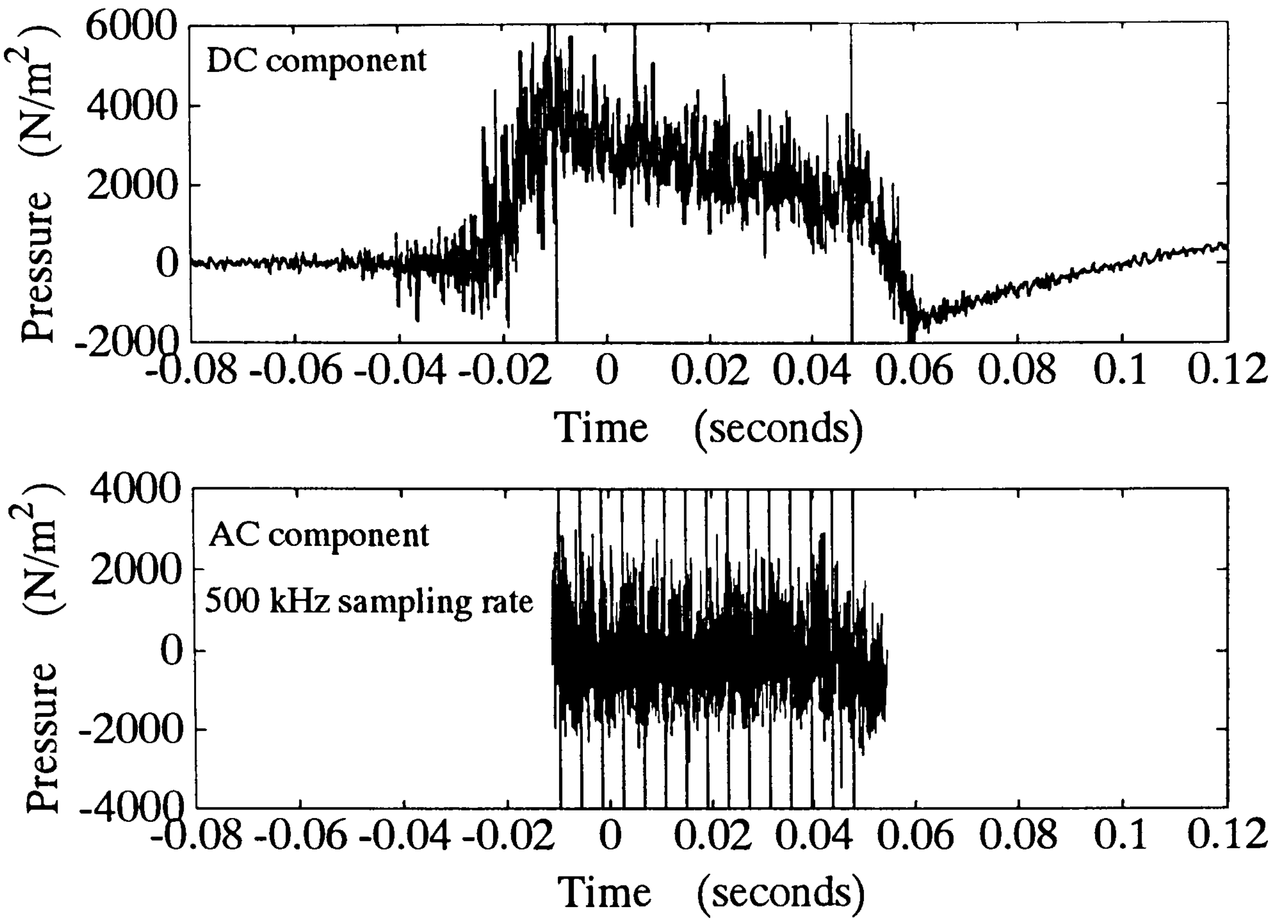

Figure 2.10. Kulite signal analysis technique.

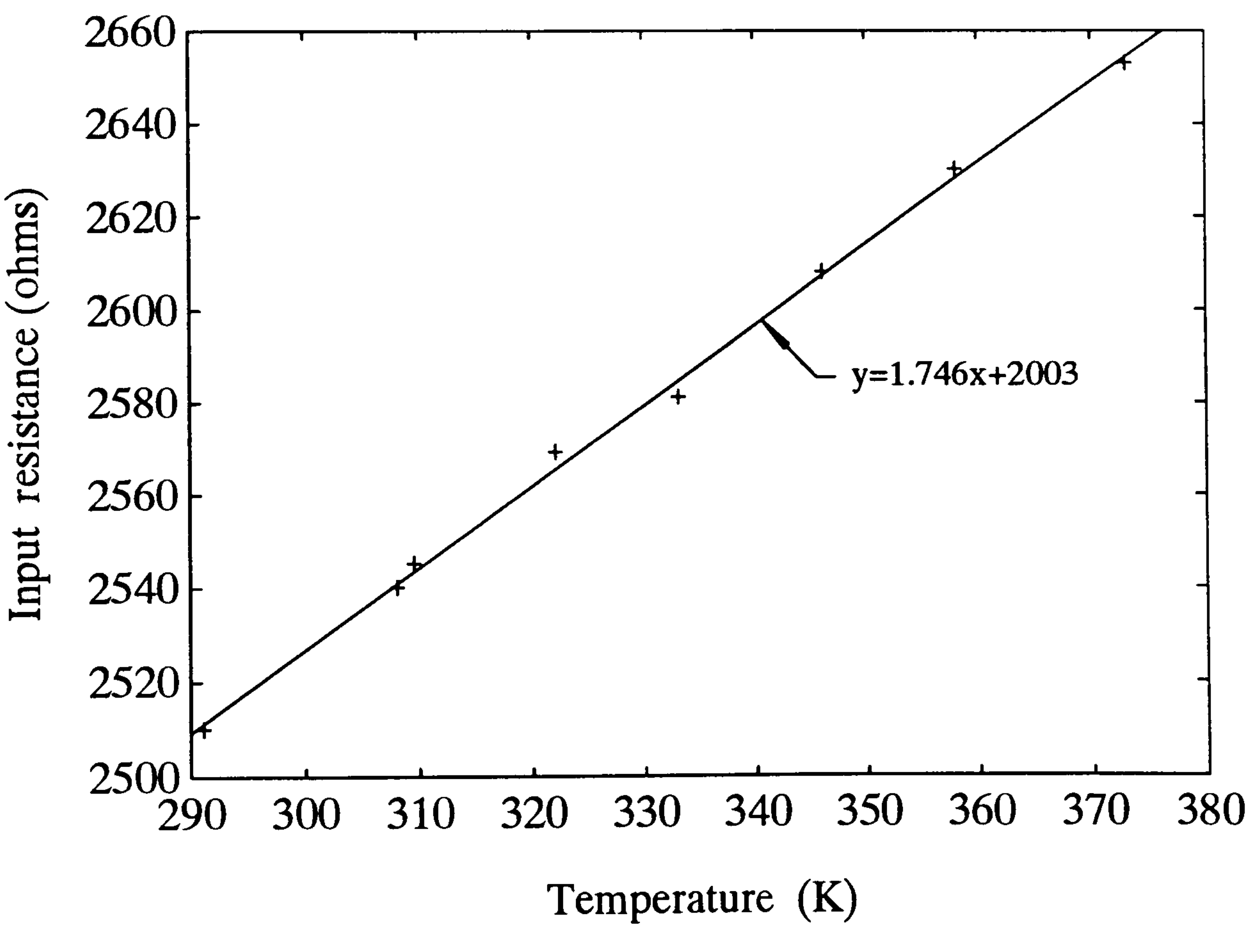

Figure 2.11. Kulite supply resistance vs temperature. (Kulite number 2, as used for combustor tests).

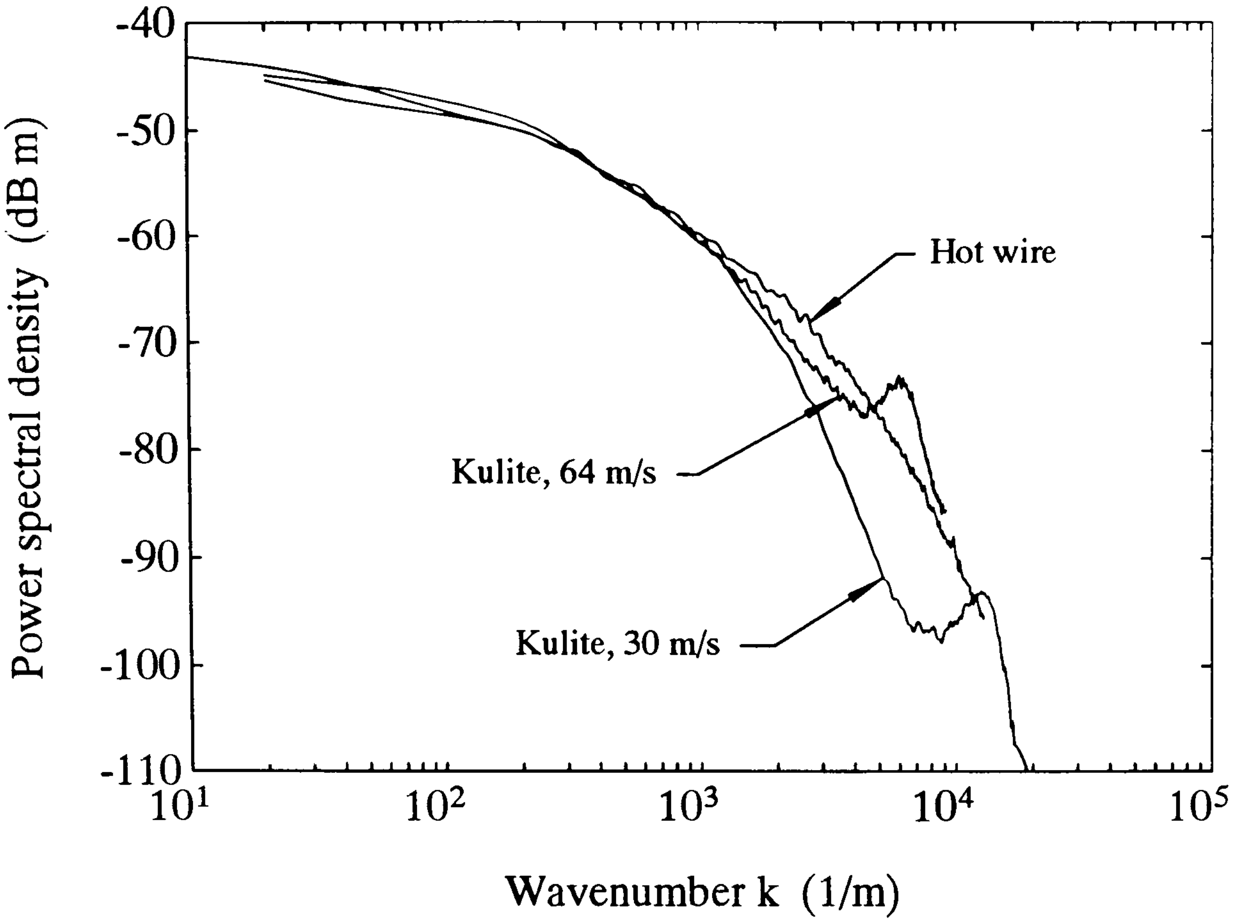

Figure 3.1. Comparison of grid turbulence spectrum (as measured by a hot wire) and apparent spectrum from Kulite 2 at two different velocities.

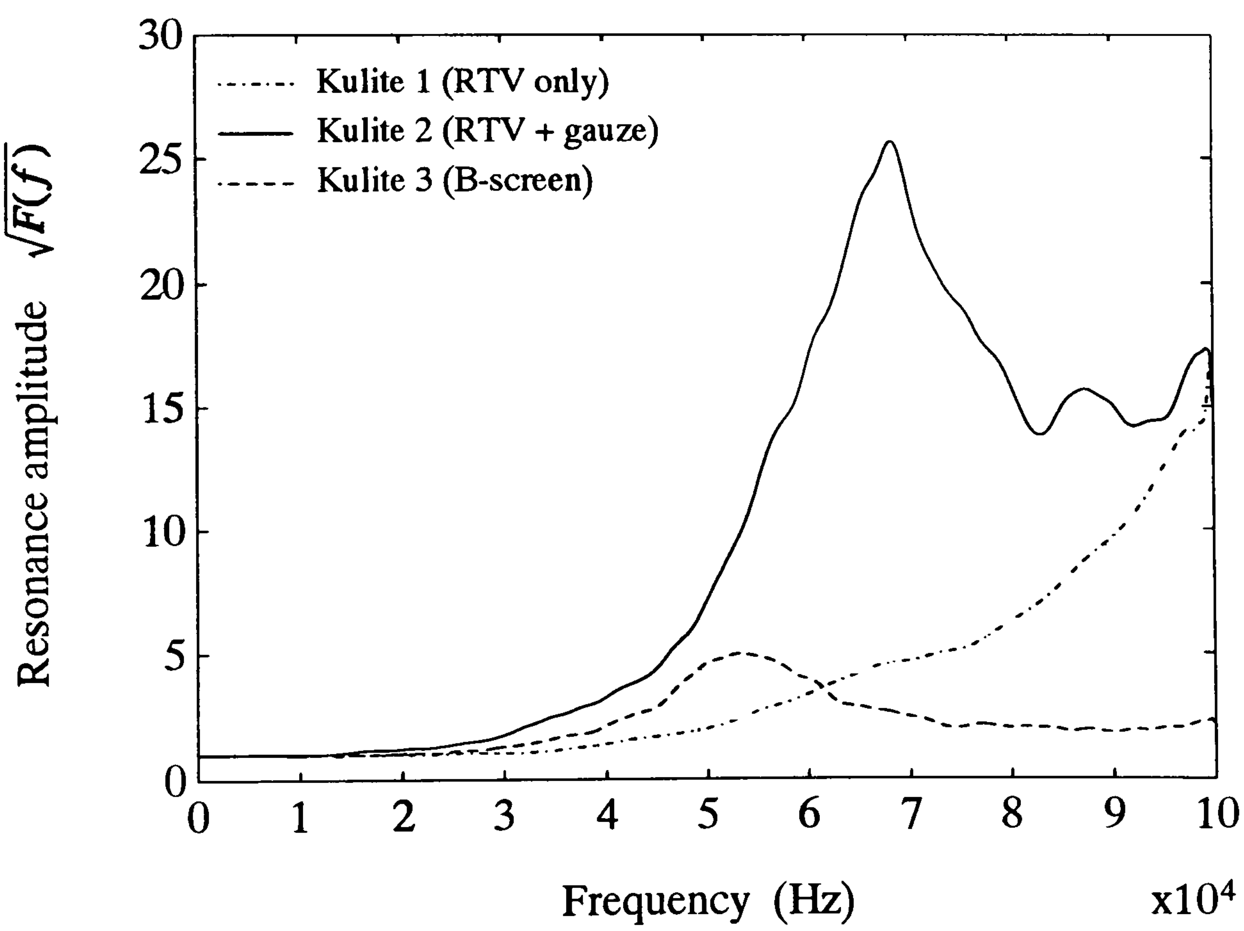

Figure 3.2. Kulite frequency response. Kulite 2 trace (solid line) shows resonance of air behind gauze at ≈70 kHz.

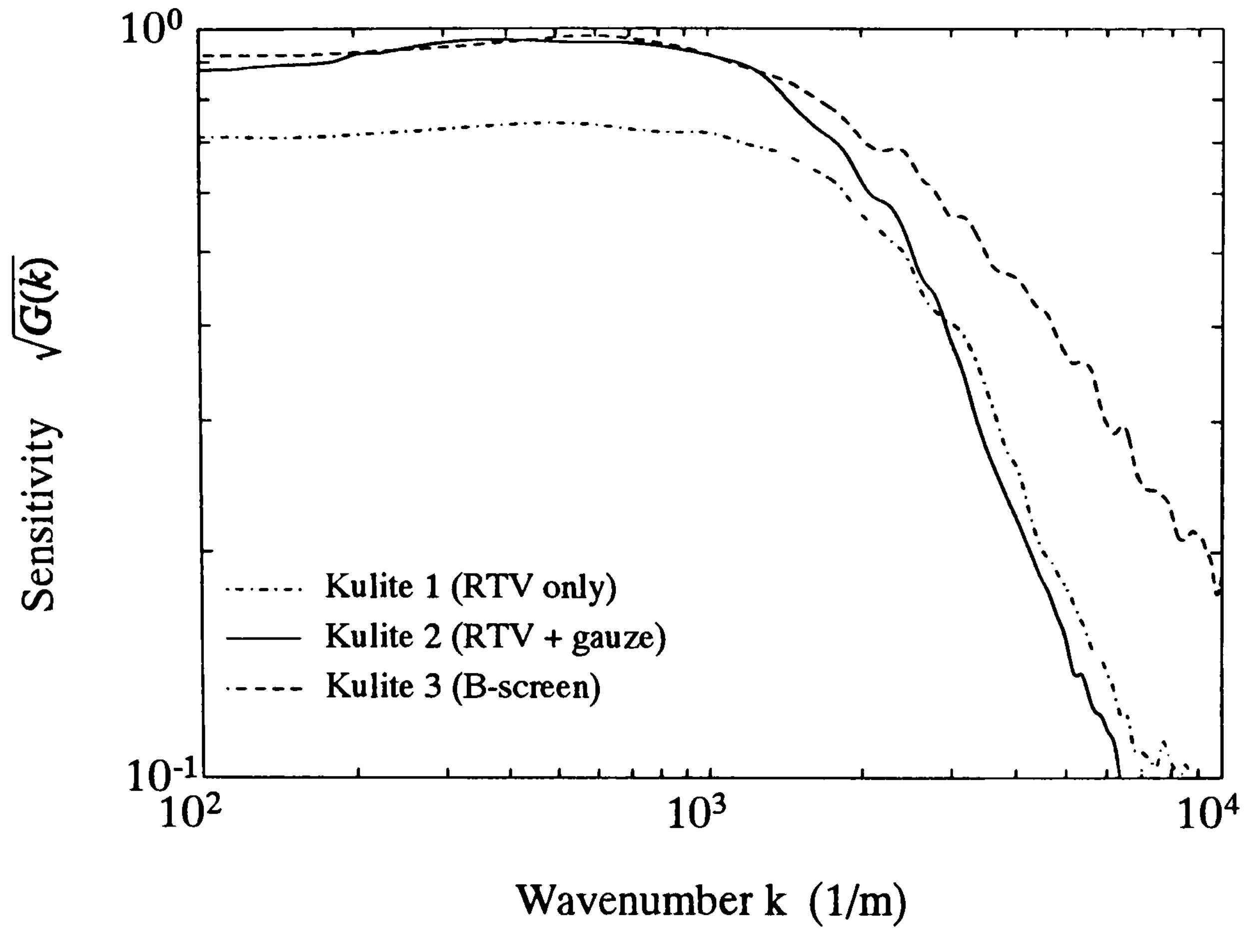

Figure 3.3. Effect of wavenumber on sensitivity to turbulence.

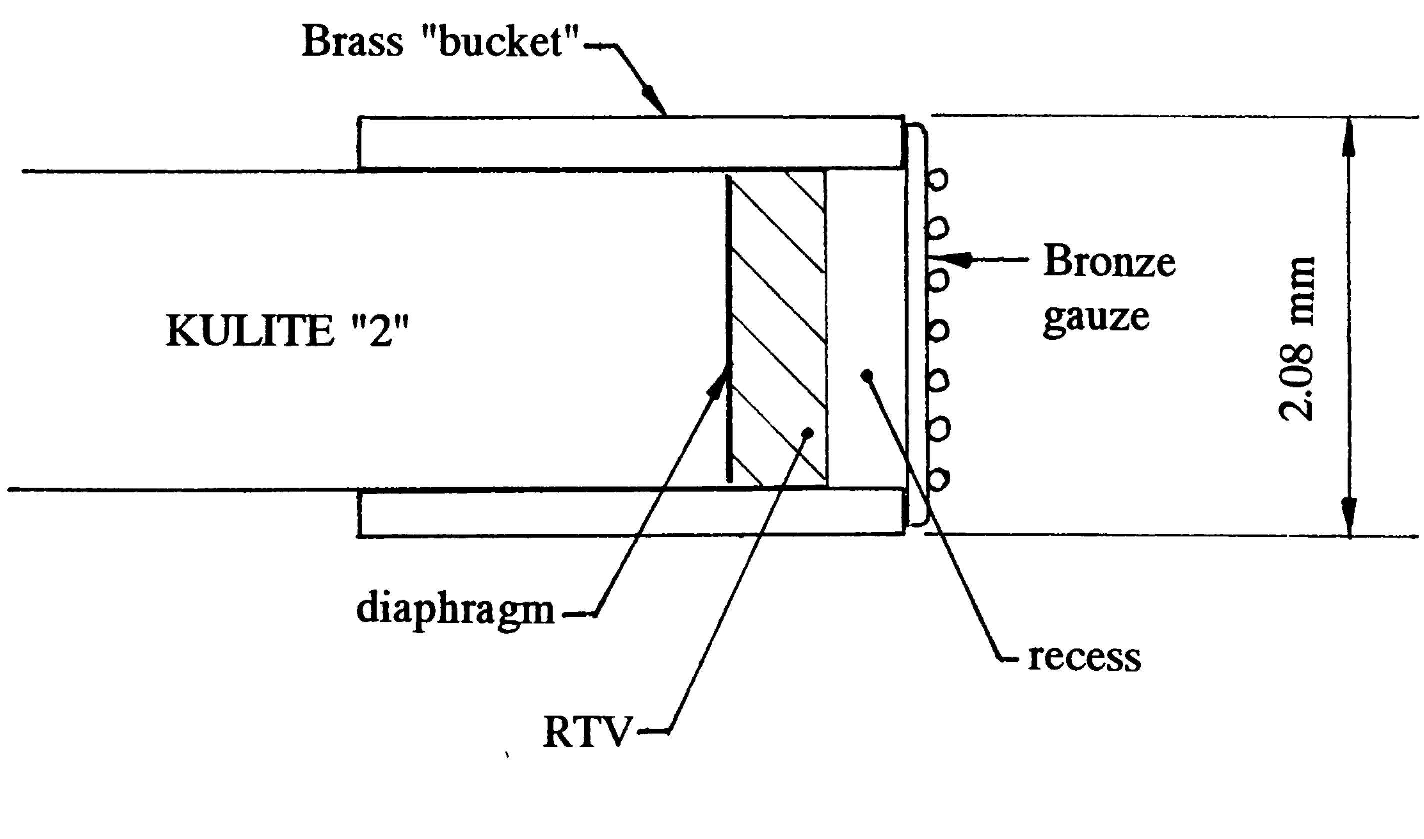

Figure 3.4. Kulite 2 tip configuration showing mounting of gauze screen.

	Combustor *A*	Combustor *B*	Combustor *C*
Cold, half speed	H		
Cold, nominal speed	TKHX	K	K
Cold, 1.7 × speed	H		
Air, 410 K		TK	TK
Air, 410 K, 62 mm d/s		TK	
100:1 *AFR* paraffin	TK(M)	TK	
100:1 paraffin, 62 mm d/s		TK	
65:1 paraffin	TKQ	TK	
65:1 paraffin, 30% main jet	TK		
65:1 diesel		TK	TKQ
50:1 paraffin		TK	

Key: **T** temperature
K kulite turbulence measurement
H hot wire turbulence measurement
X crossed hot wire turbulence measurement
M multiple traverses across different regions of flame.

Figure 4.1. Nominal test conditions and types of measurement taken using combustors *A*, *B* and *C*.

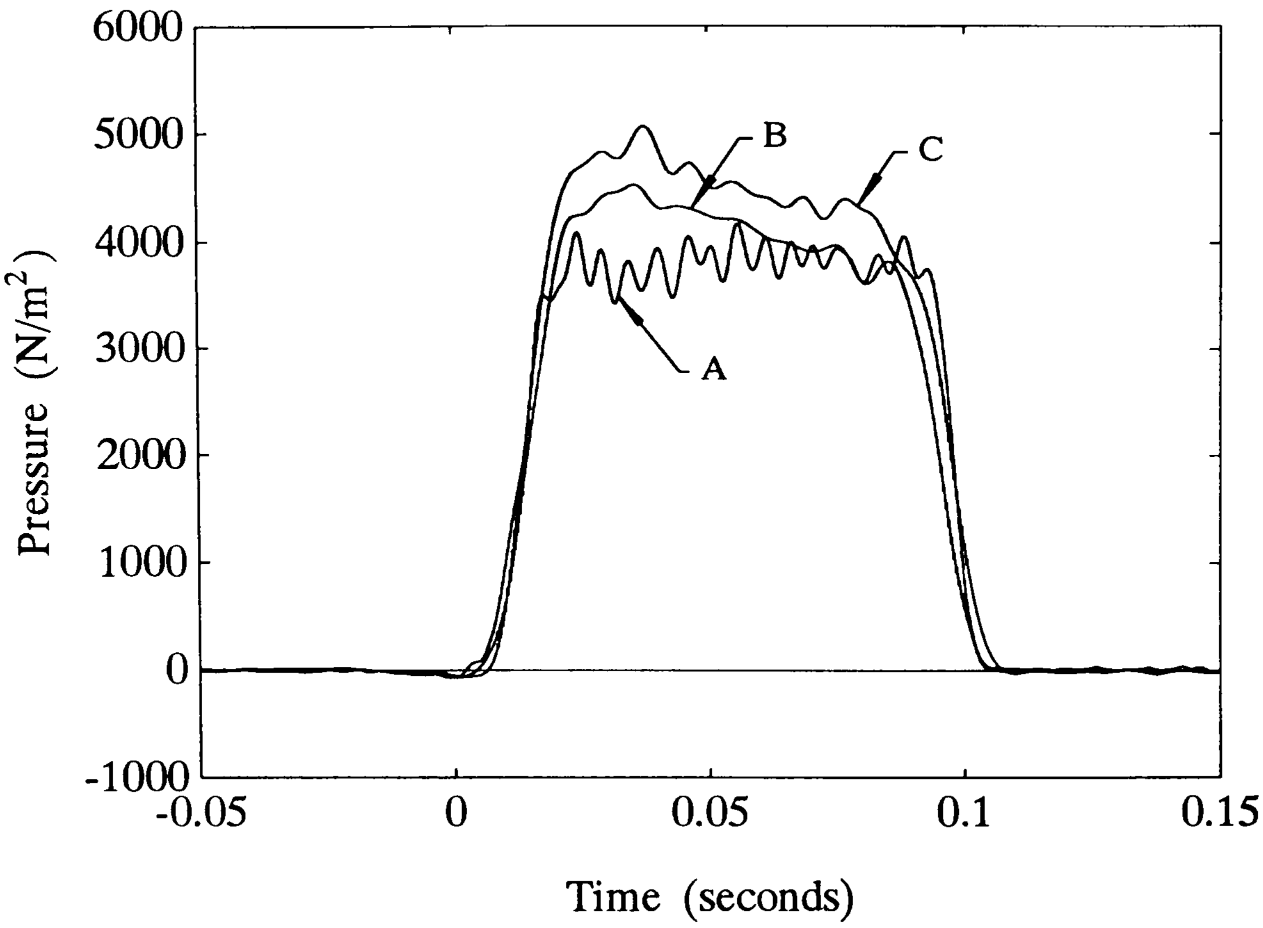

Figure 4.2. Combustors A, B and C: total pressure traverses. Oscillations on trace A are due to mechanical vibration and are not a feature of the flow.

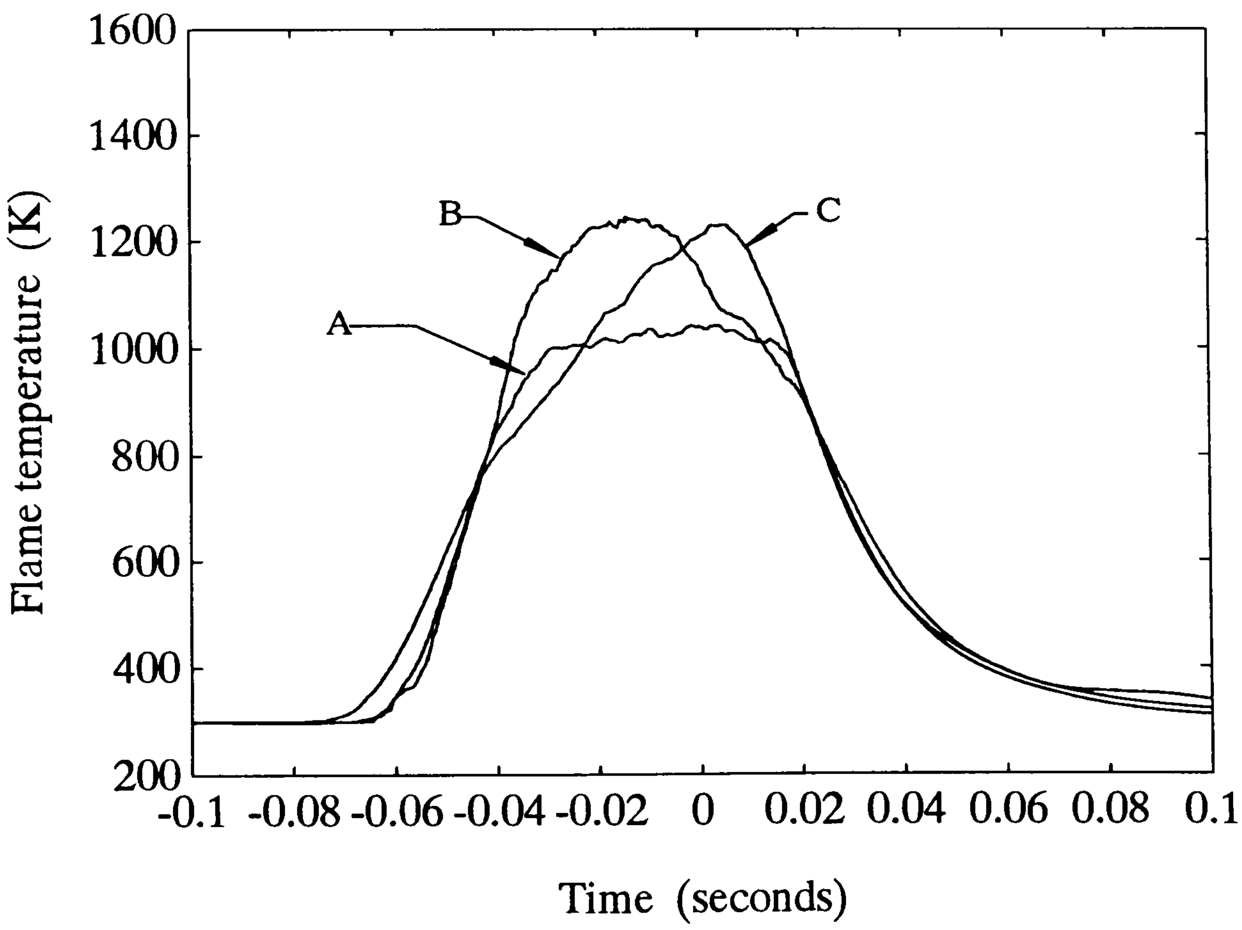

Figure 4.3. Temperature traverses from combustors *A*, *B* and *C* at 65:1 *AFR*. *A* includes 30% main jet flow (see Figure 4.5).

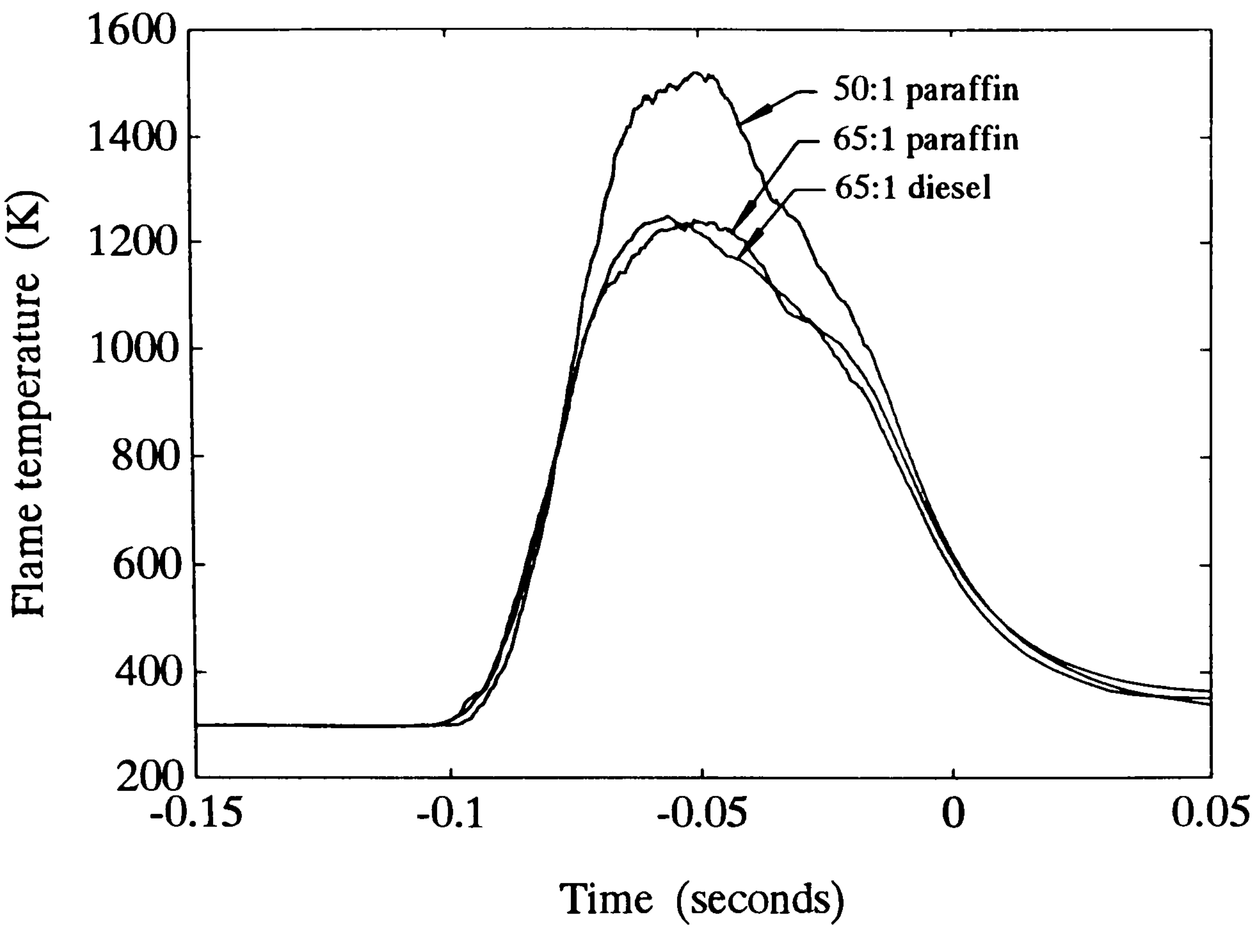

Figure 4.4. Combustor B: comparison between temperature traverses at 65:1 *AFR* with paraffin and diesel fuels, plus highest temperature experienced, at 50:1 *AFR* with paraffin.

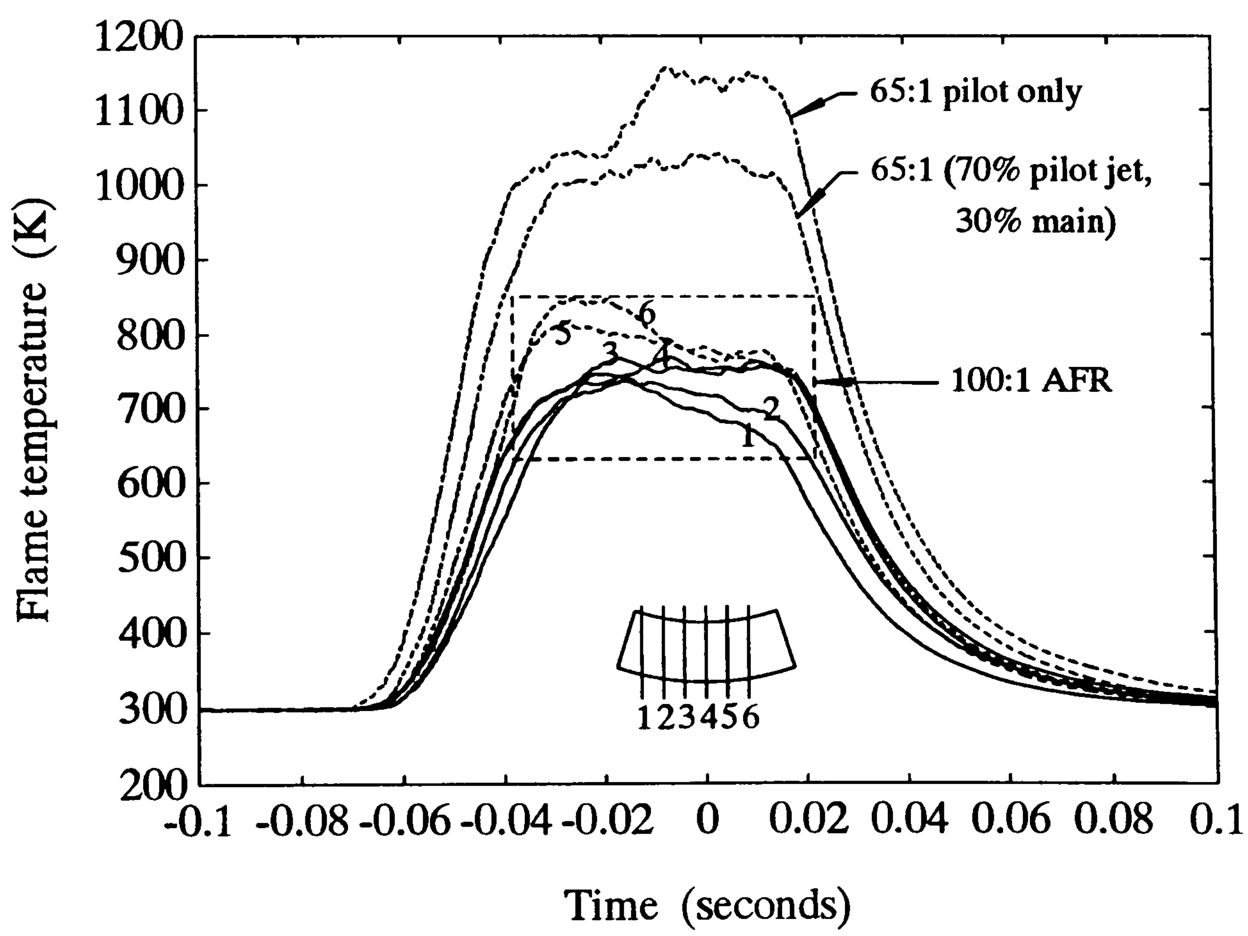

Figure 4.5. Combustor A: uniformity of temperature traverse at 6 radial planes (100:1 *AFR*), and comparison between 100% pilot jet (normal situation), and 70% pilot jet, 30% main case.

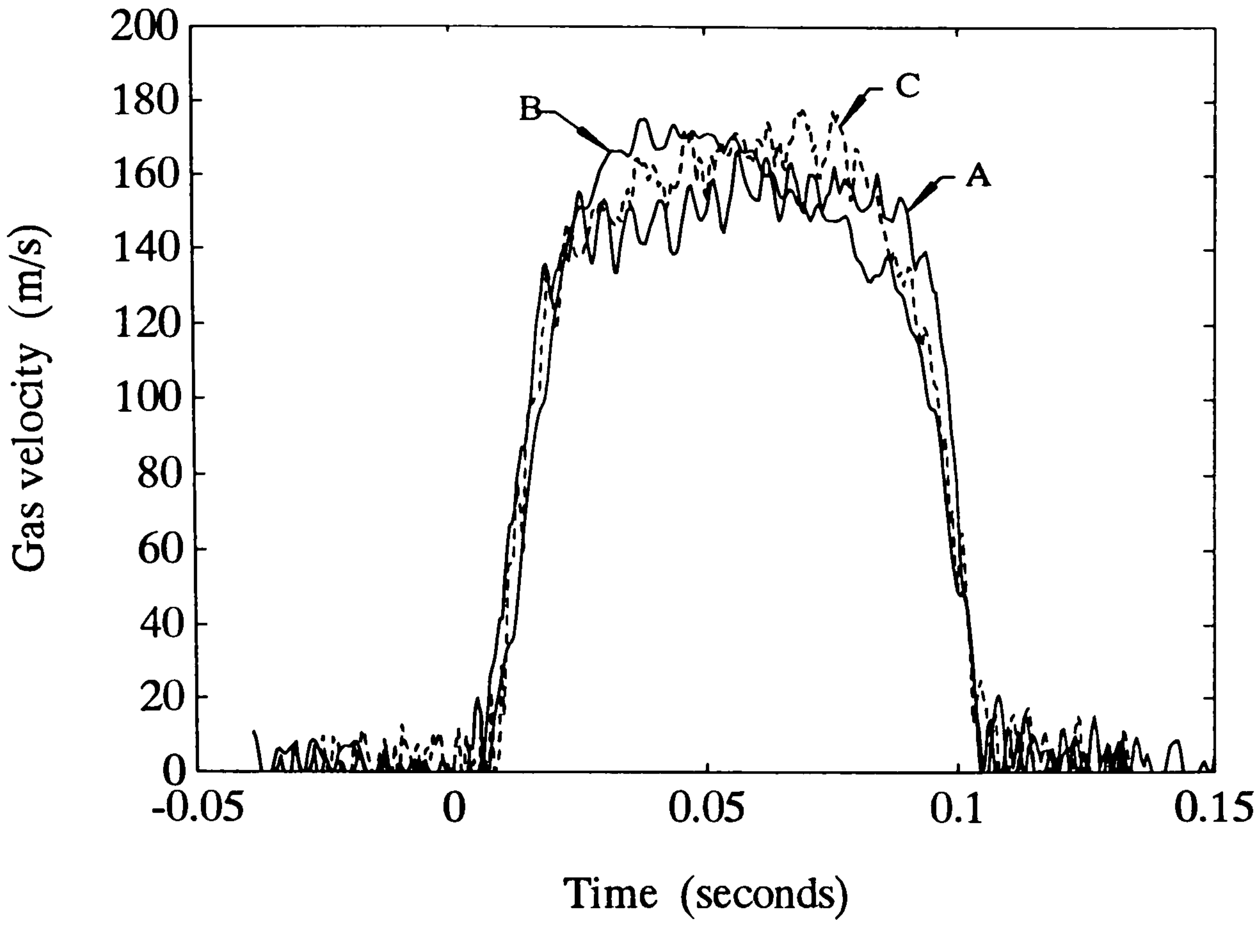

Figure 4.6. Combustors A, B and C: exit velocity profiles at *AFR* = 65:1.

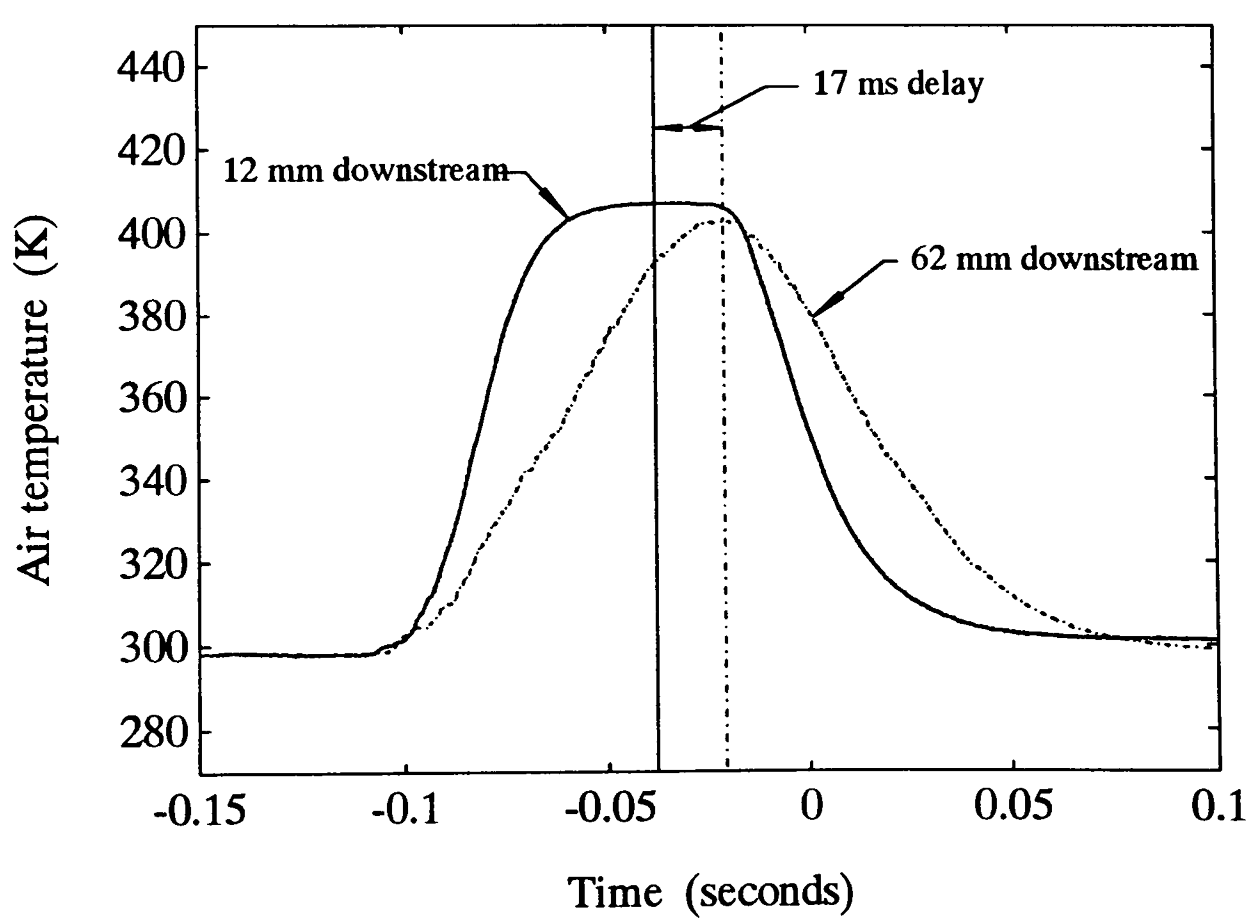

Figure 4.7. Temperature traverses 12 and 62 mm downstream of combustor (blowing hot air). Flow exit angle has been inferred from 17 ms delay on 62 mm signal.

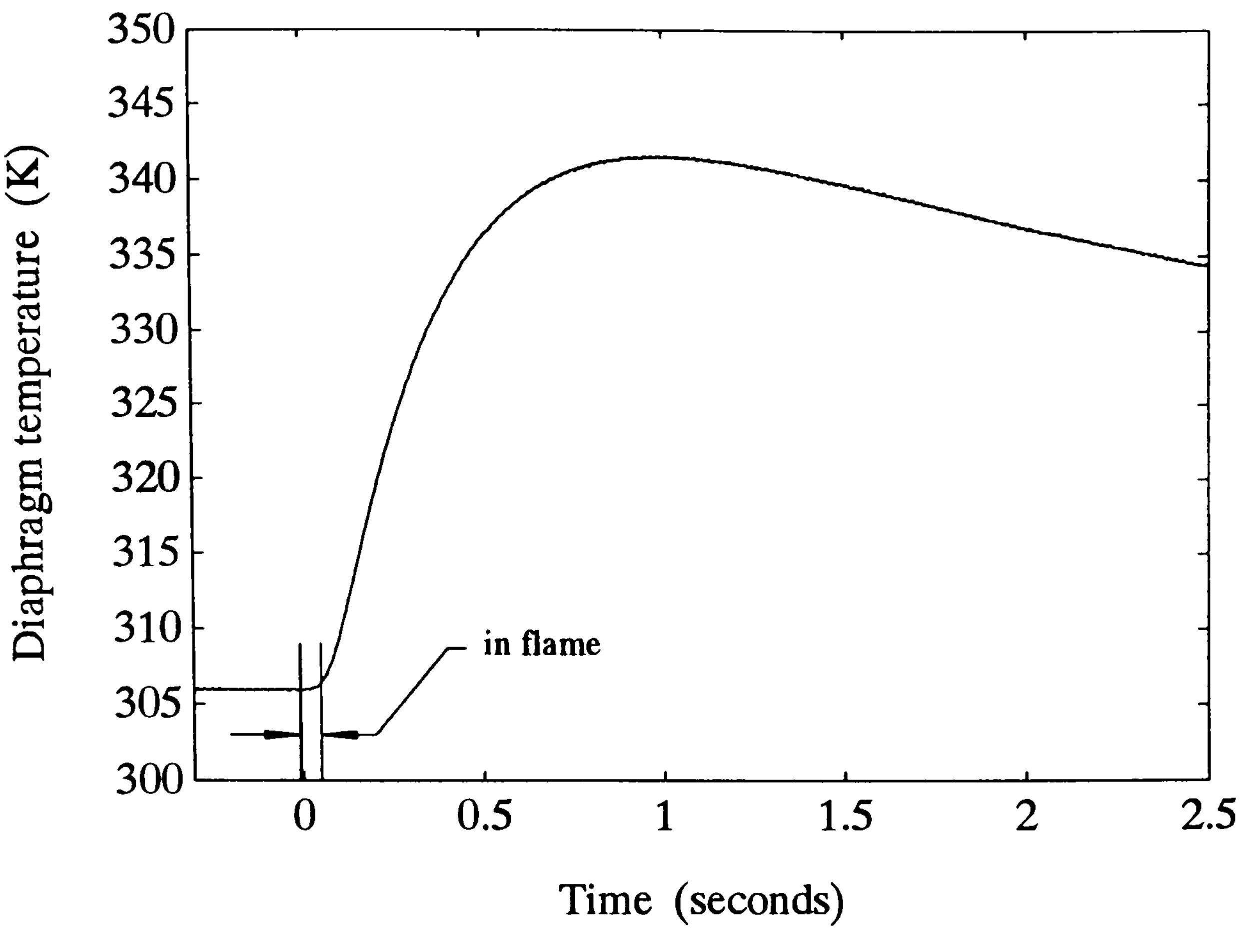

Figure 4.8. Kulite diaphragm temperature rise. Combustor B, 50:1 *AFR*, time in flame = 56 ms. The transducer is mounted flush with the probe tip.

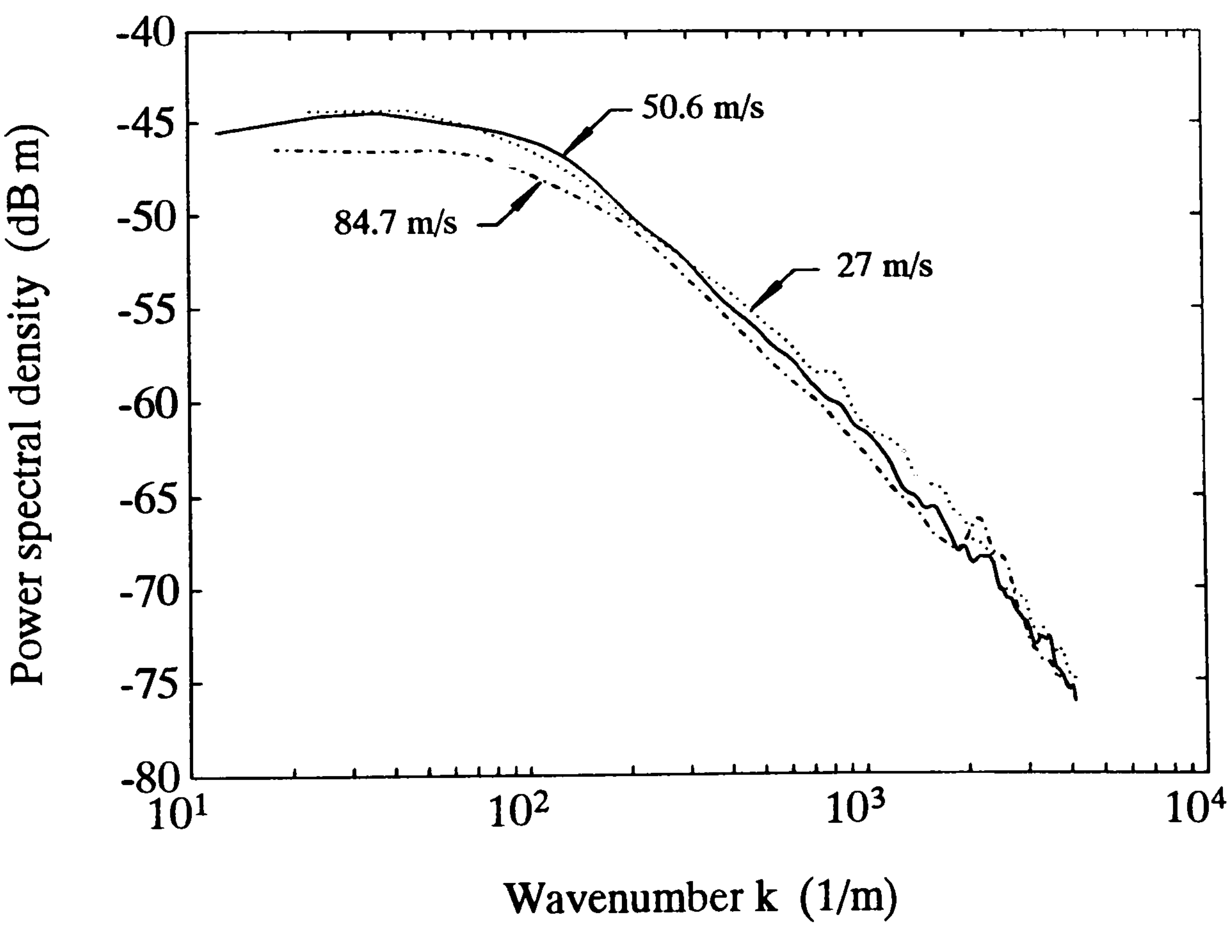

Figure 4.9. Combustor A: Turbulence spectra at 27, 50.6 and 84.7 m/s, measured by hot wire (cold flow). Bump on 84 m/s trace at k = 2000 is wire resonance rather than a genuine flow feature.

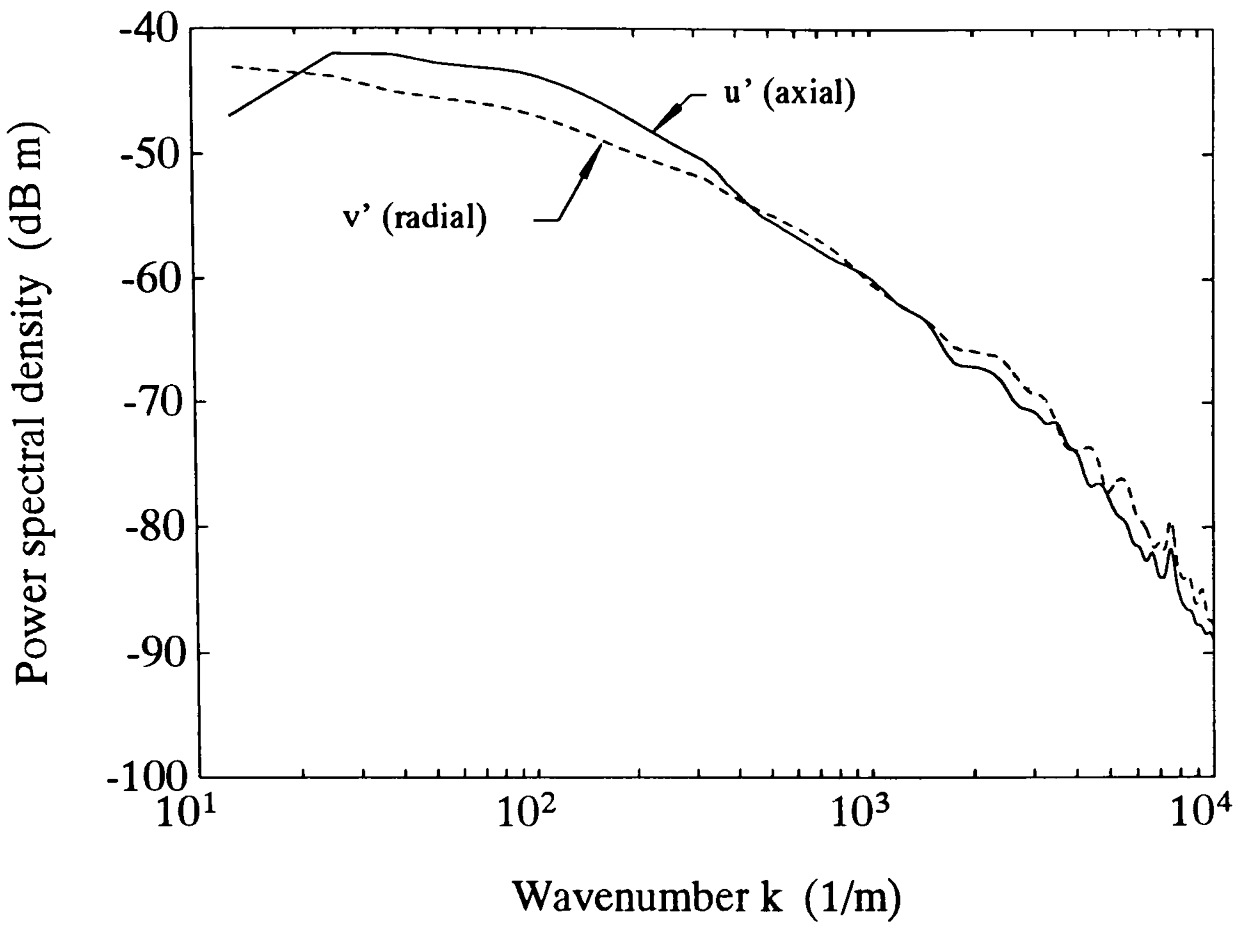

Figure 4.10. Crossed hot wire measurement of anisotropy. (Combustor A, 47.5 m/s, cold).

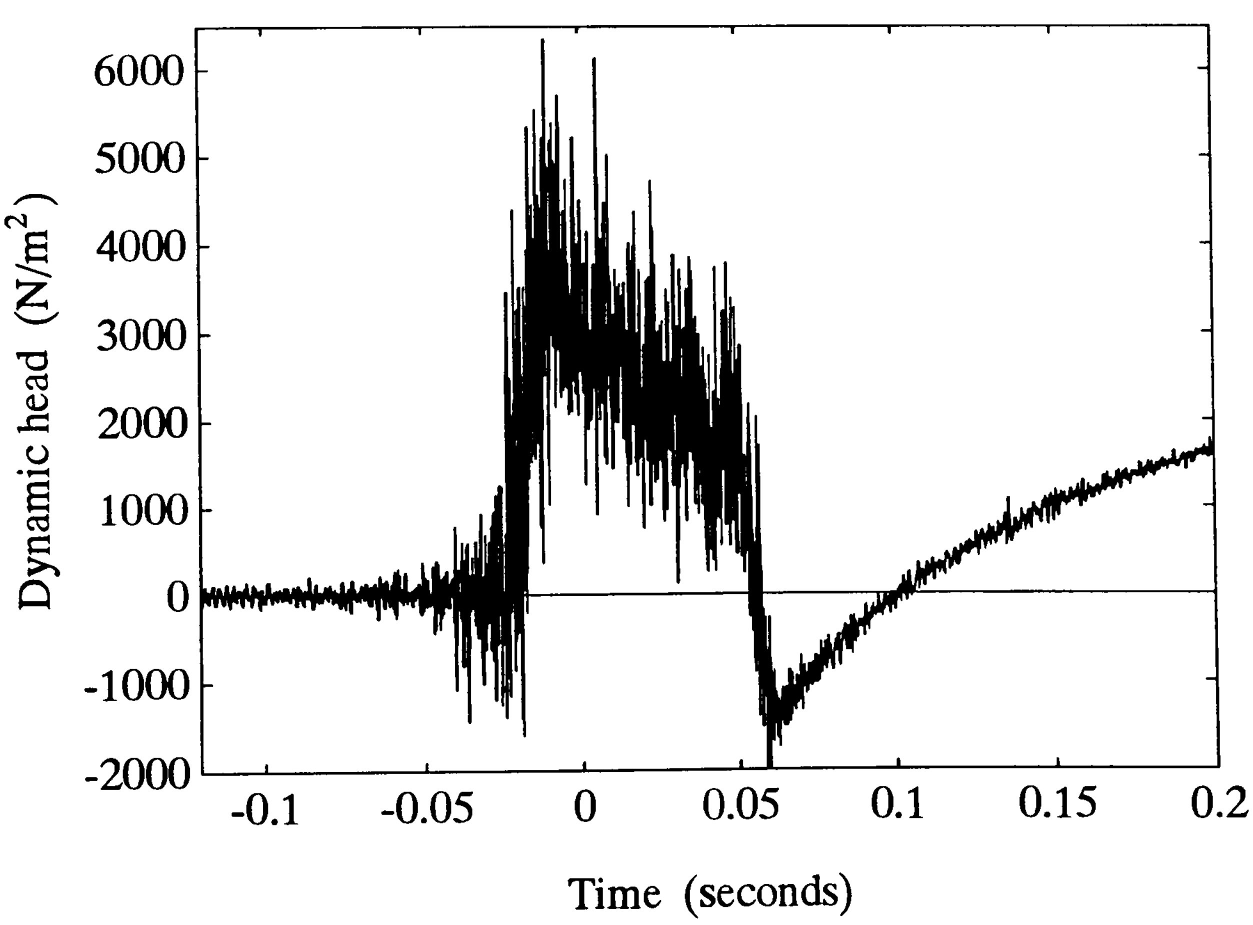

Figure 4.11. Typical kulite total pressure measurement. (Combustor B, *AFR* = 65, paraffin).

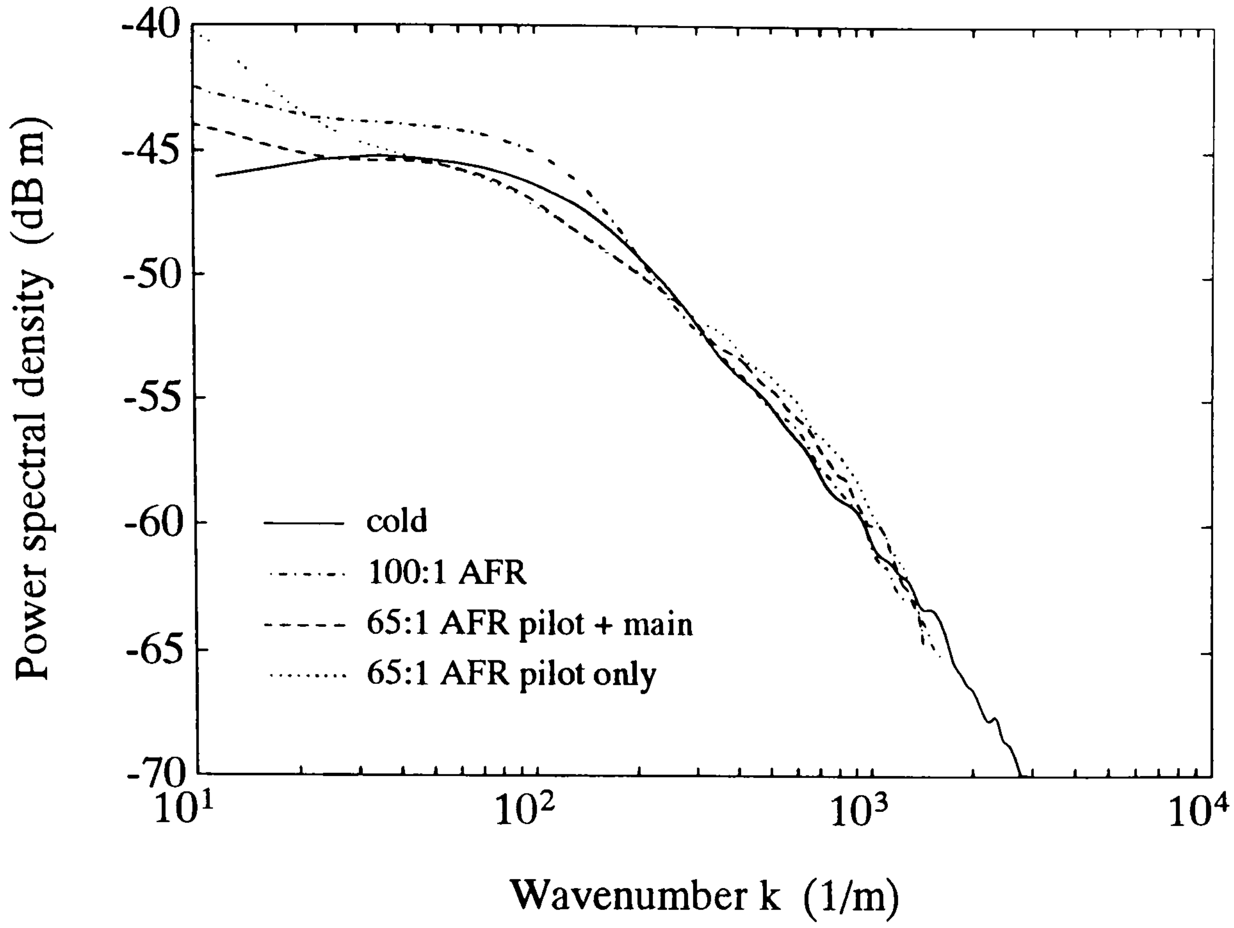

Figure 4.12. Combustor A wavenumber spectra at cold, 100:1 *AFR* and 65:1 *AFR* conditions.

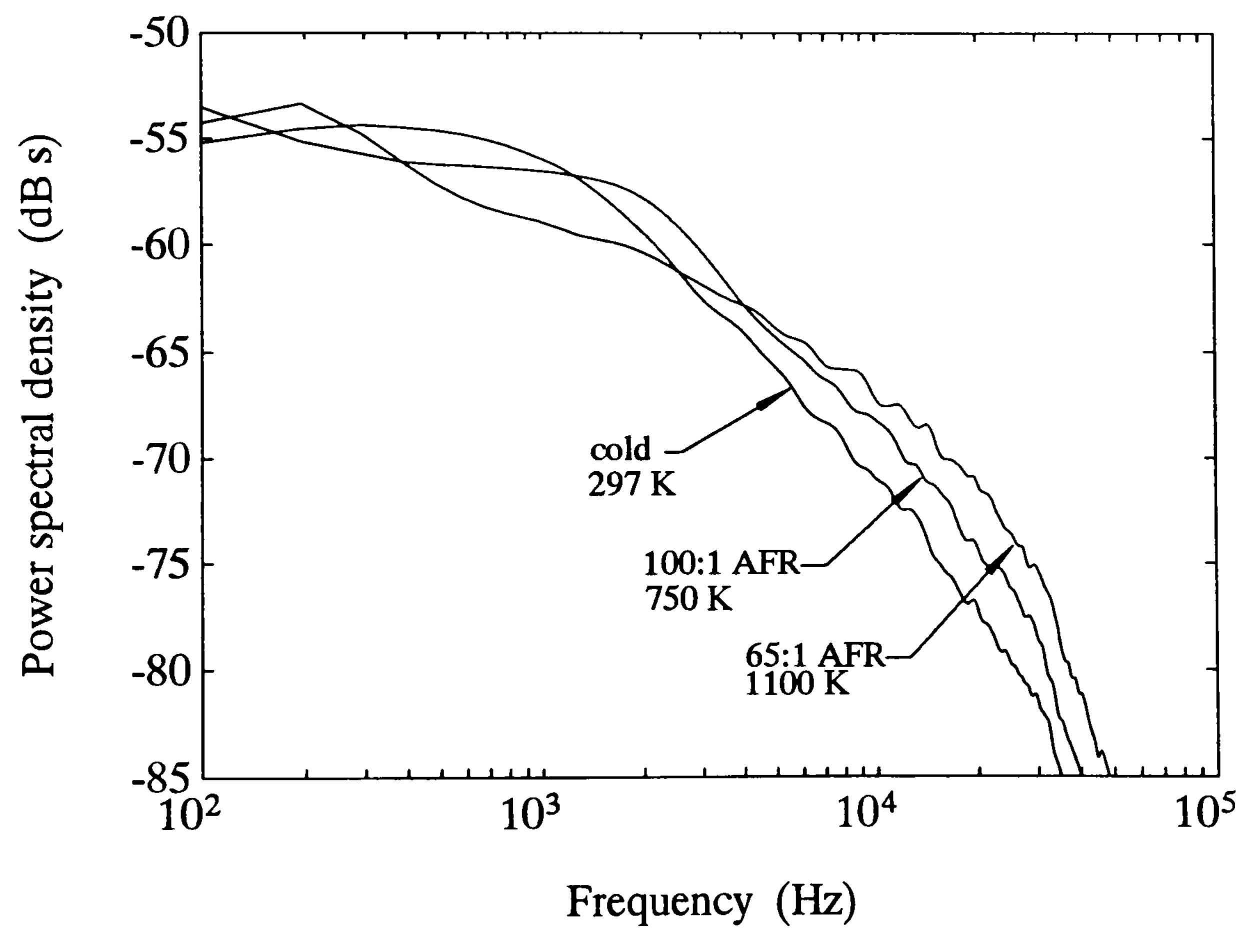

Figure 4.13. Combustor A turbulence frequency spectra. Plotting spectra measured at different velocities against frequency is not as informative as a wavenumber plot.

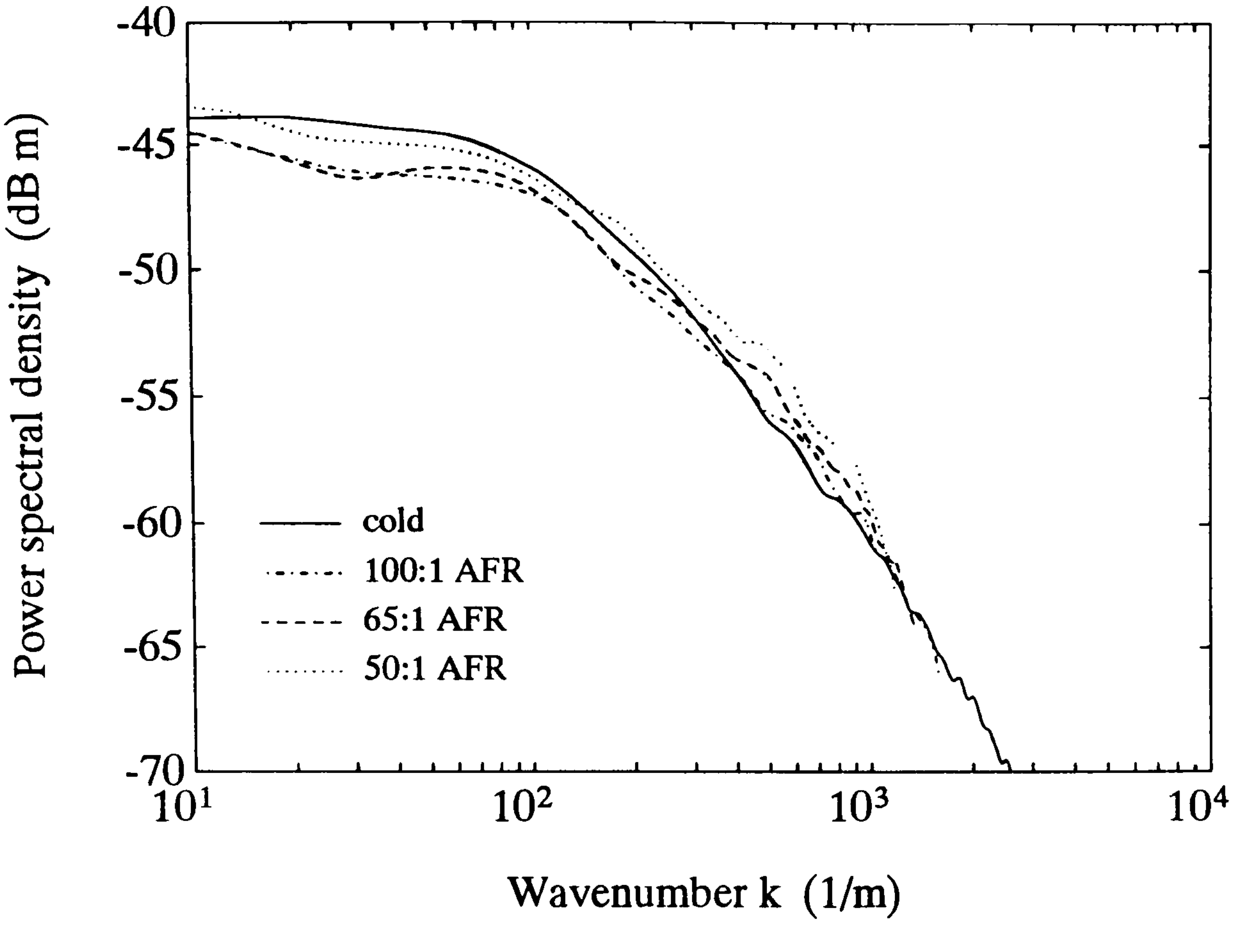

Figure 4.14. Combustor B turbulence wavenumber spectra: cold, 100:1, 65:1 and 50:1 *AFR* burning paraffin.

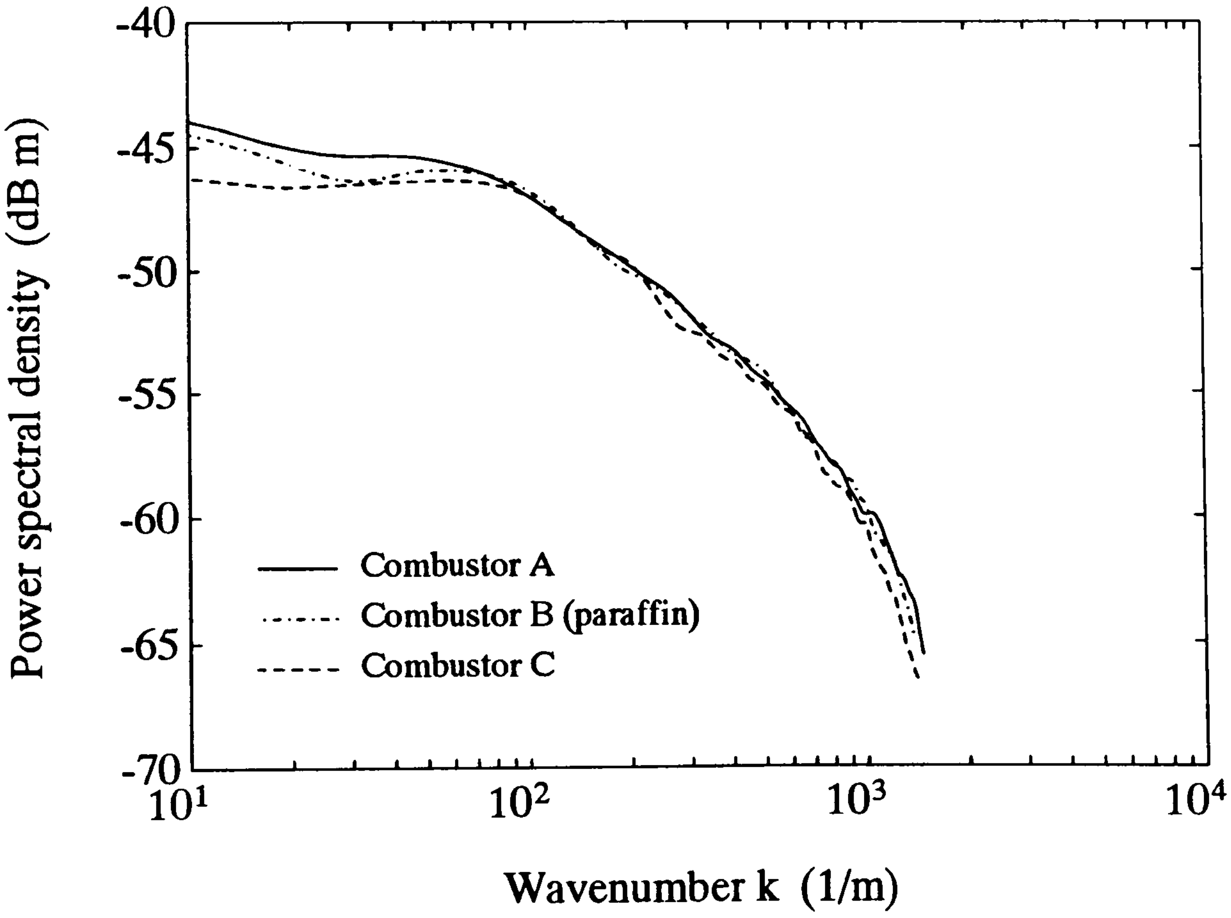

Figure 4.15. Comparison of turbulence spectra from combustors A, B and C at *AFR* = 65.

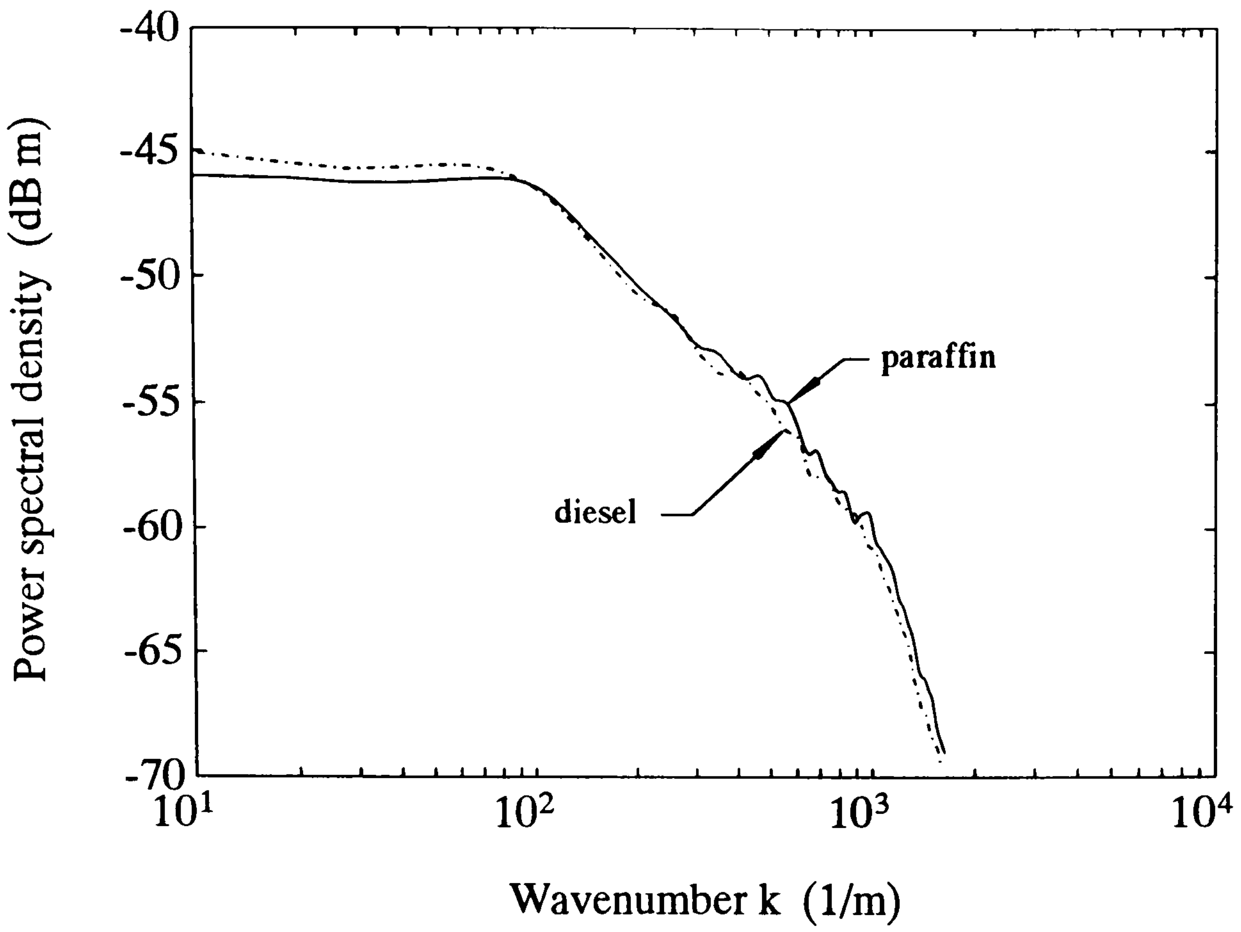

Figure 4.16. Effect on turbulence spectrum of changing burning rate by using diesel fuel instead of paraffin. (Combustor B, *AFR* = 65).

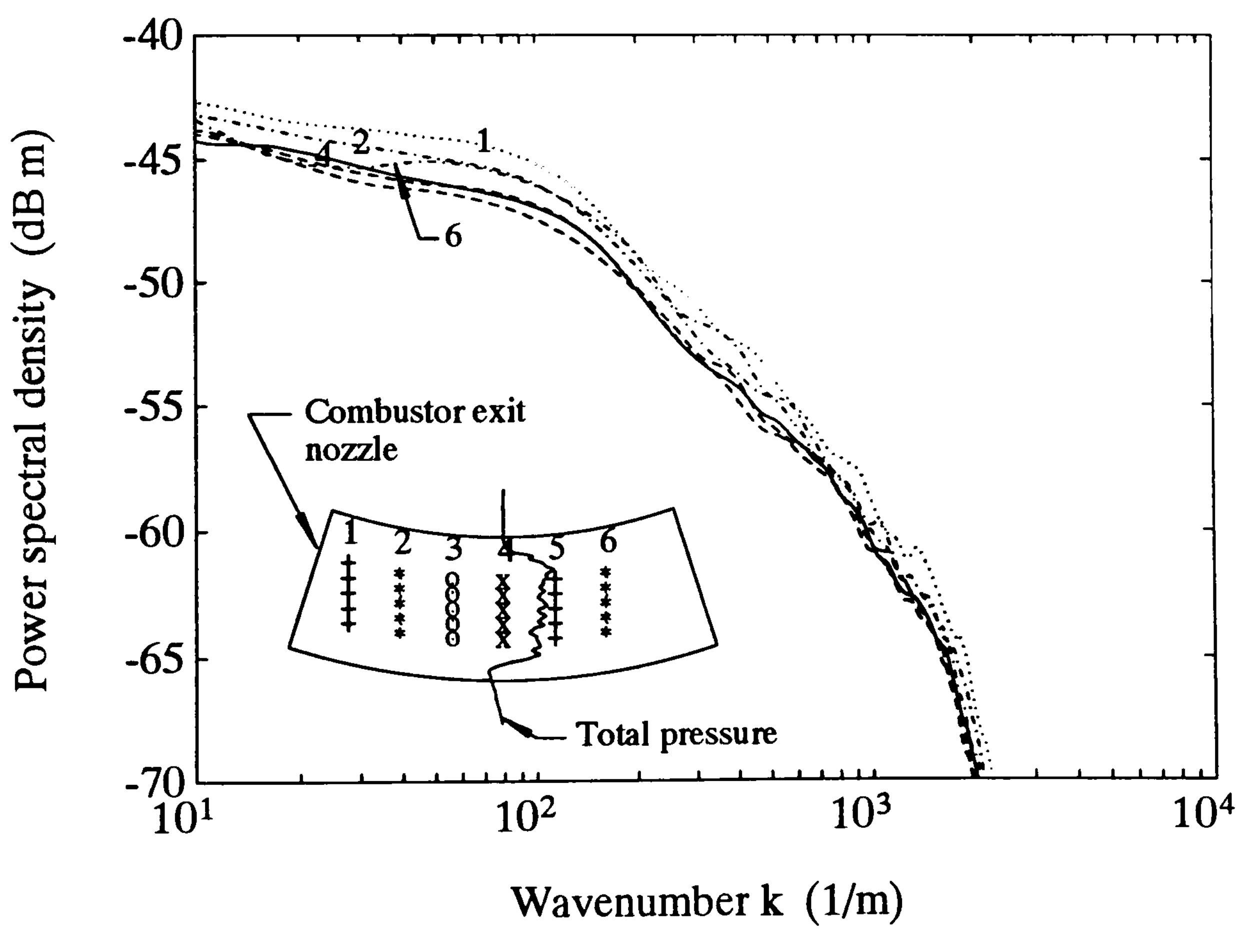

Figure 4.17. Circumferential uniformity of turbulence field. (Combustor A, *AFR* = 100:1).

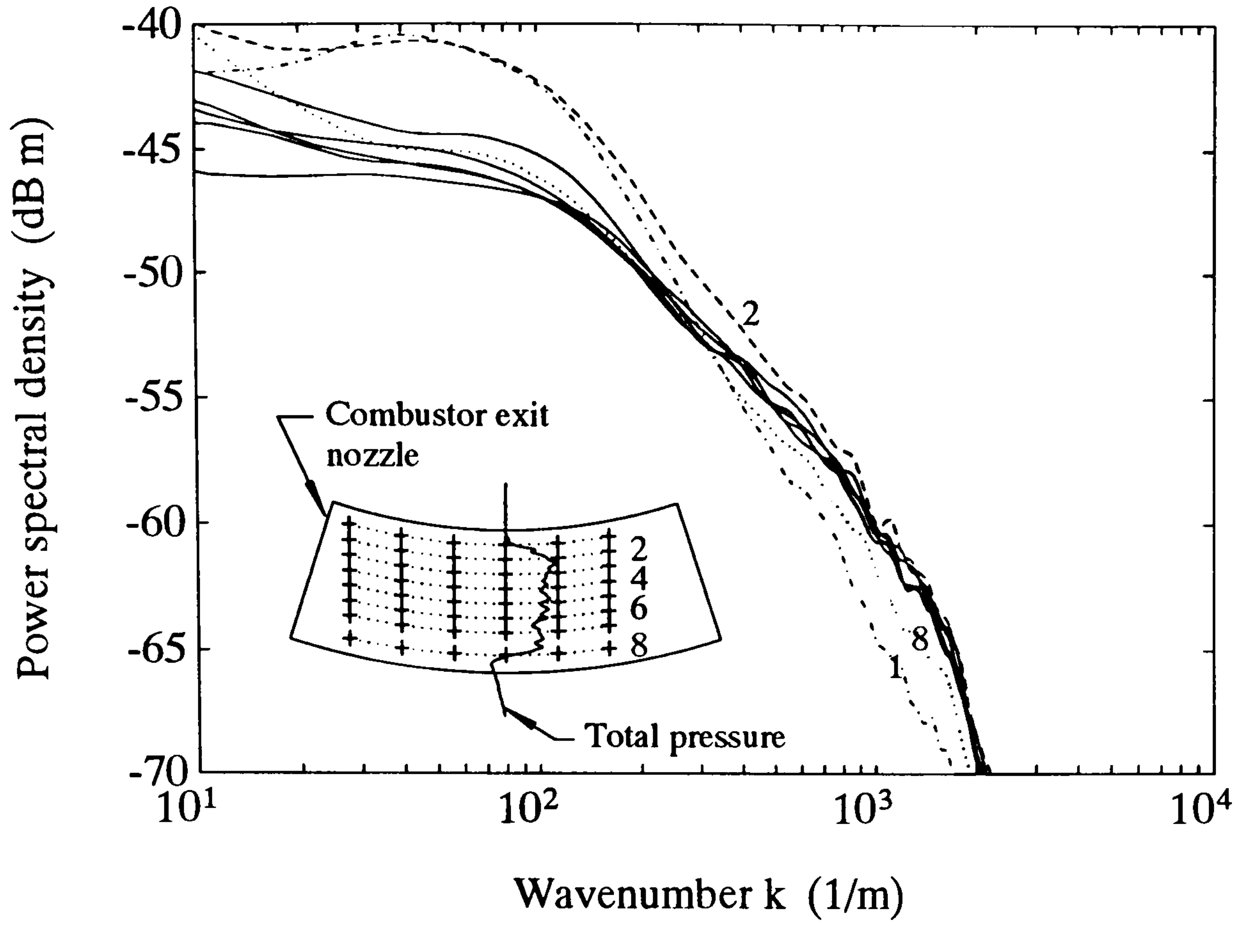

Figure 4.18. Radial uniformity of turbulence field: spectra at eight radial positions across nozzle as shown.

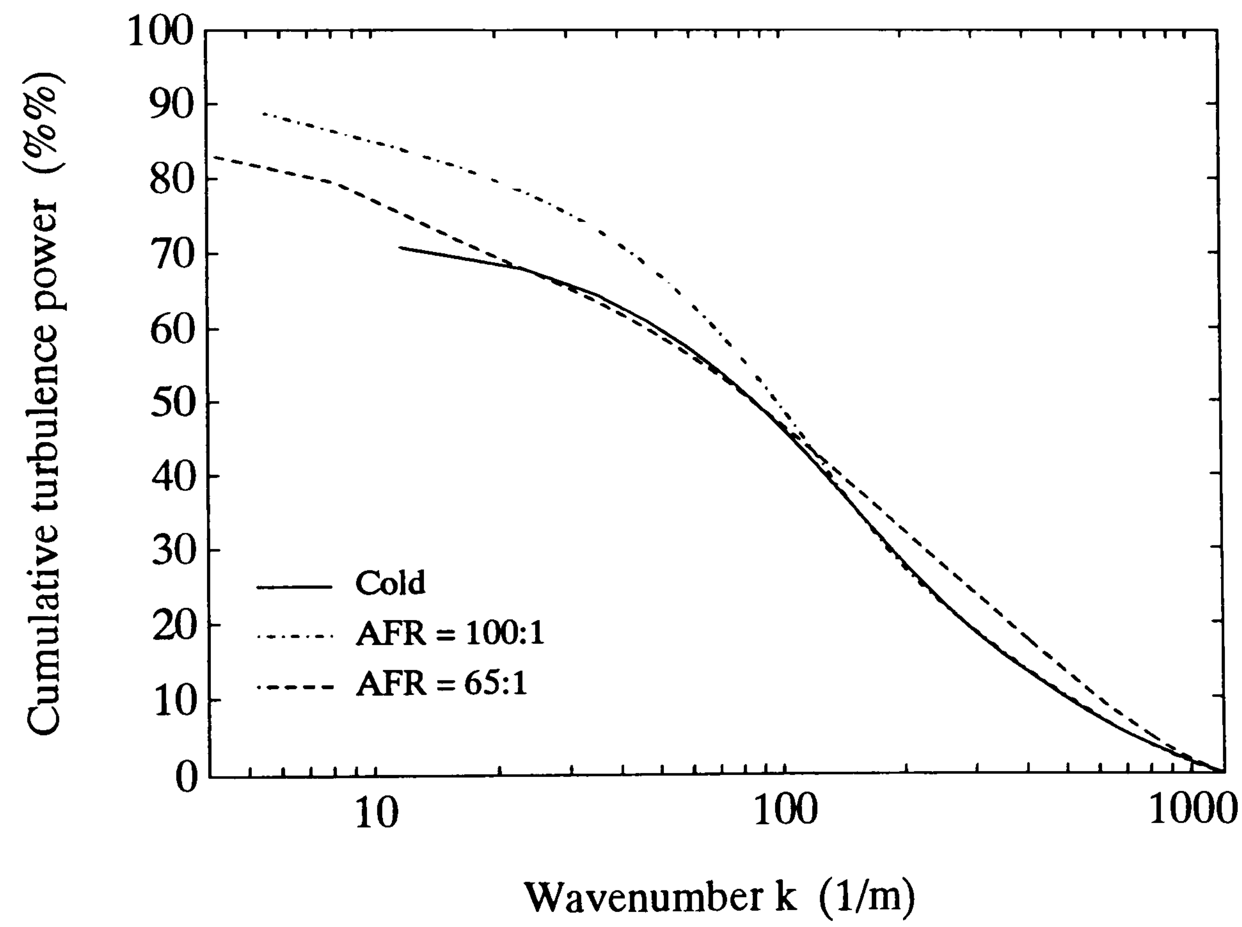

Figure 4.19. Cumulative turbulence power plot. (Combustor *A*).

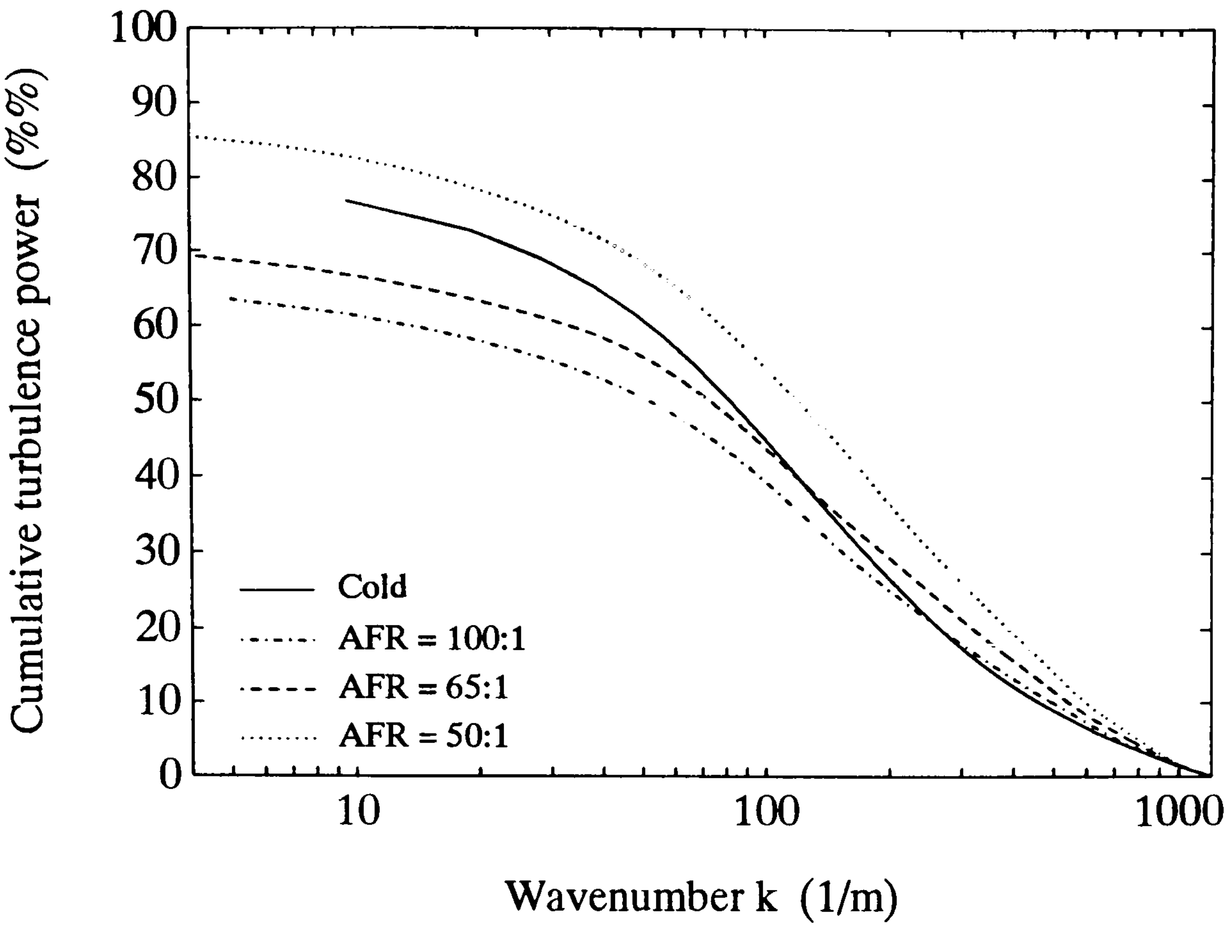

Figure 4.20. Cumulative turbulence power, combustor *B*.

	Intensity *Tu*	Integral scale Λ_x
Combustor A, cold	8.7 %	5.6 mm
Combustor A, p & m, AFR = 65	8.6 %	7.6 mm
Combustor A, pilot only, AFR = 65	9.2 %	15.6 mm
Combustor B, cold	9.0 %	7.1 mm
Combustor B, AFR = 50	9.3 %	7.5 mm
Combustor C, AFR = 65	8.0 %	5.6 mm
6 mm bar grid at x/d = 24	9.0 %	7.5 mm
Correlation by Roach, 5 mm bars at x/d = 22	8.8 %	4.6 mm

Figure 4.21. Combustor turbulence intensity and integral length scales, plus comparison with parameters for a similar grid-generated spectrum.

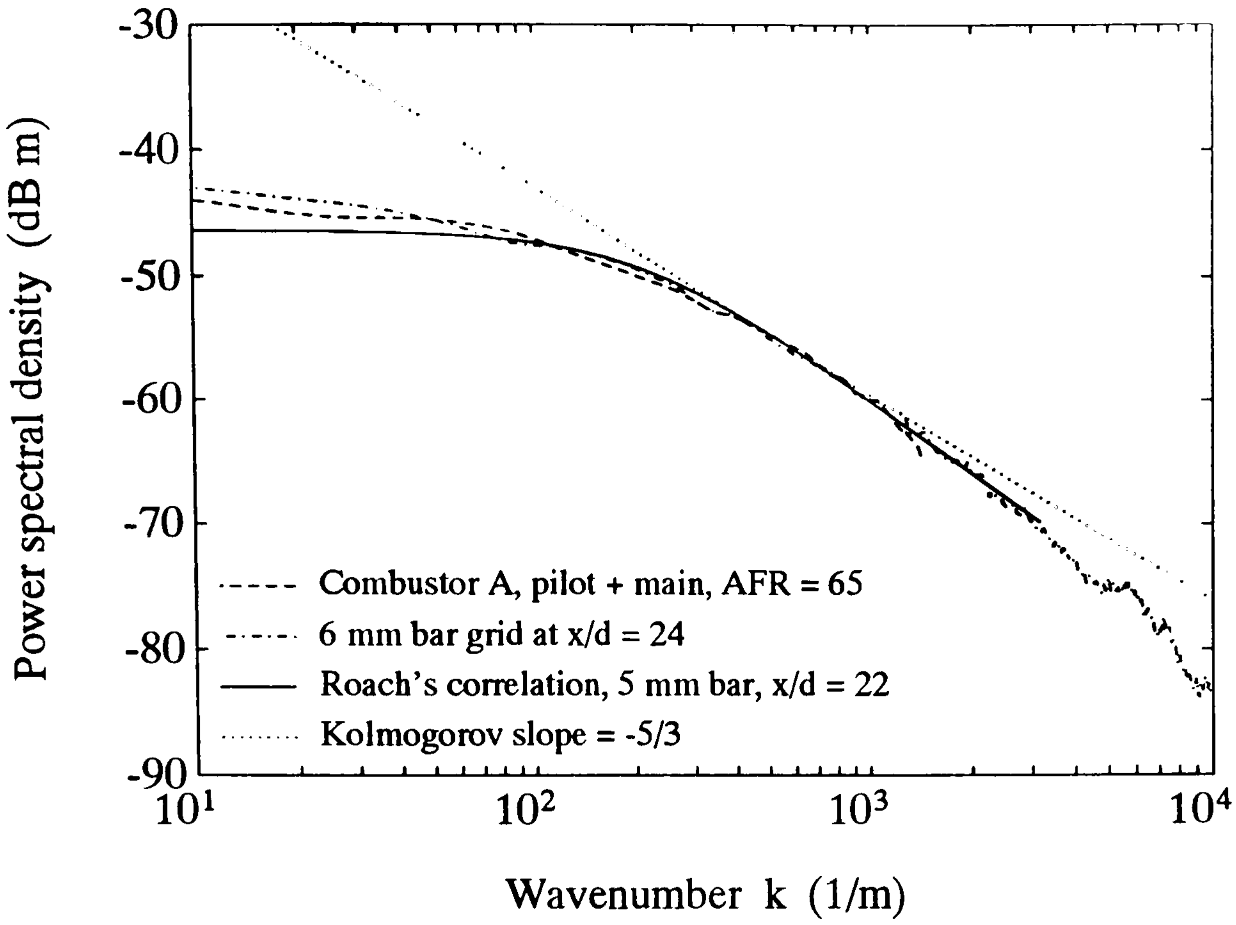

Figure 4.22. Comparison of typical combustor turbulence spectrum with spectra from bar grid and Roach's correlation, plus Kolmogorov decay rate for inertial subrange.

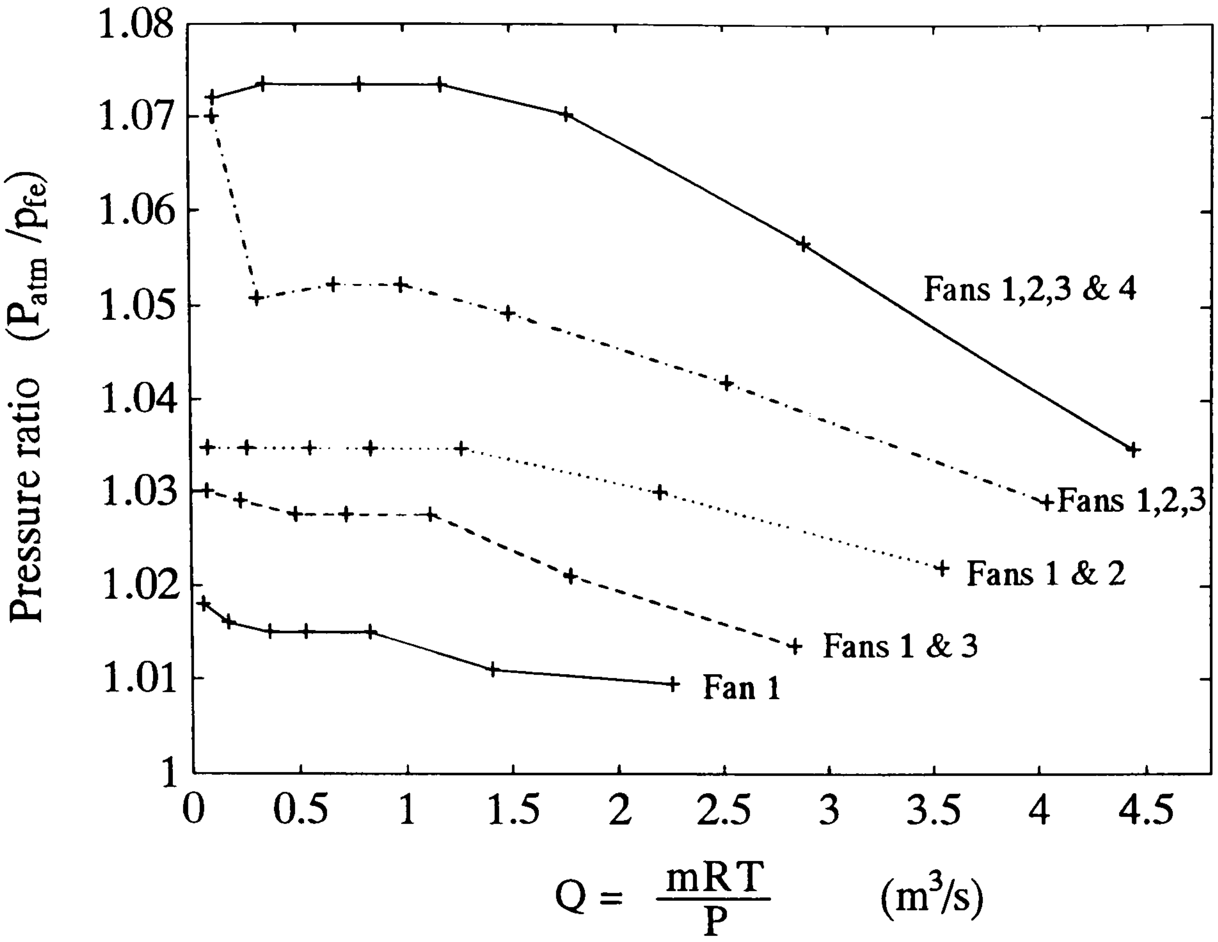

Figure 5.1. Fan performance on the OUEL 6" × 8" high speed tunnel. Plane "*fe*" is at fan entry, measured by Pitot and static between diffuser and large settling box.

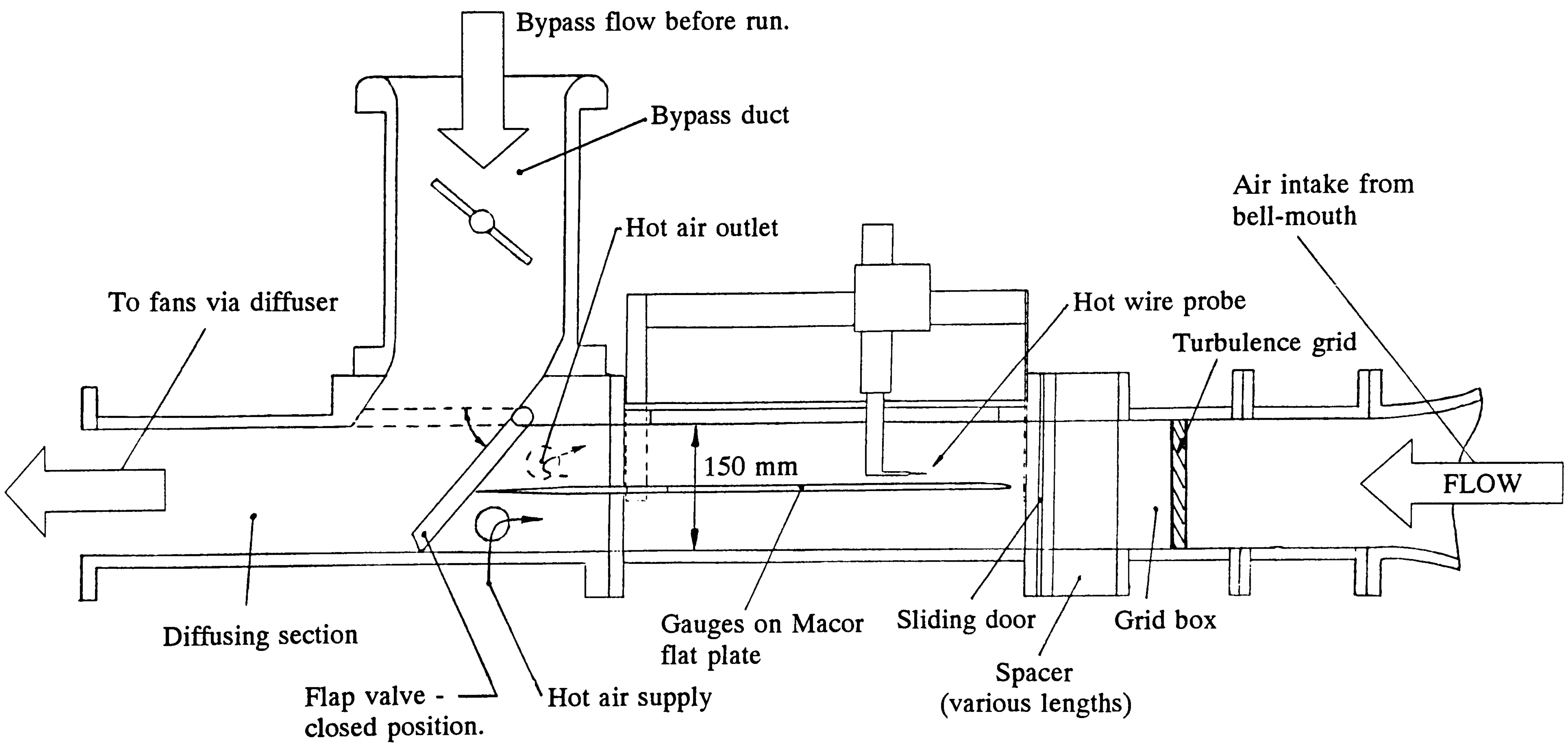

Figure 5.2. Wind tunnel working section showing flat plate.

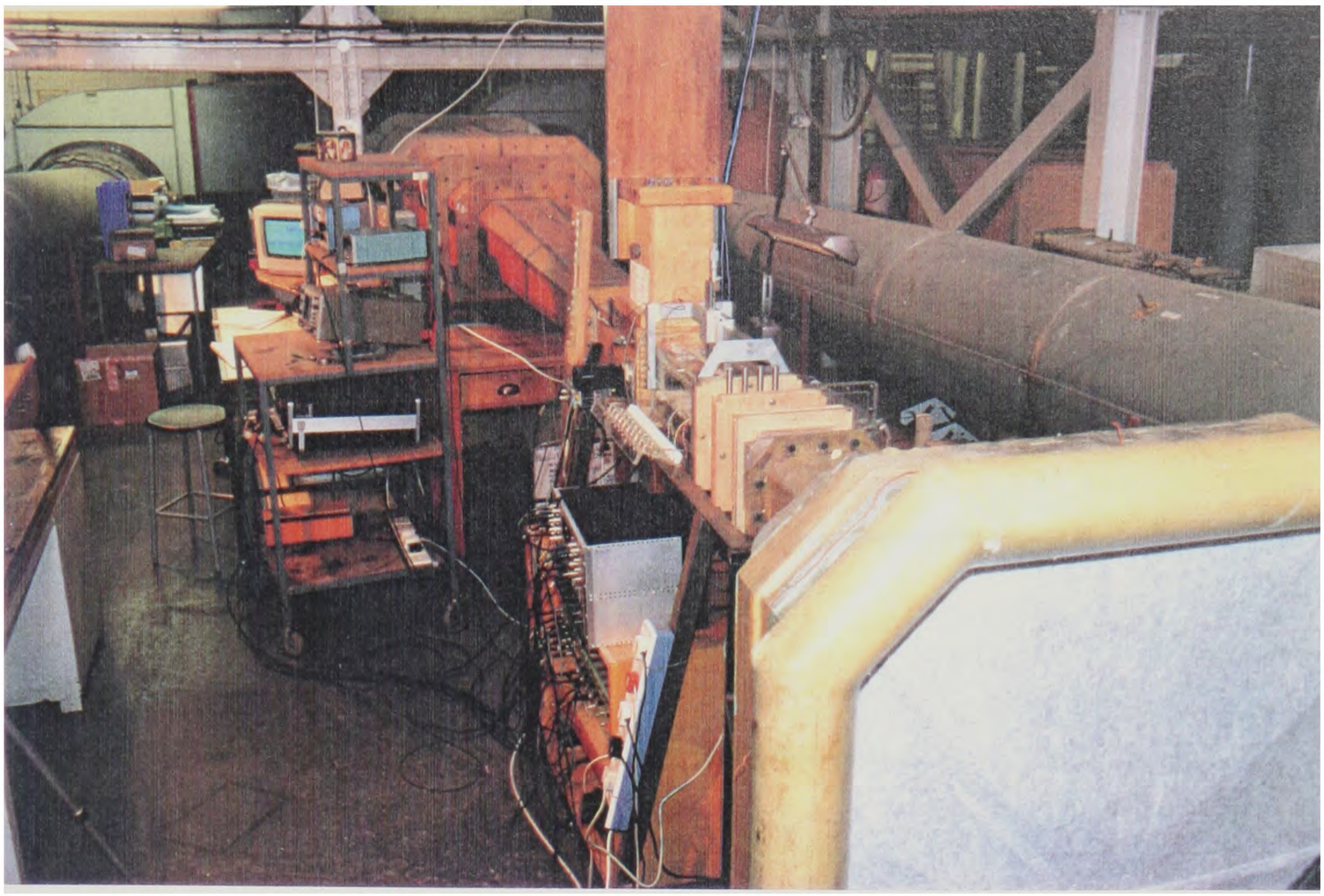

Figure 5.3. Photograph of the OUEL 6" × 8" high speed wind tunnel. The Macor plate is visible in the working section.

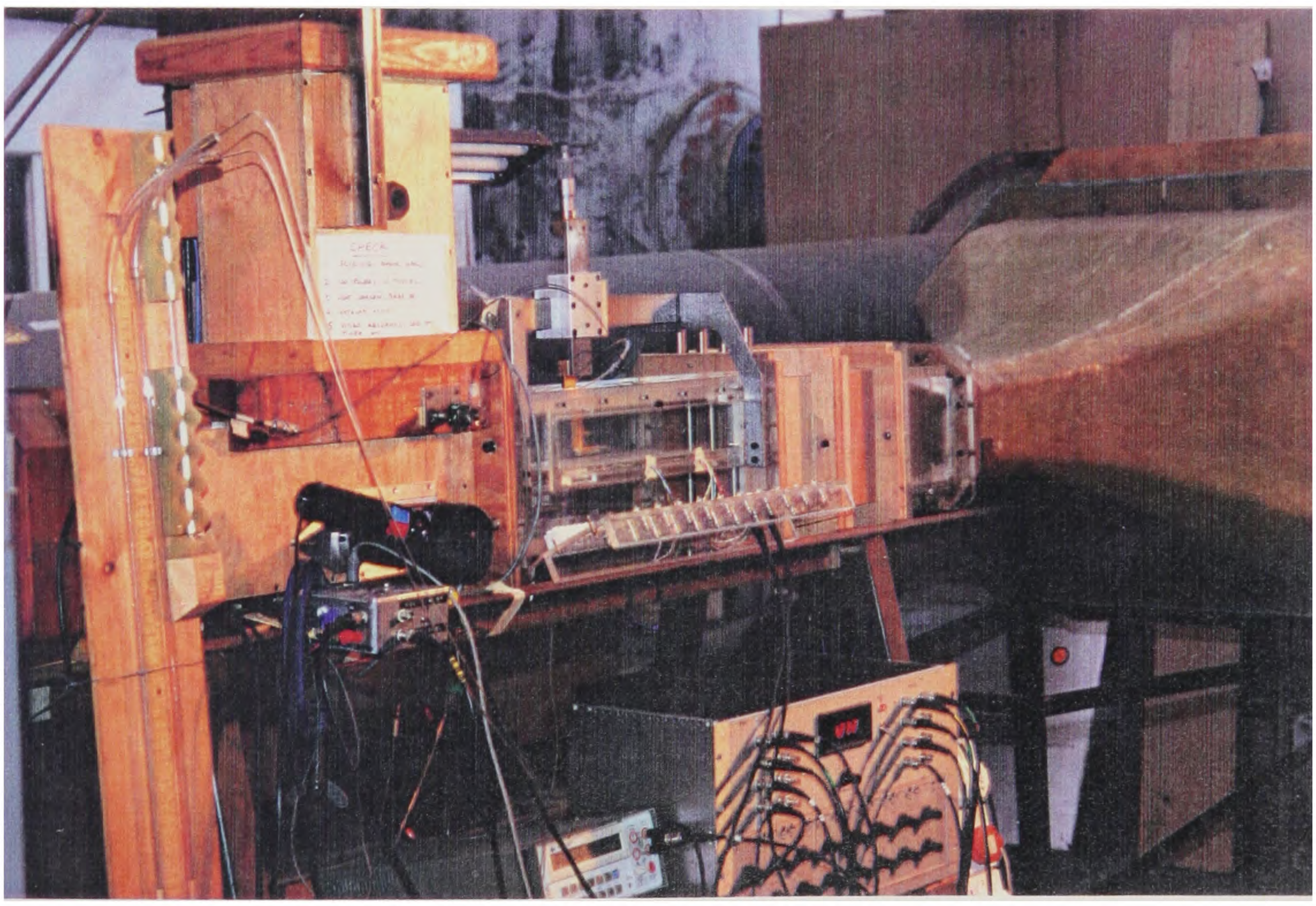

Figure 5.4. Photograph of working section used for the flat plate heat transfer experiment. This was used for both the liquid crystal tests (perspex plate) and the thin film gauge tests (Macor plate).

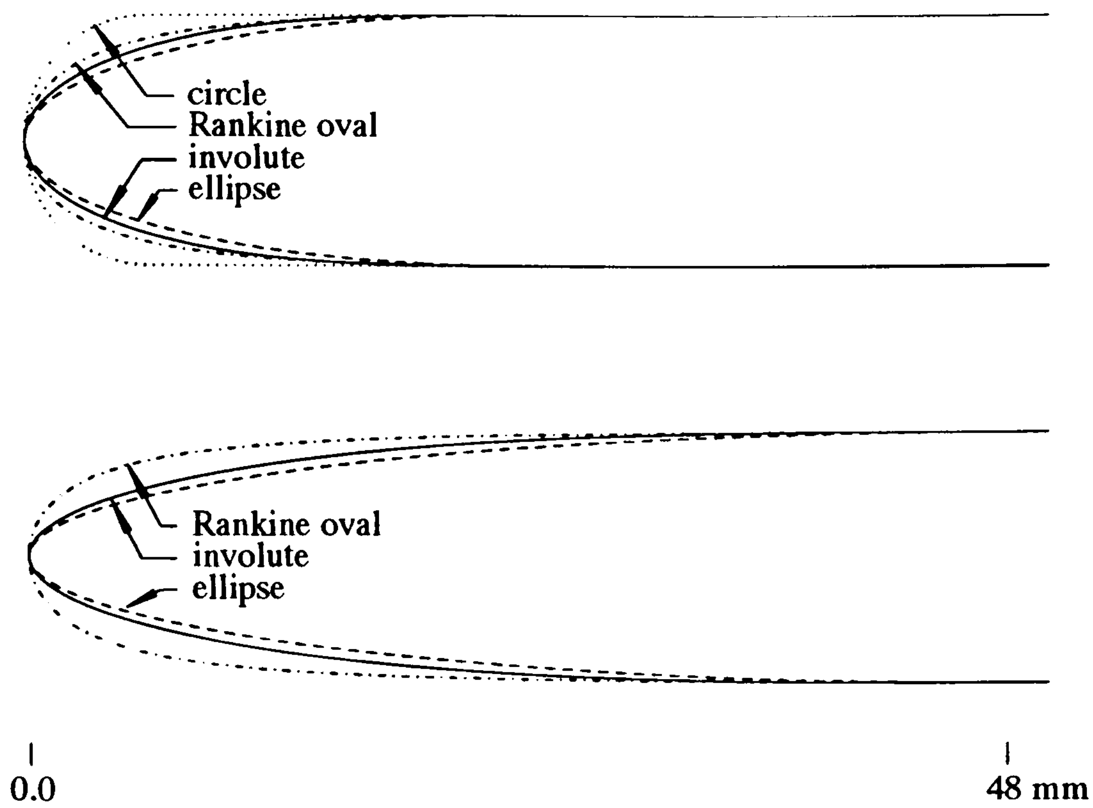

Figure 5.5. Flat plate leading edge profiles tested for sensitivity to separation at incidence: top, length:half thickness = 4:1; bottom, 8:1. The 8:1 involute was chosen.

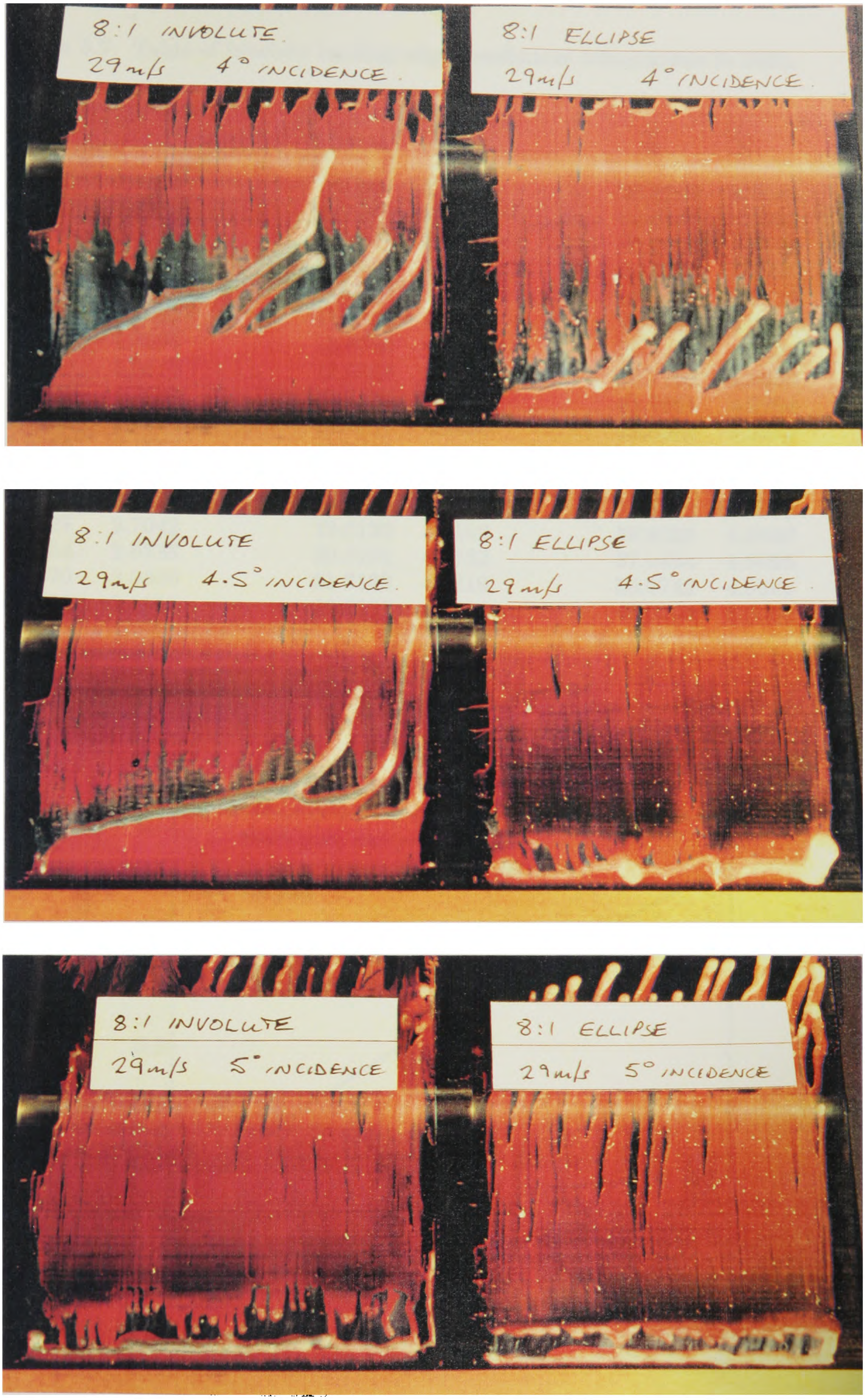

Figure 5.6. Flow visualisation of proposed flat plate leading edge profiles using shear sensitive liquid crystals.

Figure 5.7. Table of involute leading edge coordinates (dimensions in mm).

X	Y	X	Y	X	Y
0.0000	0.0000	7.7000	3.3390	23.6299	4.8044
0.0320	0.2280	8.5080	3.4796	24.6440	4.8387
0.1270	0.4552	9.3407	3.6128	25.6608	4.8688
0.2834	0.6806	10.1961	3.7387	26.6798	4.8949
0.4994	0.9036	11.0722	3.8573	27.7007	4.9173
0.7729	1.1235	11.9672	3.9688	28.7229	4.9362
1.1019	1.3396	12.8793	4.0732	29.7462	4.9520
1.4840	1.5513	13.8068	4.1706	30.7703	4.9650
1.9171	1.7581	14.7481	4.2613	31.7951	4.9754
2.3985	1.9596	15.7017	4.3453	32.8202	4.9835
2.9260	2.1552	16.6663	4.4229	33.8456	4.9895
3.4970	2.3447	17.6406	4.4943	34.8712	4.9939
4.1090	2.5278	18.6233	4.5596	35.8969	4.9968
4.7597	2.7042	19.6135	4.6192	36.9226	4.9986
5.4464	2.8736	20.6101	4.6732	37.9484	4.9995
6.1670	3.0360	21.6123	4.7219	38.9742	4.9999
6.9190	3.1911	22.6191	4.7656	40.0000	5.0000

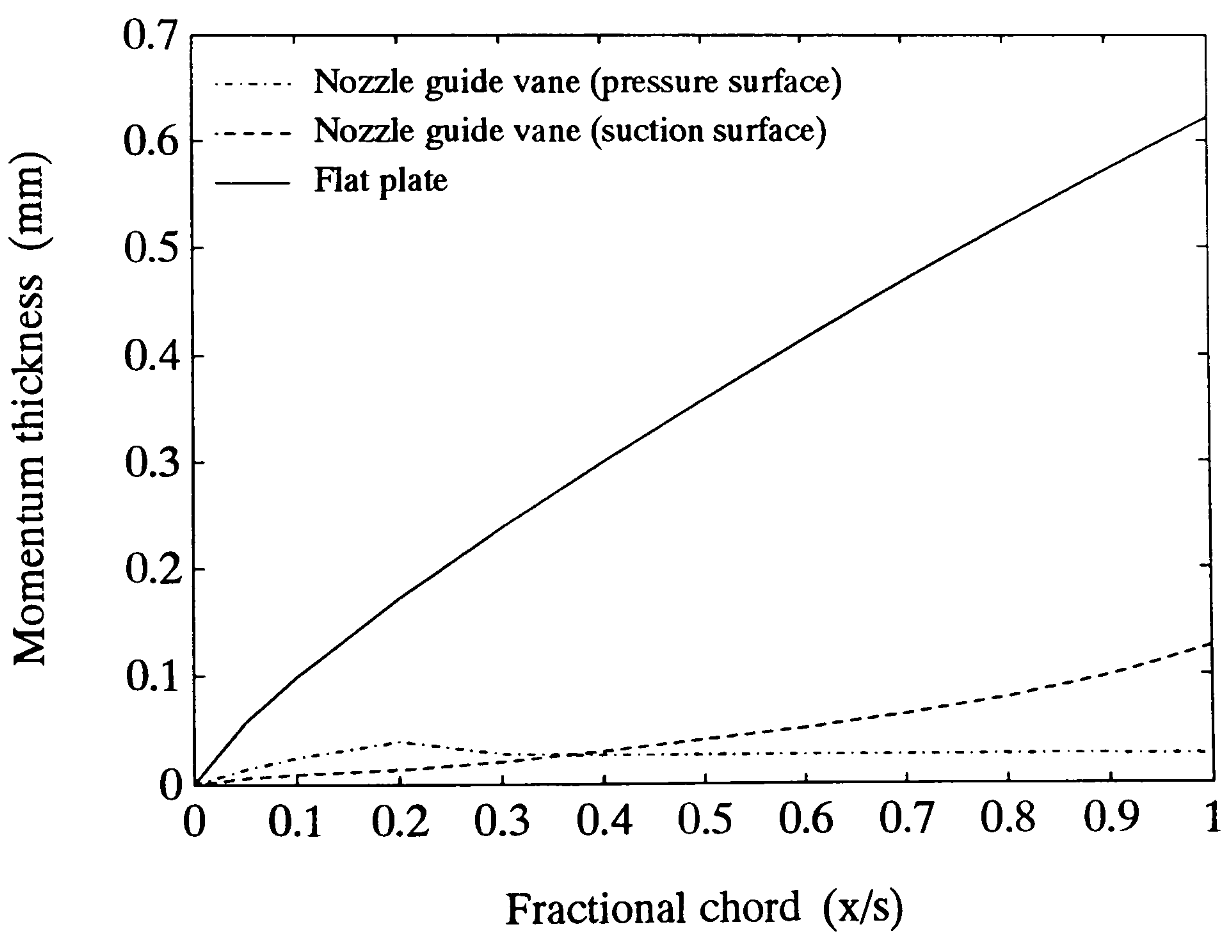

Figure 5.8. Comparison of predicted flat plate and typical nozzle guide vane boundary layer momentum thicknesses.

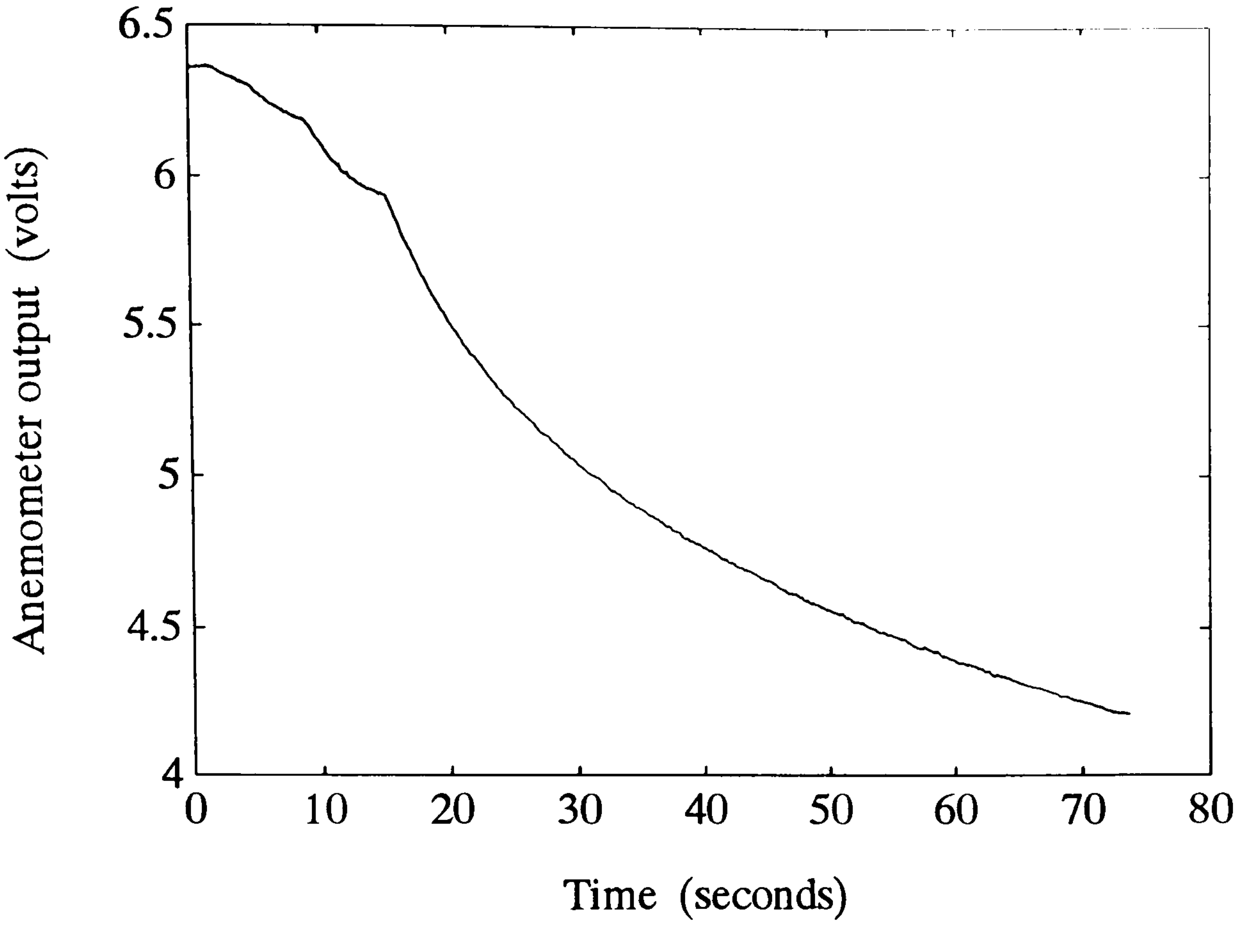

Figure 6.1. Hot wire calibration: typical wire voltage record.

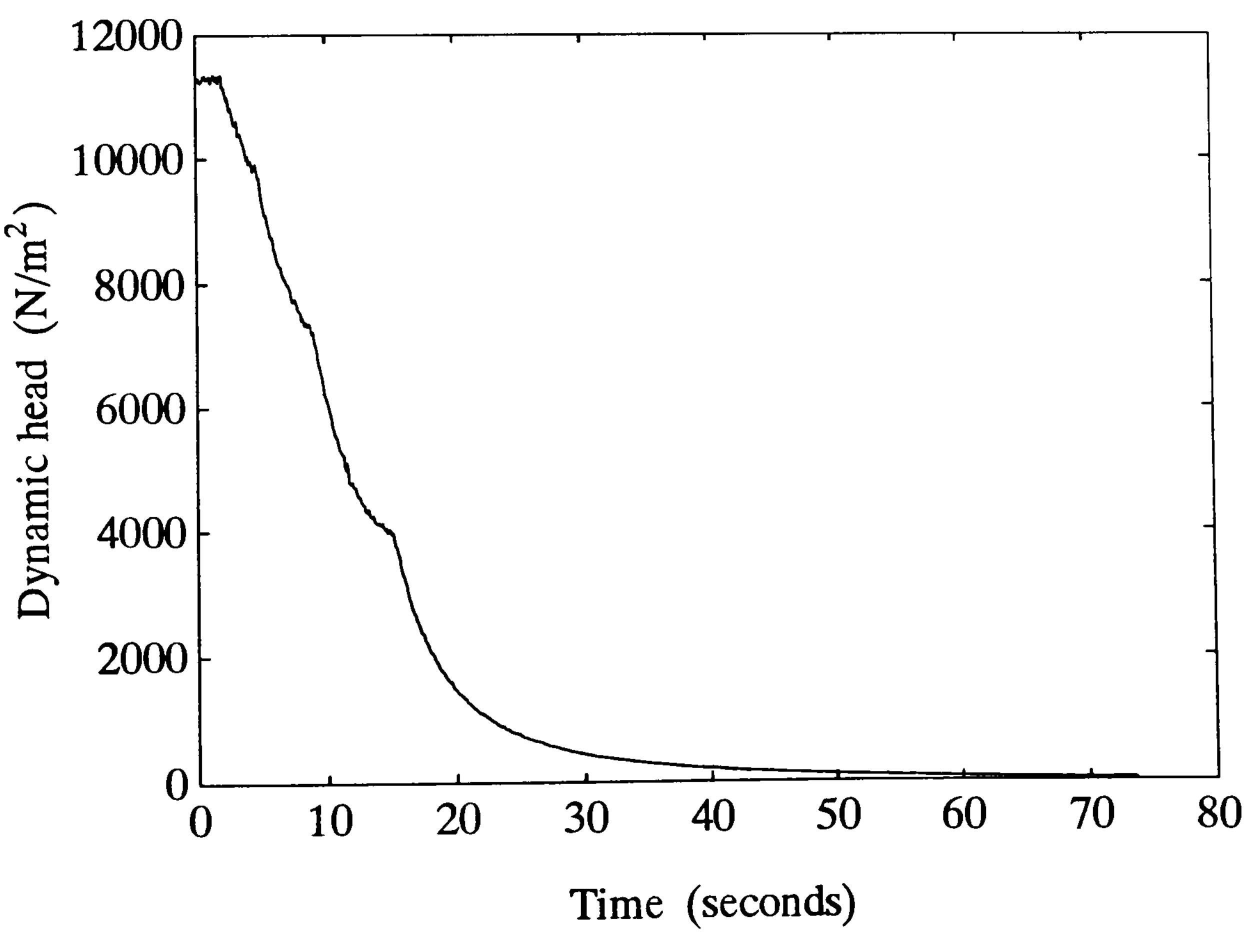

Figure 6.2. Hot wire calibration: typical dynamic head.

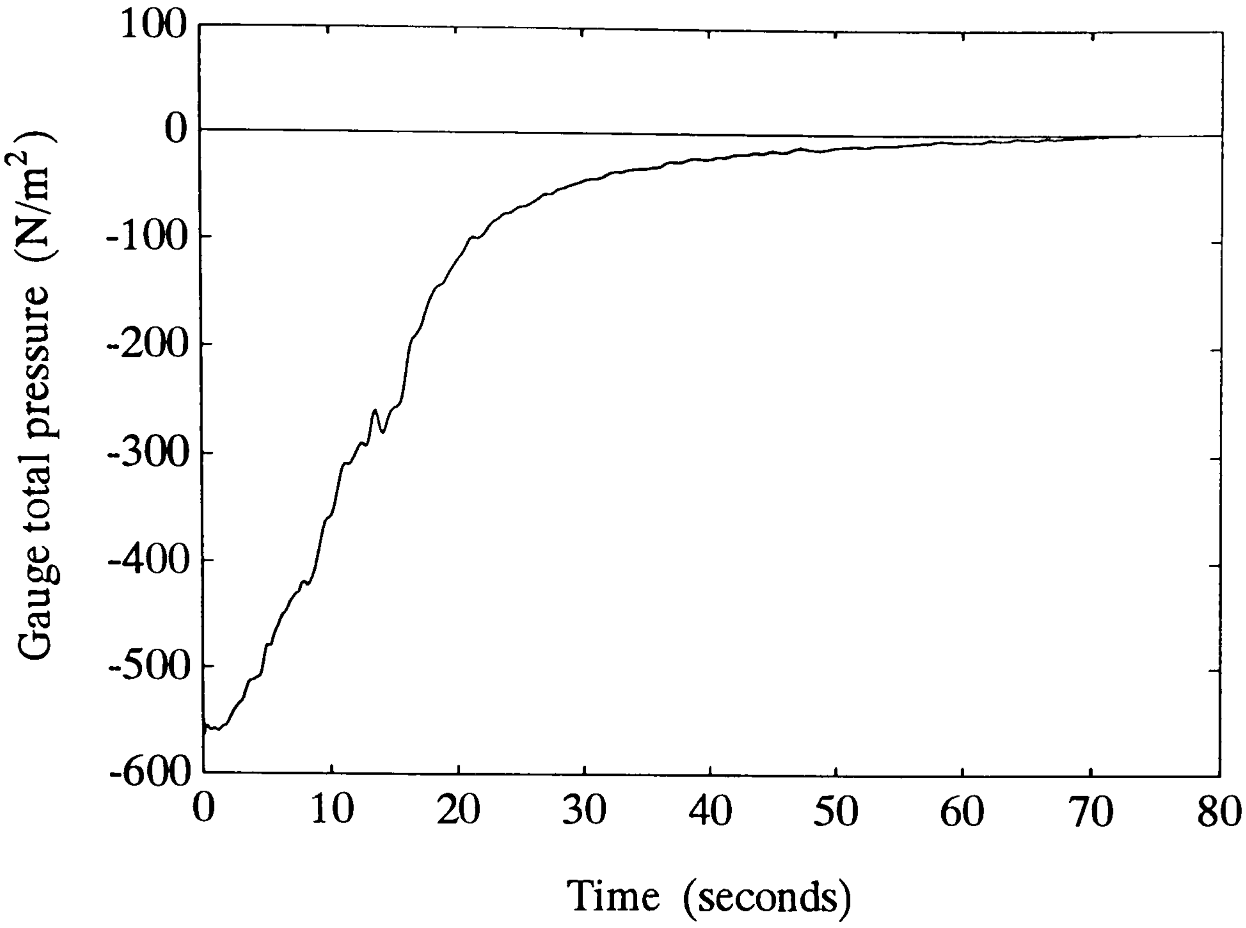

Figure 6.3. Hot wire calibration: typical total pressure deficit. (Pressure drop across gauze over bellmouth inlet).

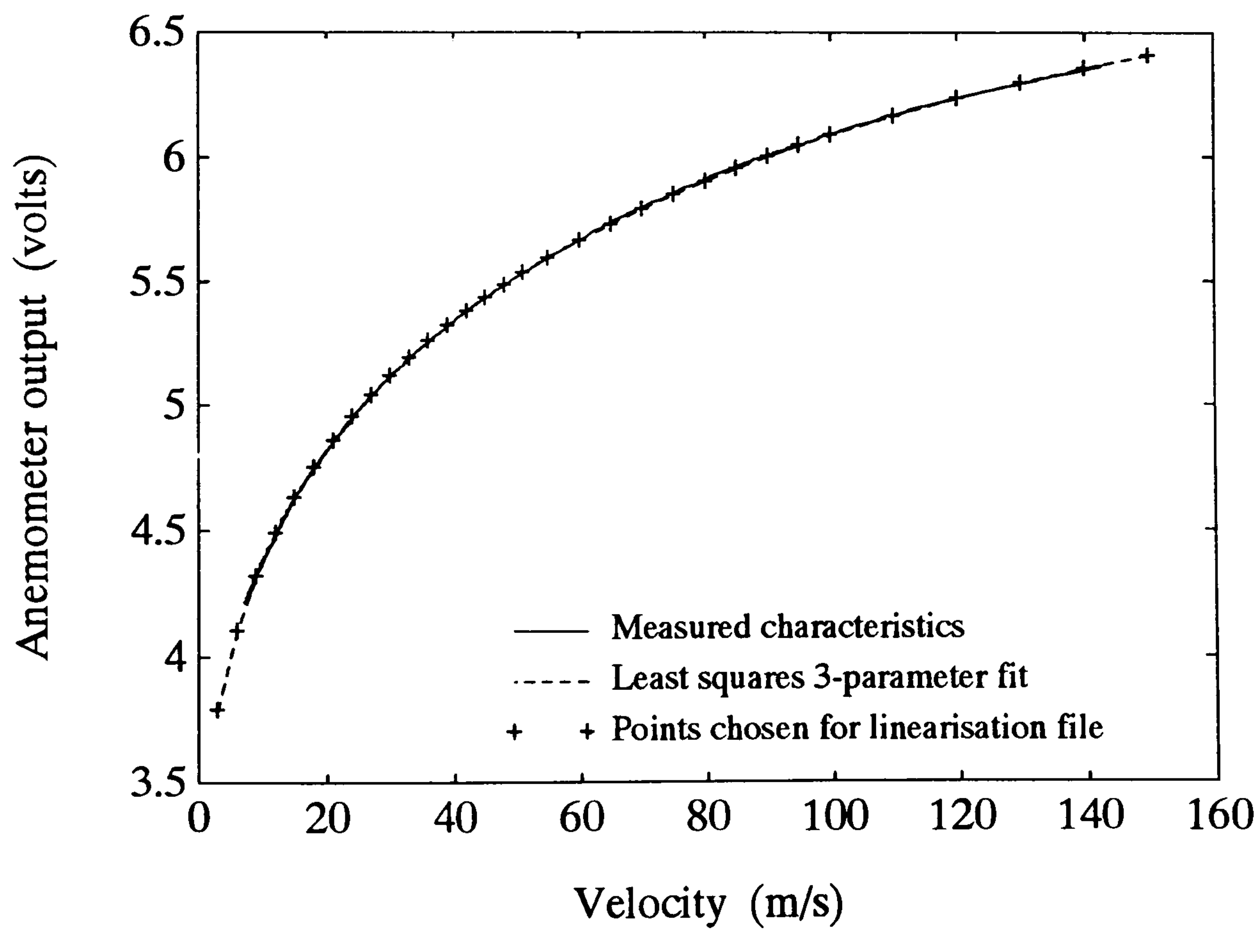

Figure 6.4. Hot wire calibration: curve fit to calibration data.

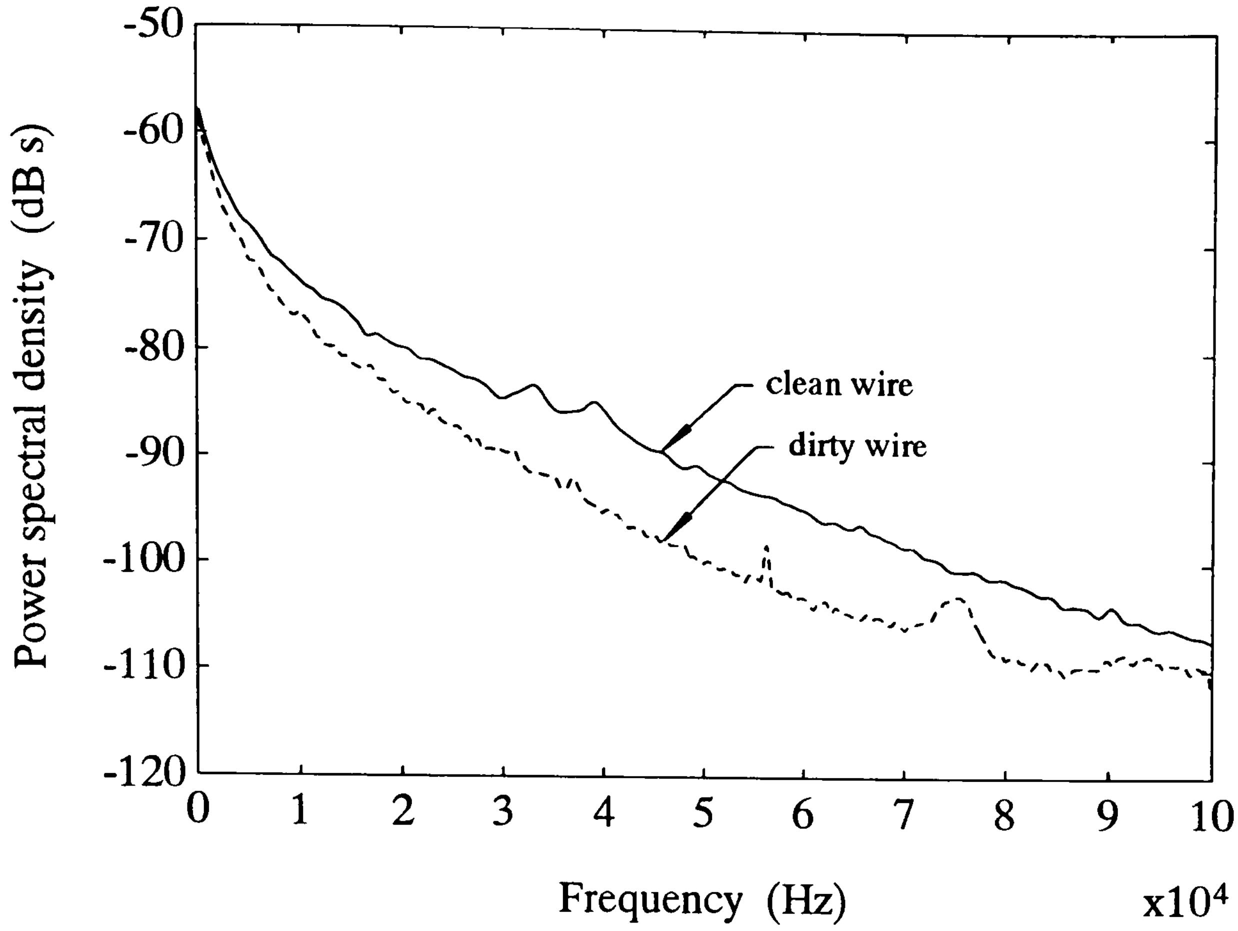

Figure 6.5. Effect of dirt on hot wire frequency response.

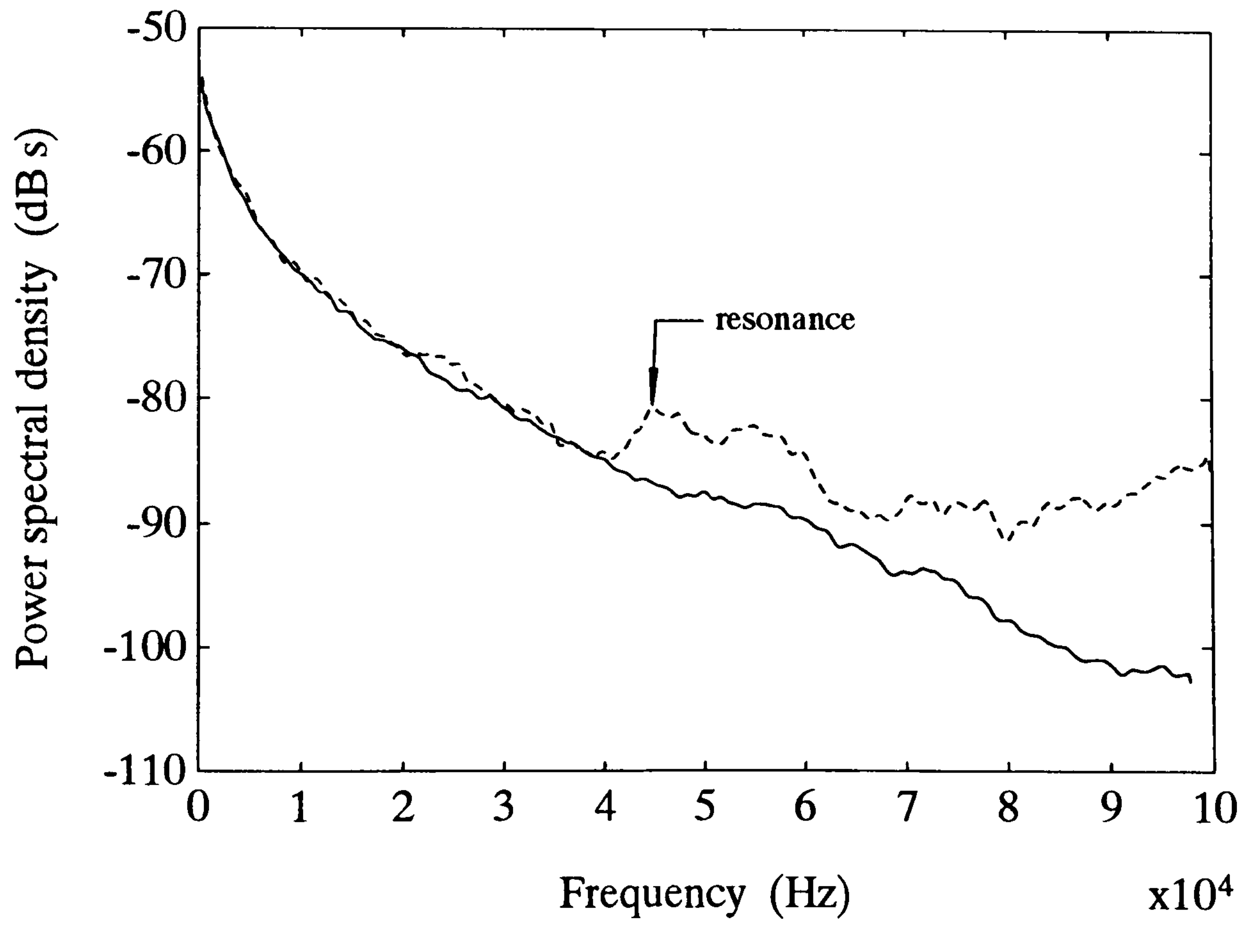

Figure 6.6. Effect of hot wire vibration on turbulence spectra. Solid line is typical of a "good" wire, but still shows some vibration between 50 kHz and 80 kHz.

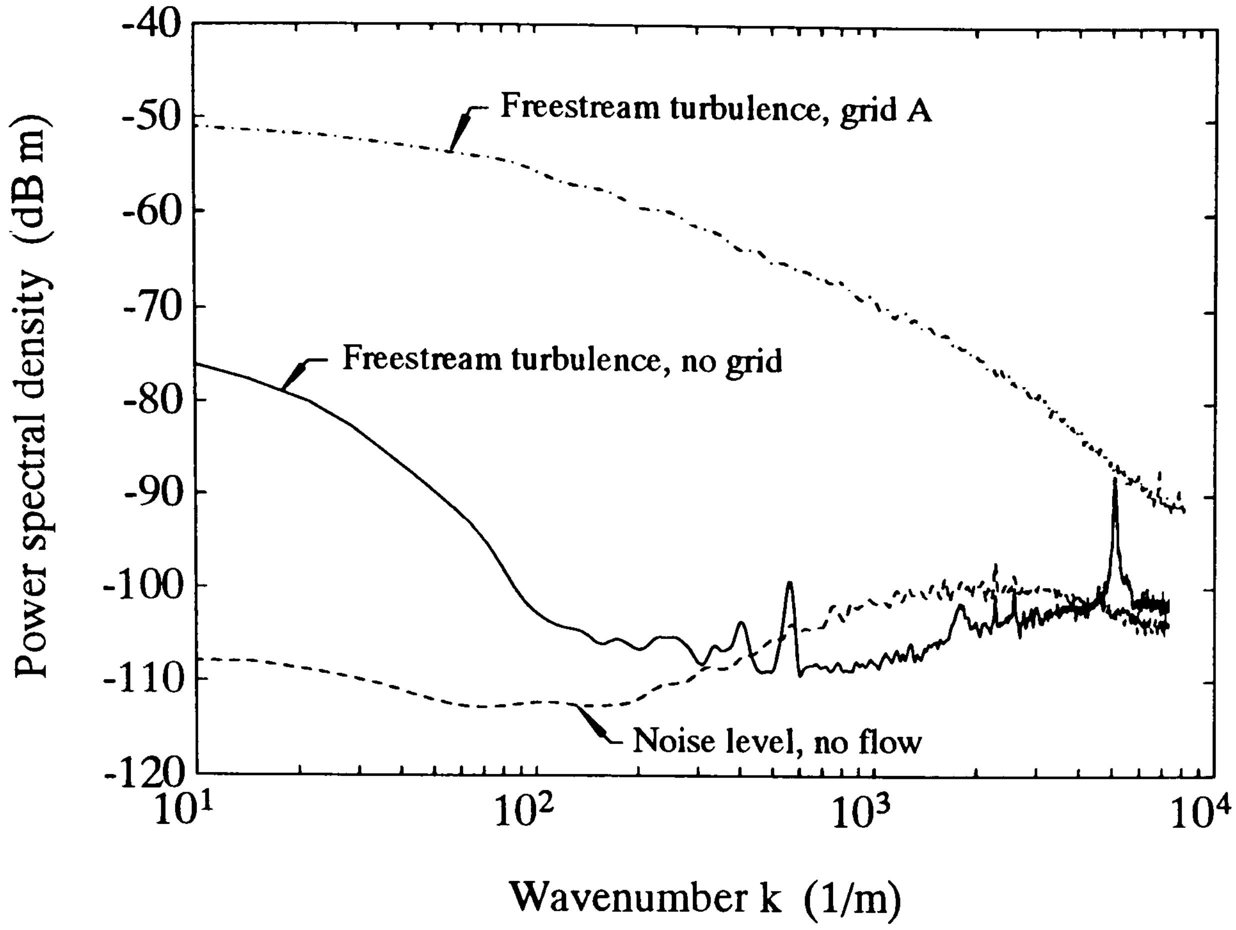

Figure 6.7. Grid-out turbulence spectrum and no flow noise spectrum compared with typical grid generated turbulence, showing excellent signal to noise ratio.

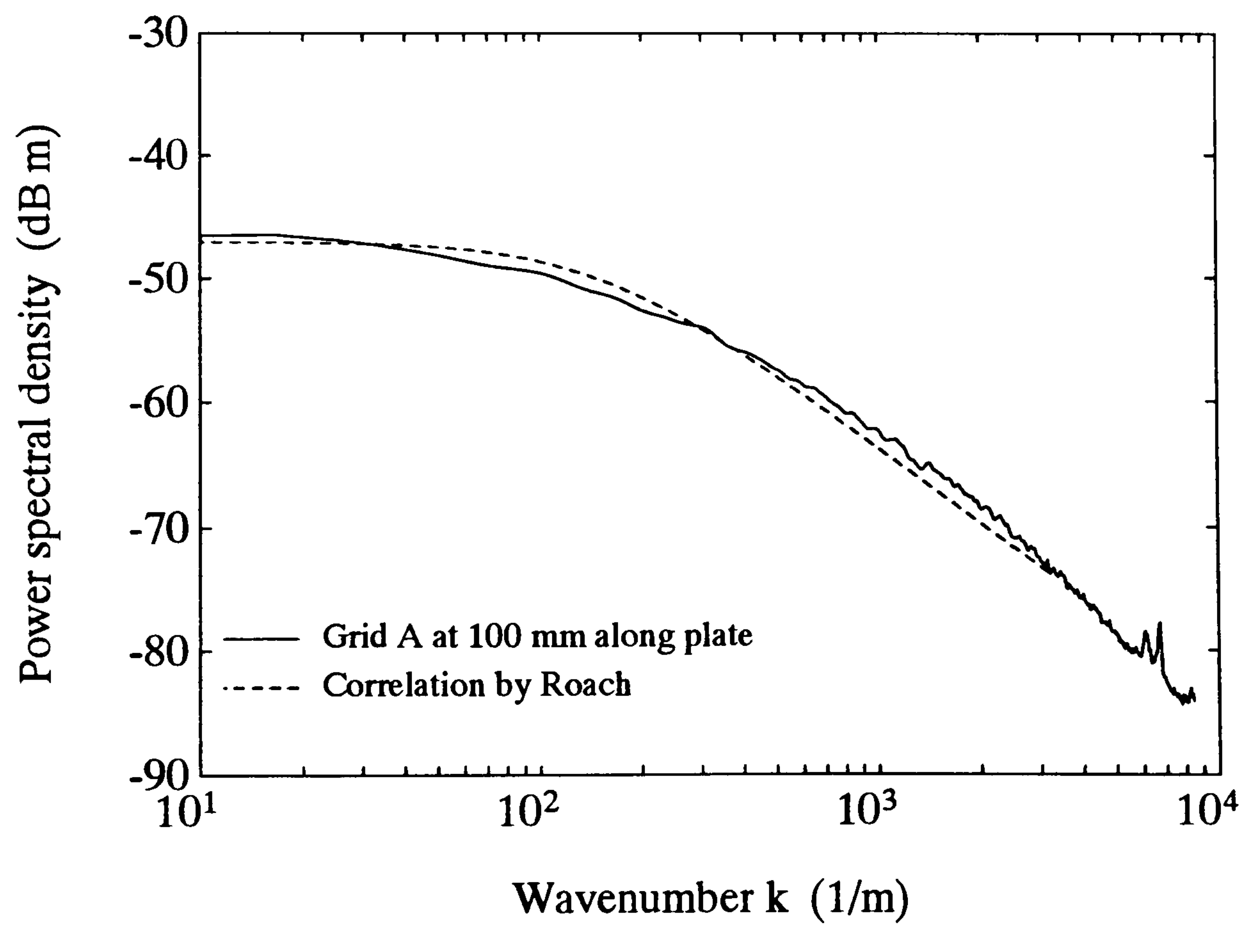

Figure 6.8. Comparison of measured grid turbulence spectrum with correlation by **Roach (1987)**.

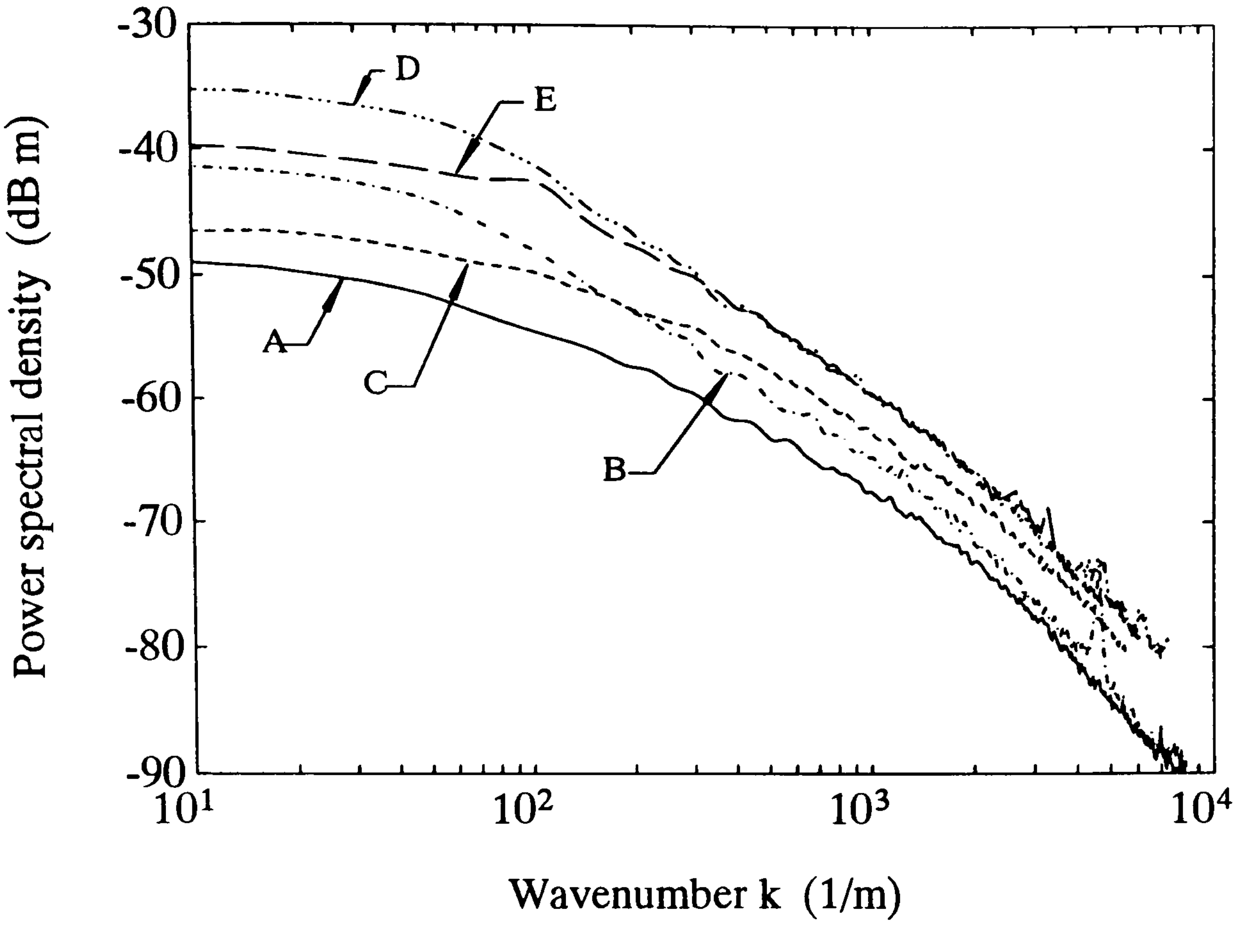

Figure 6.9. Grid turbulence spectra for flat plate testing, x = 100 mm, grids A to E.

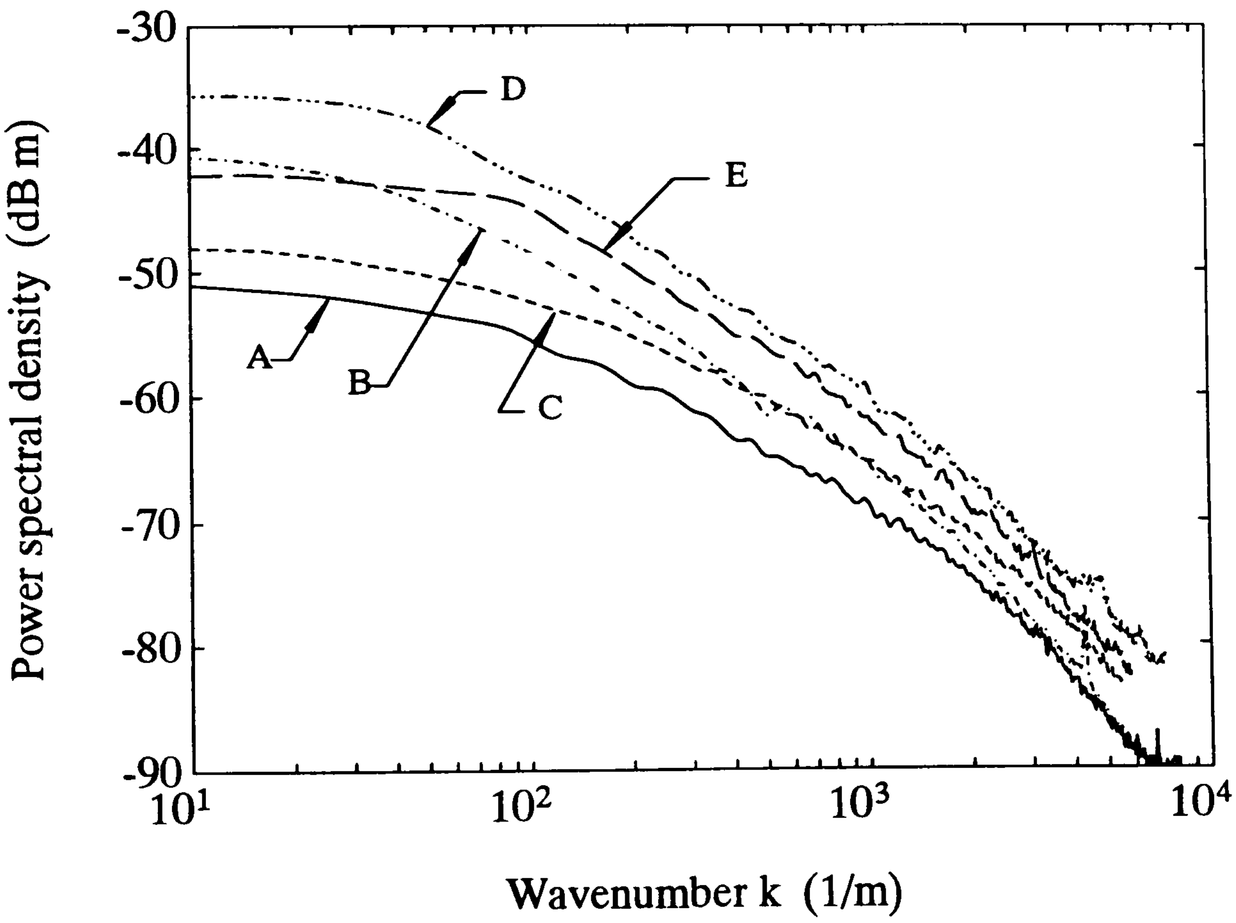

Figure 6.10. Grid turbulence spectra for flat plate testing, x = 180 mm.

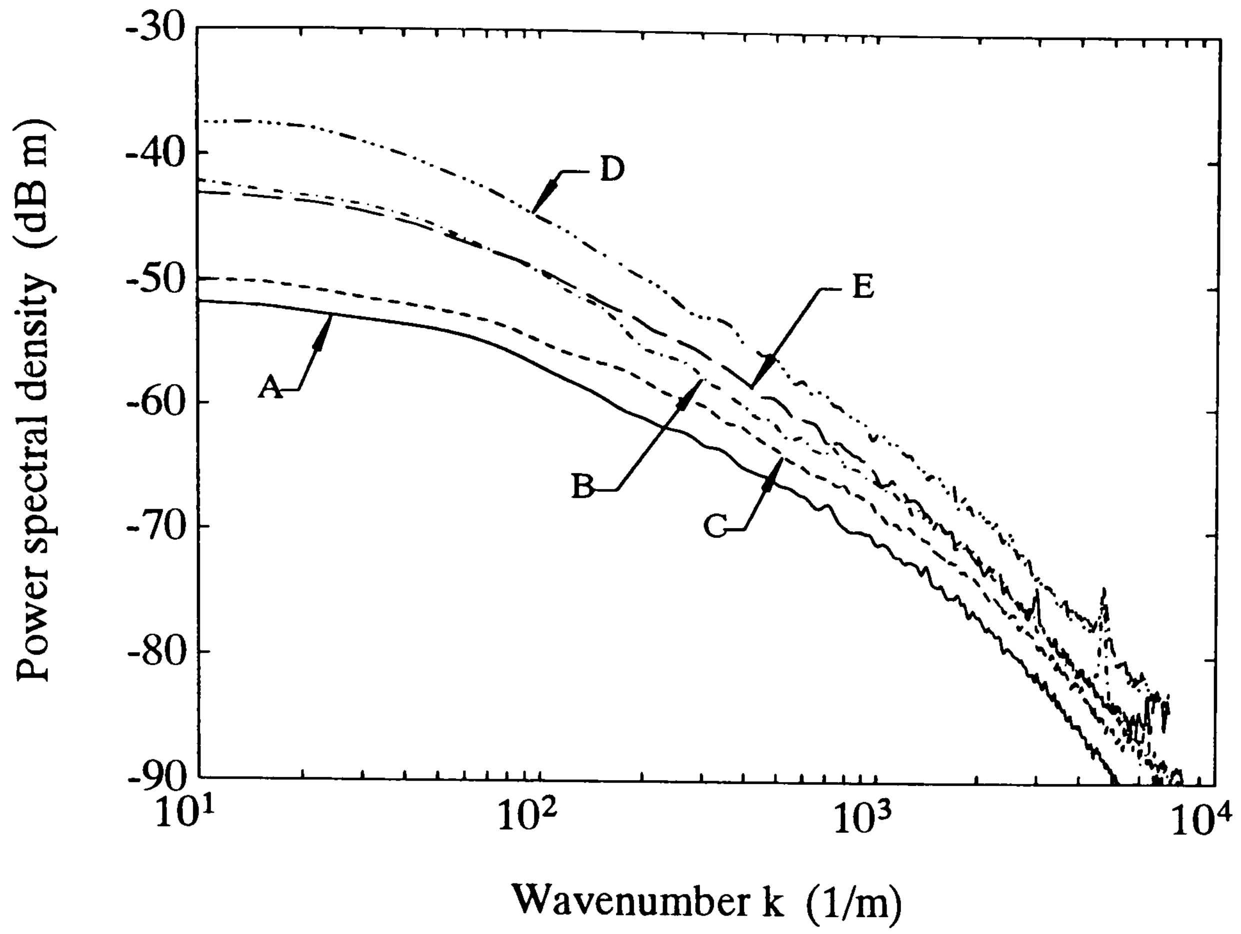

Figure 6.11. Grid turbulence spectra for flat plate testing, x = 300 mm.

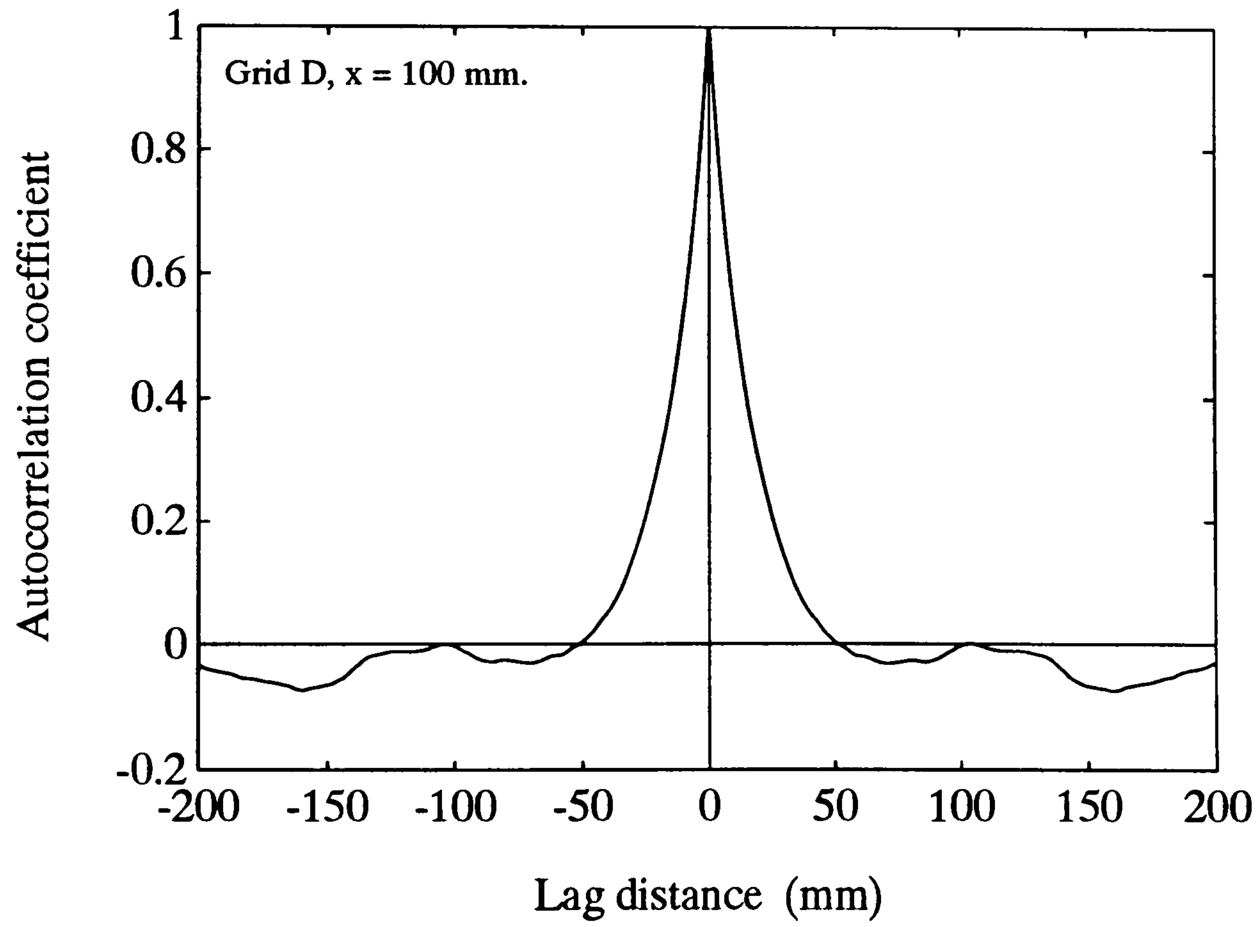

Figure 6.12. Typical autocorrelation of freestream $u'(t)$ plotted against lag distance $U\tau$. Integral length scale Λ_x = 14.6 mm.

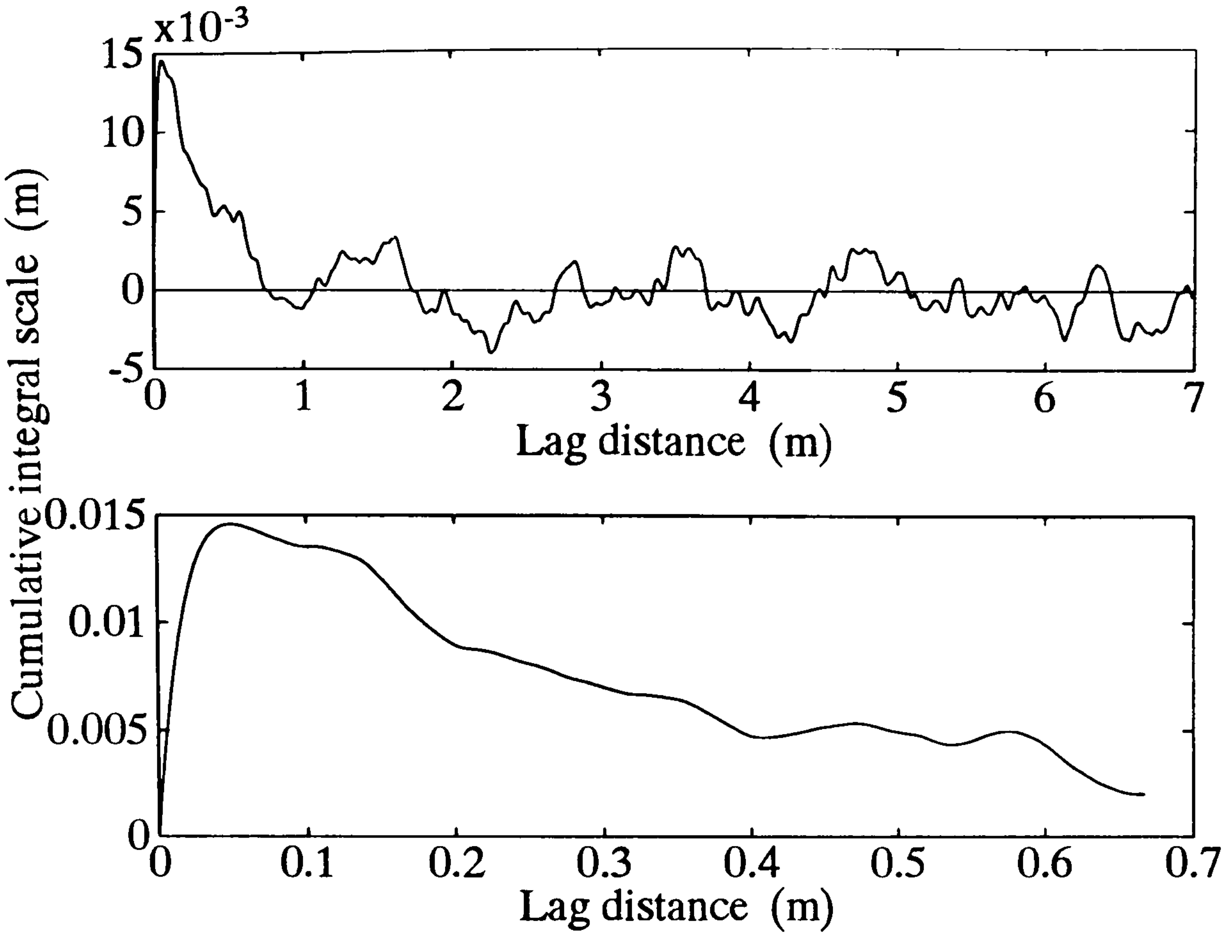

Figure 6.13. Cumulative integral scale showing approach to zero. (Grid D, x = 100 mm).

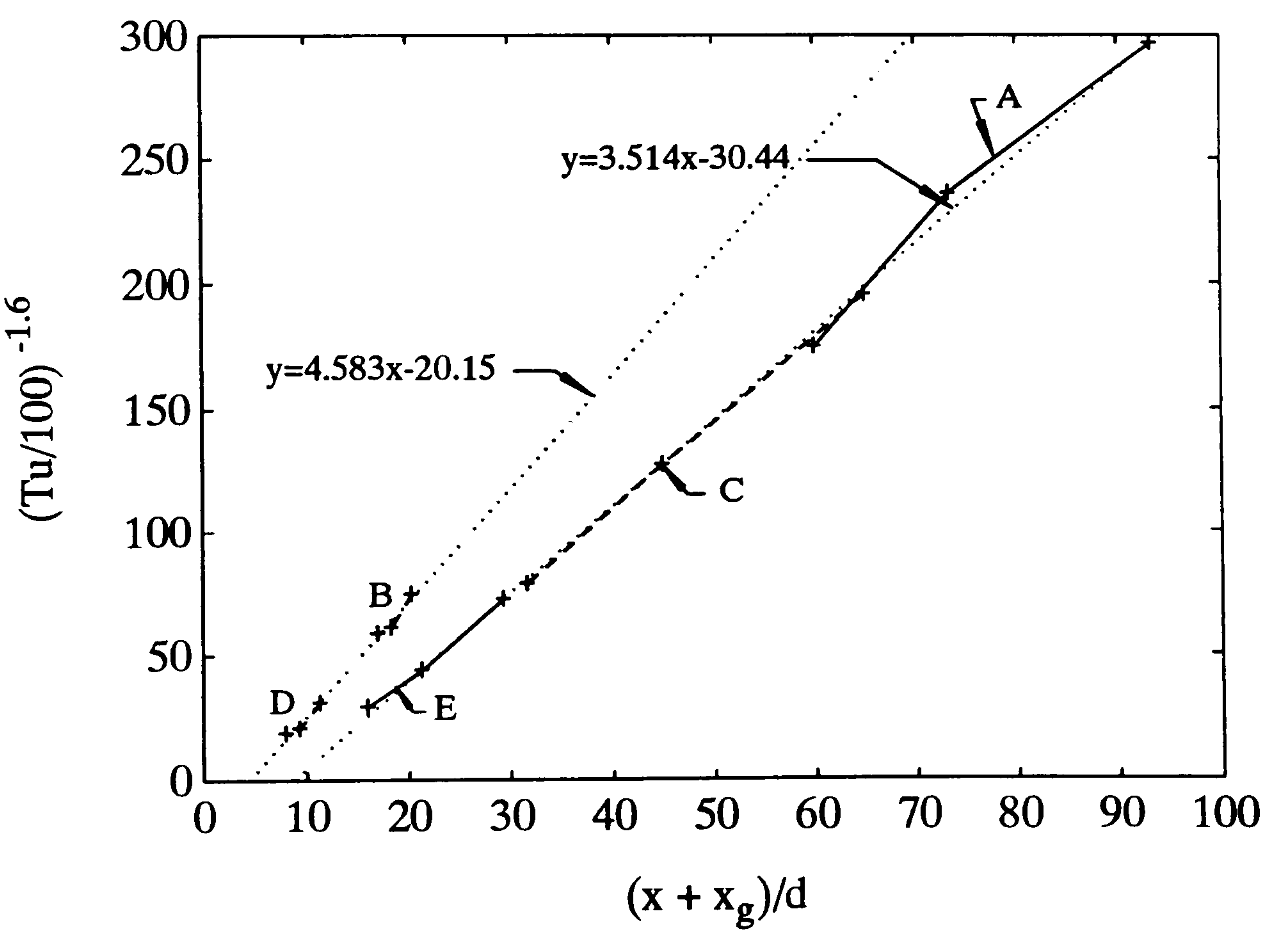

Figure 6.14. Turbulence decay rate from single (B, D) and multiple (A, C, E) bar grids, for calculating L_e^u.

Figure 6.15.
Table of grid dimensions, turbulence intensities and length scales.

GRID:	A	B	C	D	E
Bar diameter (mm)	6	60	6	60	15
Bar pitch (mm)	15	single	15	single	37.5
Distance to LE x_g (mm)	260	920	90	380	140
Tu (%) at x = 100 mm	4	7.8	6.5	16	12.1
180 mm	3.3	7.6	4.8	15	9.4
300 mm	2.9	6.7	3.7	11.7	6.9
Λ_x (mm) at x = 100 mm	9.4	14.7	6.5	14.6	8.5
180 mm	9.0	17.5	8.4	15.3	9.7
300 mm	10.0	17.3	8.7	16.6	12.1
L_e^u (mm) at x = 100 mm	9.5	48.3	7.0	31.4	12.1
180 mm	10.6	49.0	8.4	32.7	14.1
300 mm	11.5	52.8	9.9	38.0	17.0

The L_e^u and Λ_x values are similar for grids A, C and E, but vastly different for the single bar grids B and D.

Predicted boundary layer thicknesses:

Position x (mm)	Re_x	δ_{995} (mm)	θ (mm)
100	5.3×10^5	2.65	0.258
180	9.47×10^5	4.25	0.413
300	1.58×10^6	6.39	0.622

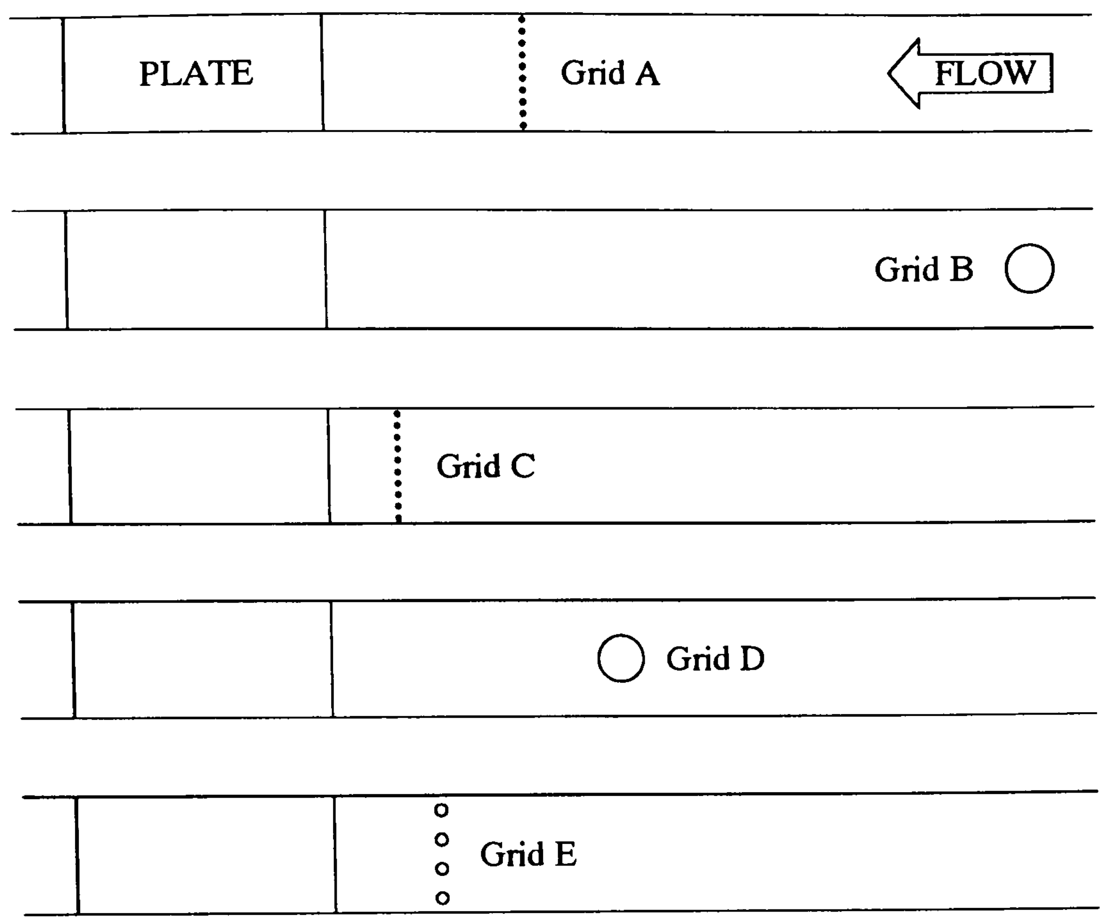

Figure 6.16. Grid configurations, drawn to scale. Working section width is 150 mm.

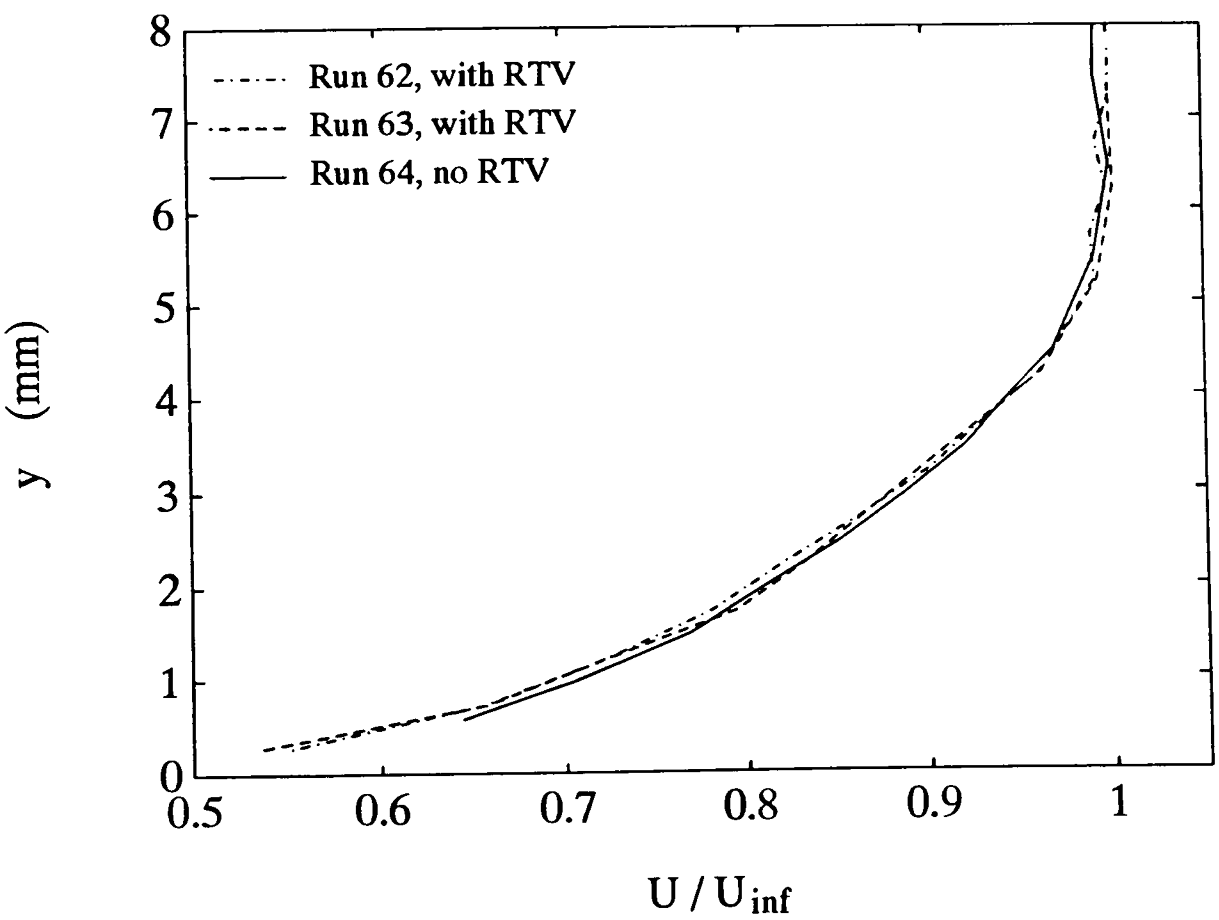

Figure 6.17. Repeatability of boundary layer velocity profile measurements.
(No grid, x = 300 mm, Re = 1.73×10^6, tripped).

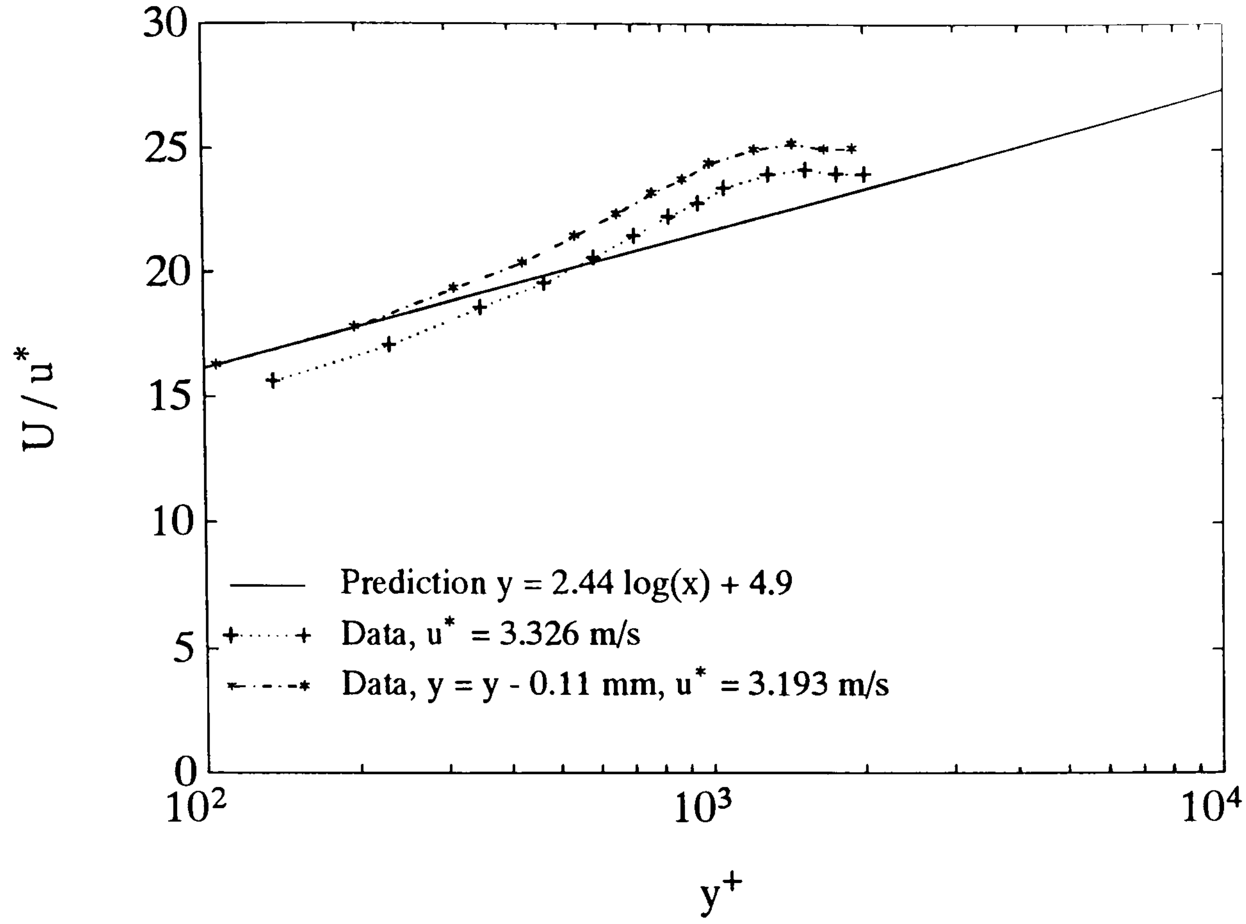

Figure 6.18. Comparison of boundary layer measurements against "log-law" prediction. (No grid, x = 300 mm, Re = 1.73 × 10^6).

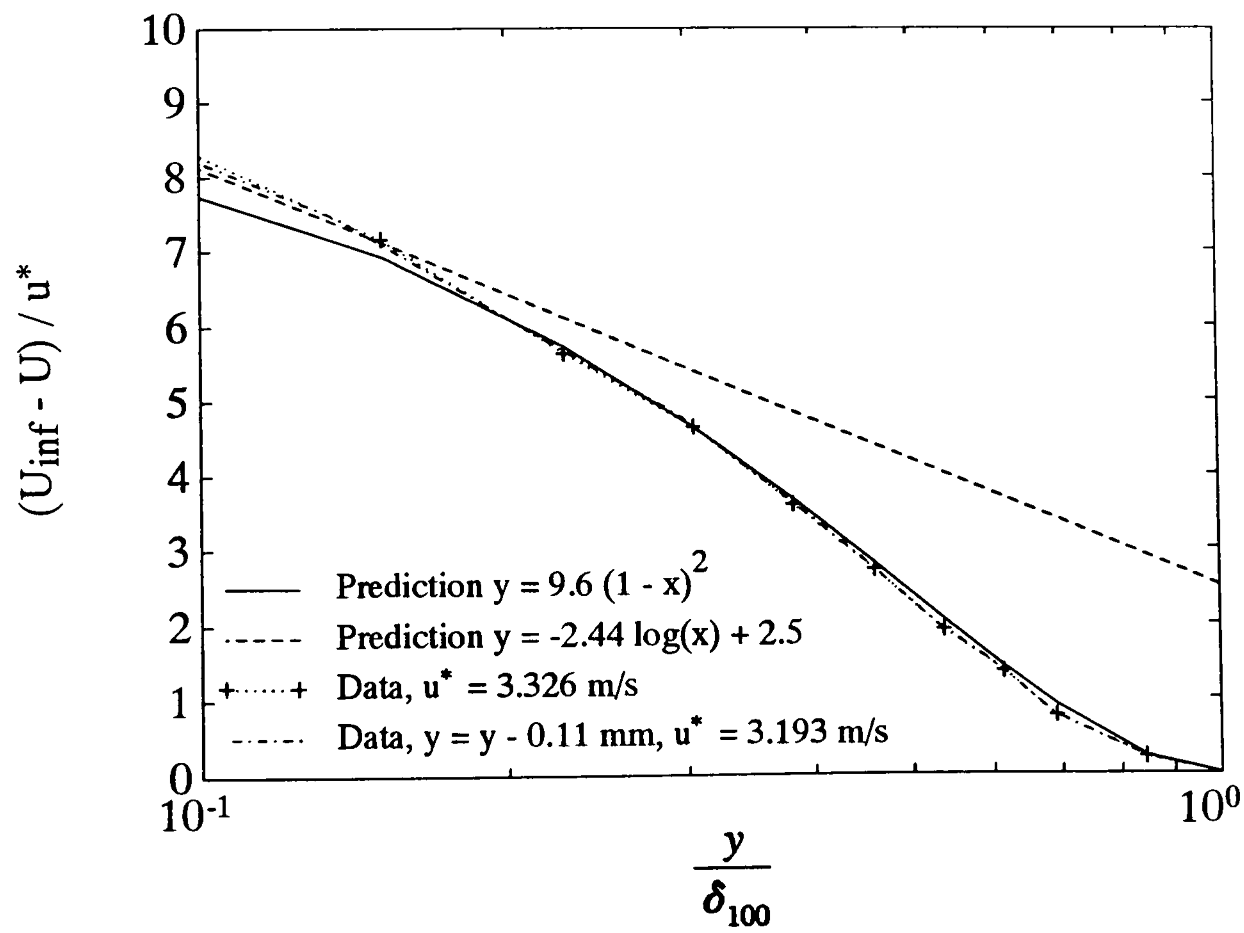

Figure 6.19. Comparison of boundary layer data with "velocity defect" correlation. (No grid, x = 300 mm, Re = 1.73 × 10^6).

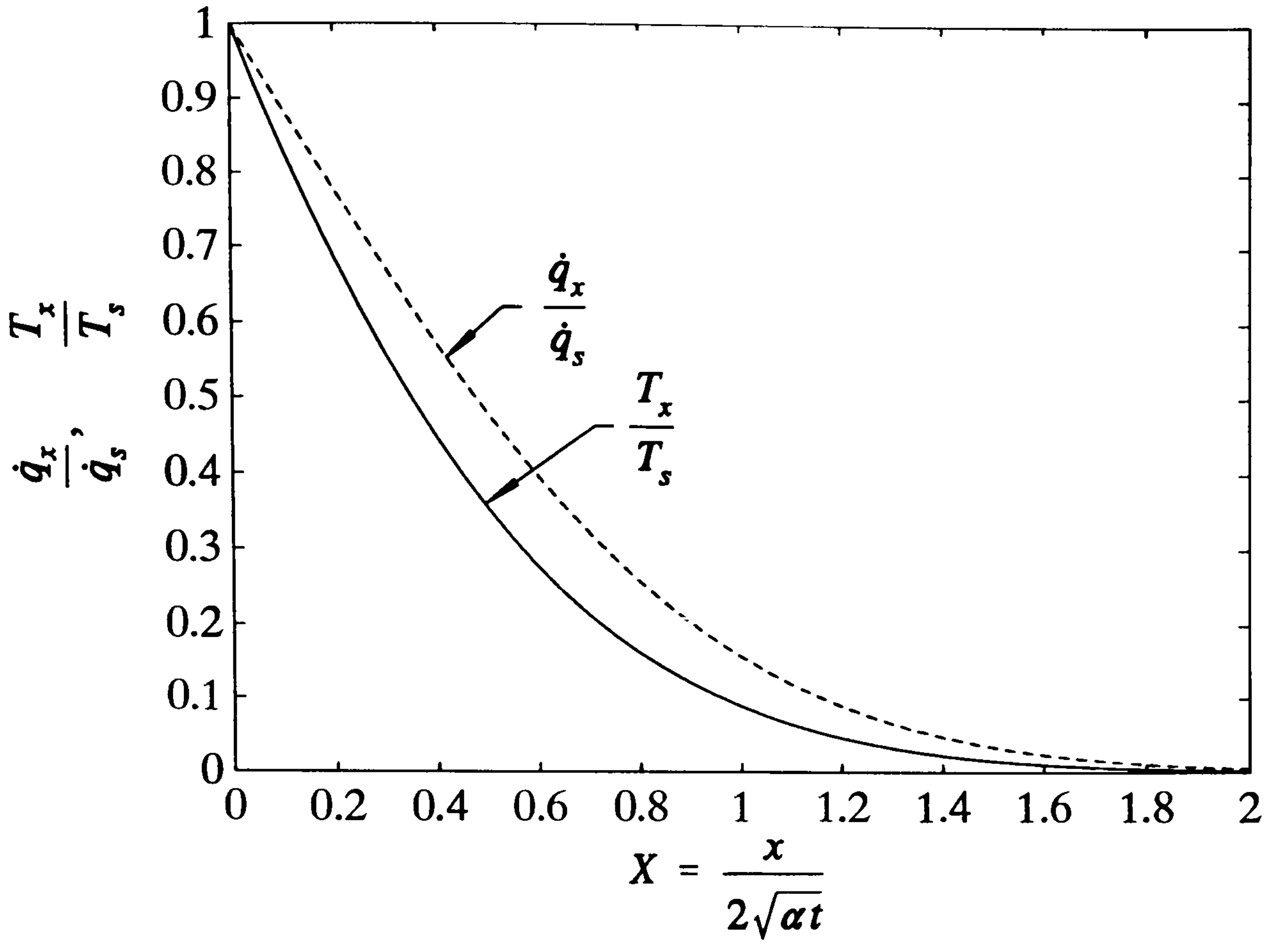

Figure 7.1. Shape of thermal pulse penetrating into semi-infinite solid (from **Schultz and Jones, 1973**).

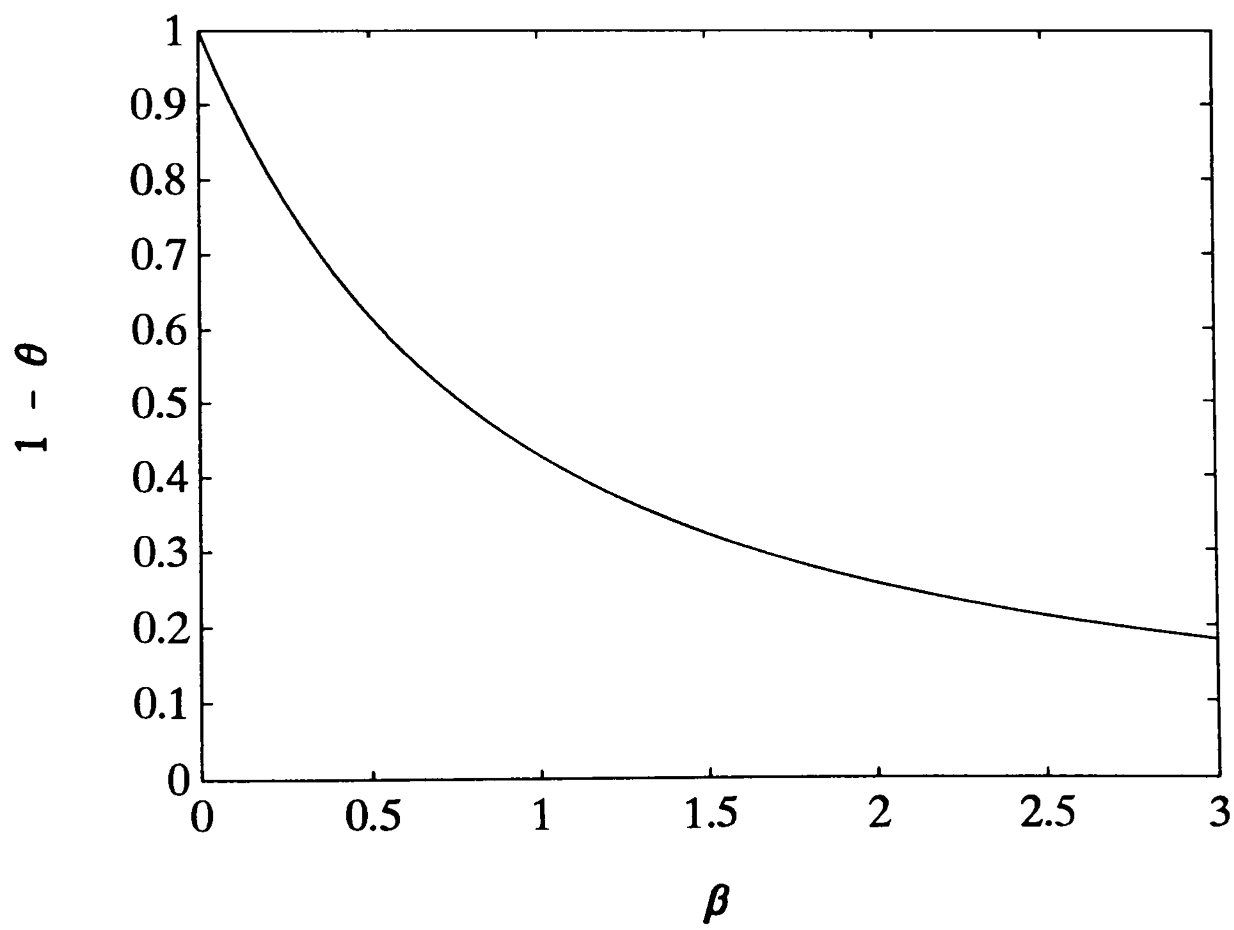

Figure 7.2. Rate of change of surface temperature resulting from a constant heat transfer coefficient.

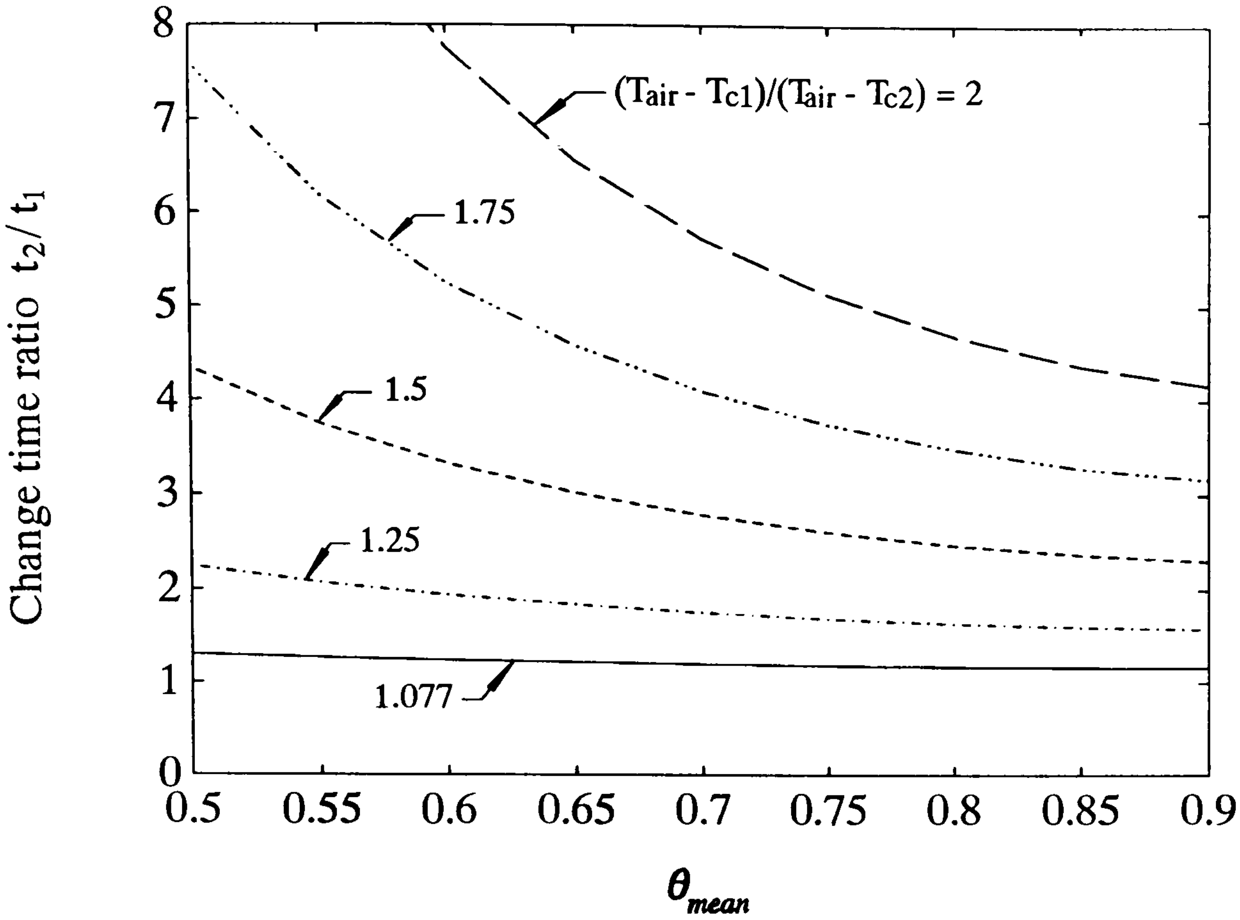

Figure 7.3. Sensitivity of double crystal technique to crystal change temperatures.

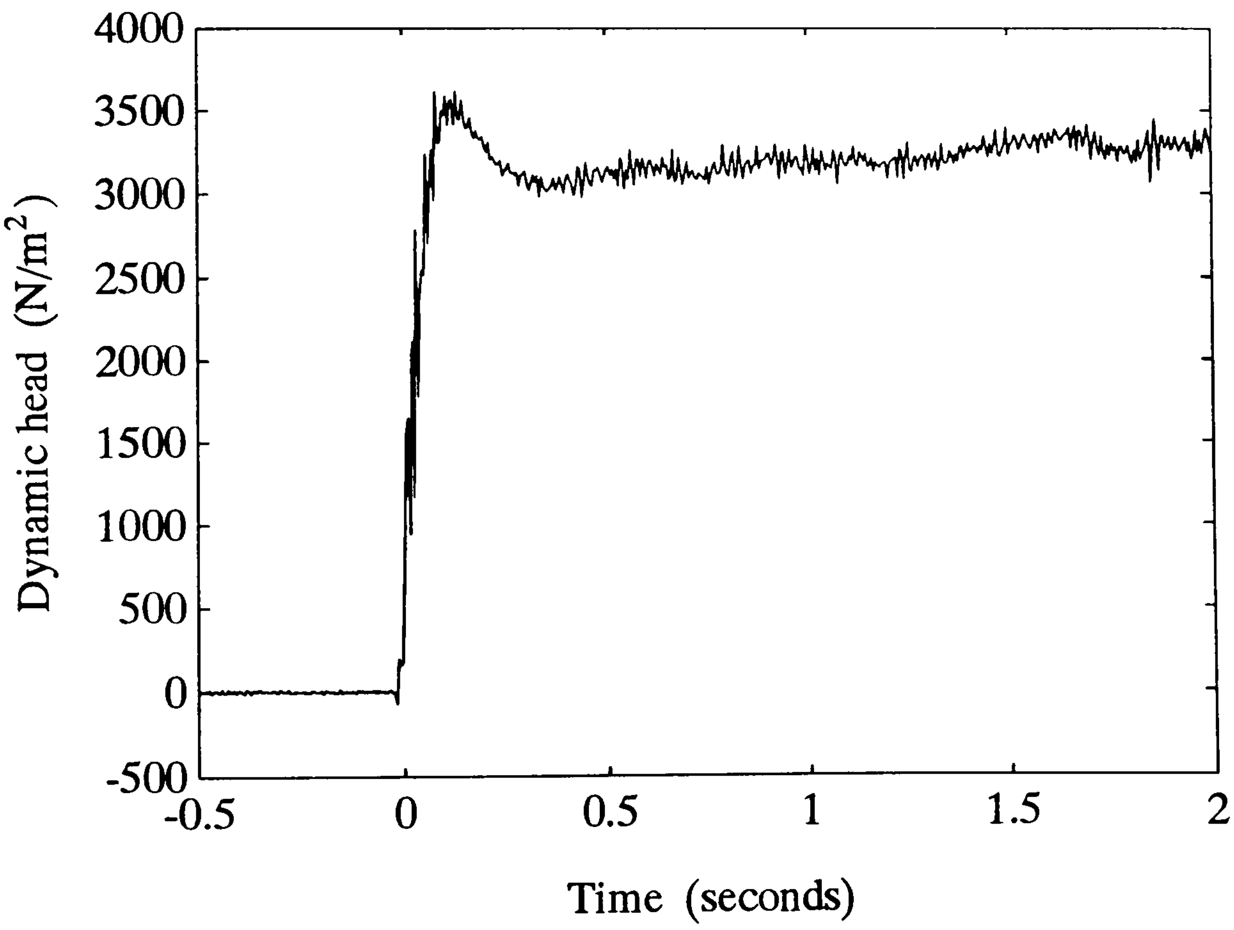

Figure 7.4. Typical dynamic head trace during start of tunnel flow. (No grid).

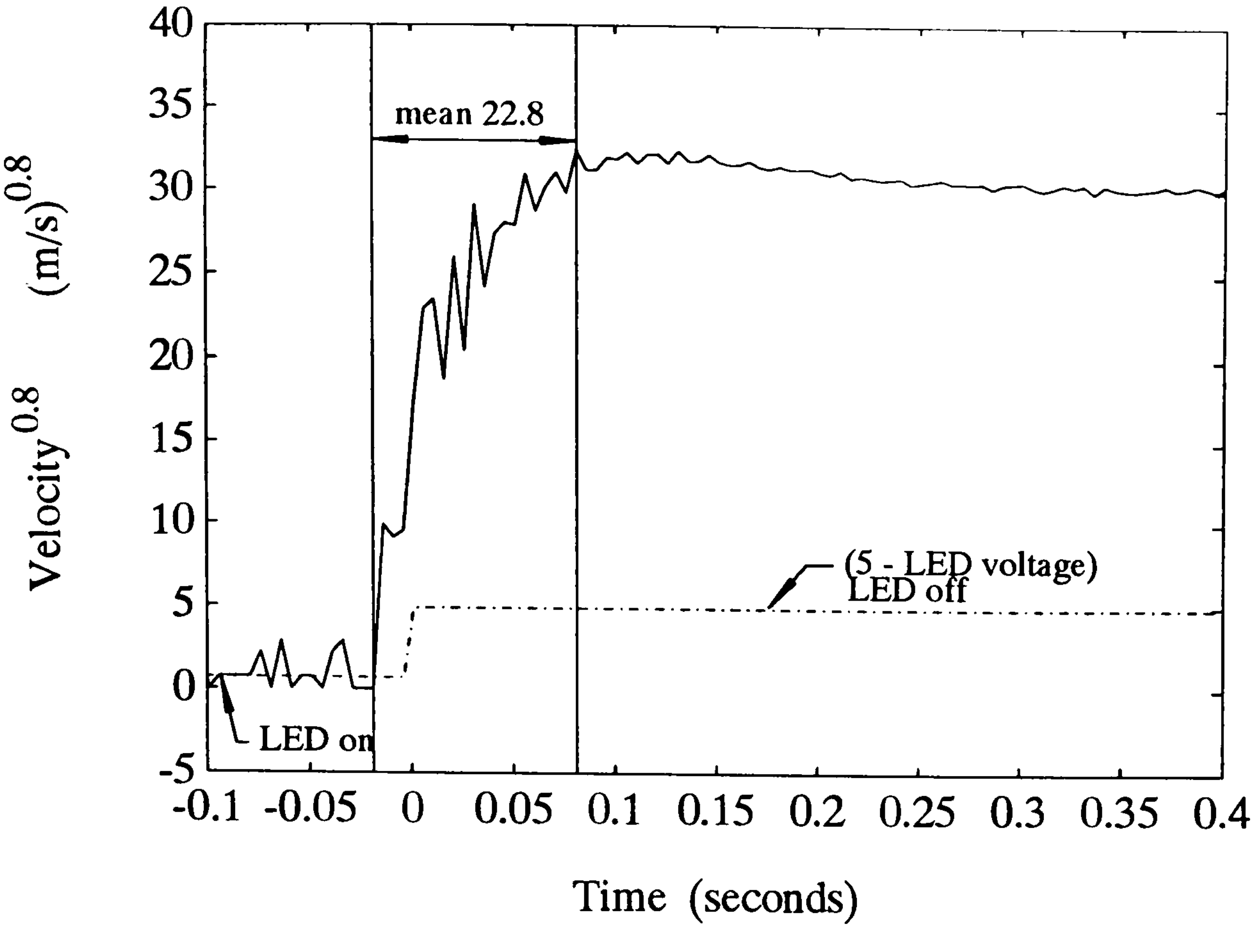

Figure 7.5. Derivation of "start delay" in terms of effect on mean heat transfer coefficients ($\propto v^{0.8}$). Effective start delay relative to LED signal is 8.5 ms.

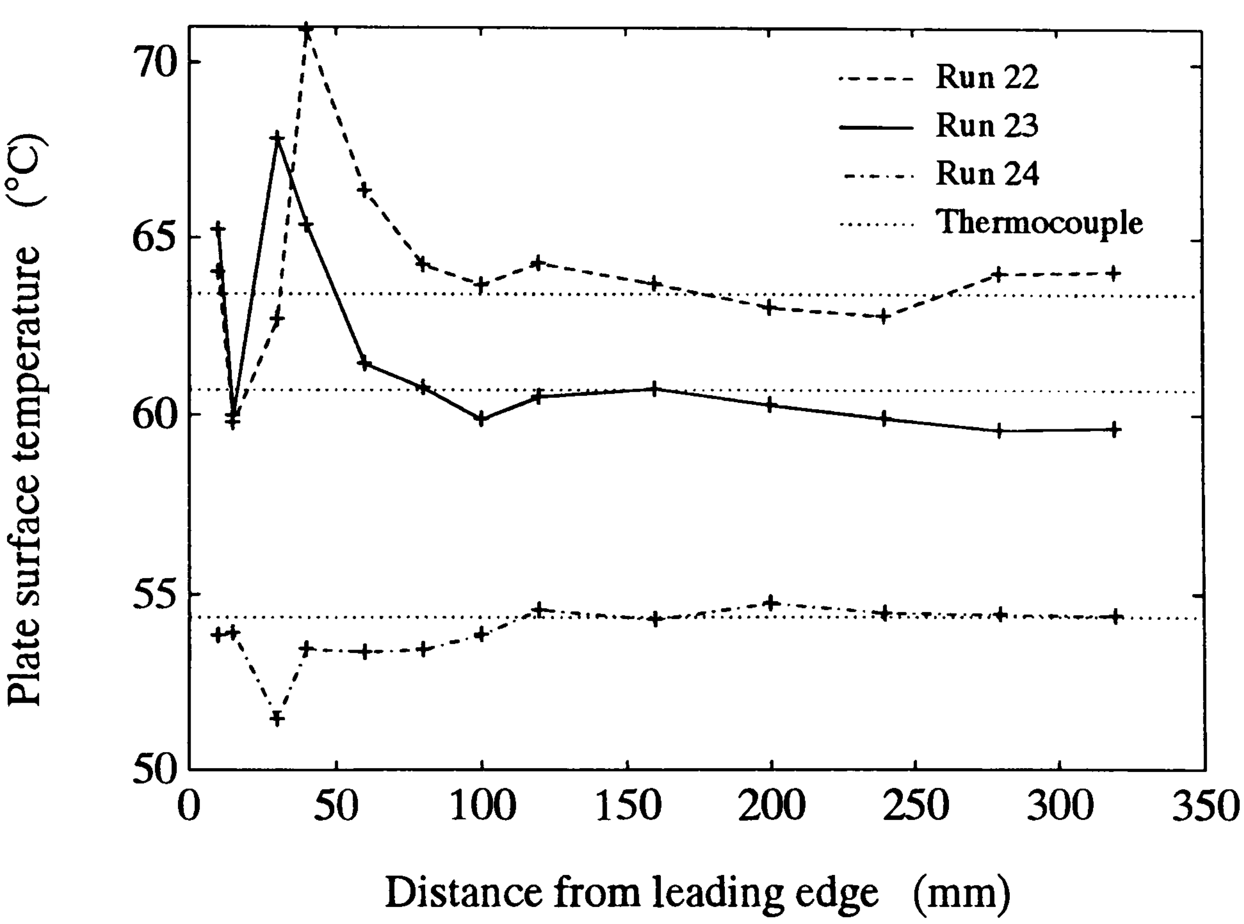

Figure 7.6. Initial temperature along plate from double crystal technique. Dotted line shows thermocouple reading; this is on one side of the plate rather than the centreline.

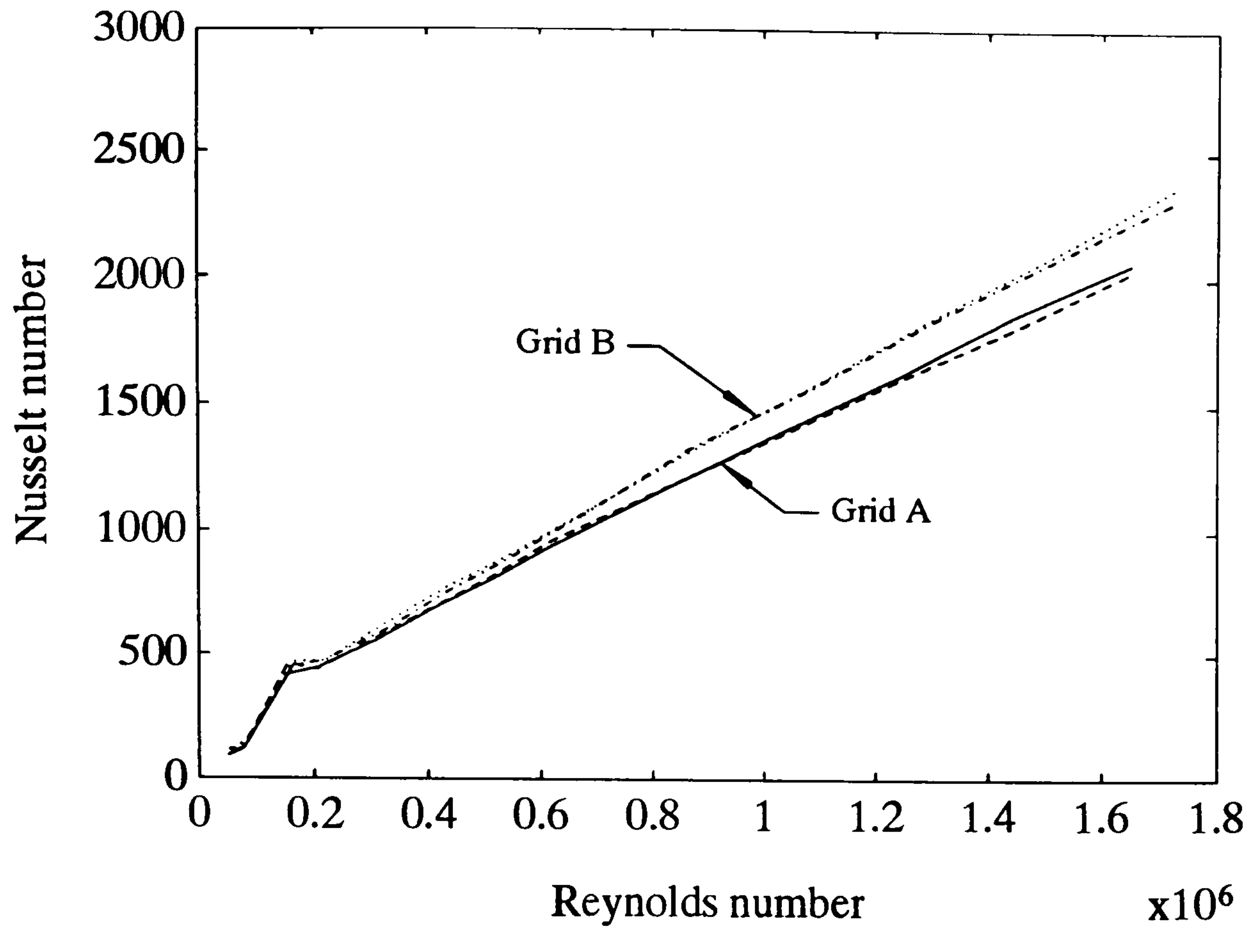

Figure 7.7. Repeatability of liquid crystal tests.

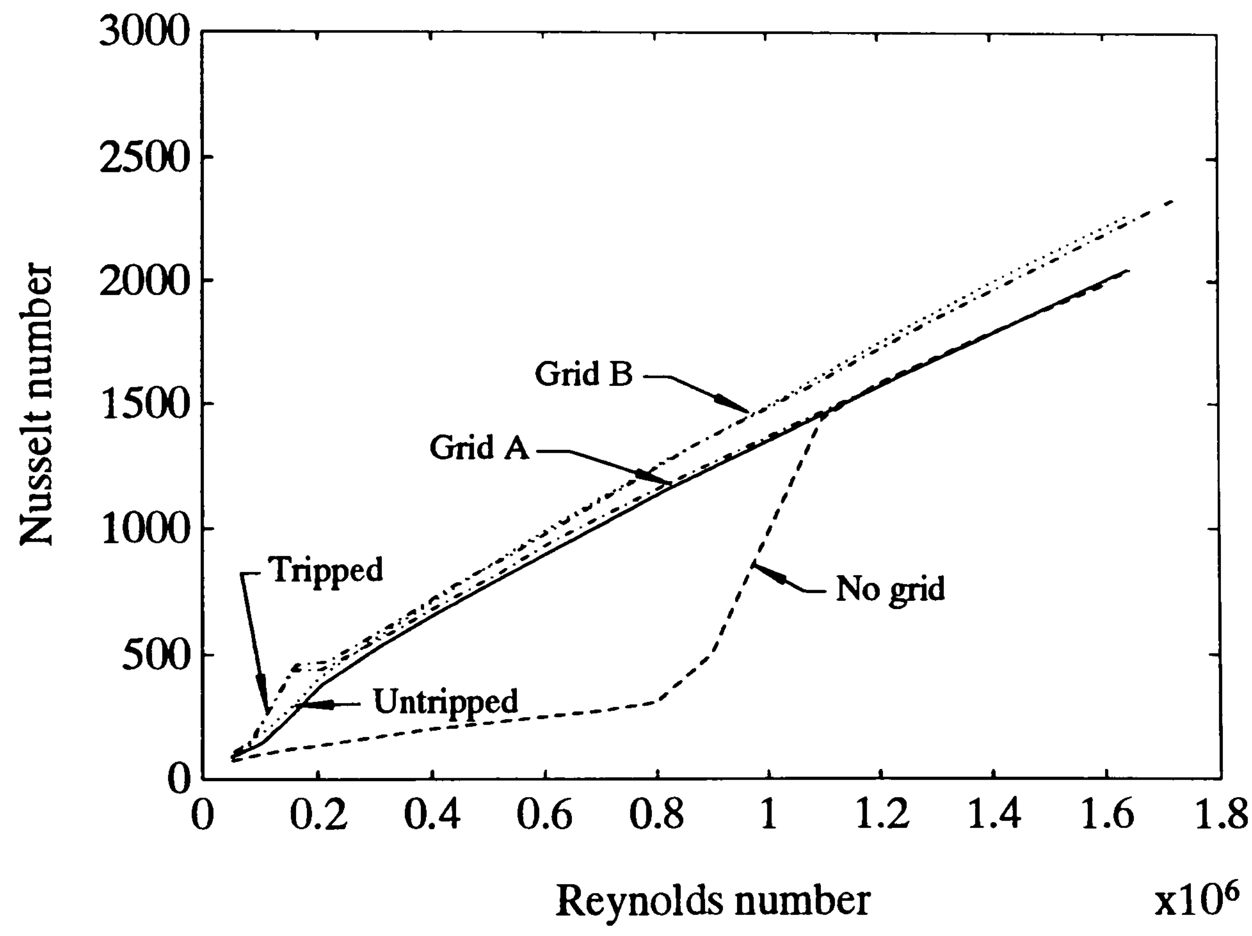

Figure 7.8. Effect of trip strip. The strip causes rapid transition, but does not increase the Nusselt number above the turbulent level when grids are present.

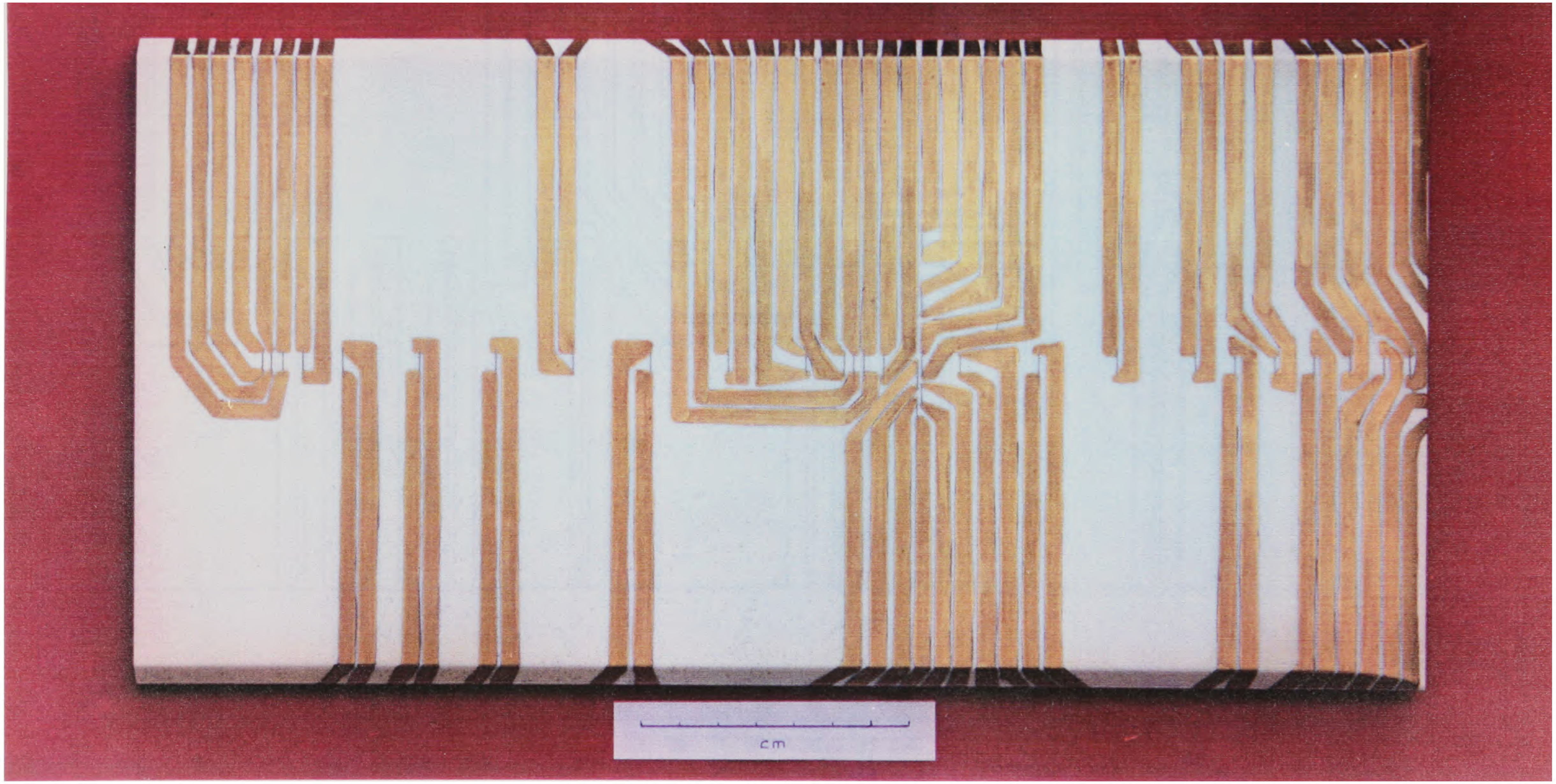

Figure 8.1. Photograph of Macor plate. Flow direction is from right to left.

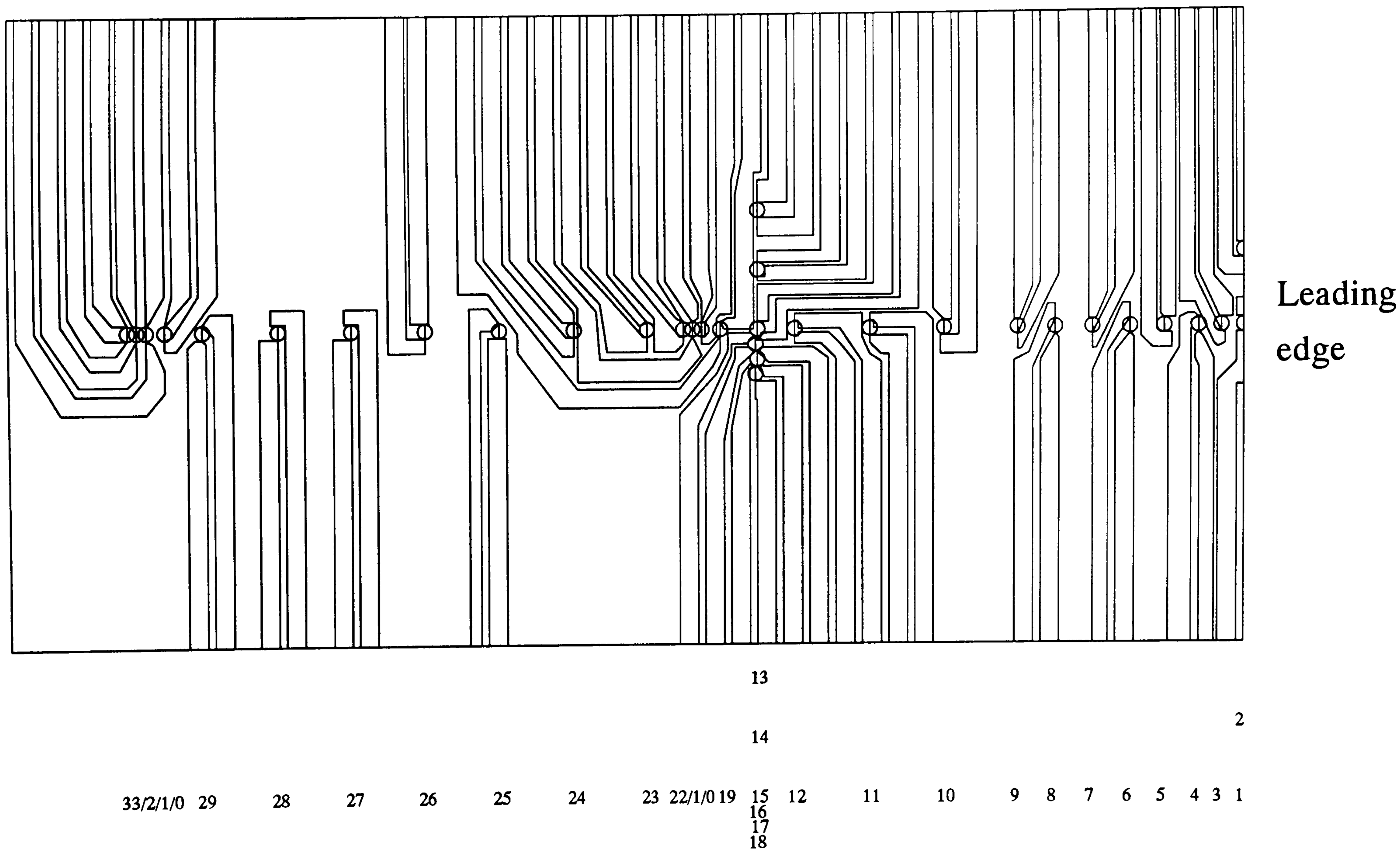

Figure 8.2. Gauge layout on plate. Gauge numbers are shown below plate for clarity.

Figure 8.3.
Thin film gauge coordinates and resistances.

Gauge number	Perimeter (mm)	Z (mm)	R_{20} (ohms)	$\frac{1}{R_{20}}\frac{dR}{dT}$
1	0	0	52.47	0.002274
2	0	-20	42.0	0.002281
3	6	0	55.28	0.002268
4	12	0	52.88	0.002289
5	21	0	58.83	0.002219
6	30	0	47.48	0.002281
7	40	0	47.57	0.002308
8	50	0	52.48	0.002317
9	60	0	55.5	0.002339
10	80	0	40.91	0.002377
11	100	0	51.59	0.002281
12	120	0	54.04	0.002308
13	130	-32	57.23	0.002365
14	130	-16	46.78	0.002222
15	130	0	60.17	0.002272
16	130.5	4	45.09	0.002206
17	130	8	60.81	0.002274
18	130.5	12	55.17	0.002282
19	140	0	47.13	0.002372
20	145	0	68.35	0.002379
21	147.5	0	56.47	0.002324
22	150	0	63.01	0.002410
23	160	0	53.44	0.002330
24	180	0	53.38	0.002360
25	200	0	55.77	0.002327
26	220	0	55.59	0.002329
27	240	0	49.33	0.002308
28	260	0	57.56	0.002239
29	280	0	57.45	0.002233
30	290	0	58.38	0.002142
31	295	0	57.57	0.001920
32	297.5	0	62.1	0.001872
33	300	0	58.96	0.001919

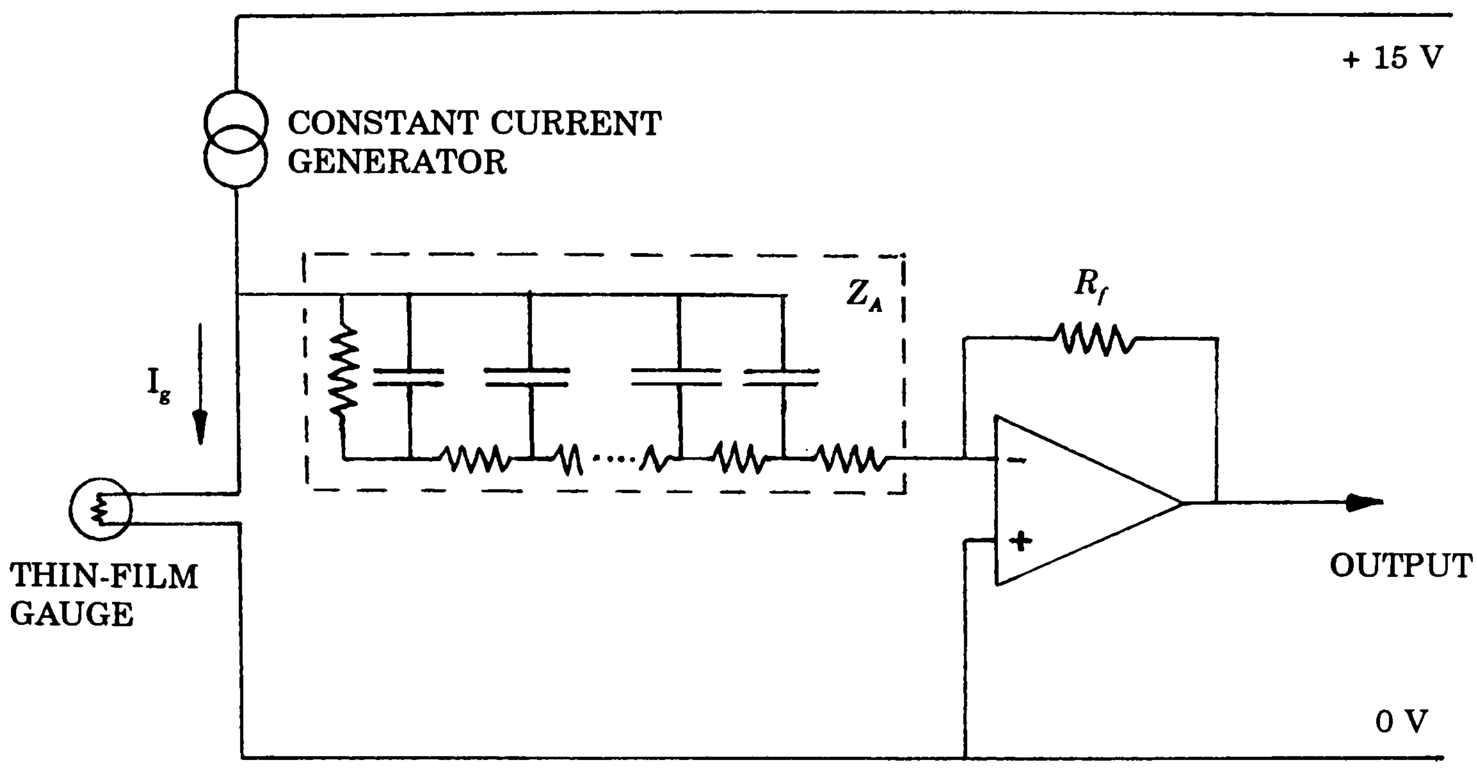

Figure 8.4. Block diagram of "analogue" circuit for measuring gauge resistance and converting it to a heat flux signal.

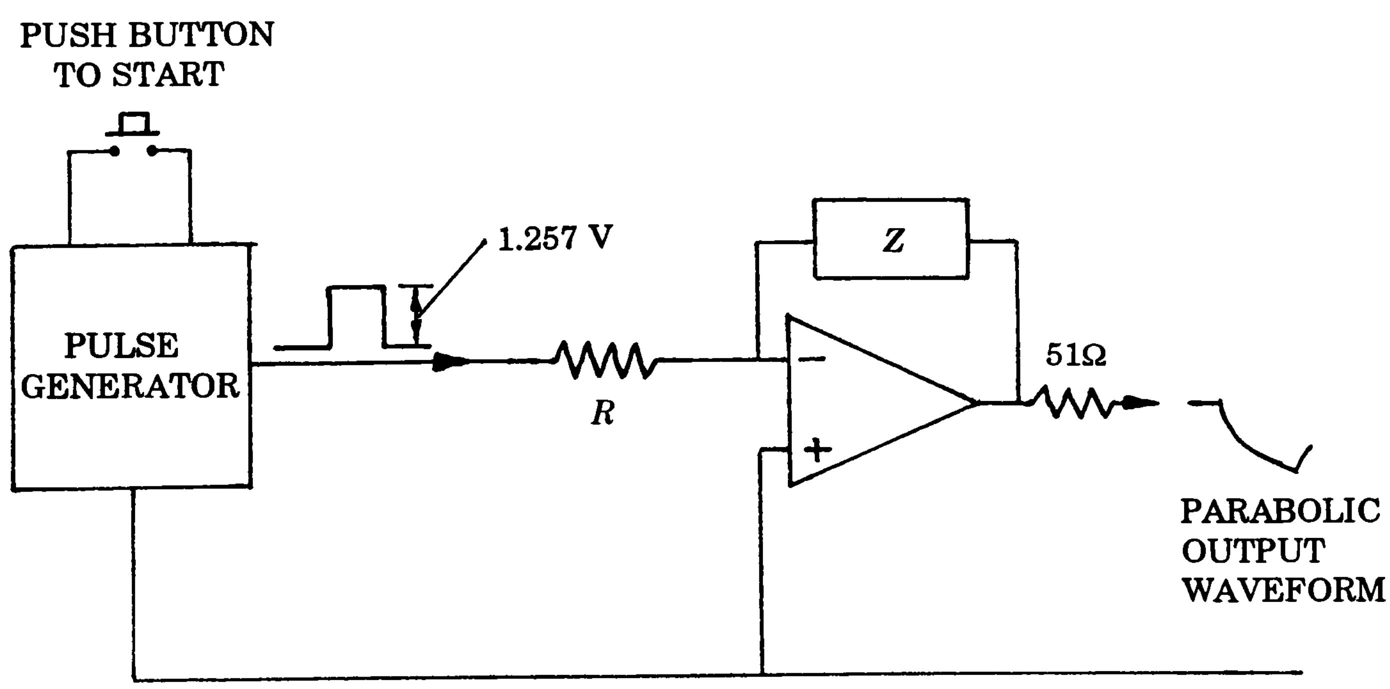

Figure 8.5. Block diagram of "anti-analogue" circuit for calibrating analogues. The gauge is replaced by this circuit; the analogue should then reproduce the square pulse.

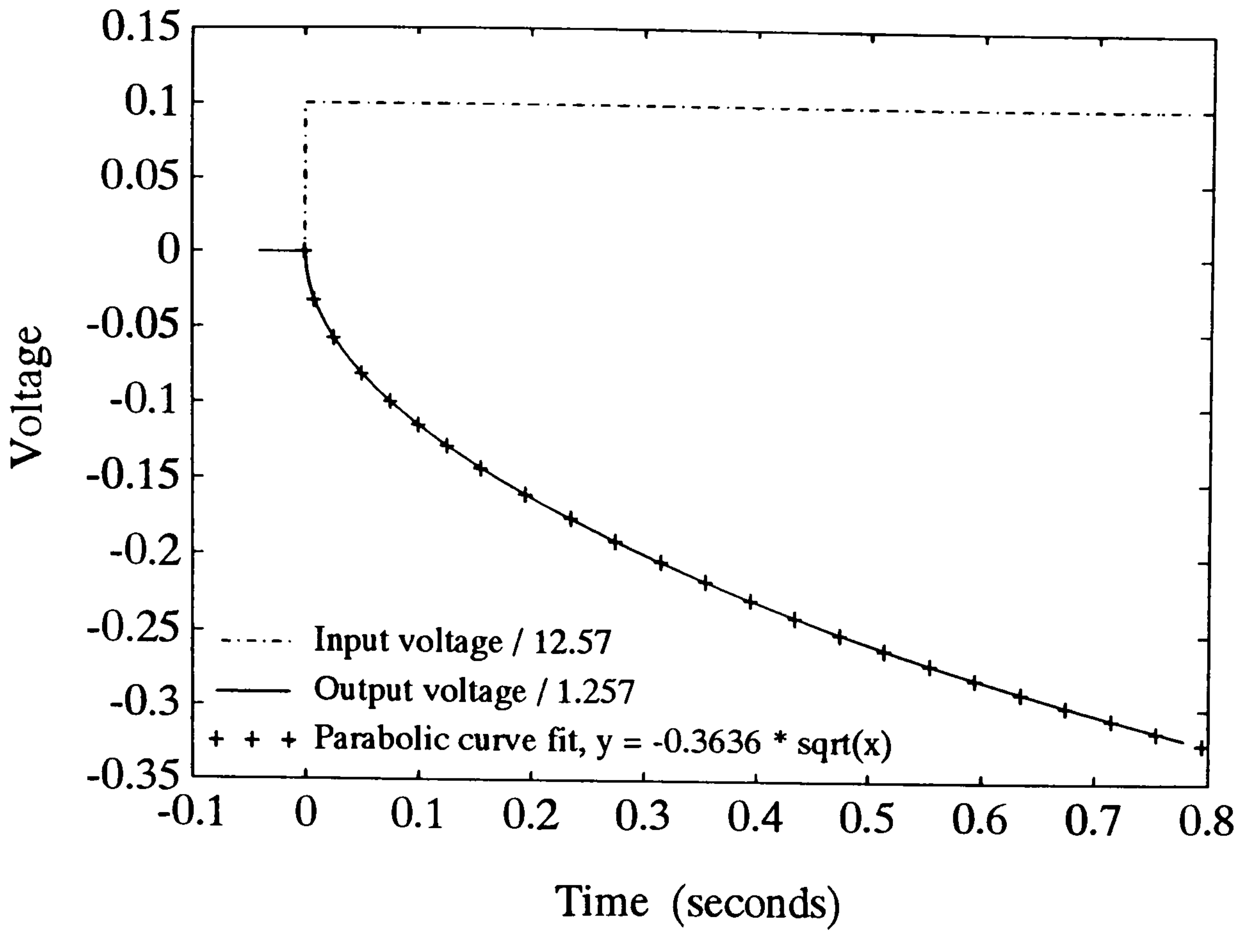

Figure 8.6. Calibration waveforms at anti-analogue input and output.

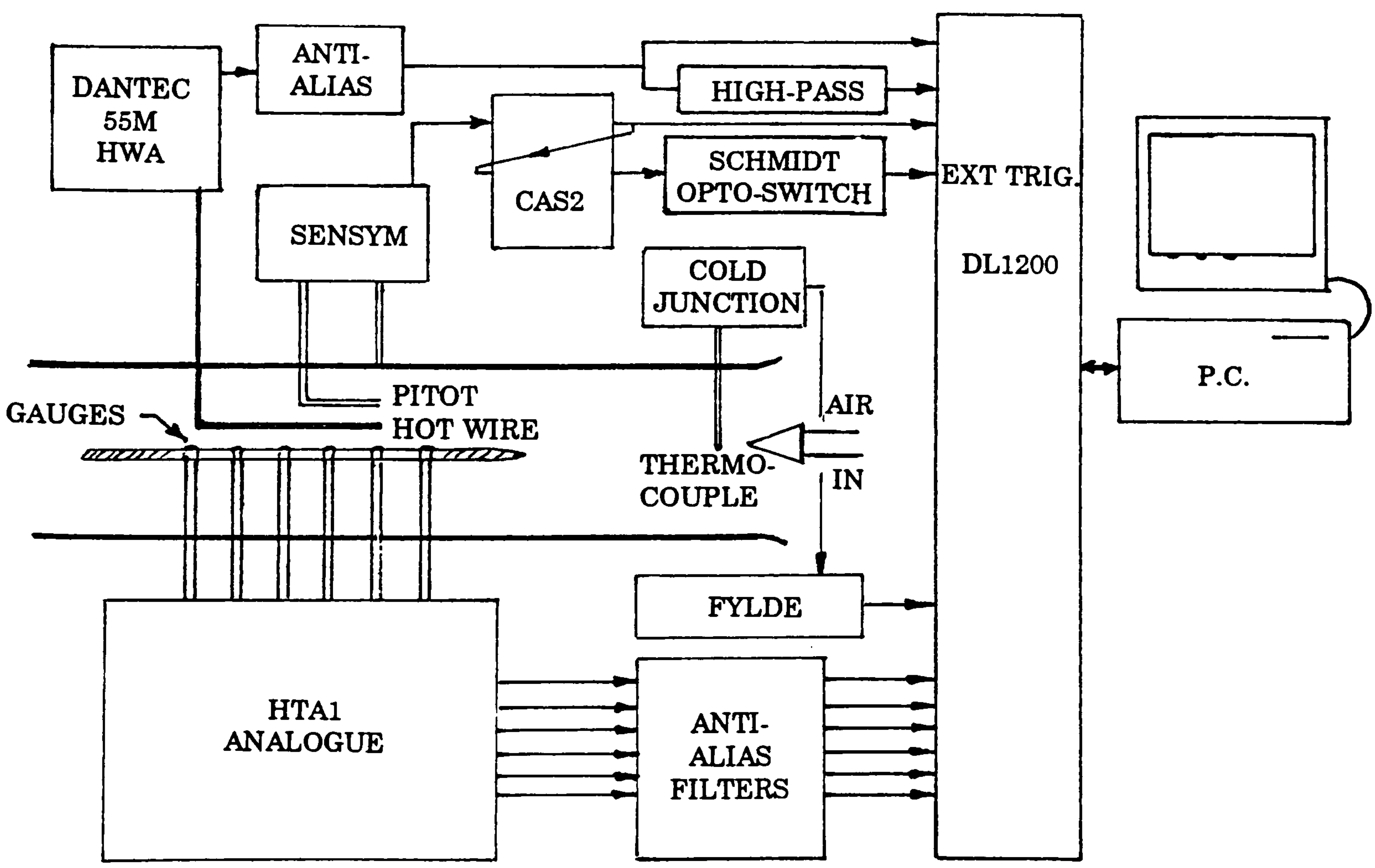

Figure 8.7. Tunnel instrumentation diagram.

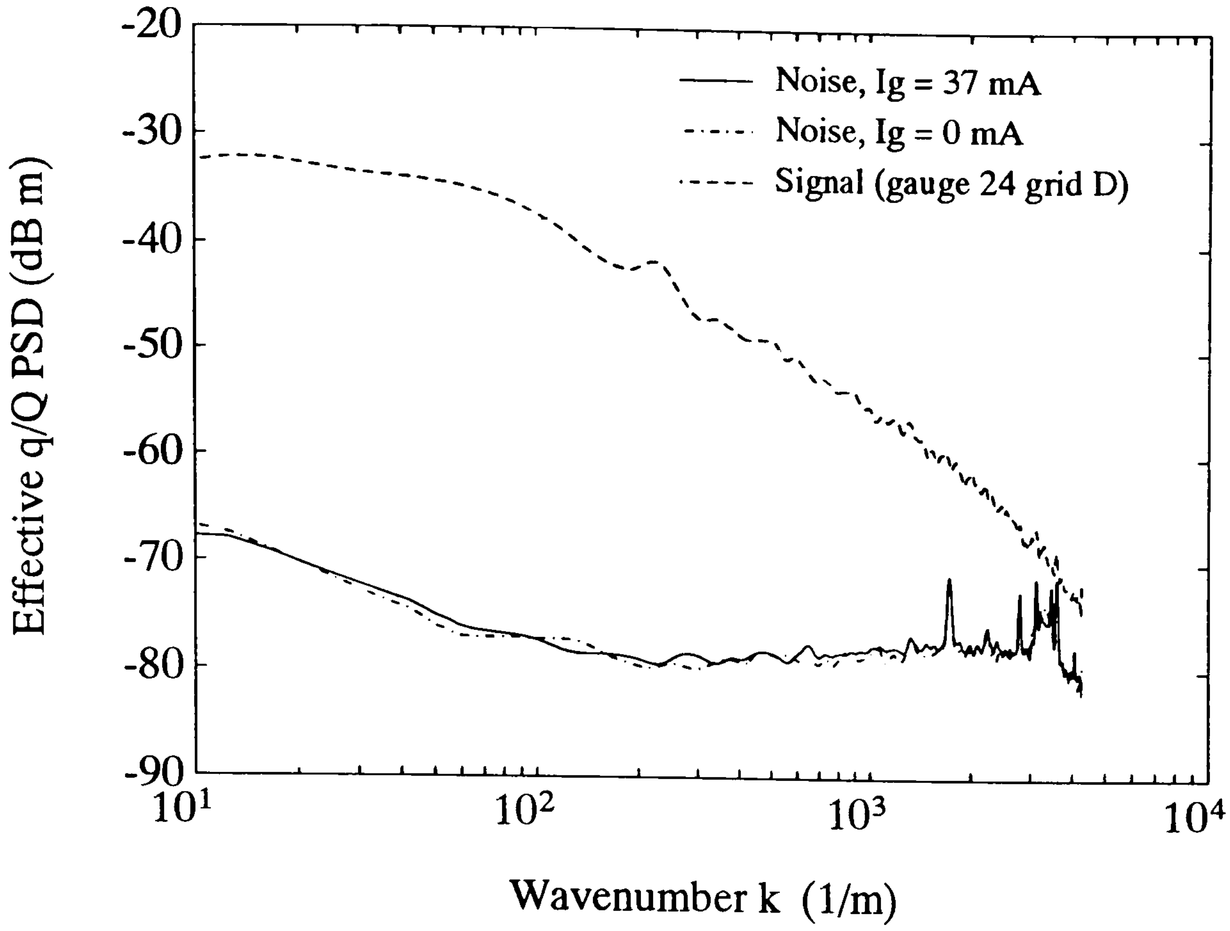

Figure 8.8. Effect of gauge current on noise level. The noise is not a function of gauge current, so the signal to noise ratio is proportional to the current applied.

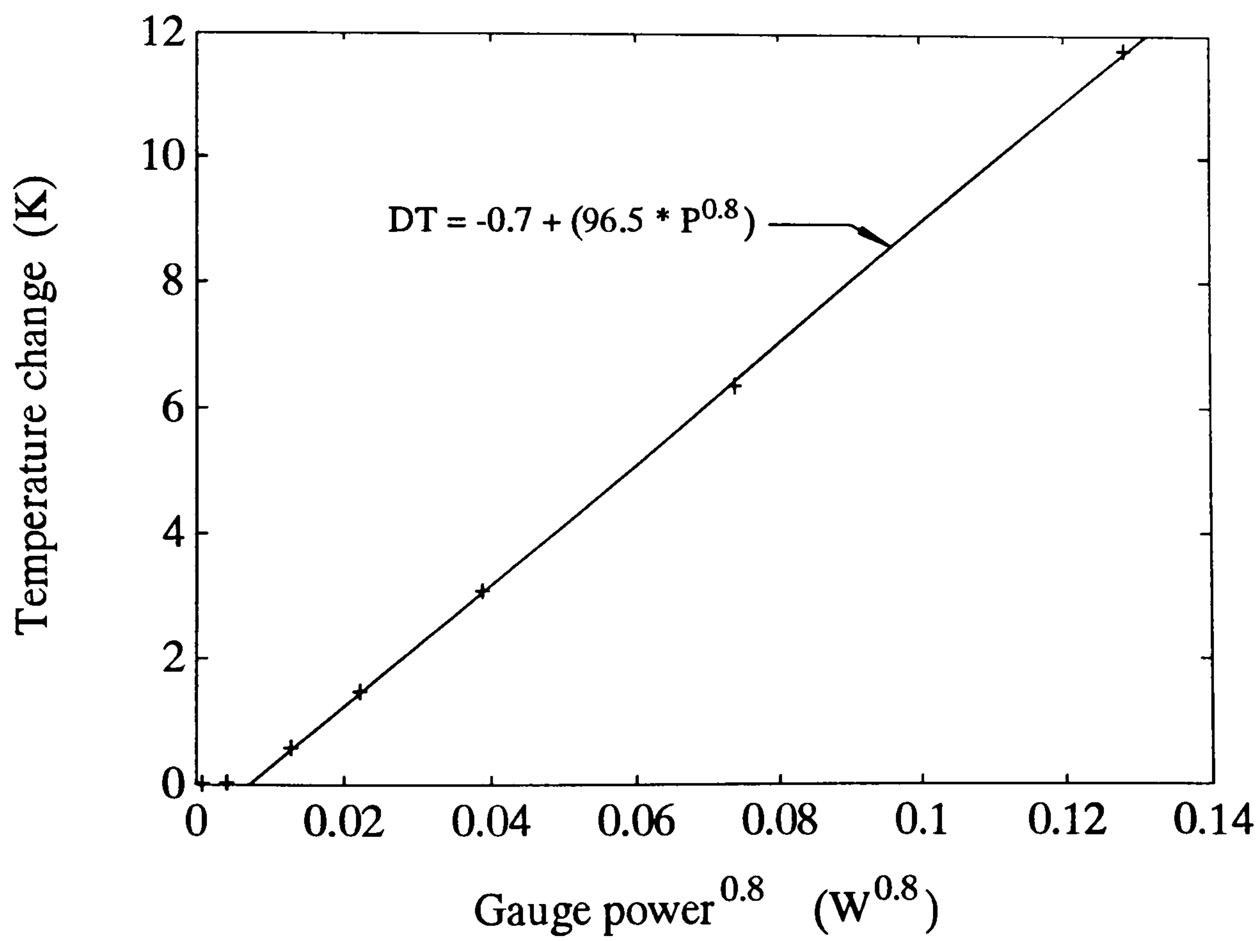

Figure 8.9. Plate heating due to gauge current.

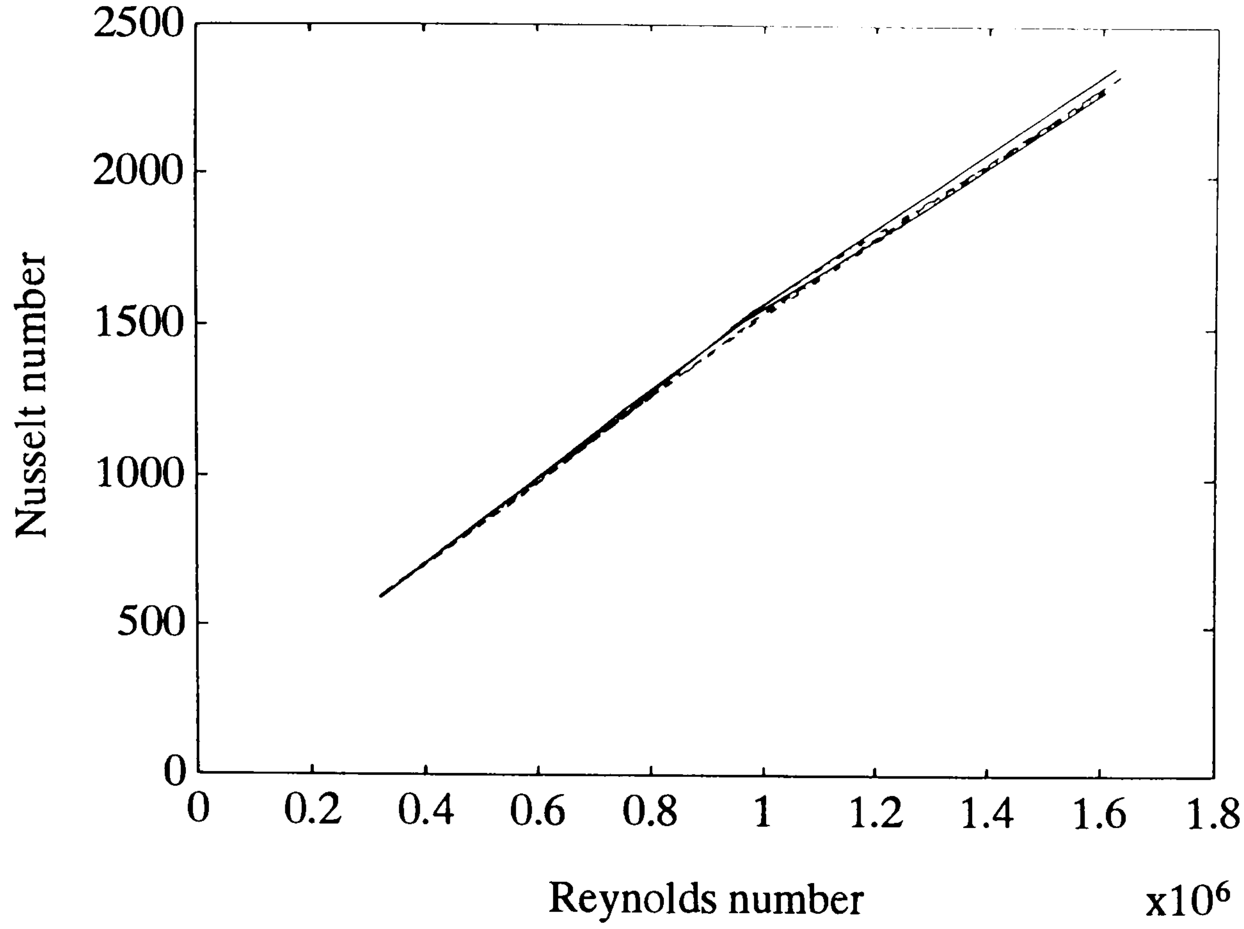

Figure 8.10. Repeatability of thin-film heat flux measurements. (Five runs with grid B, tripped).

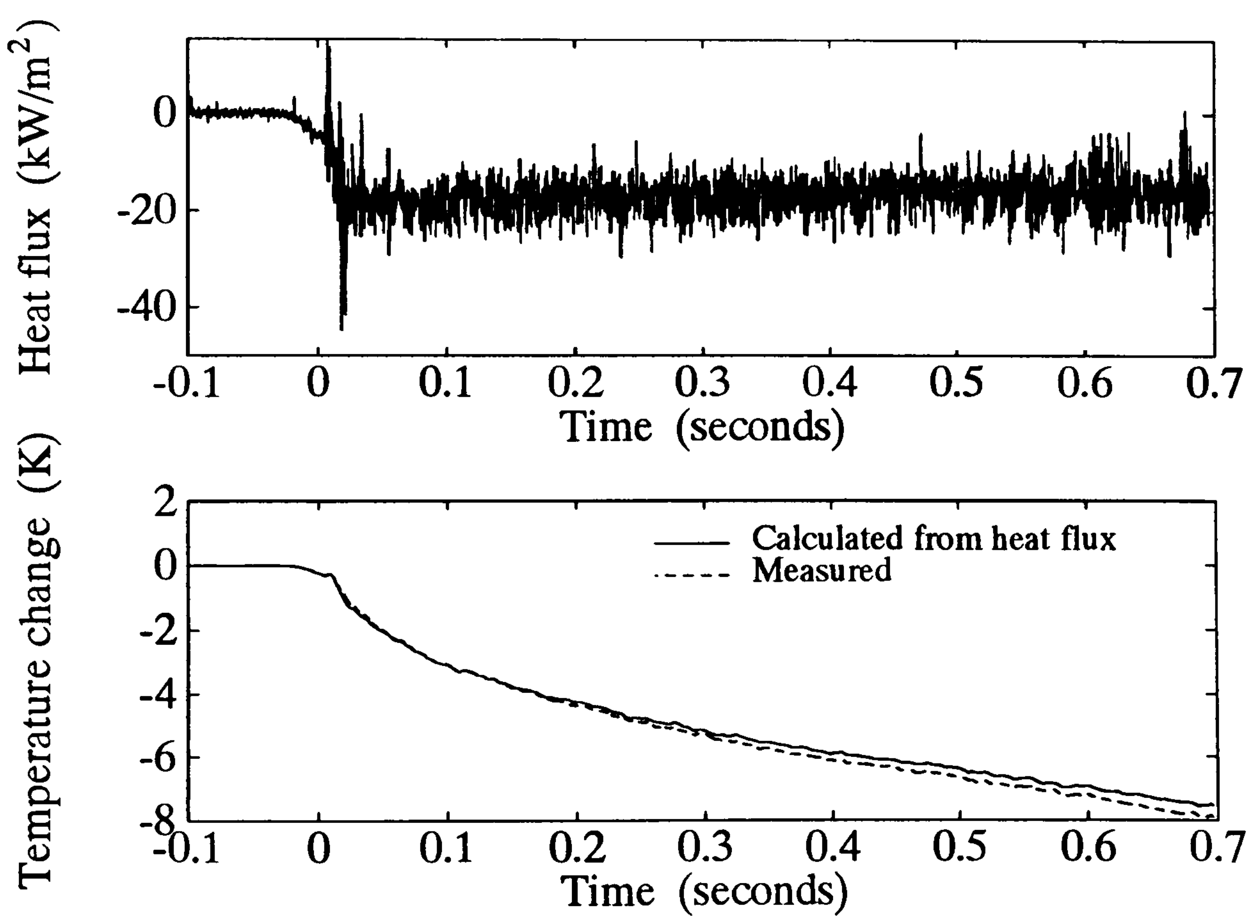

Figure 8.11. Plate temperature change during test calculated from heat flux signal (gauge 24).

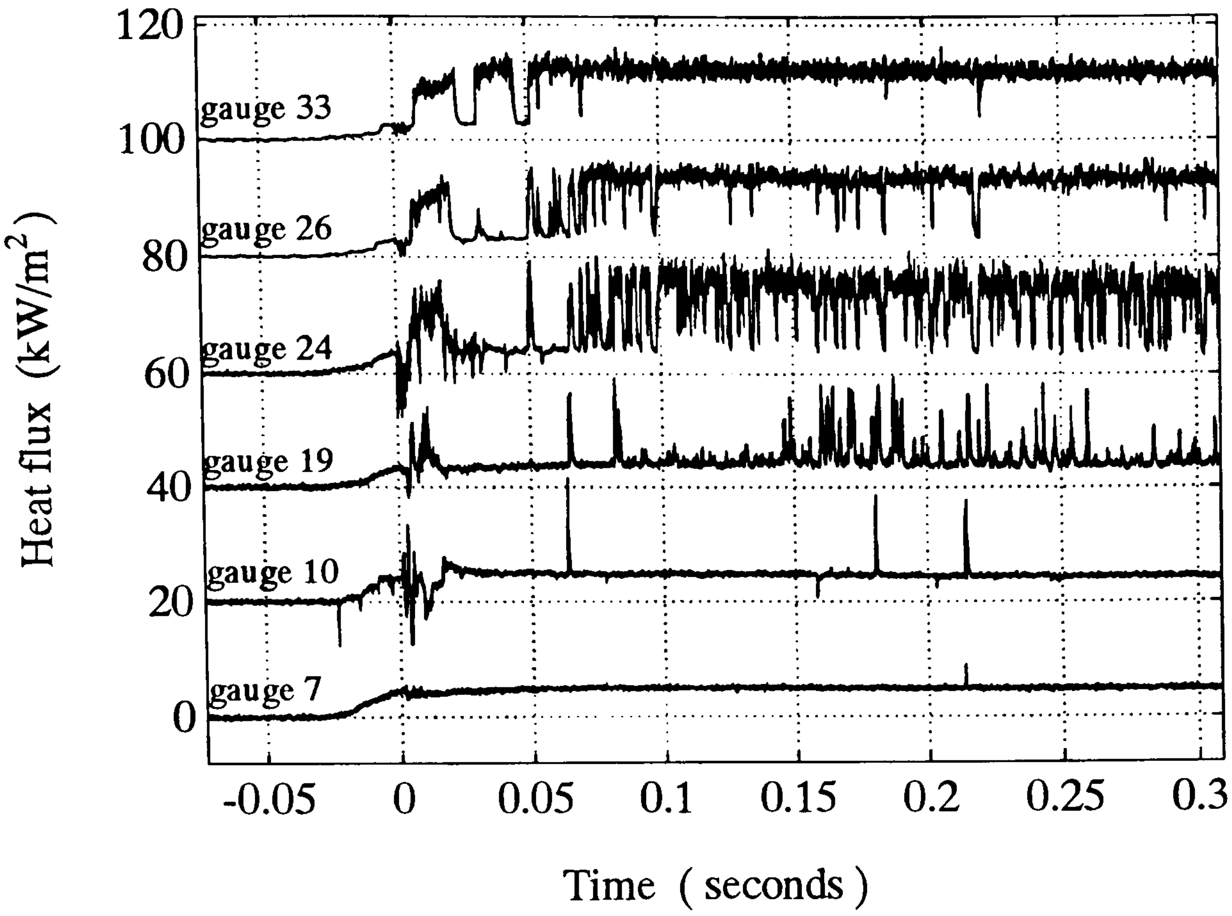

Figure 8.12. Natural transition with no trip strip or grid. Gauge Reynolds numbers are 206000, 412000, 721000, 927000, 1133000 and 1544000; U = 77 m/s.

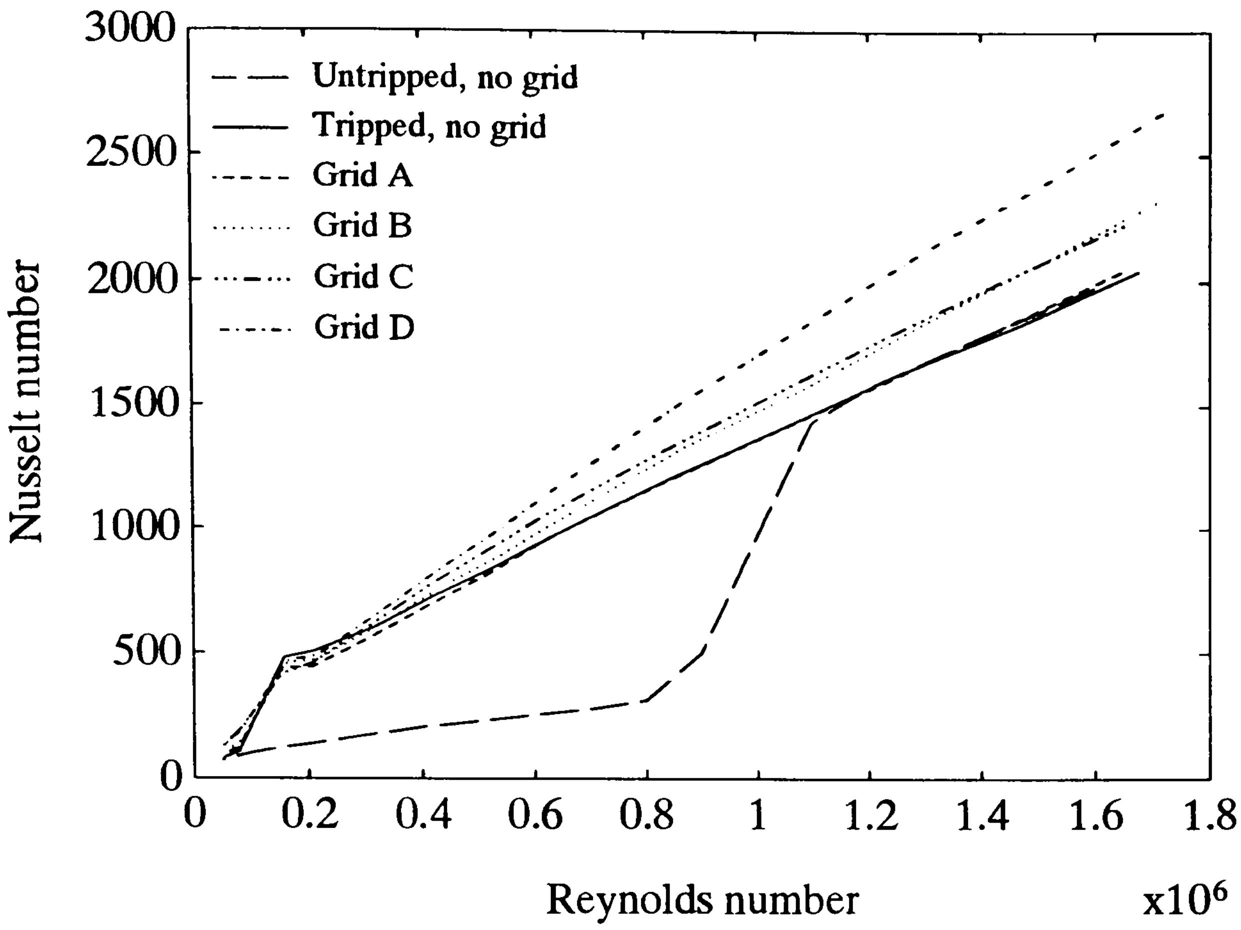

Figure 9.1. Liquid crystal results: Nusselt numbers with four different grids (tripped) compared with grid-out tripped and untripped data.

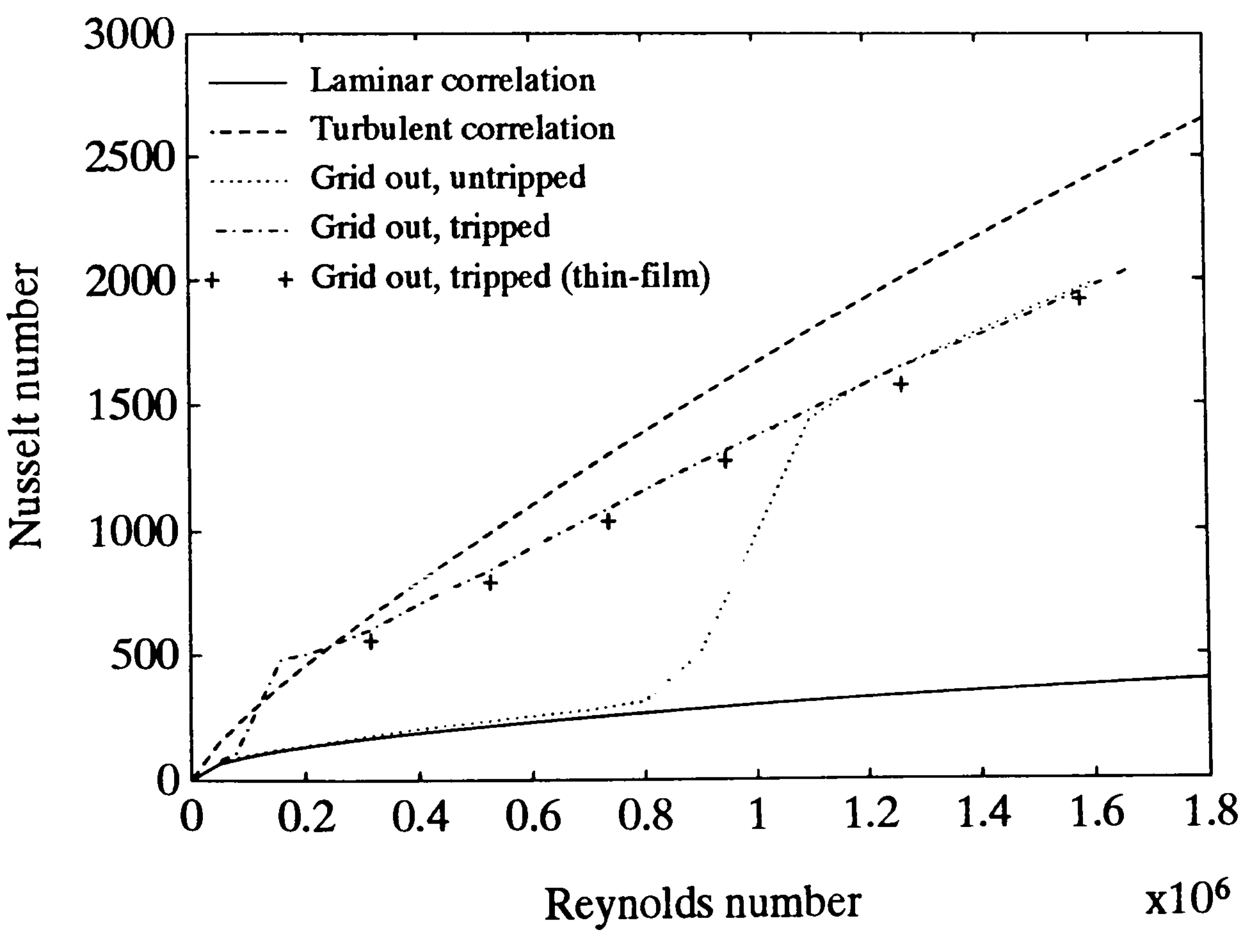

Figure 9.2. Comparison of liquid crystal datum results with laminar and turbulent Nusselt/Reynolds number correlations (**Schlichting, 1979**).

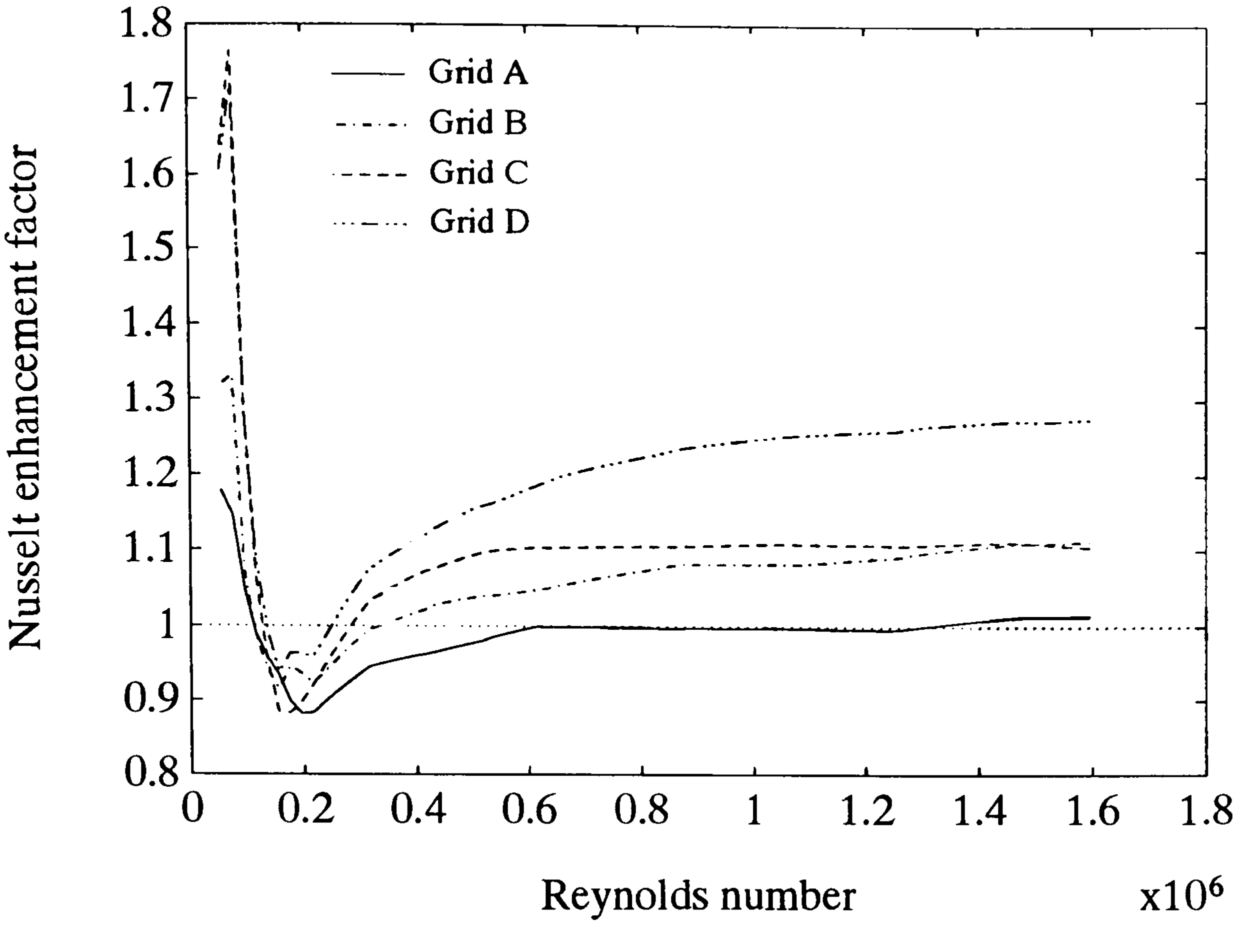

Figure 9.3. Liquid crystal results plotted as Nusselt number enhancement factors relative to (tripped) grid-out case.

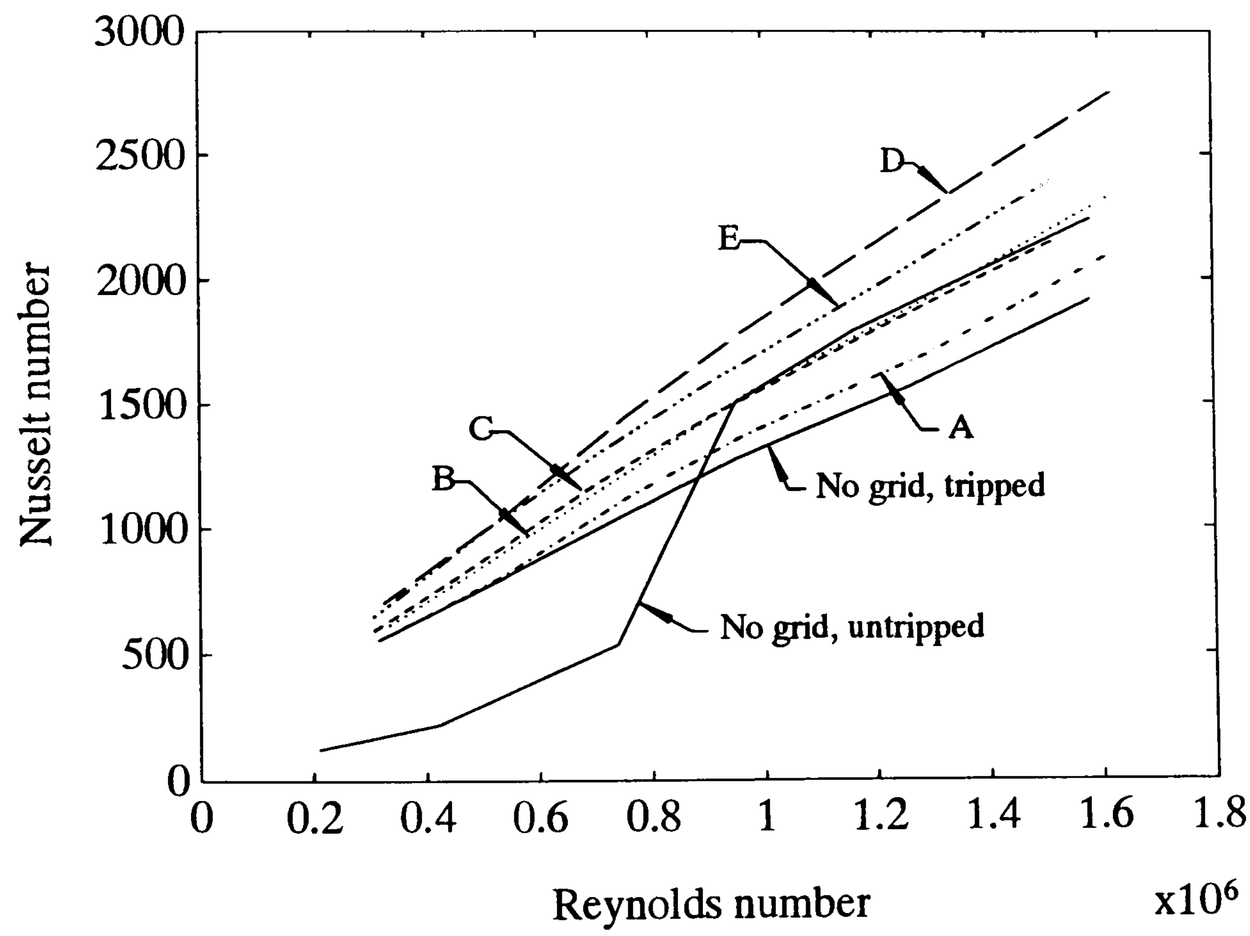

Figure 9.4. Nusselt numbers measured using thin-film gauges and grids A to E. The boundary layer is tripped unless stated otherwise.

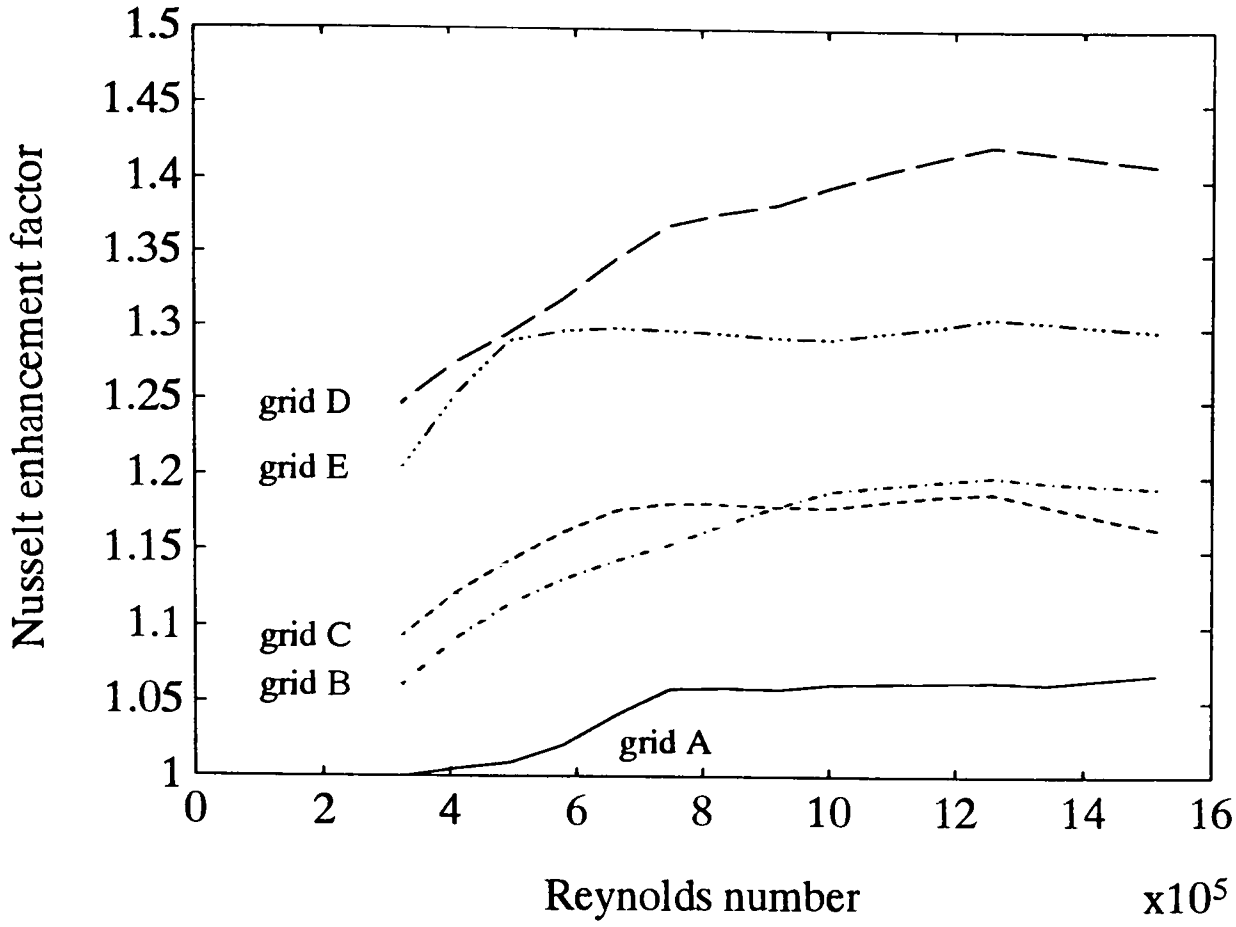

Figure 9.5. Nusselt number enhancement (Nu/Nu_0) on flat plate for grids A to E. (Thin film gauge measurements).

Figure 9.6.

Table of enhancement factors from thin-film measurements.

GRID:	A	B	C	D	E
Bar diameter (mm)	6	60	6	60	15
Bar pitch (mm)	15	single	15	single	37.5
Distance to LE x_g (mm)	260	920	90	380	140
Nu/Nu_0 at x = 100 mm	1.01	1.121	1.151	1.302	1.296
180 mm	1.059	1.183	1.177	1.386	1.299
300 mm	1.069	1.193	1.166	1.41	1.298

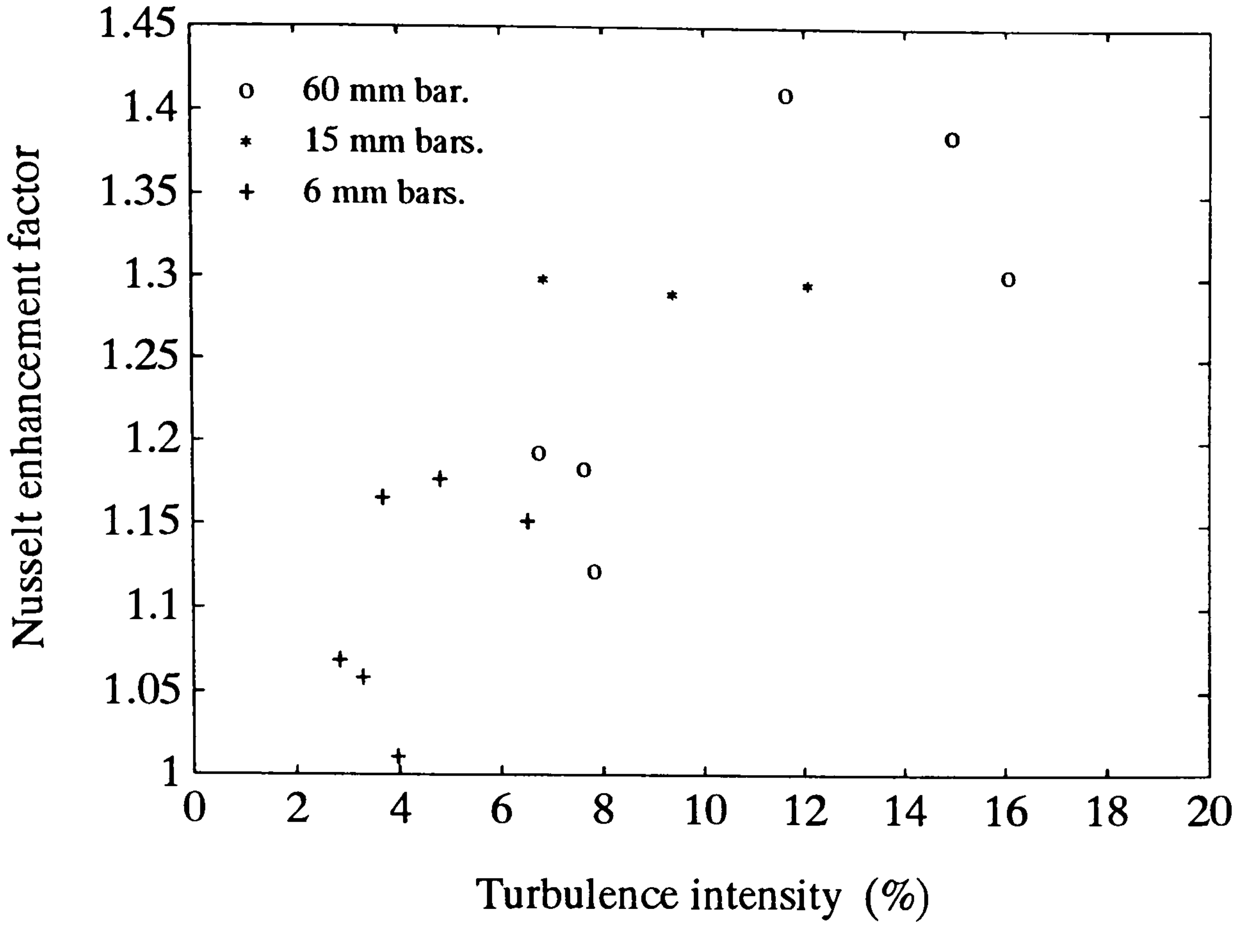

Figure 9.7. Nusselt number enhancement factors from thin-film gauge tests, plotted against turbulence intensity. The intensity is not, by itself, a suitable correlating parameter.

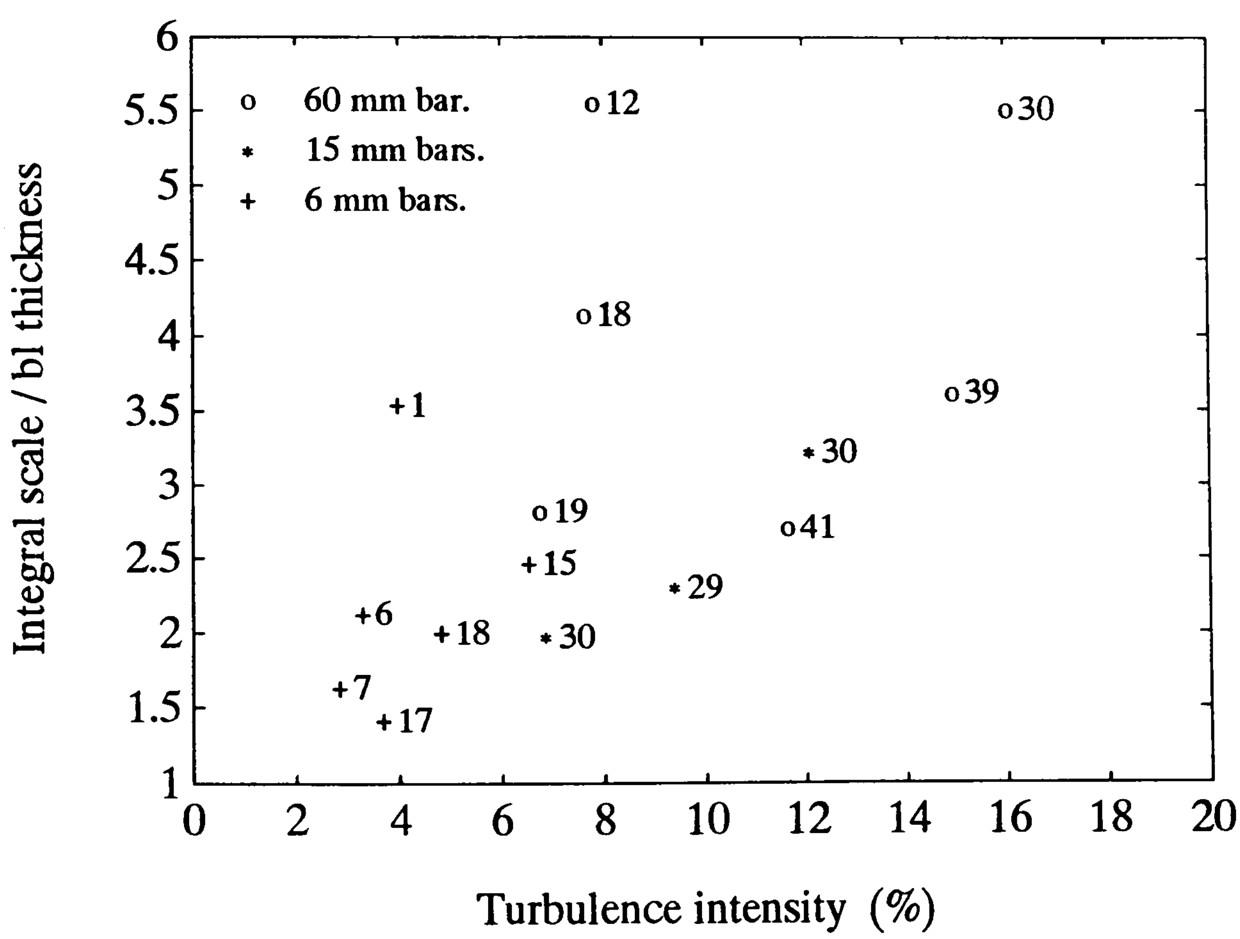

Figure 9.8. Nusselt number enhancement factors (values given as %) plotted against turbulence intensity and integral length scale.

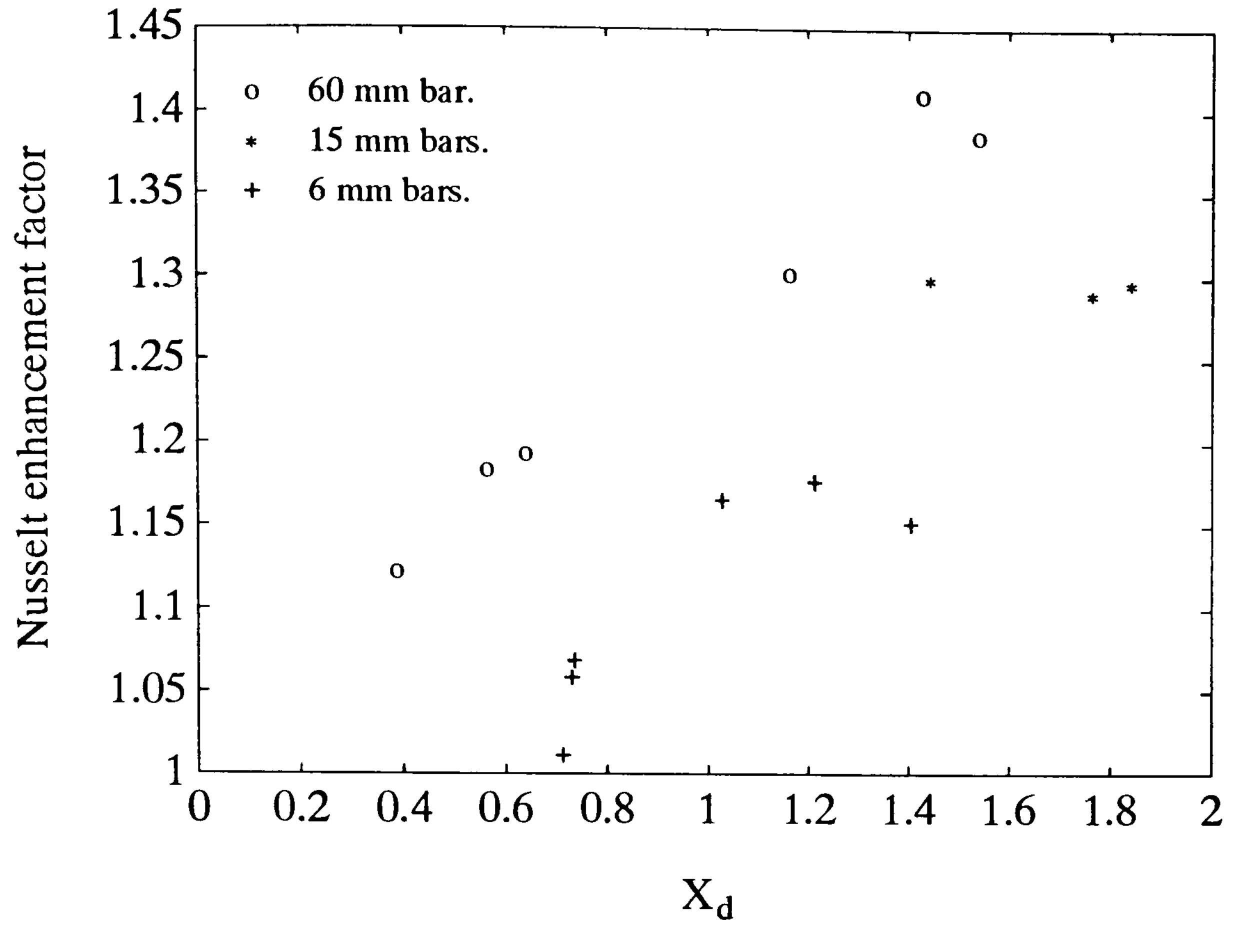

Figure 9.9. Attempt to correlate enhancement factors against dissipation scale parameter X_d (from **Hancock, 1980**). This does not appear suitable for the present data.

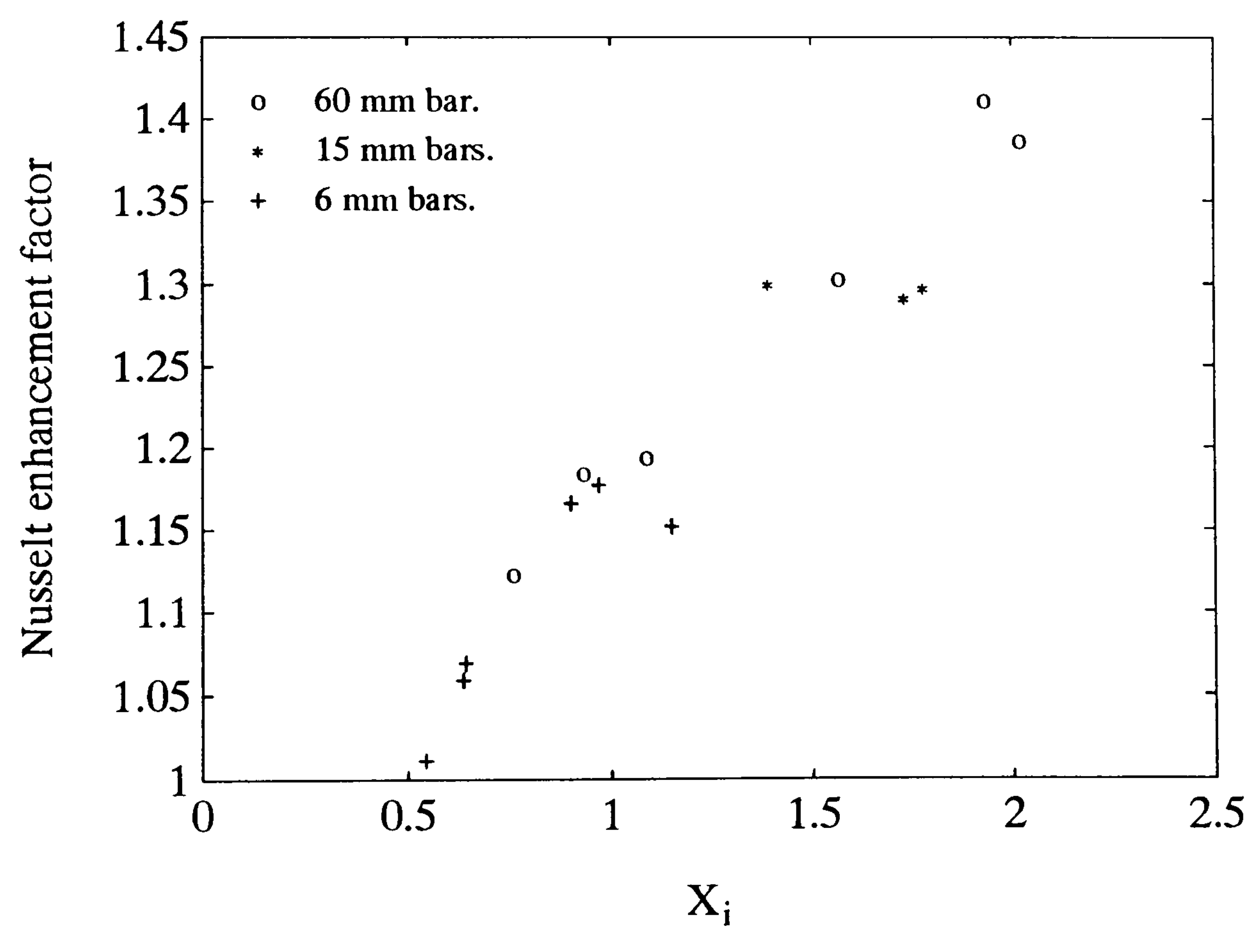

Figure 9.10. Nusselt number enhancement factor plotted against integral length scale parameter X_i.

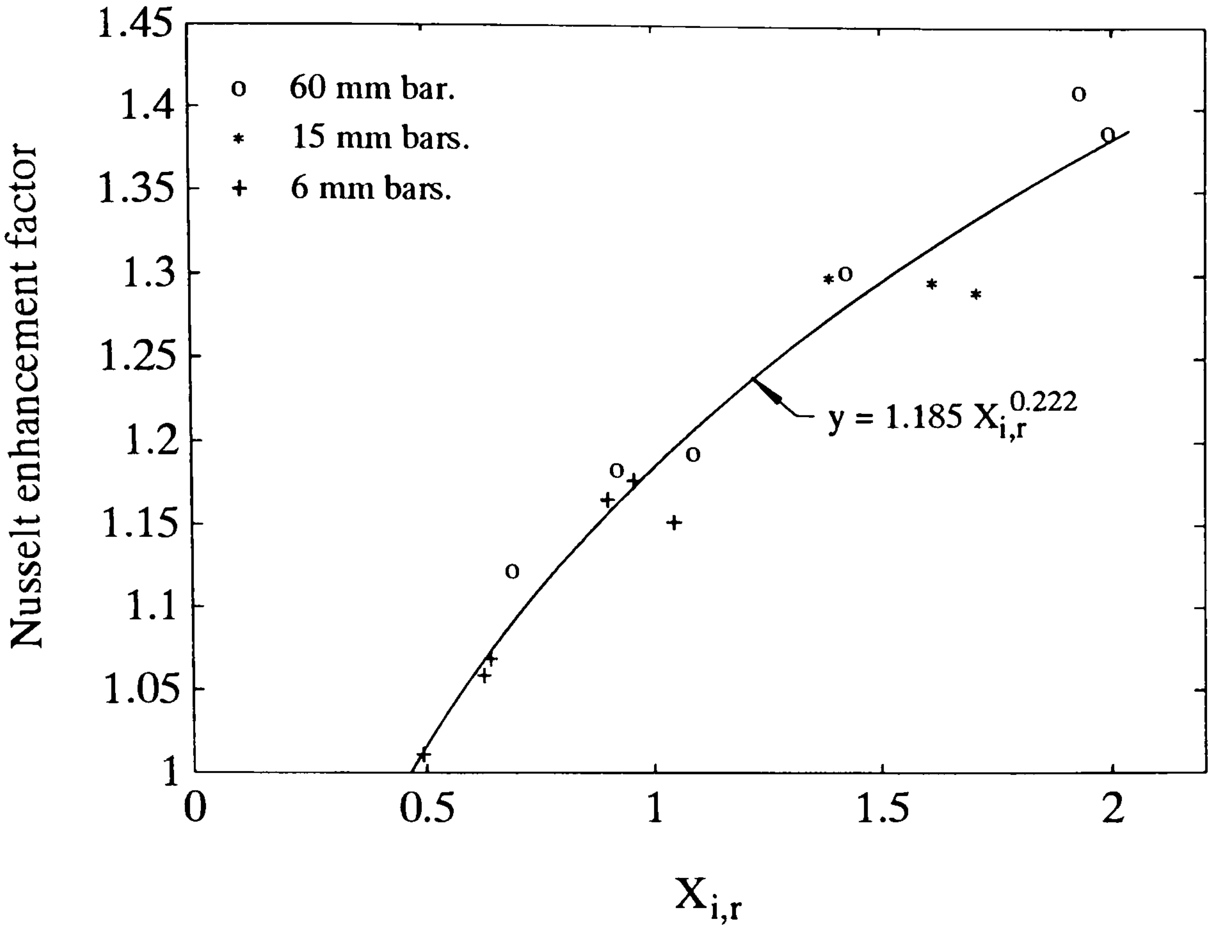

Figure 9.11. Nusselt number enhancement factor plotted against integral length scale parameter with Reynolds number correction $X_{i,r}$.

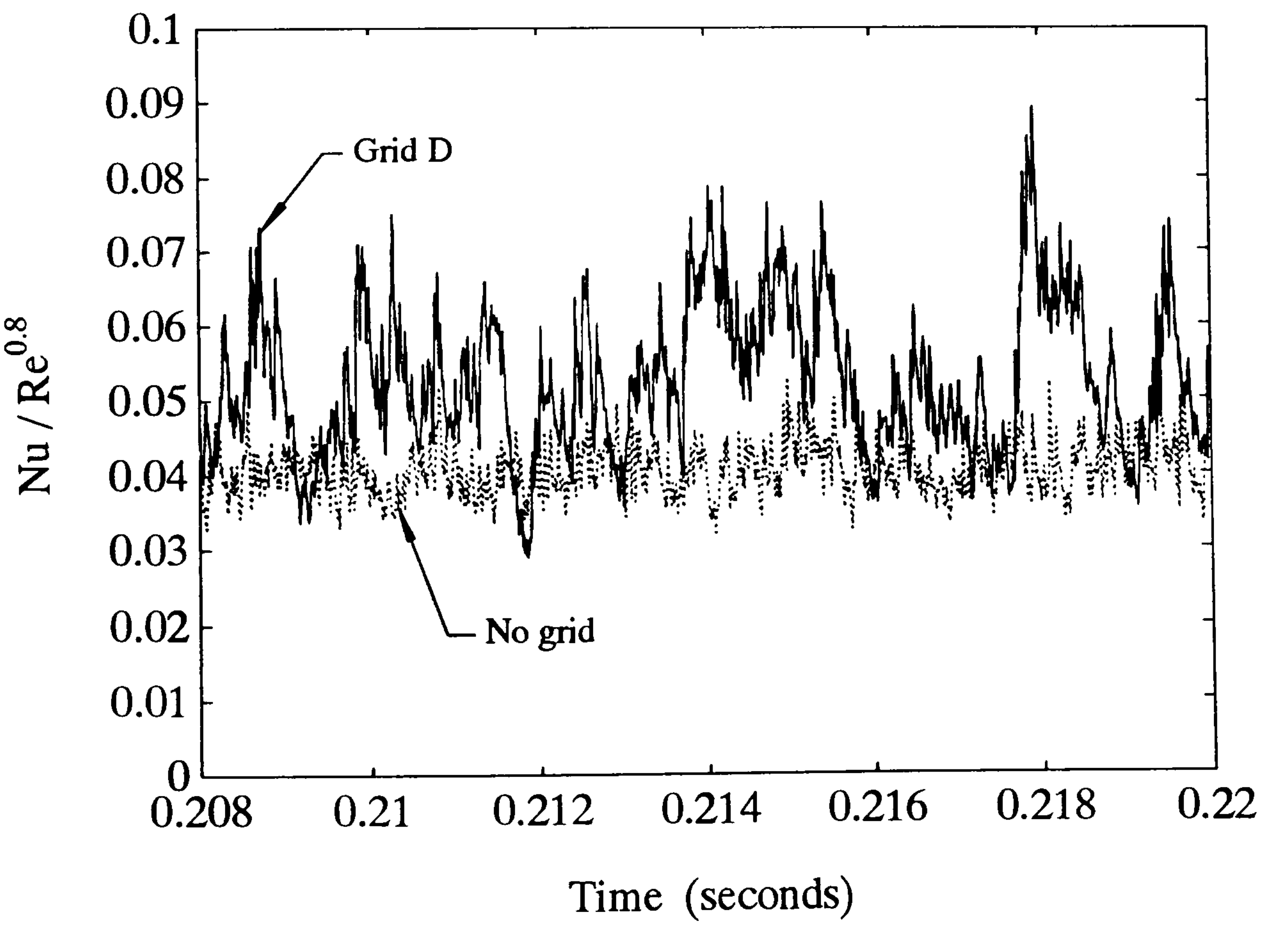

Figure 9.12. Comparison of non-dimensionalised heat flux signals with high and low freestream turbulence.

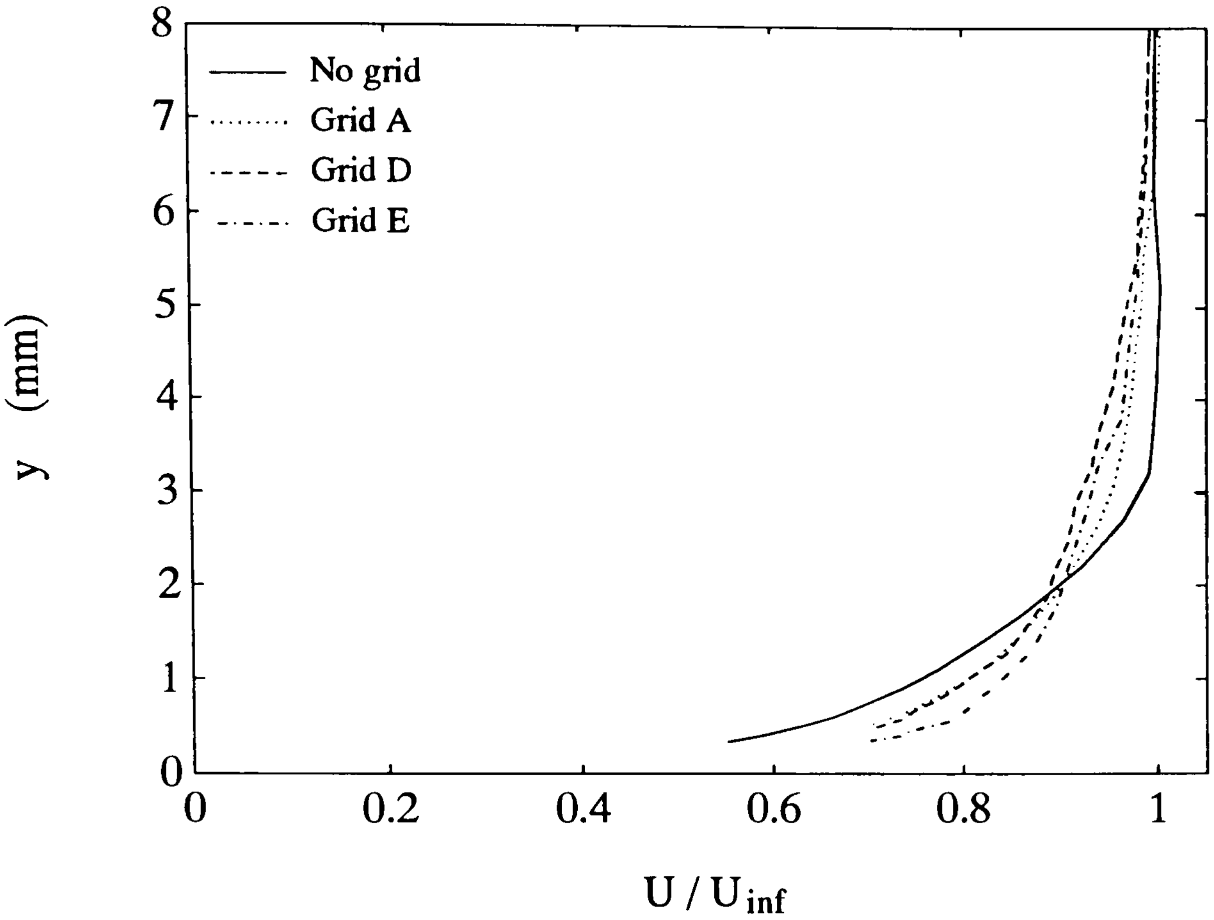

Figure 9.13. Effect of freestream turbulence on boundary layer velocity profile. (x = 150 mm, tripped).

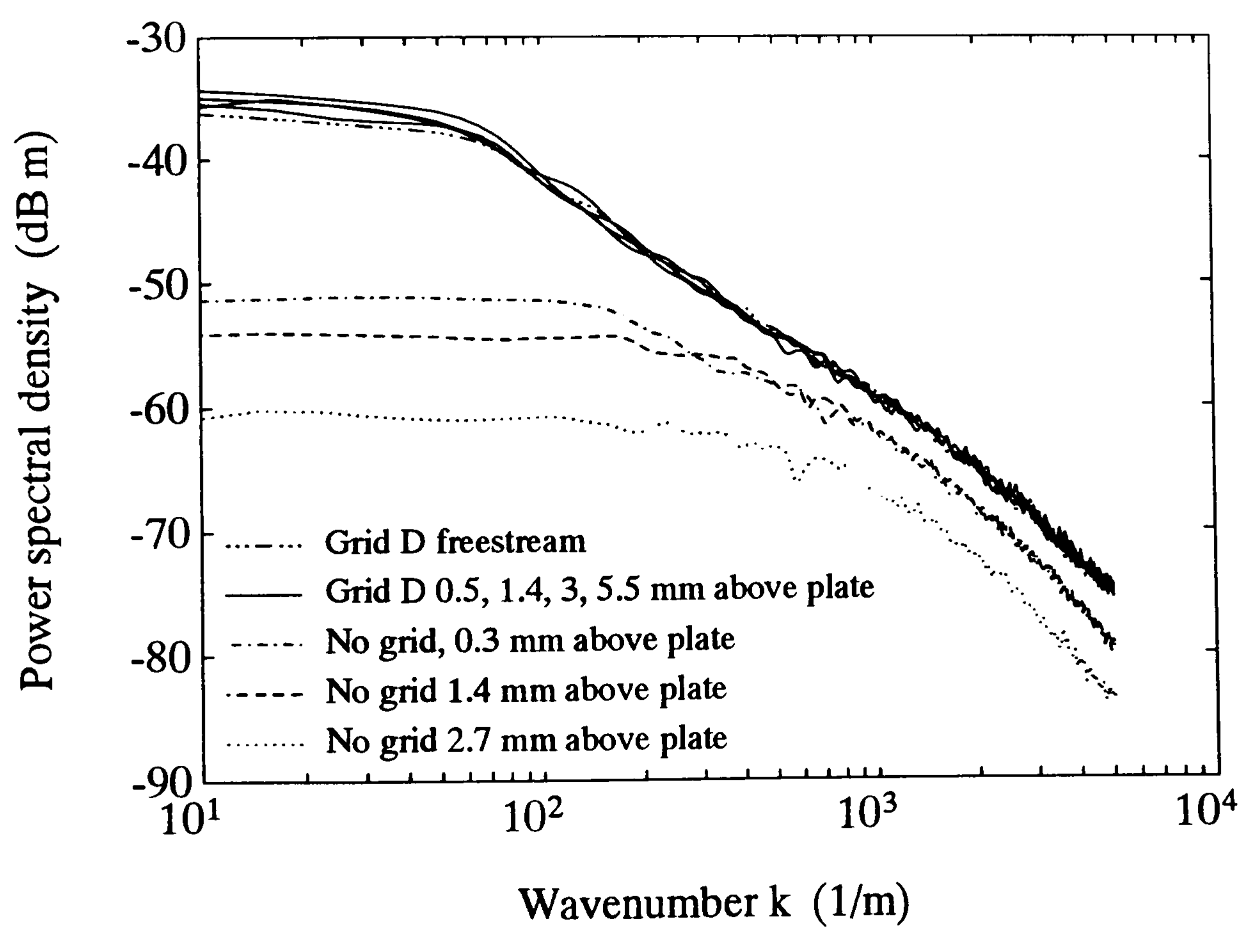

Figure 9.14. Turbulence spectra in boundary layer and freestream (grid D, x = 150 mm) compared with grid-out case.

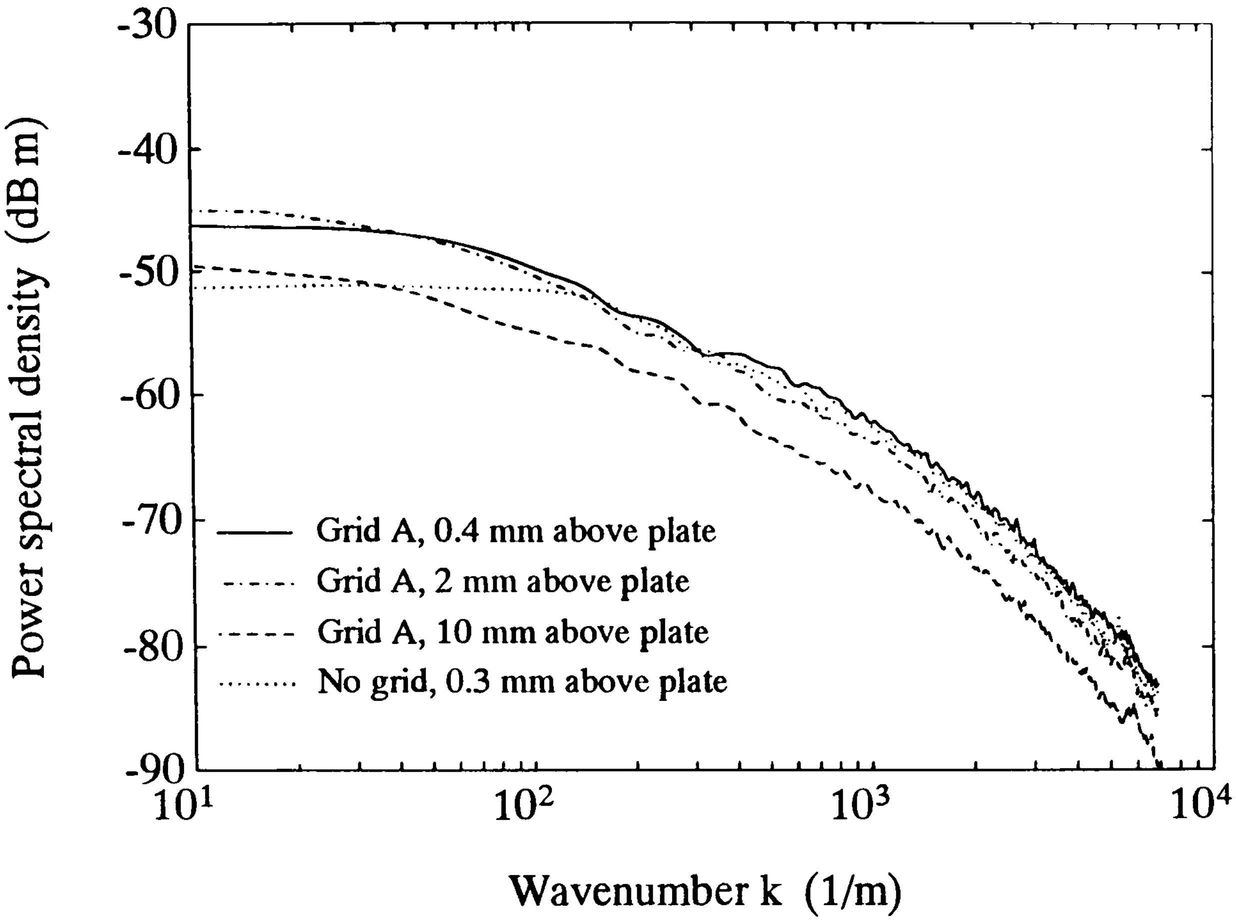

Figure 9.15. Turbulence spectra within boundary layer (grid A, x = 150 mm, tripped). 10 mm line is similar to freestream spectrum.

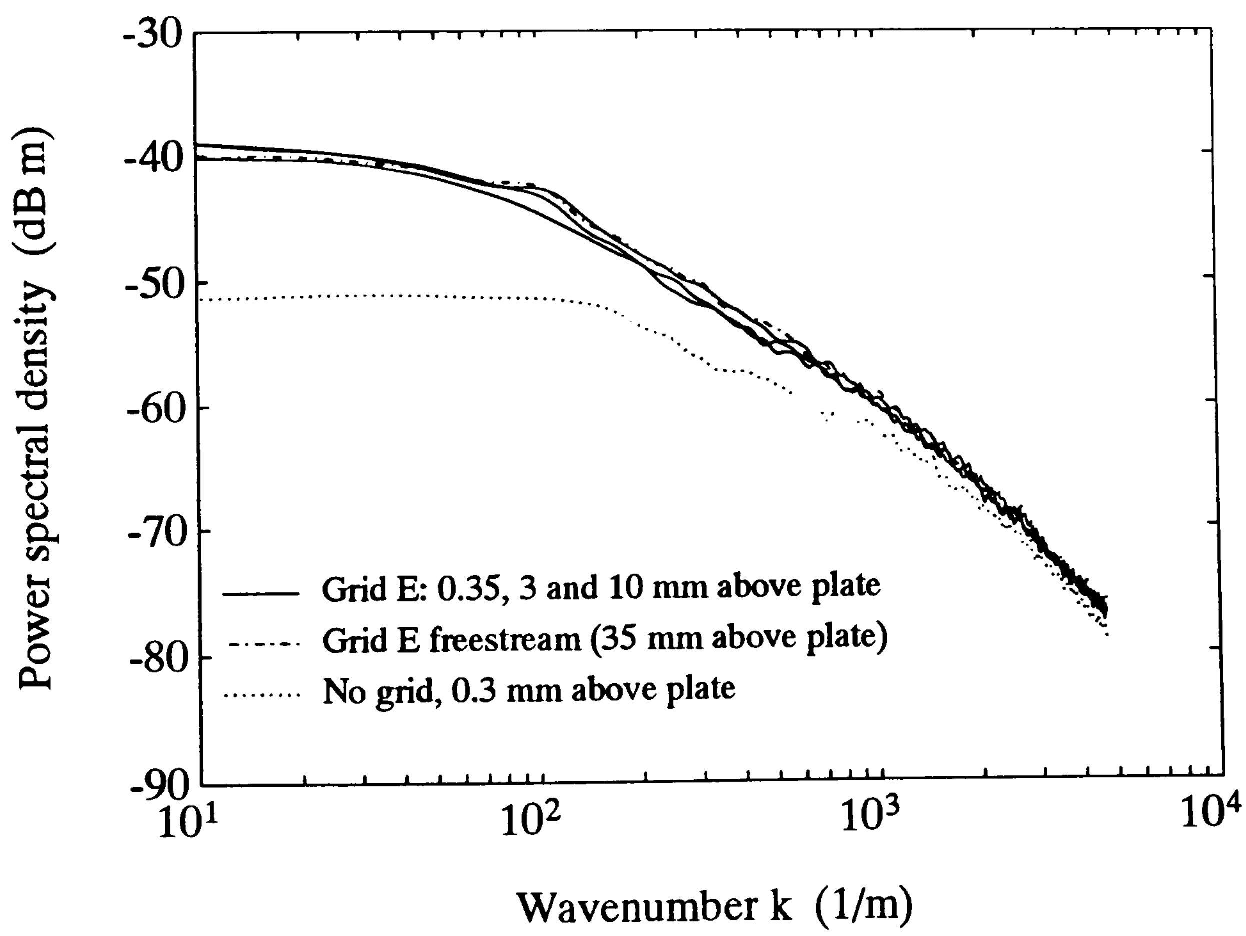

Figure 9.16. Turbulence spectra within boundary layer (grid E, x = 150 mm, tripped). Normalised using freestream velocity.

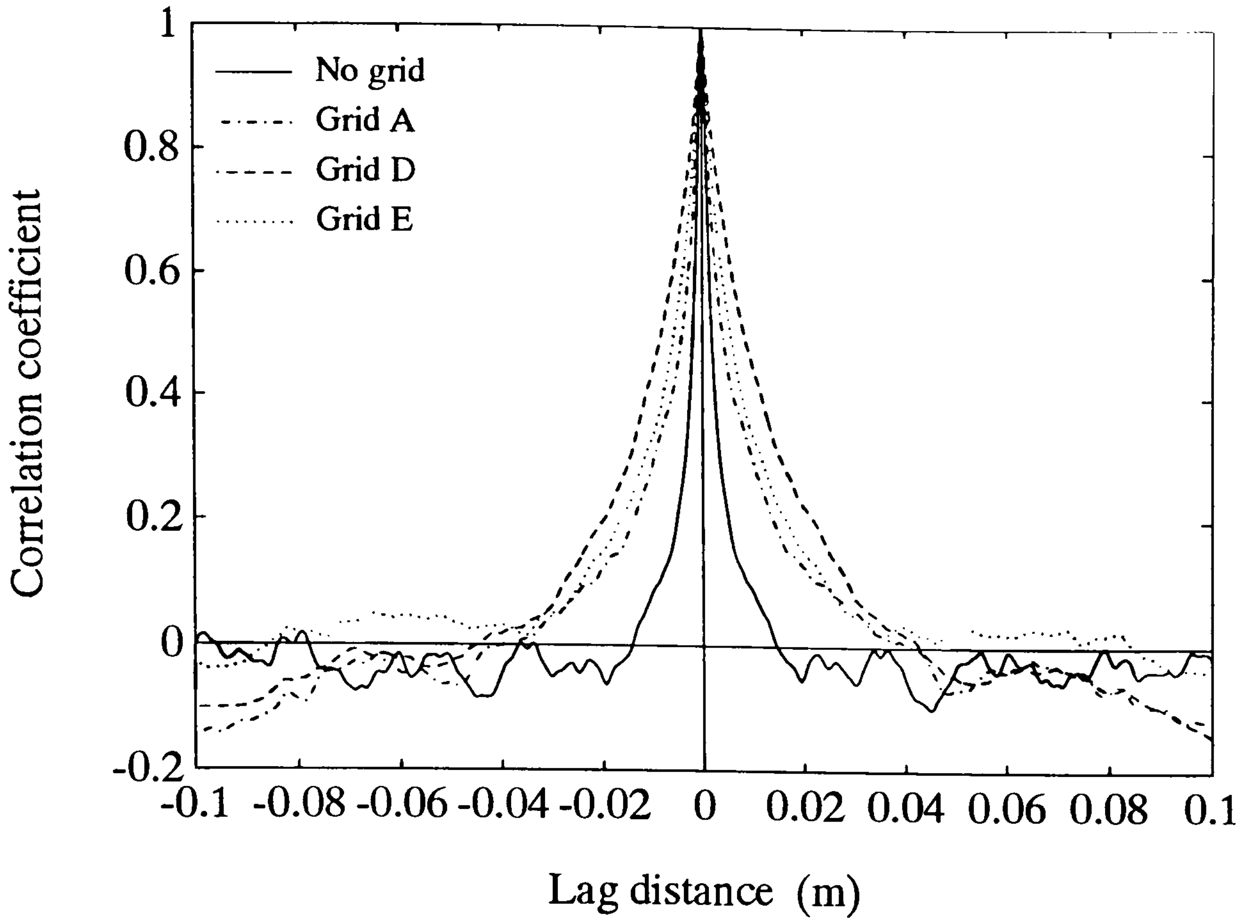

Figure 9.17. Autocorrelations of velocity signal from hot wire 0.6 mm above plate surface, x = 150 mm. Lag distance is based on freestream velocity.

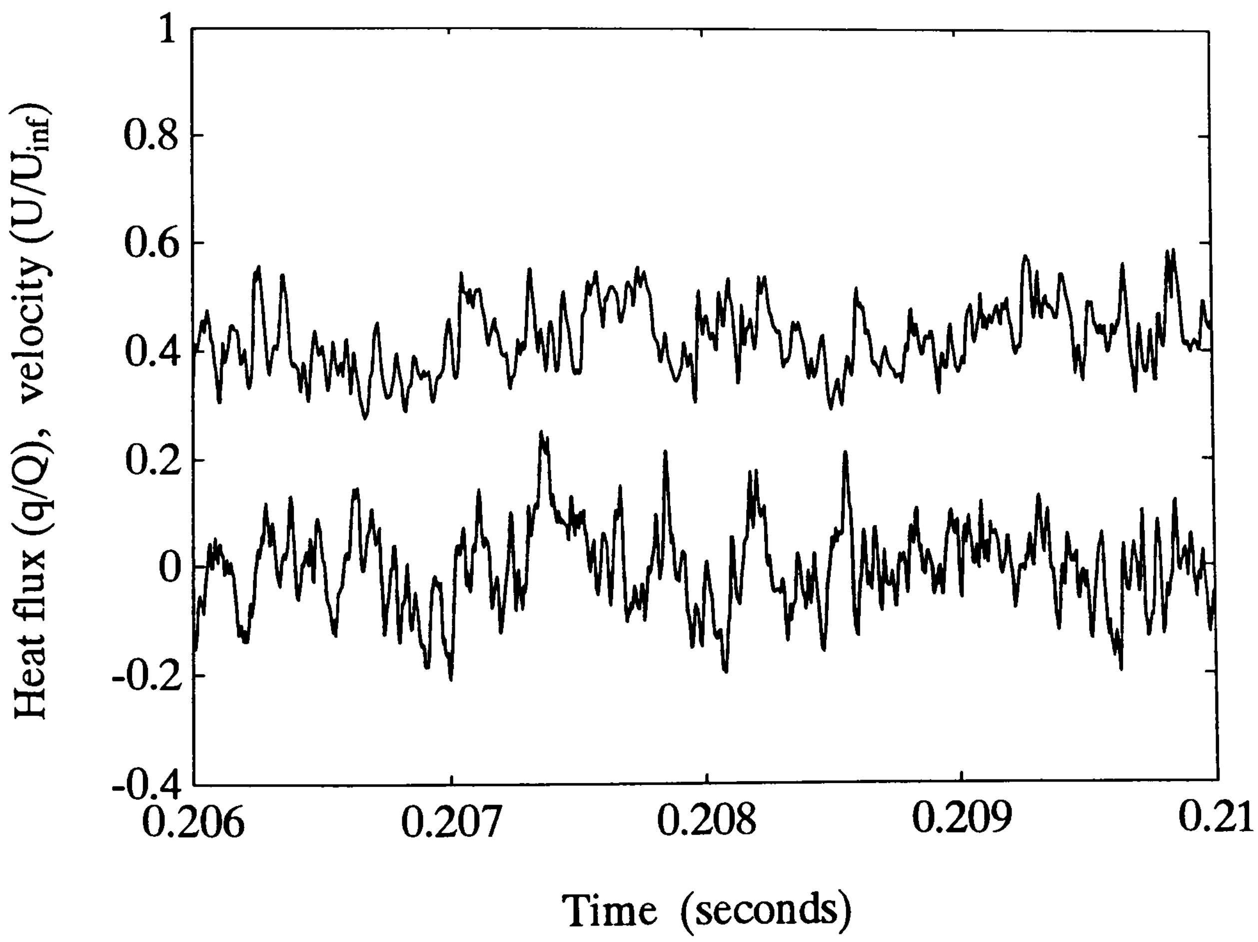

Figure 9.18. Velocity and heat flux signals with hot wire 0.5 mm above gauge. No grid.

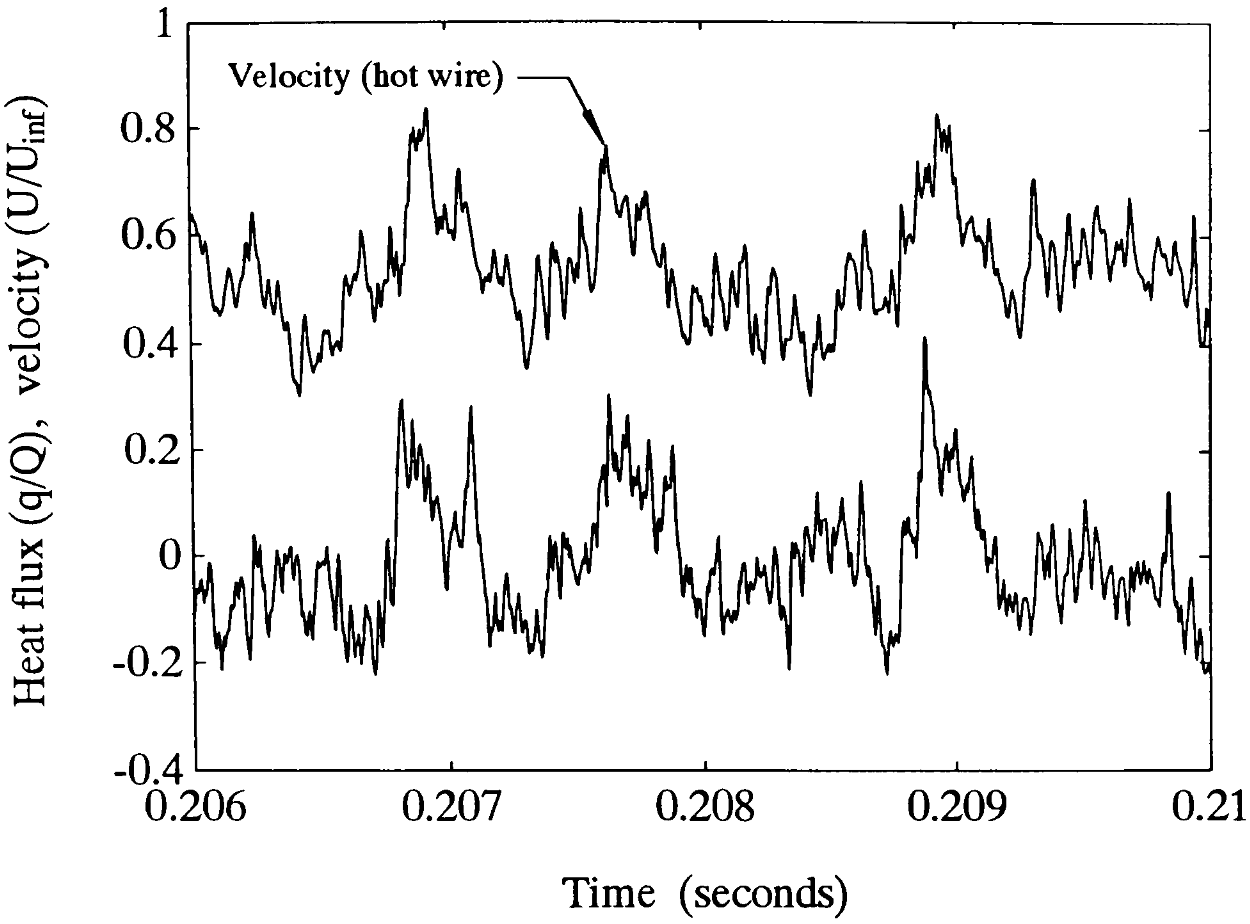

Figure 9.19. Velocity and heat flux signals, wire 0.5 mm above plate. Grid A.

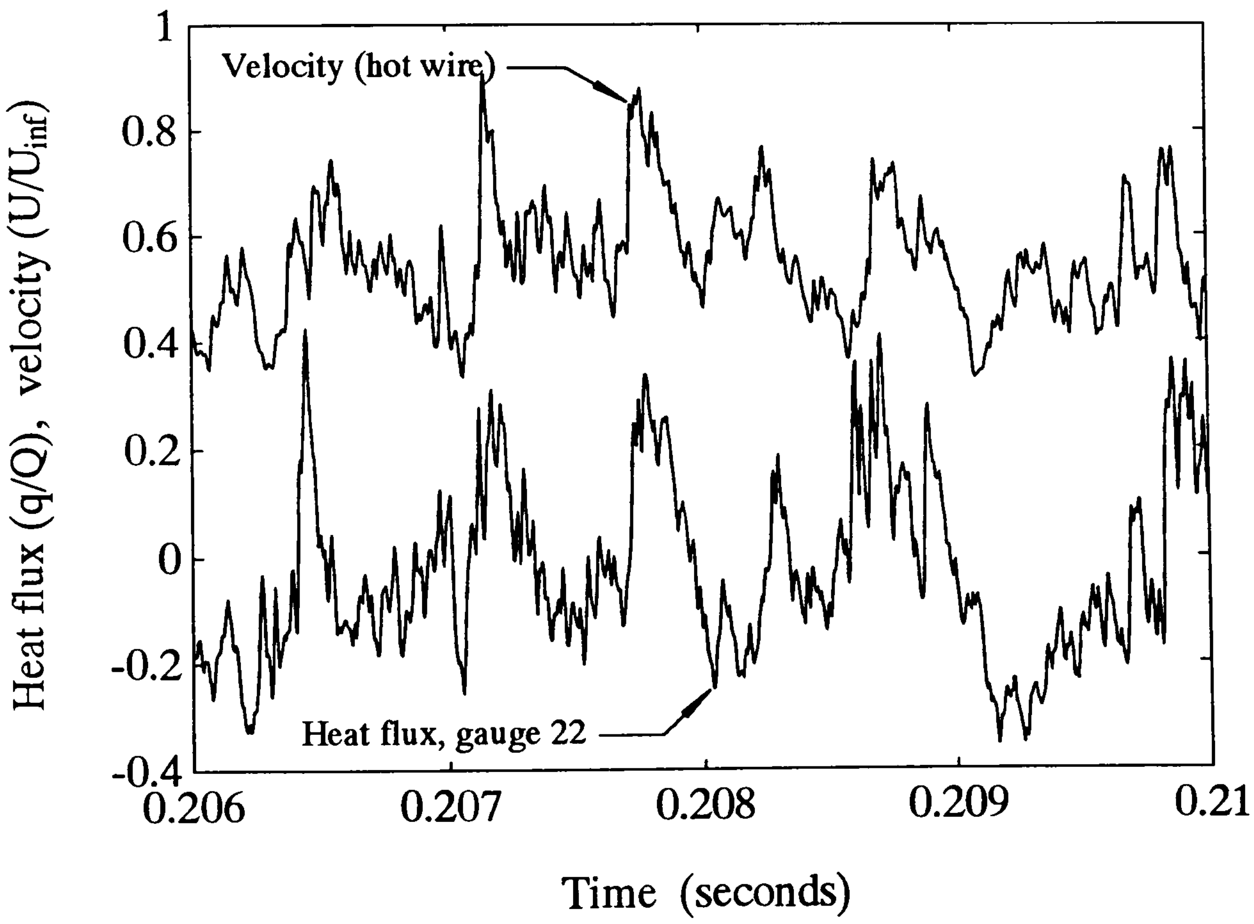

Figure 9.20. Velocity and heat flux signals, wire 0.5 mm above plate. Grid D.

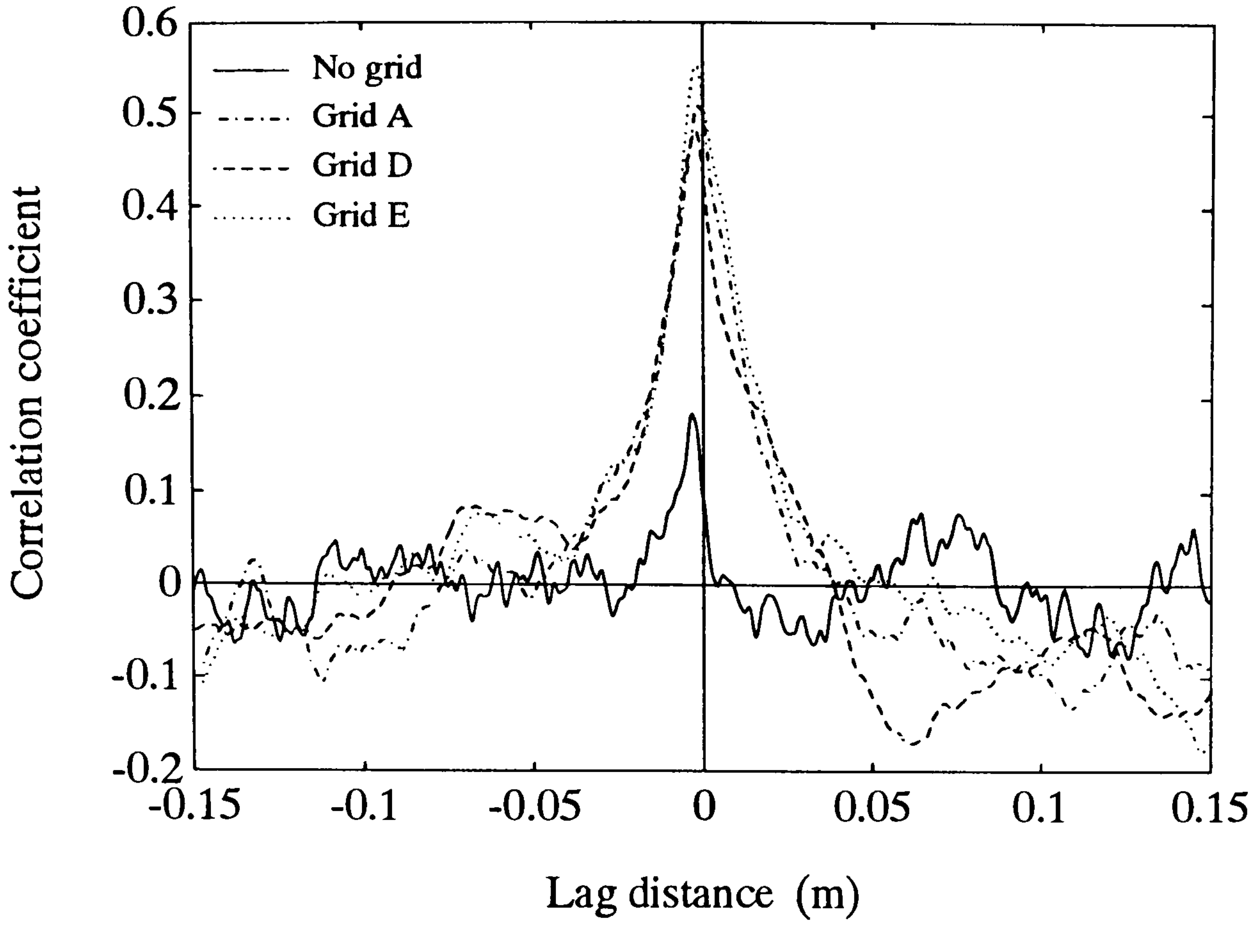

Figure 9.21. Cross-correlation of heat flux signal from gauge 22 and velocity signal from wire 0.6 mm above gauge.

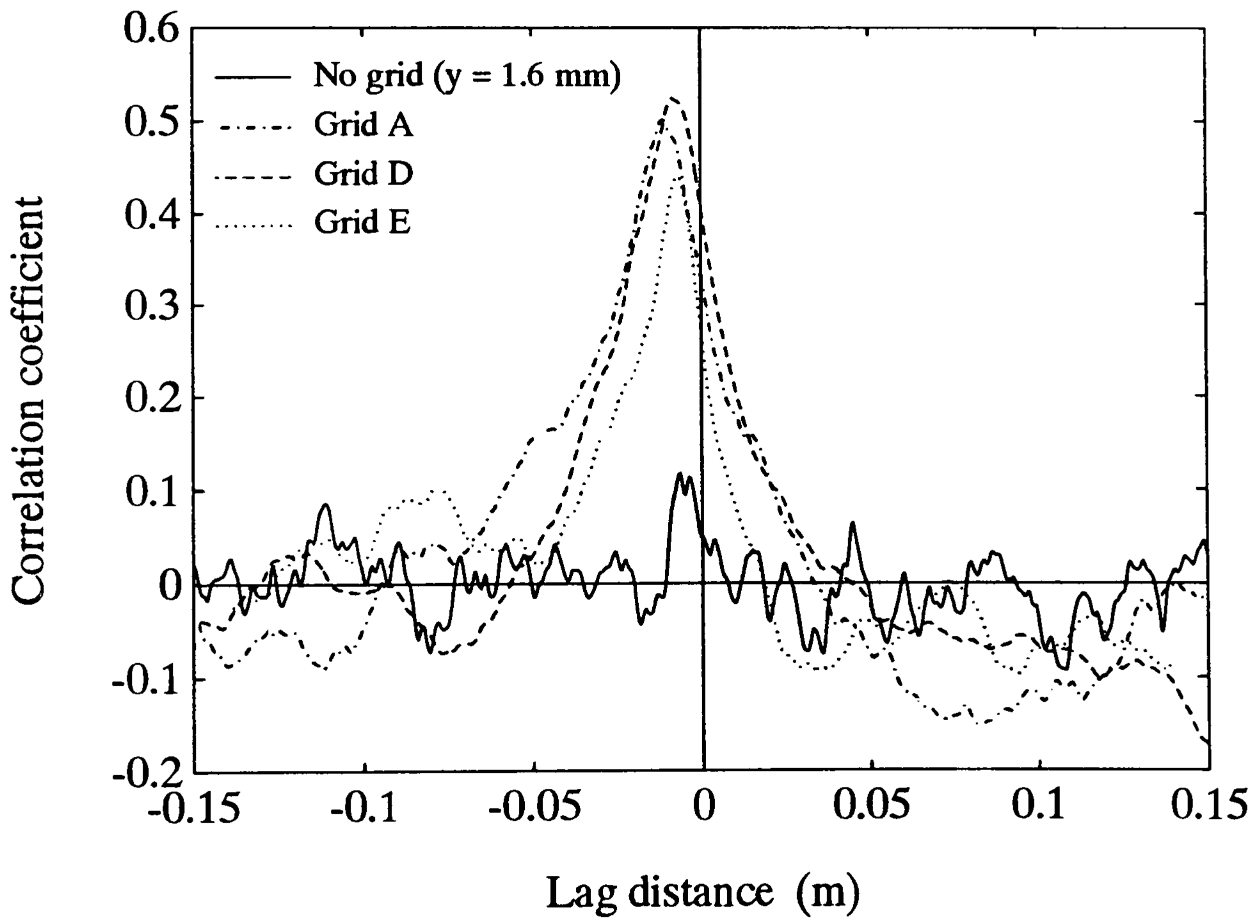

Figure 9.22. Cross-correlation of heat flux signal from gauge 22 and velocity signal from wire 3 mm above gauge.

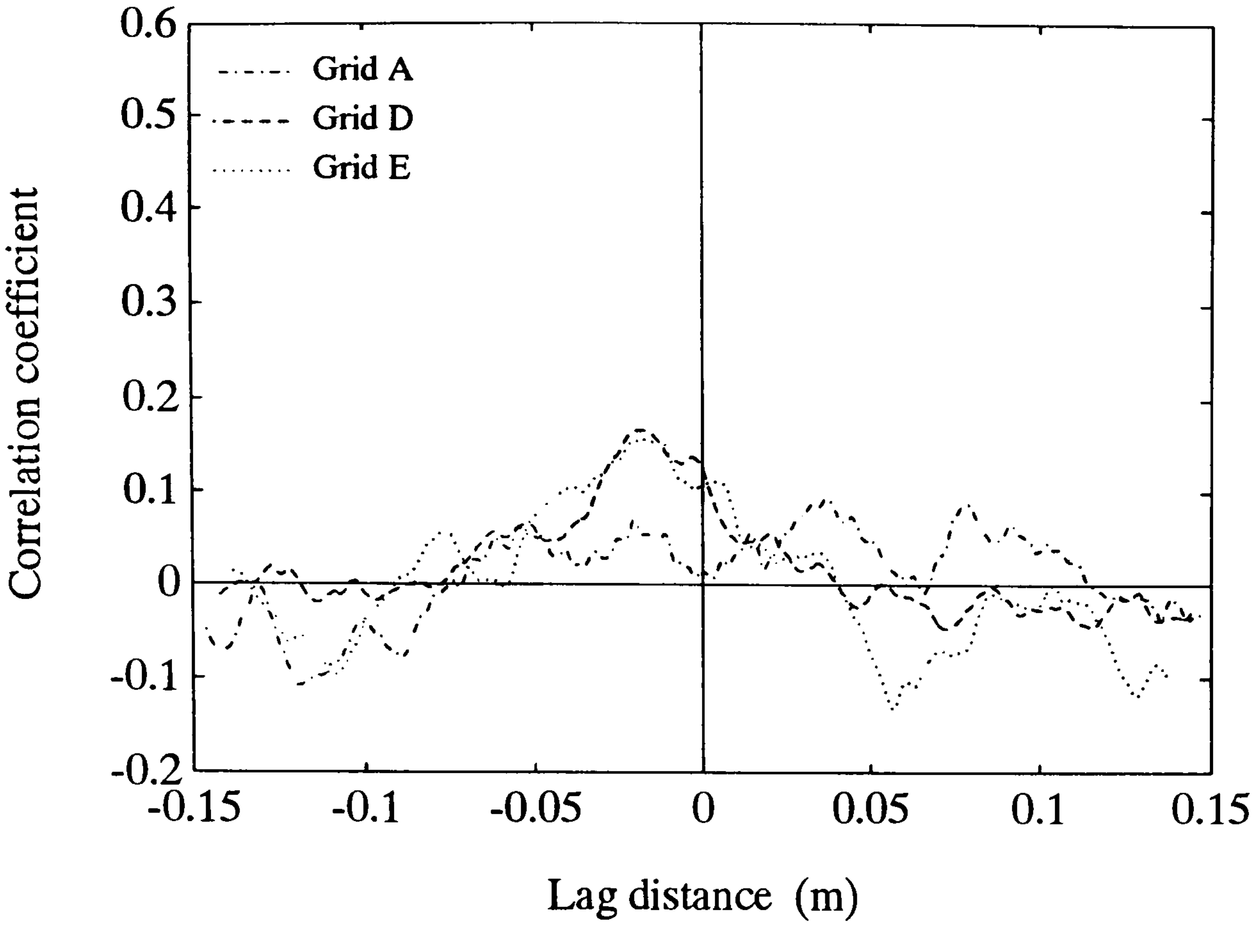

Figure 9.23. Cross-correlation of heat flux signal from gauge 22 and velocity signal from wire 10 mm above gauge.

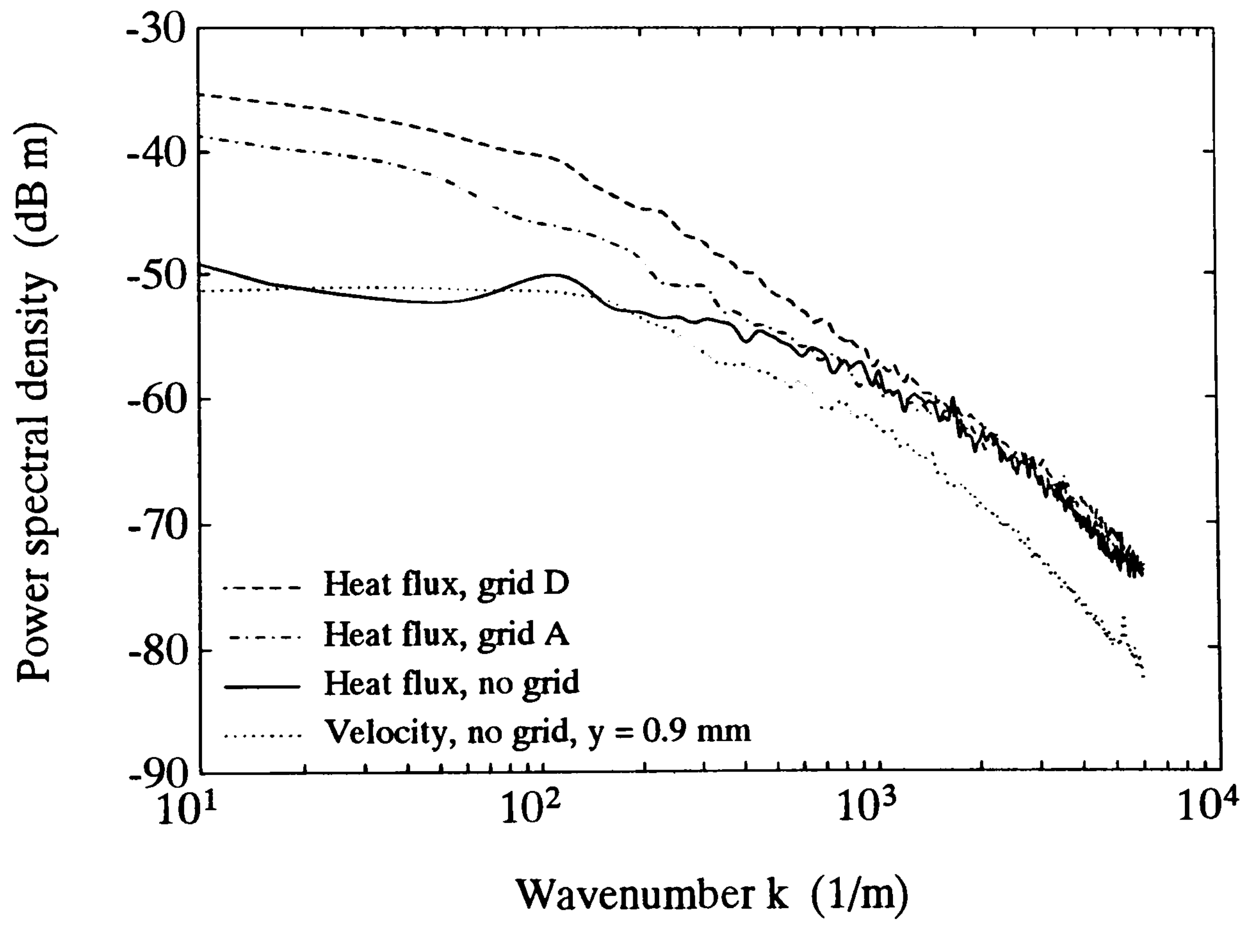

Figure 9.24. Comparison of heat flux spectra at high, low and zero freestream turbulence and velocity spectrum at y = 0.9 mm for latter.

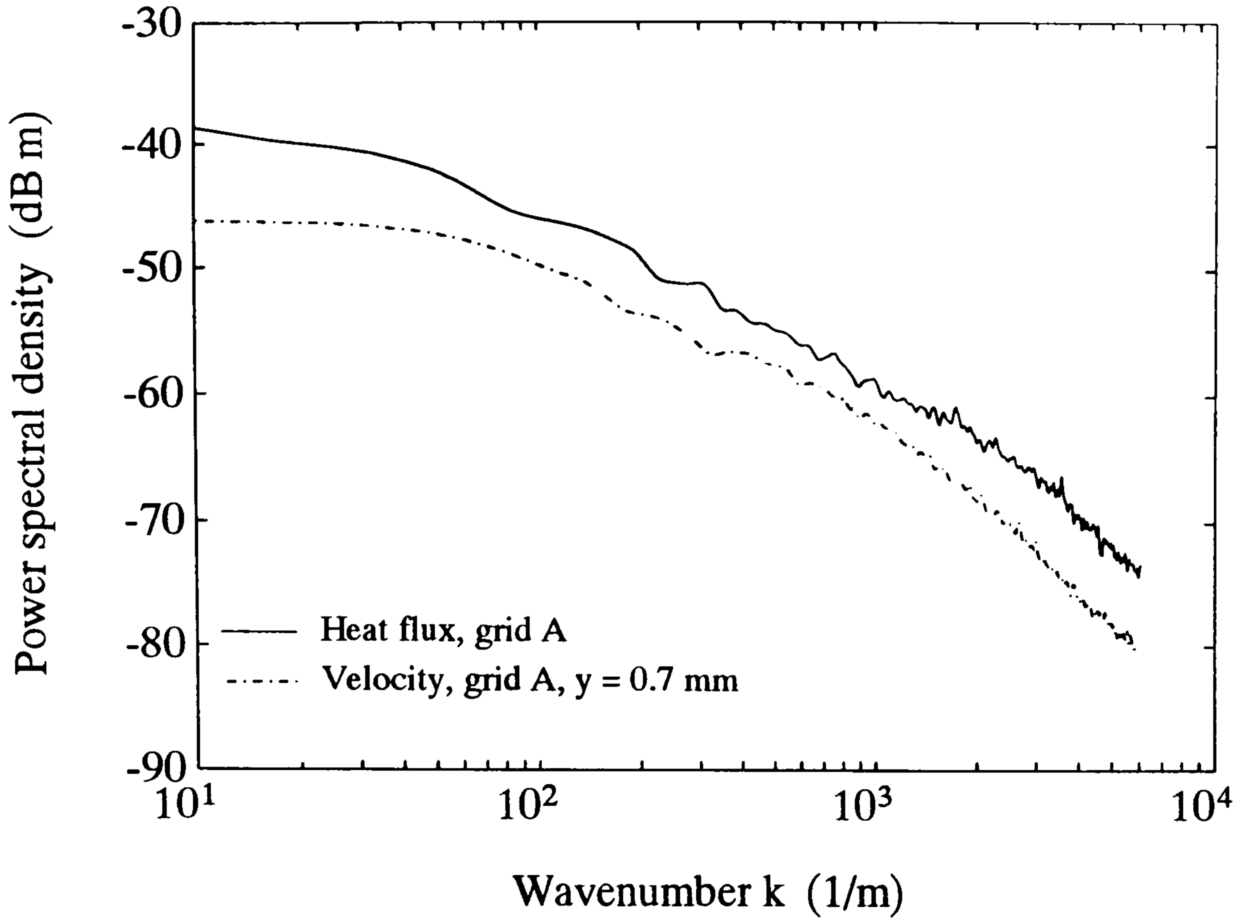

Figure 9.25. Comparison of heat flux and velocity spectra (y = 0.7 mm) with grid A.

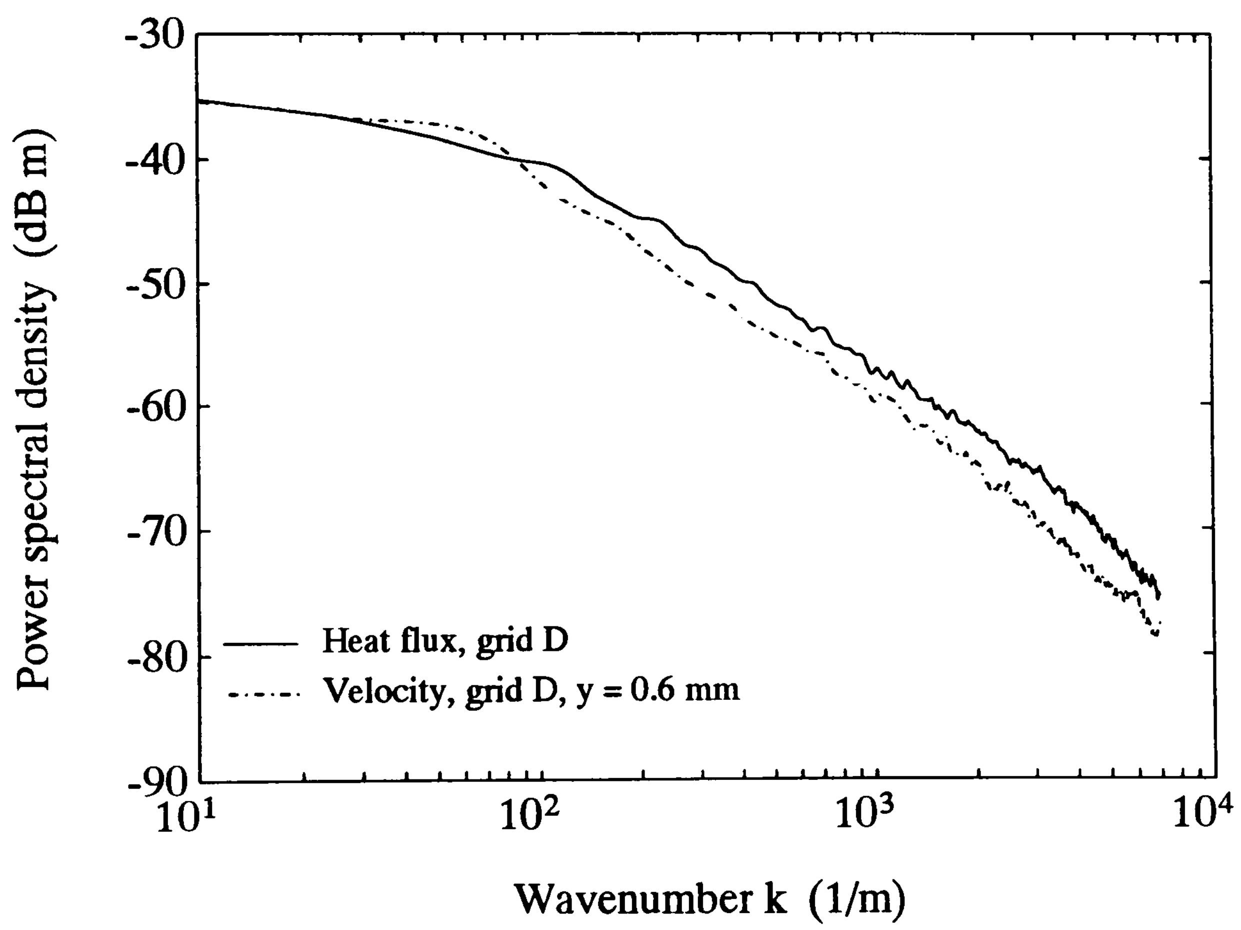

Figure 9.26. Comparison of heat flux and velocity spectra (y = 0.6 mm) with grid D.

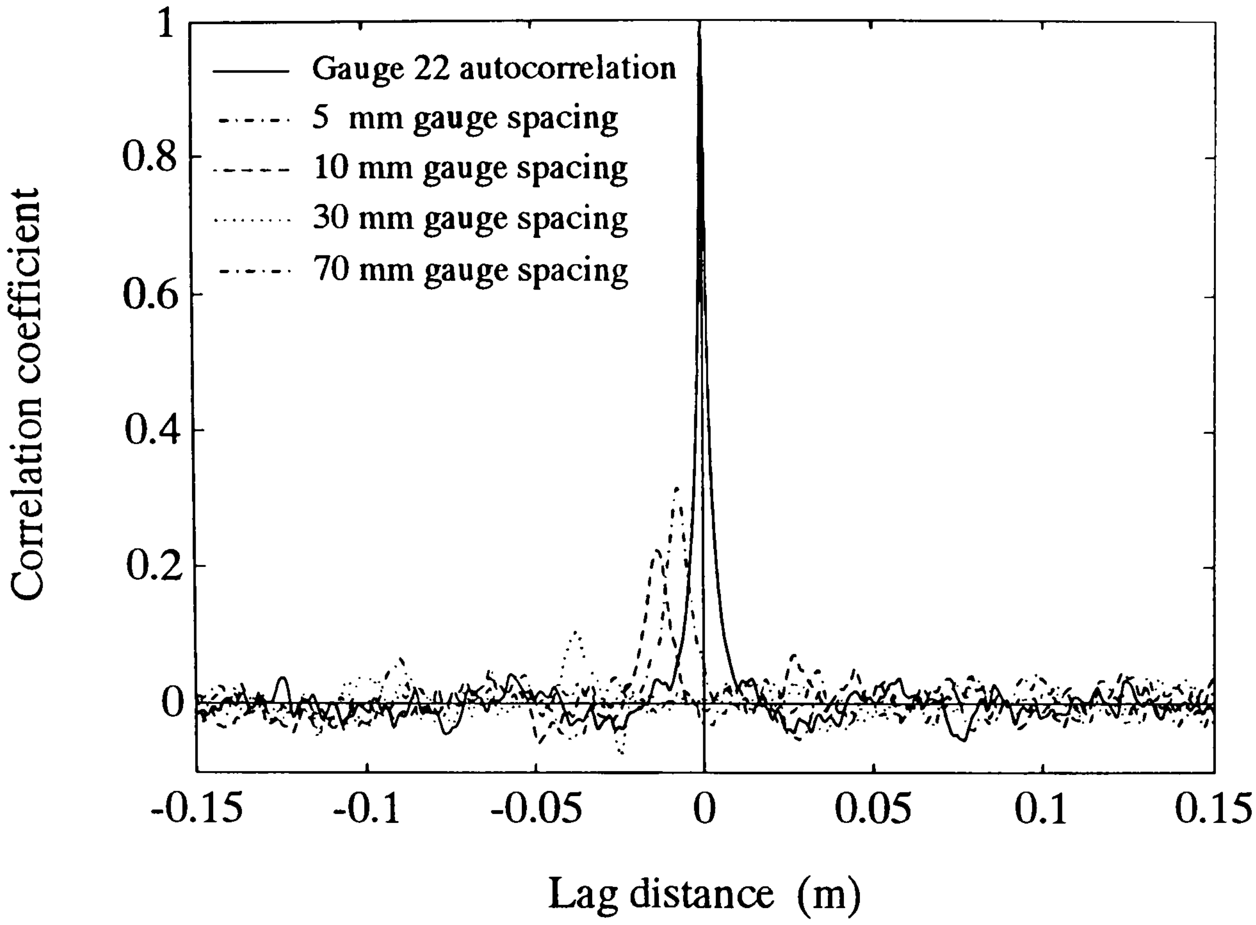

Figure 9.27. Cross correlation of gauges at x = 80, 120, 140, 145 and 150 mm with the 150 mm gauge signal. No grid.

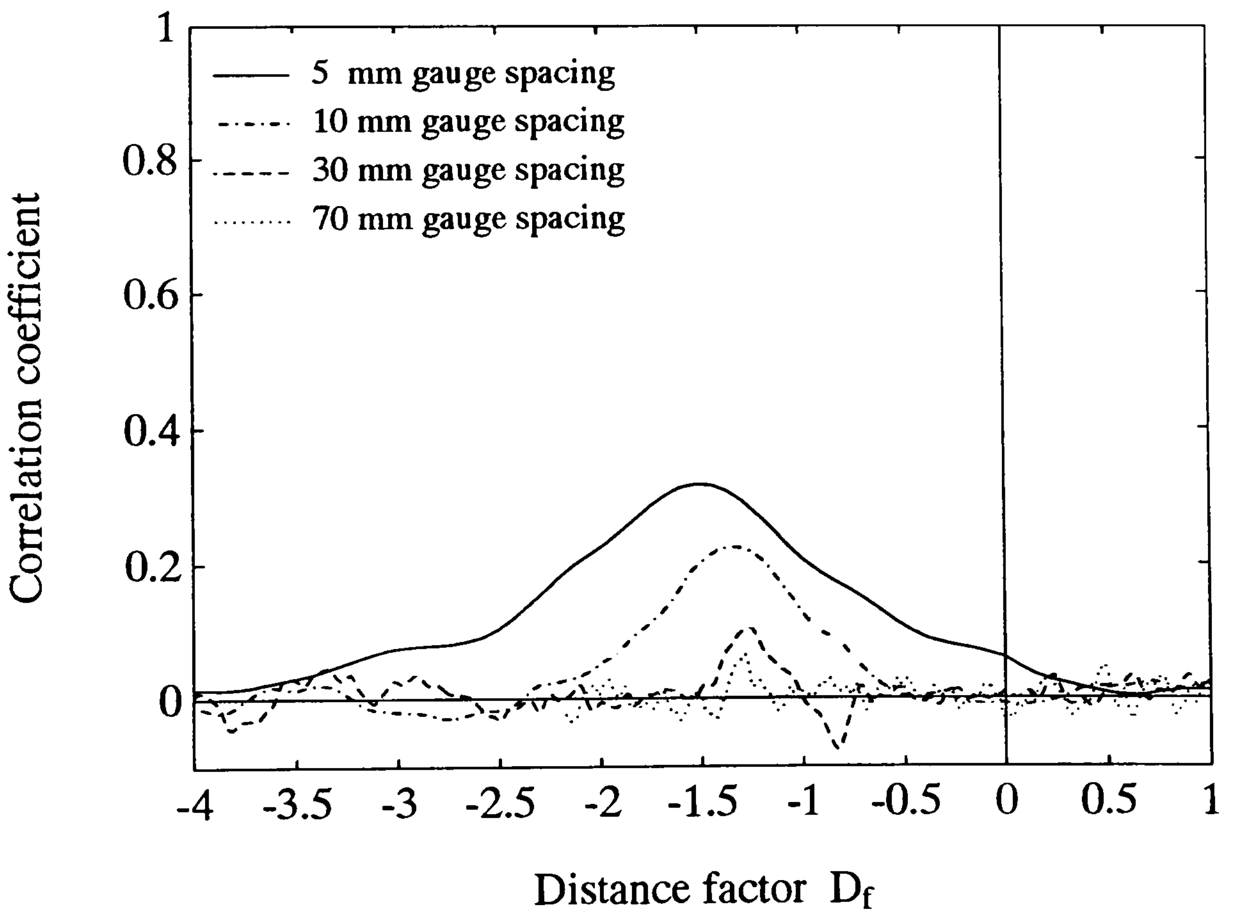

Figure 9.28. Data from Figure 9.27 with x-axis values divided by gauge spacing to show event transit time relative to time at freestream velocity. (No grid.)

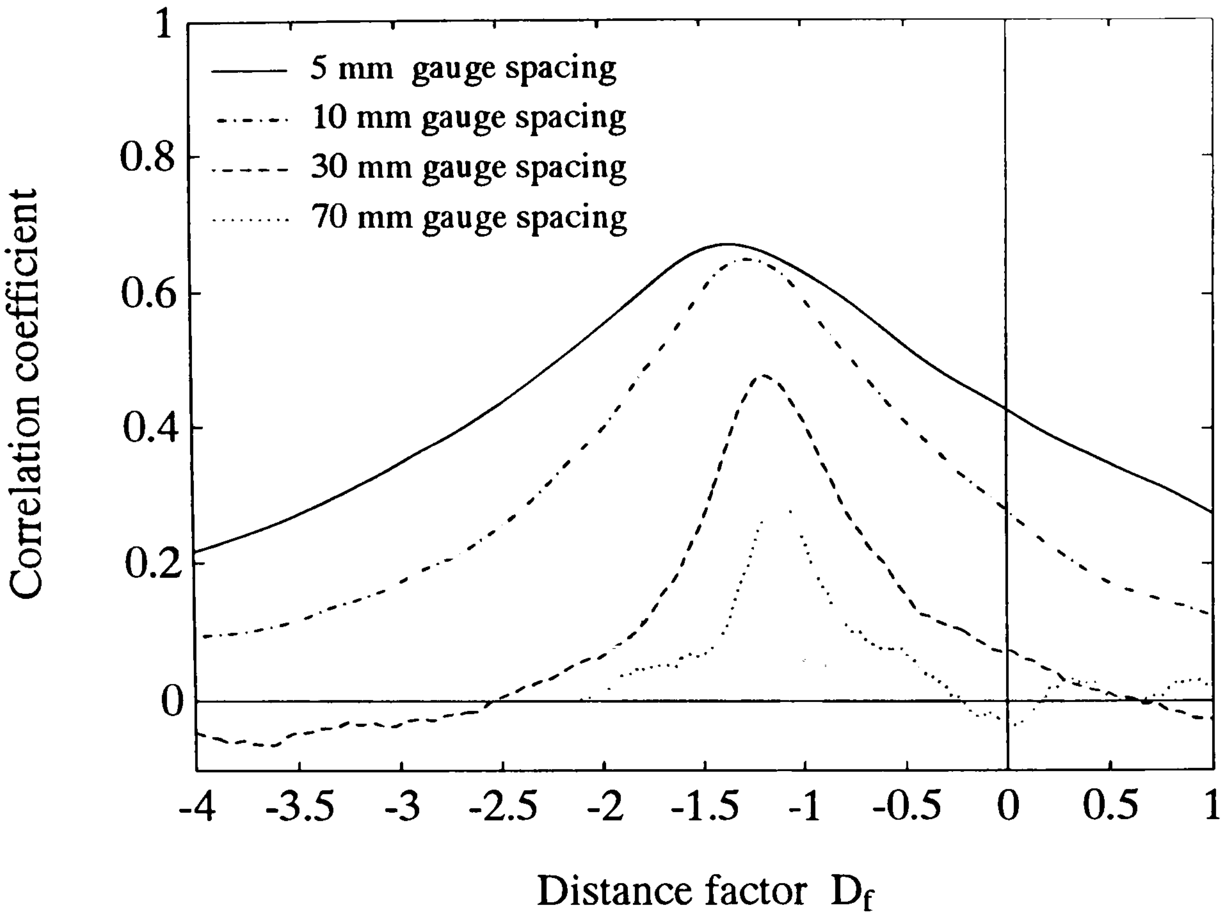

Figure 9.29. Gauge signal cross-correlation - transit time of events relative to time at freestream velocity. Grid A.

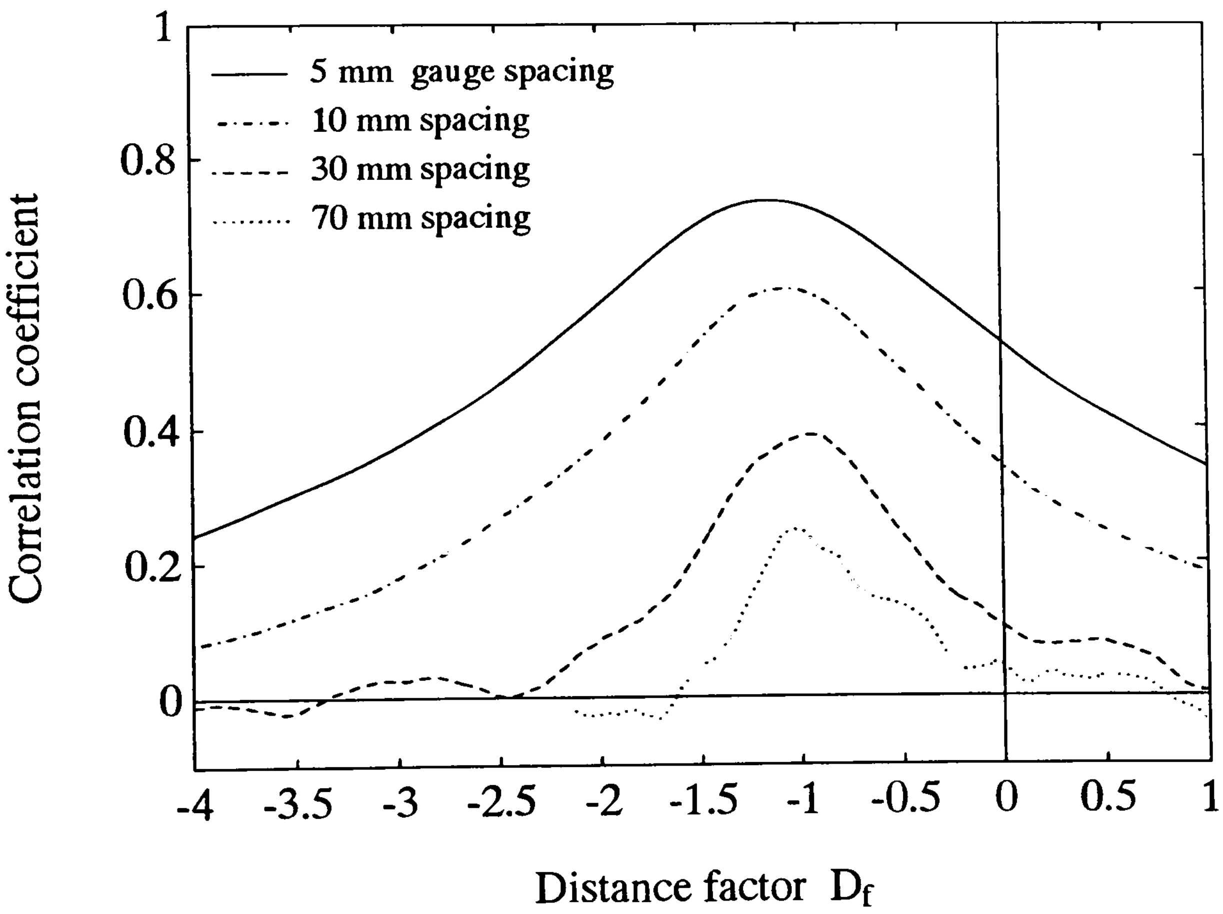

Figure 9.30. Gauge signal cross-correlation - transit time of events relative to time at freestream velocity. Grid D.

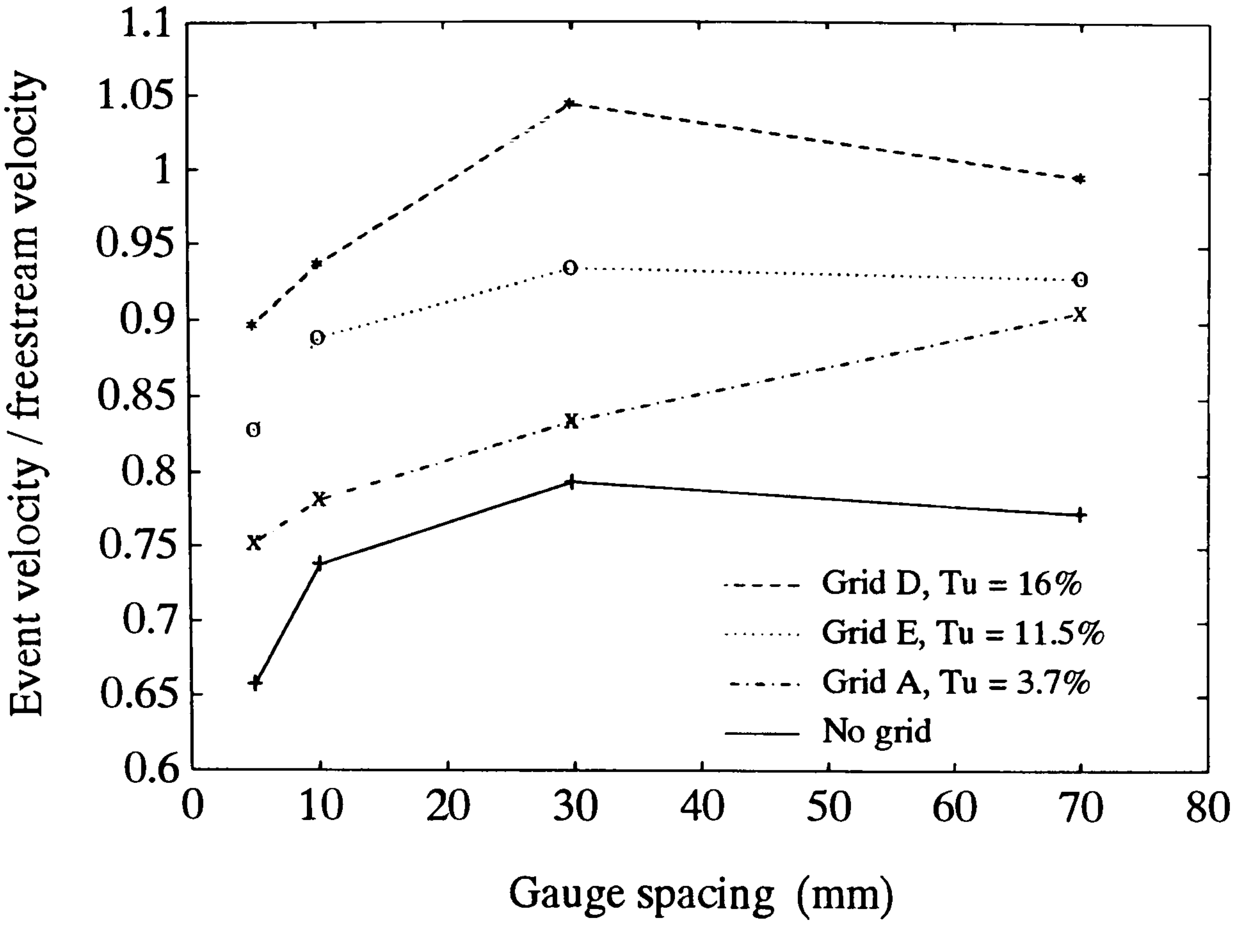

Figure 9.31. Velocity relative to freestream of heat flux perturbances, as inferred from position of correlation peaks. *Tu* given at x = 125 mm.

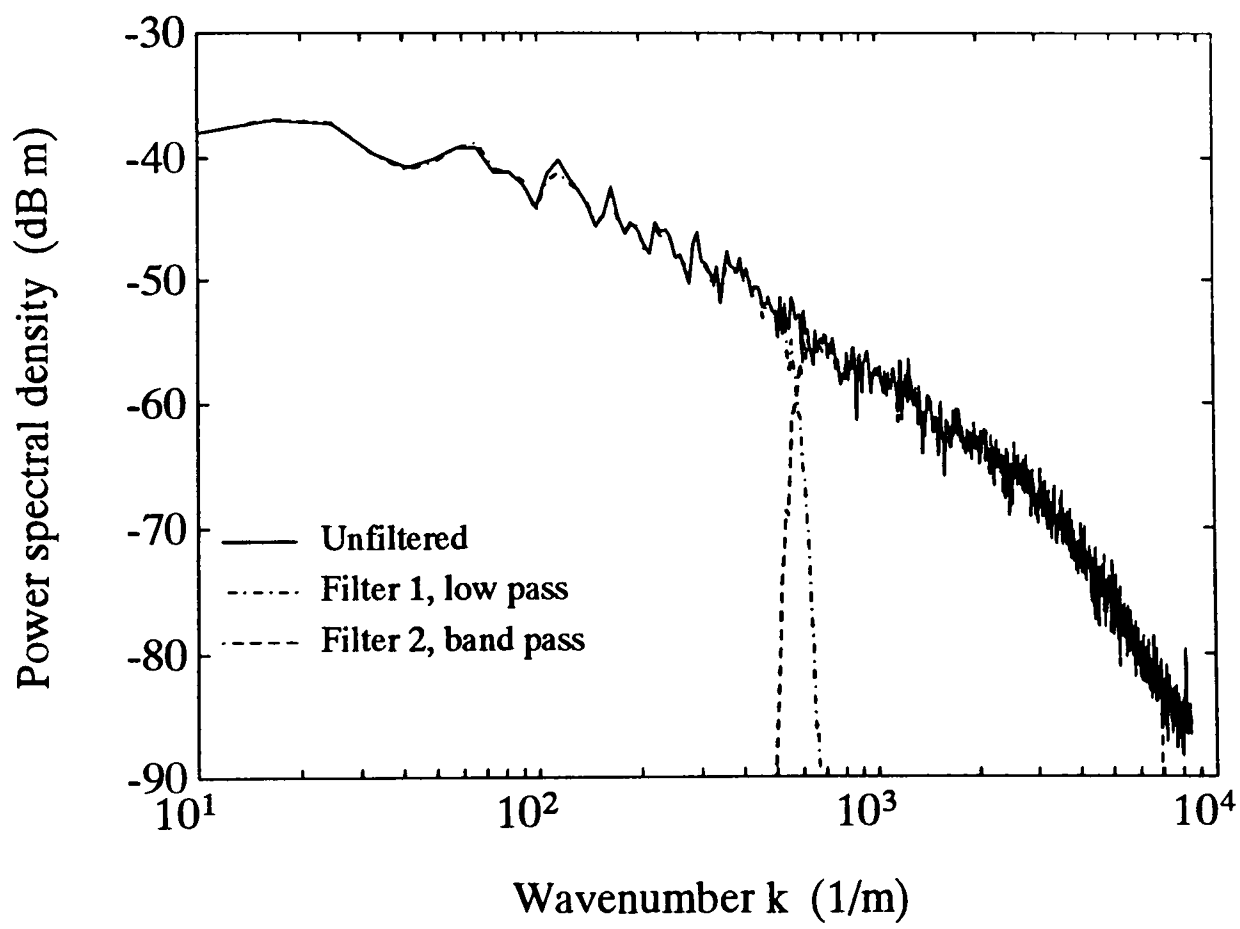

Figure 9.32. Effect of digital filters on heat flux spectrum from gauge 22. (Grid D).

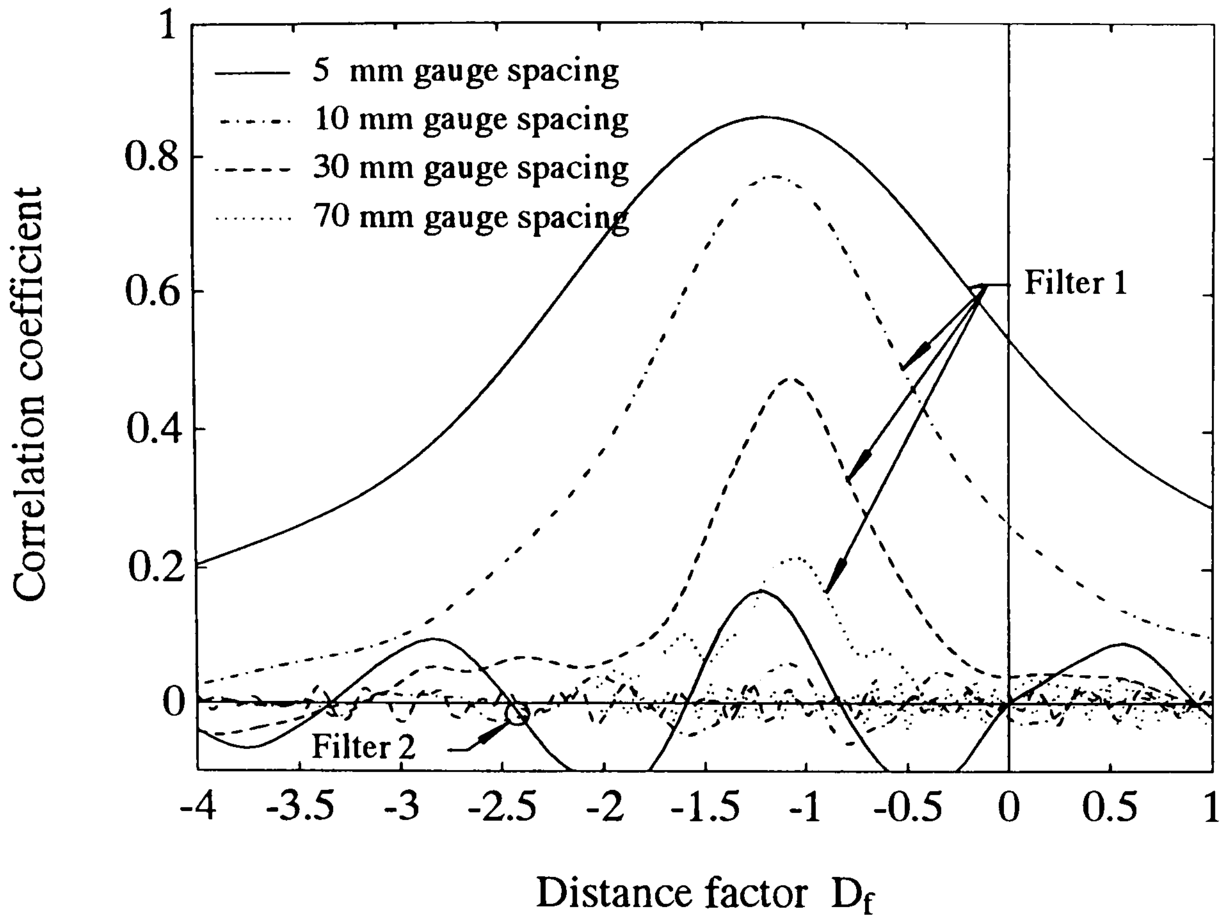

Figure 9.33. Cross-correlations after low pass (filter 1) and high pass (filter 2) filtering. Grid E.

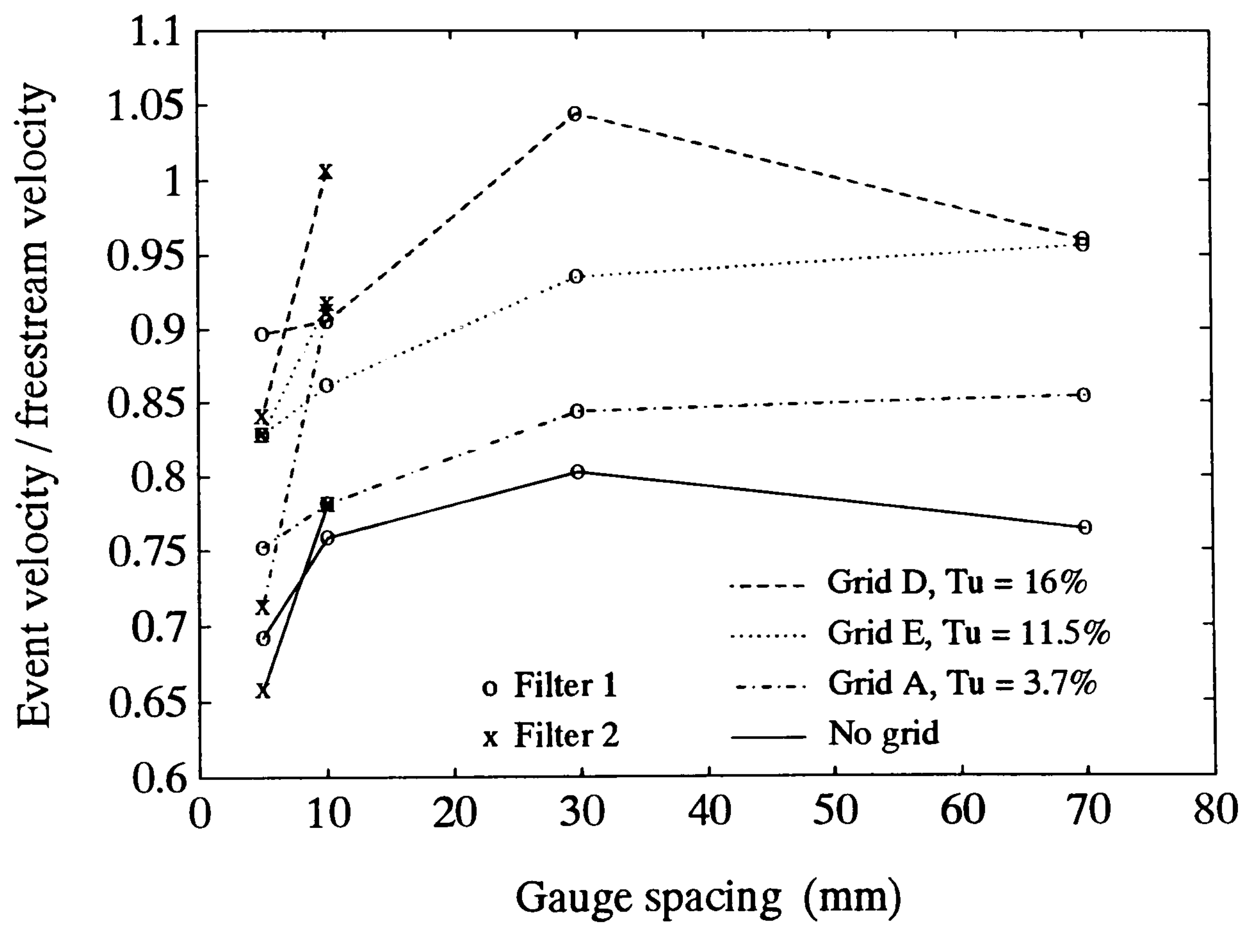

Figure 9.34. Event propagation velocity ratios determined from cross-correlations after low- and high-pass filtering.

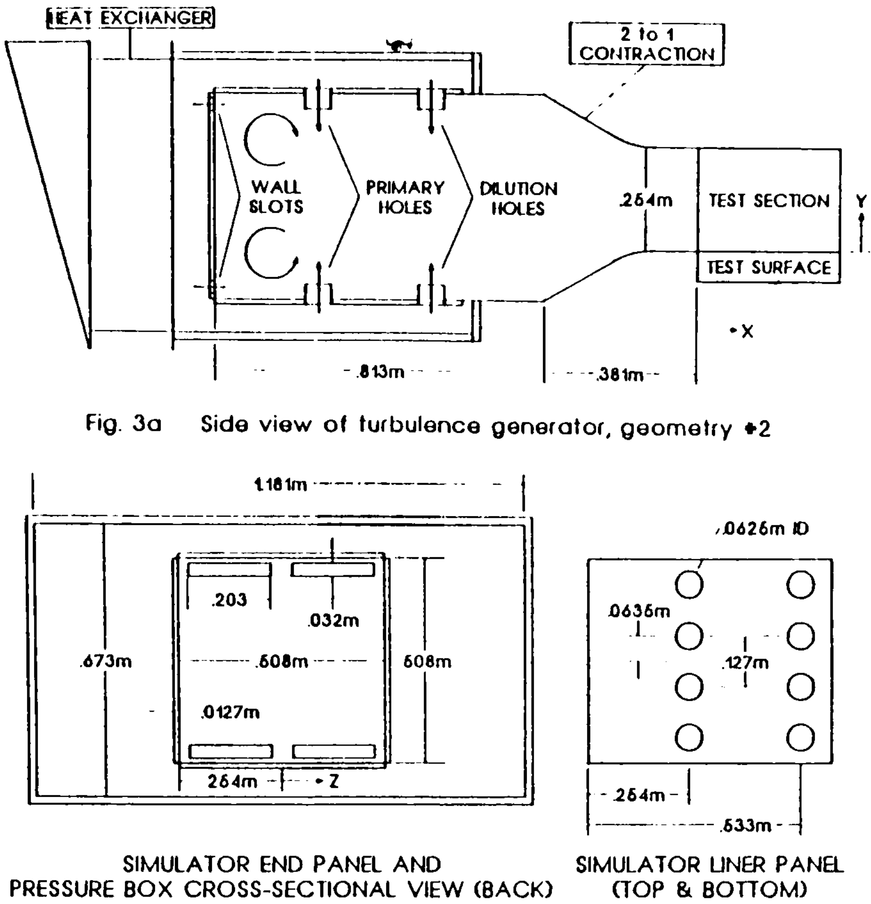

Figure 10.1. Simulated combustor design used by **Ames and Moffat (1990).**

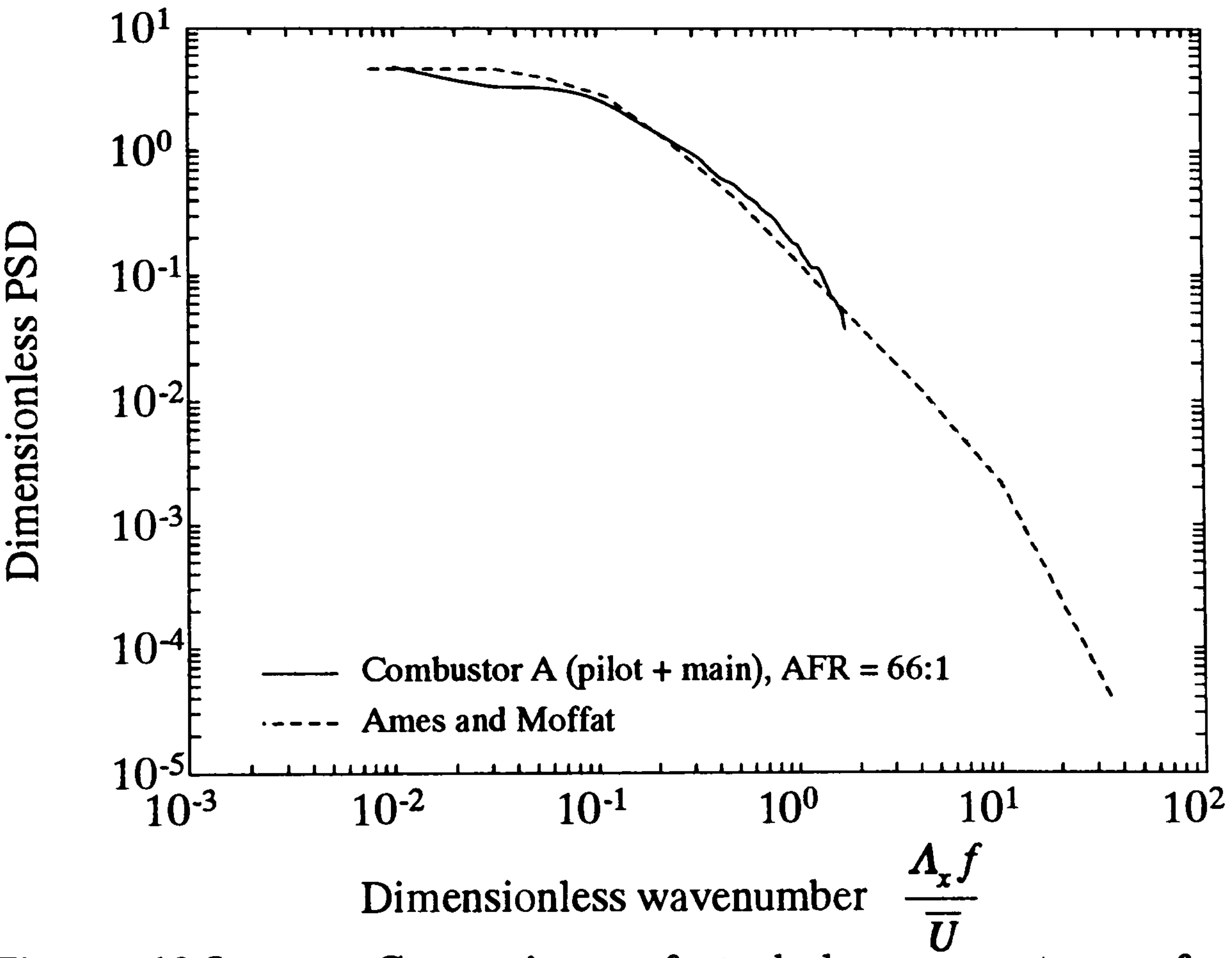

Figure 10.2. Comparison of turbulence spectrum from Combustor A (as Figure 4.12) with that measured by **Ames and Moffat.**

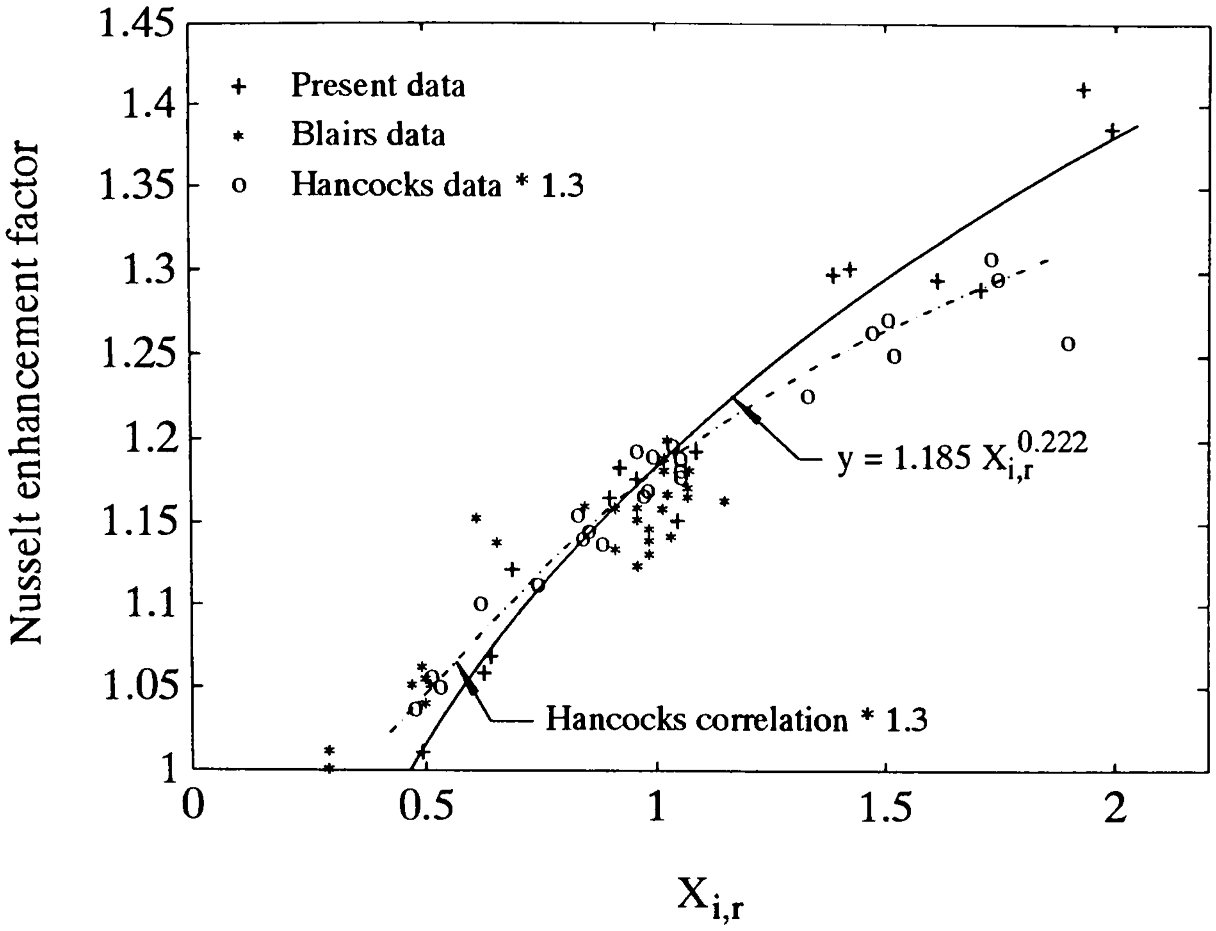

Figure 10.3. Comparison of flat plate results with data from **Blair (1983)** and **Hancock and Bradshaw (1983)**.

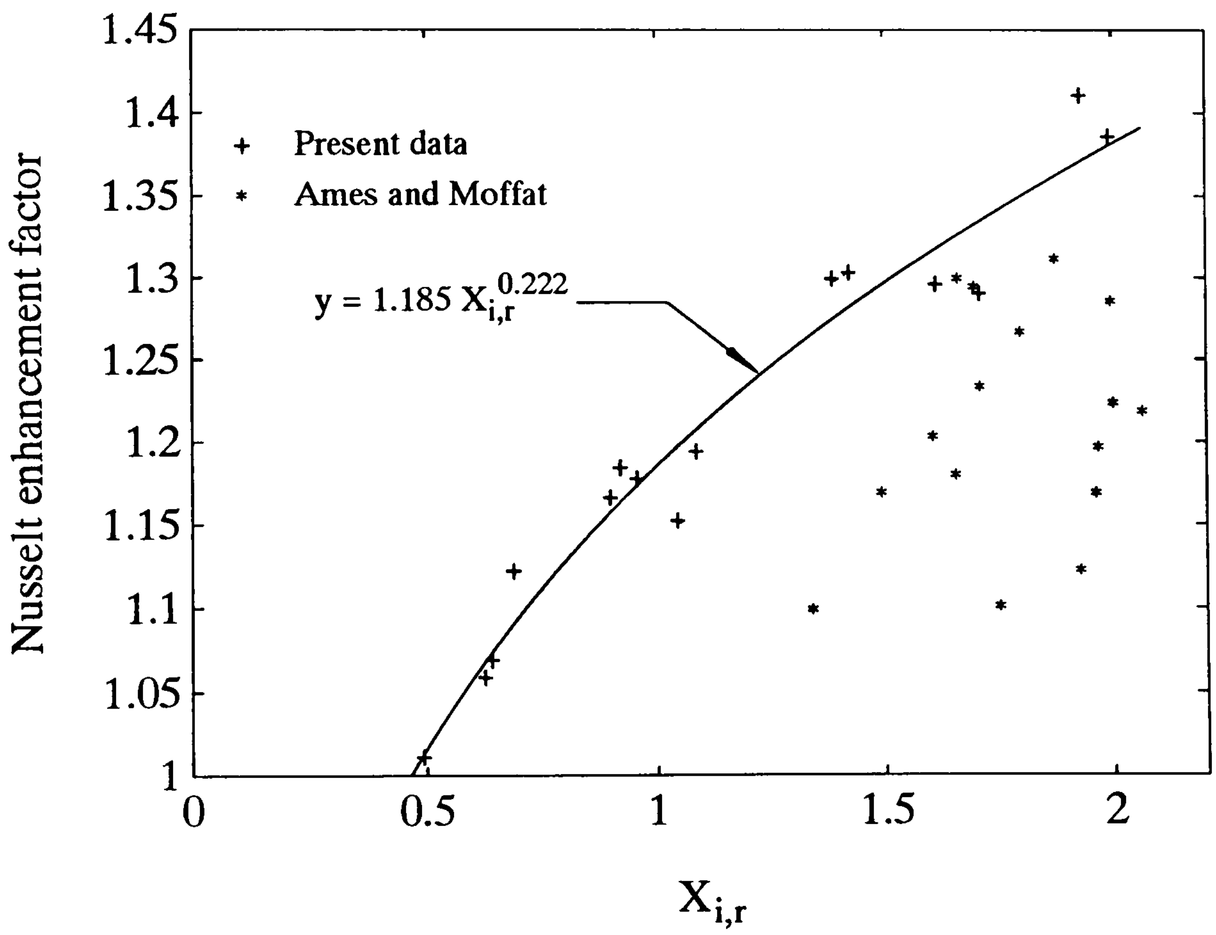

Figure 10.4. Comparison of data by **Ames and Moffat** with flat plate data and correlation.

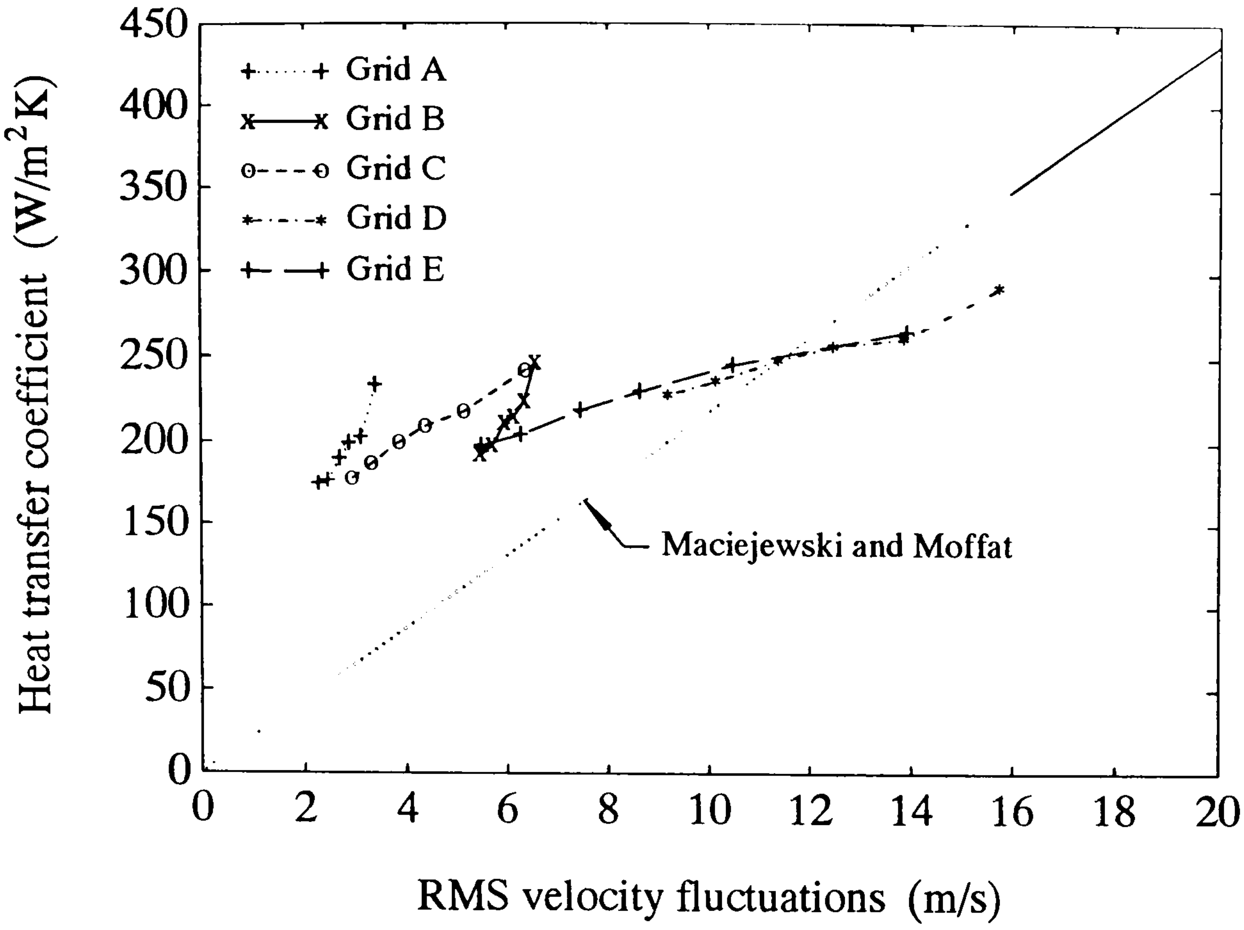

Figure 10.5. Comparison of flat plate results with high-turbulence correlation by **Maciejewski and Moffat (1989)**.

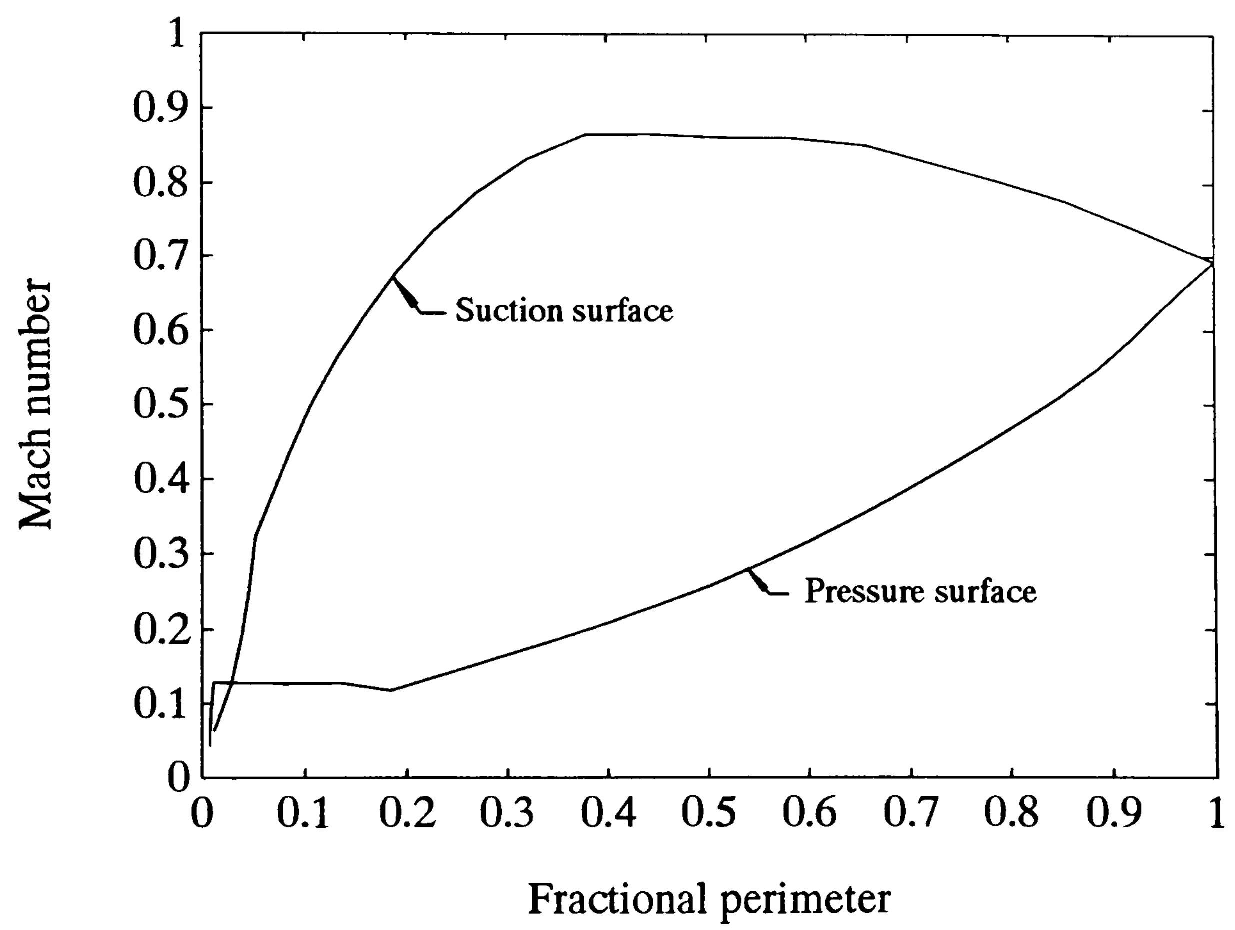

Figure 10.6. Typical Mach number distribution around a high pressure nozzle guide vane.

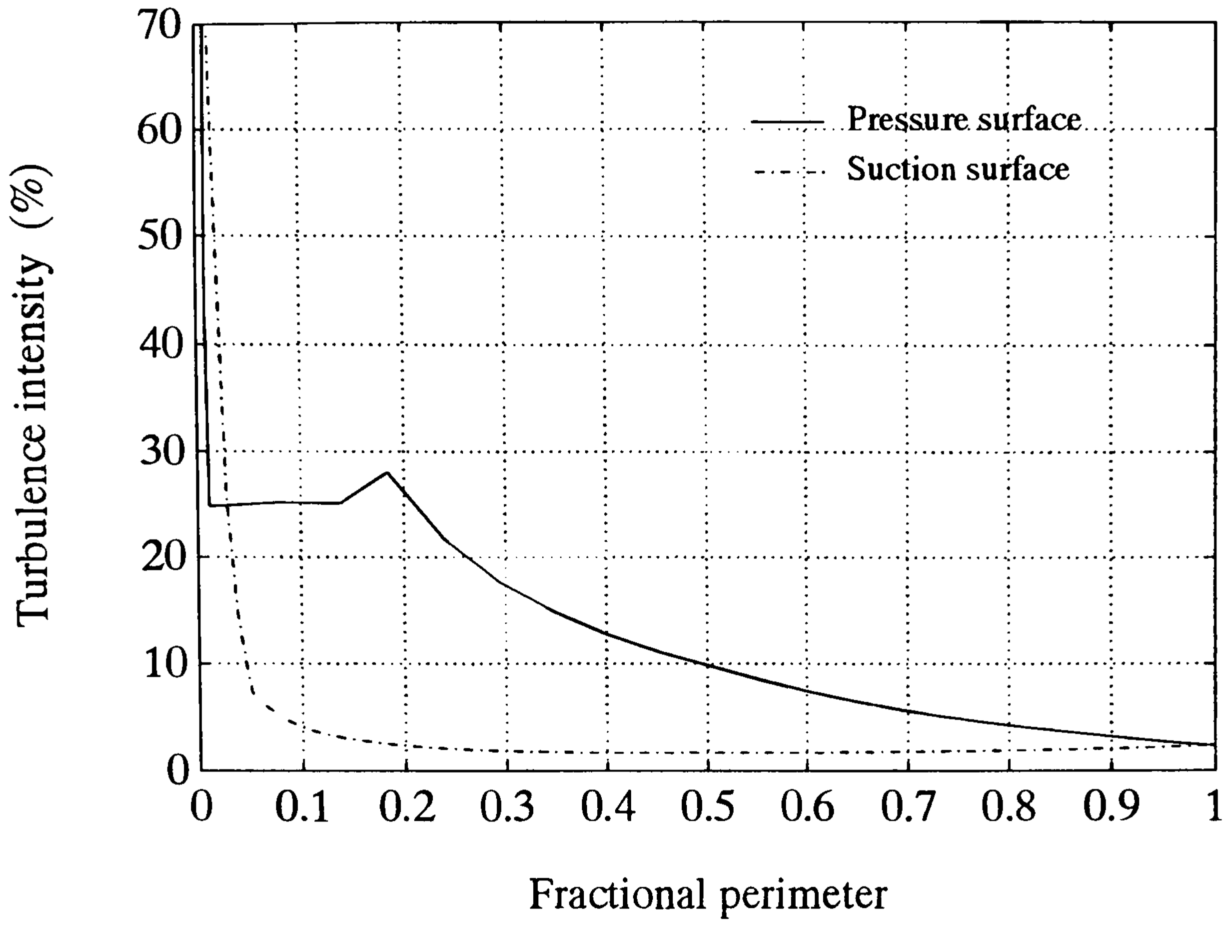

Figure 10.7. Predicted turbulence distribution around a typical nozzle guide vane.

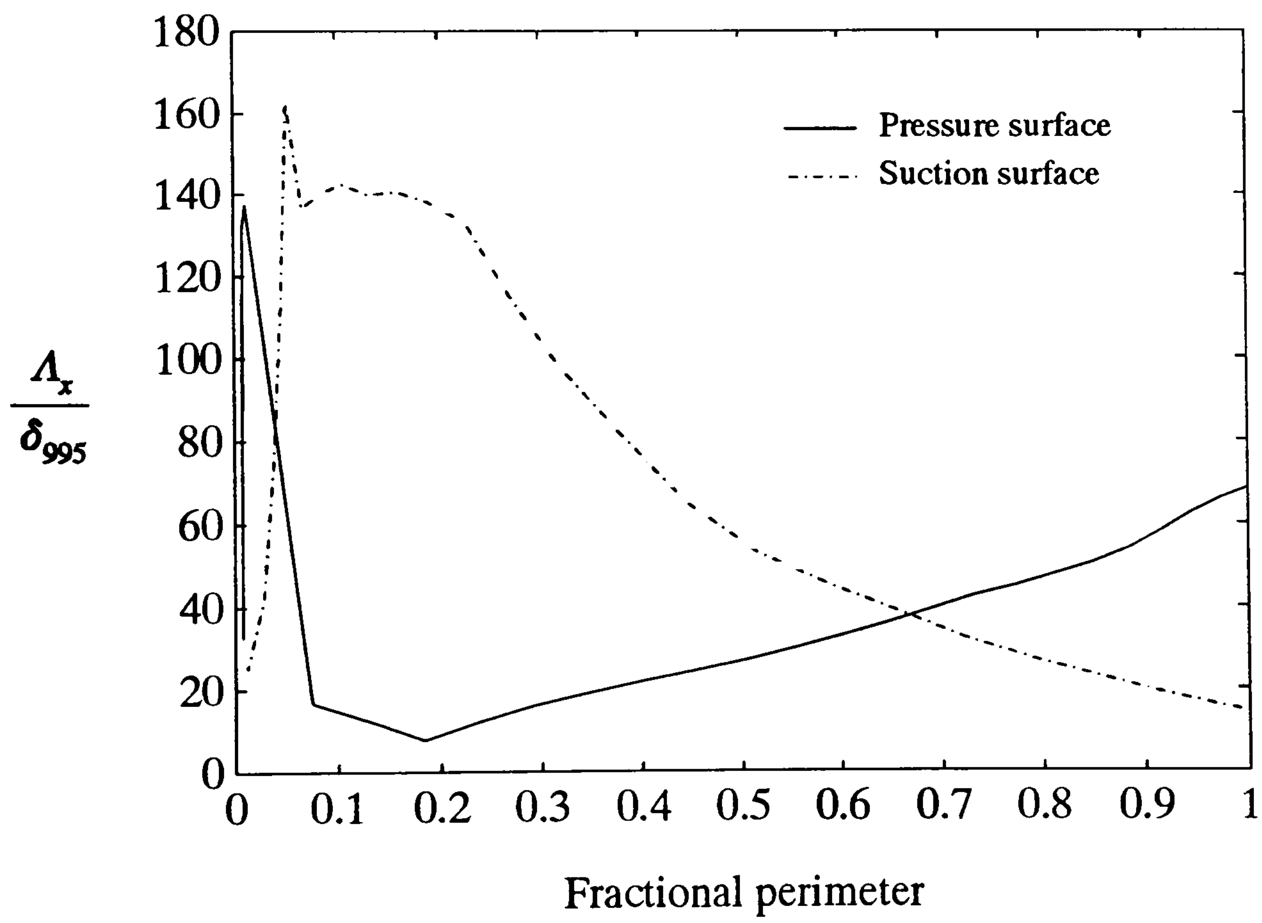

Figure 10.8. Predicted ratio of integral length scale to boundary layer thickness around a nozzle guide vane.

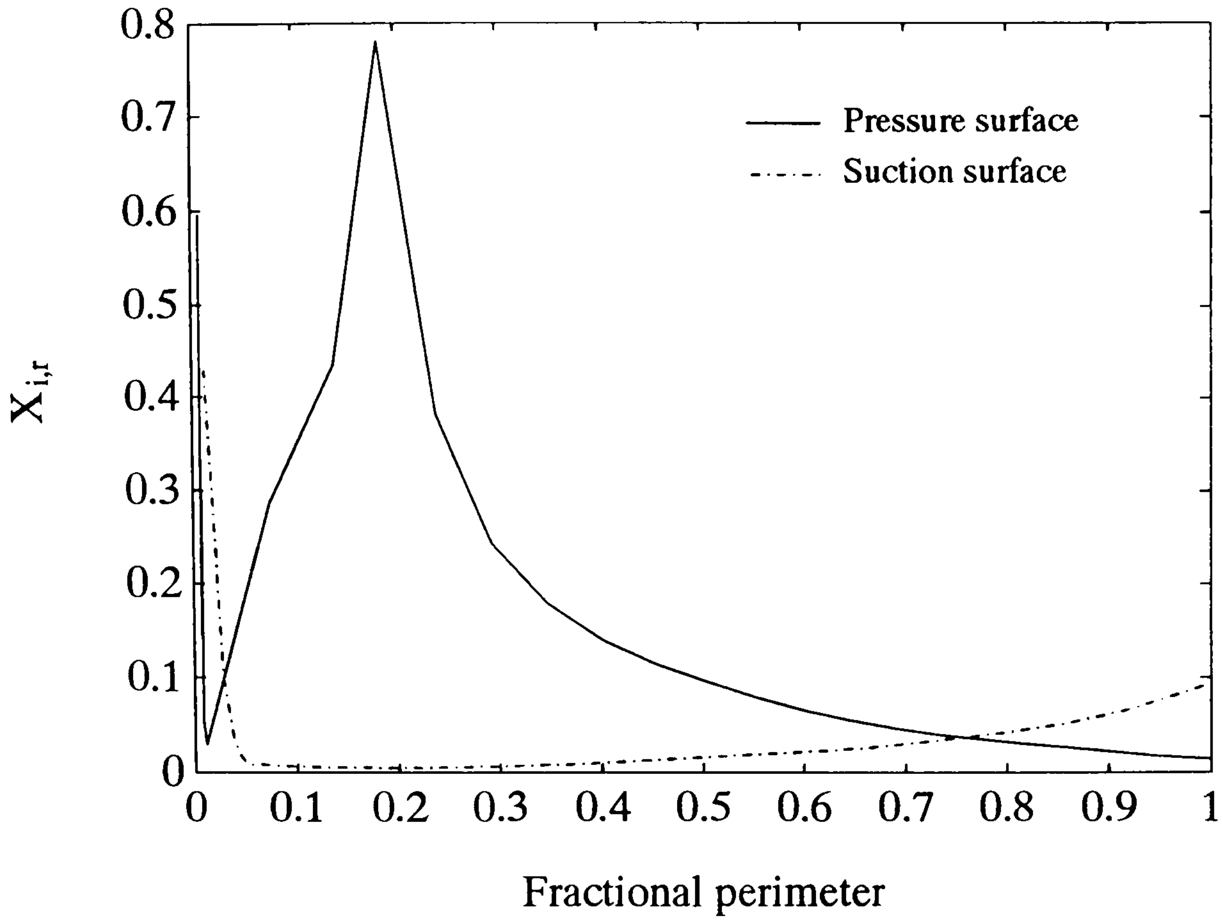

Figure 10.9. Predicted values of X_{ir} around a nozzle guide vane aerofoil.

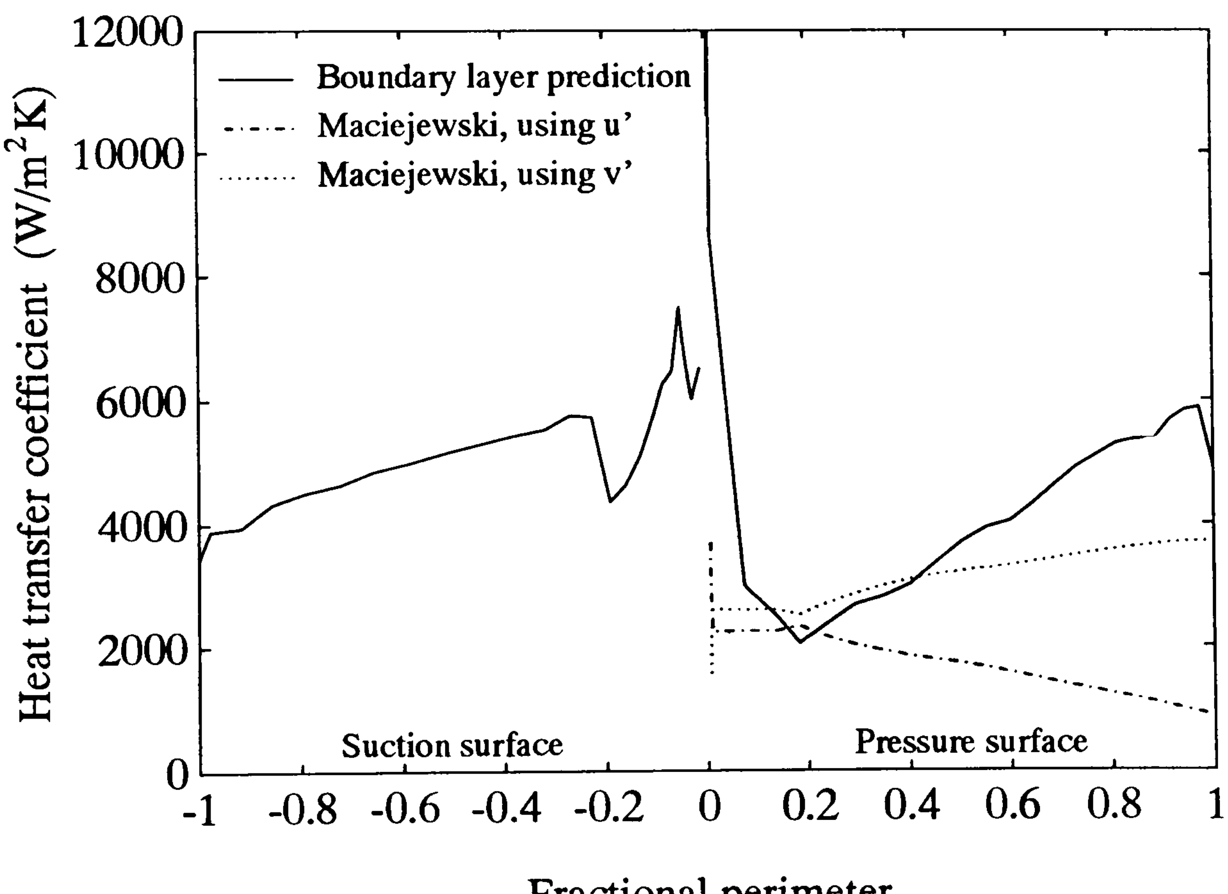

Figure 10.10. Comparison of **Maciejewski and Moffat's (1989)** correlation with a typical boundary layer code.

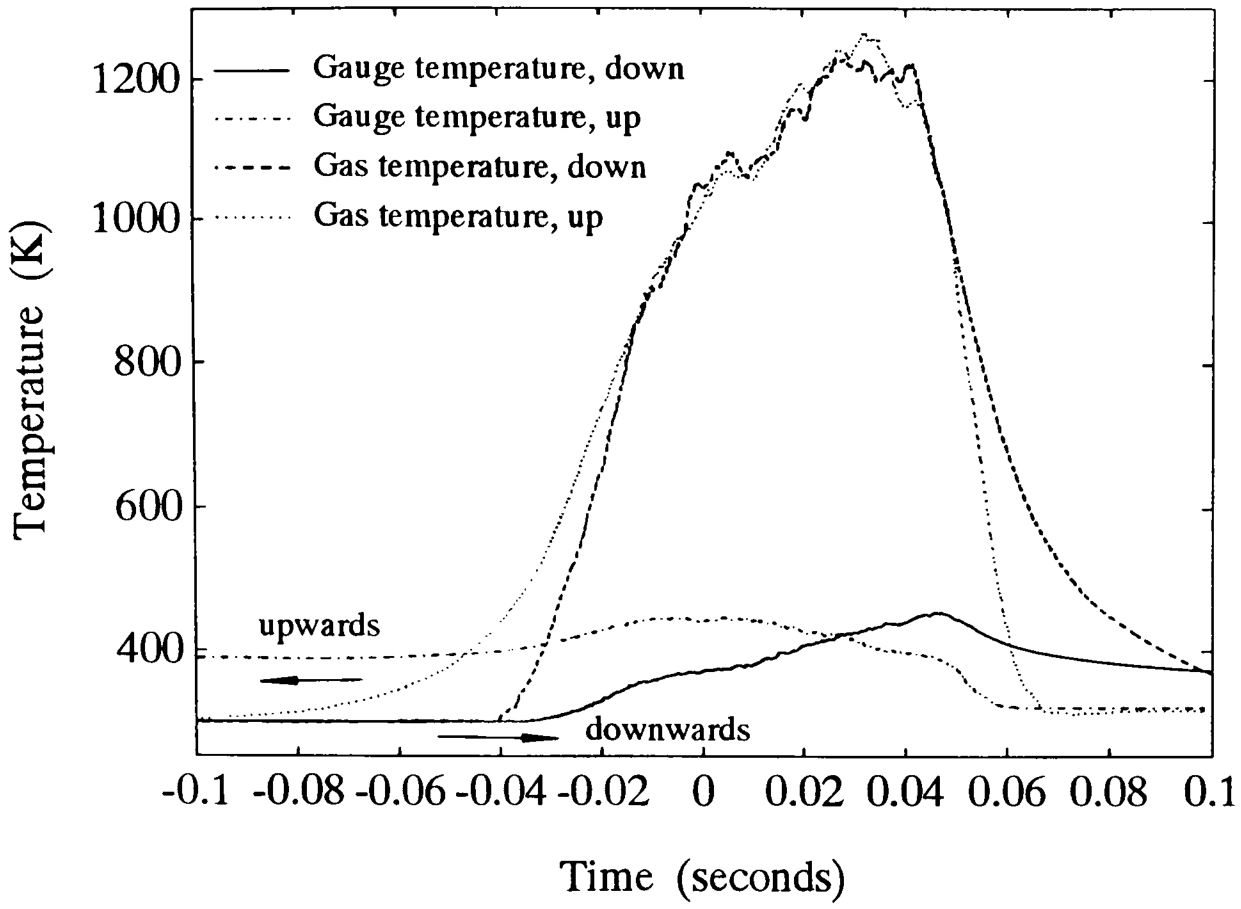

Figure A.3.1. Gas and thin film probe surface temperatures during downwards and upwards traverses. (Combustor A, *AFR* = 65:1).

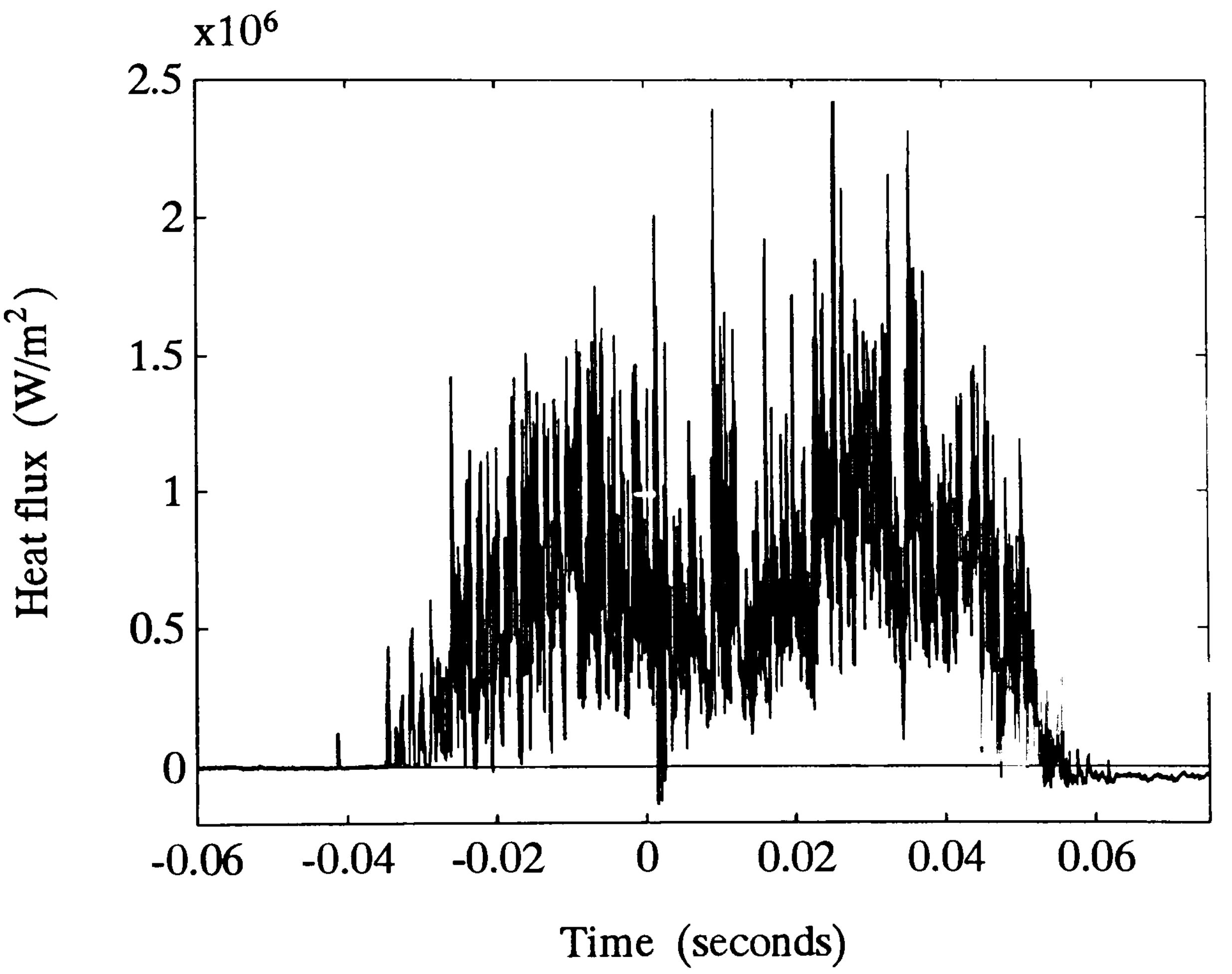

Figure A.3.2. Typical thin film probe heat flux signal, derived assuming a semi-infinite substrate. (Combustor A, *AFR* = 65, downwards traverse).

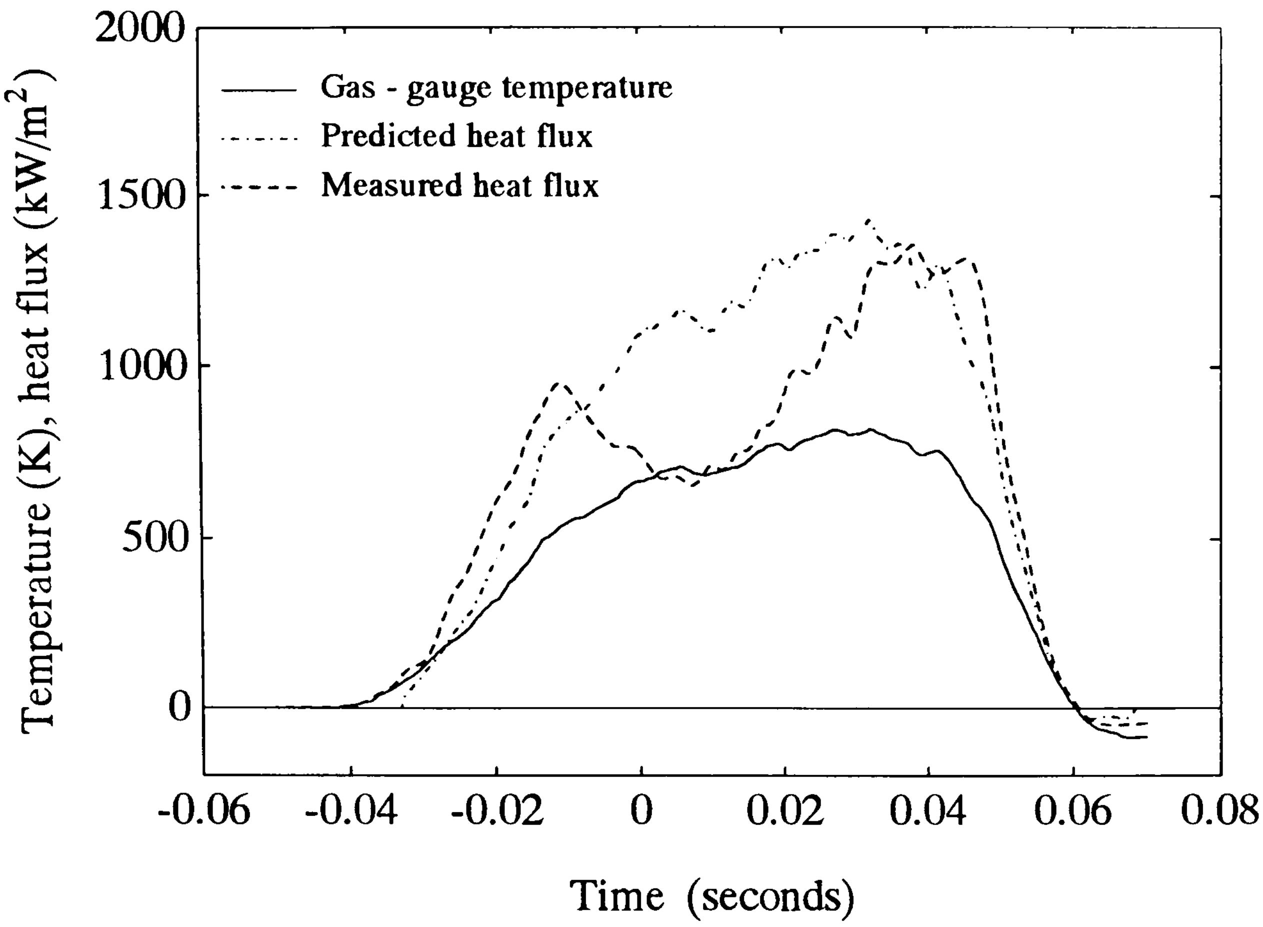

Figure A.3.3. Comparison of measured heat flux (as above, but smoothed) and laminar prediction. Downwards traverse.

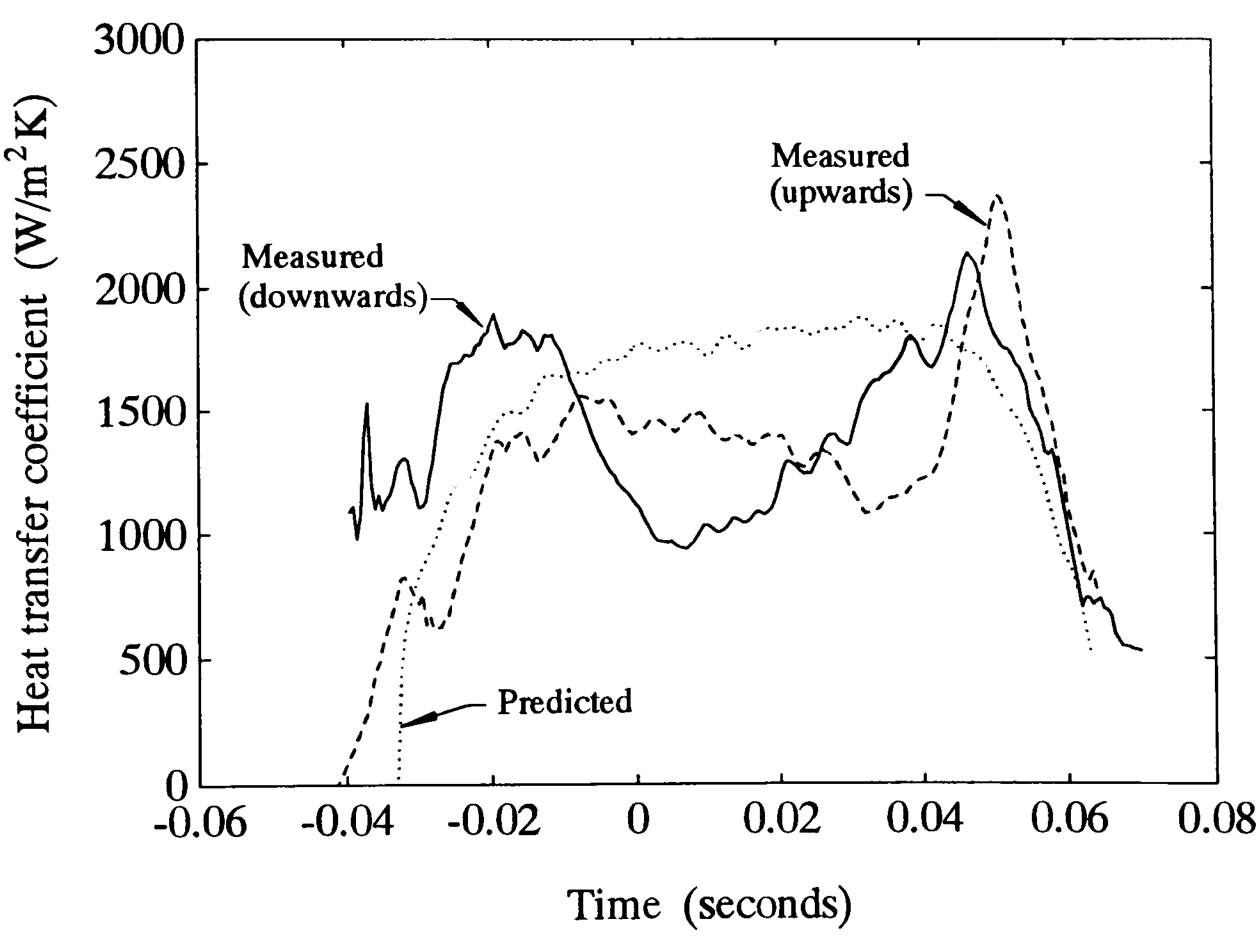

Figure A.3.4. Comparison of measured (thin film) heat transfer coefficients from upwards and downwards traverses. If central dip is a flow feature these should be the same.

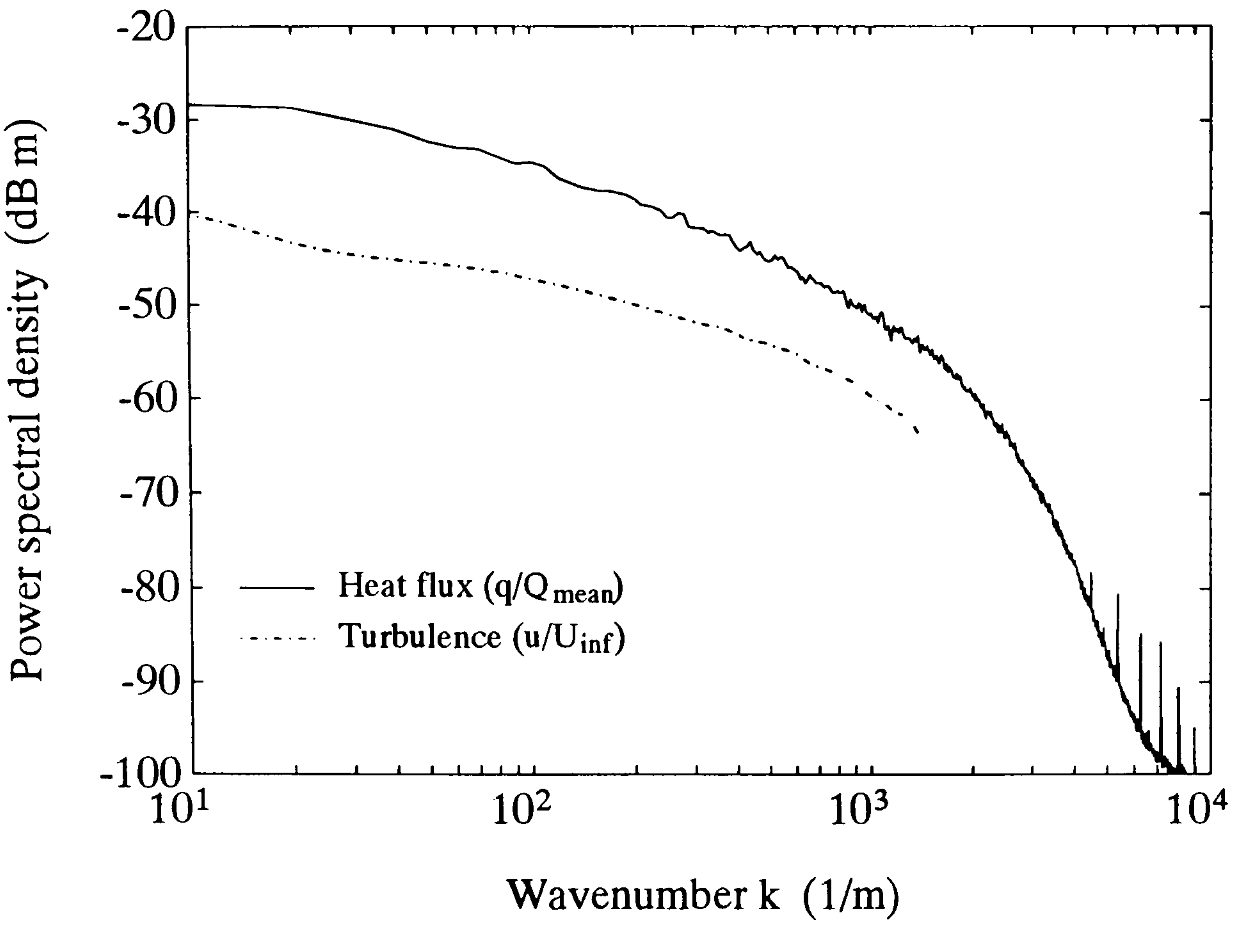

Figure A.3.5. Comparison of spectra of velocity and heat flux fluctuations. (Combustor A, *AFR* = 65).

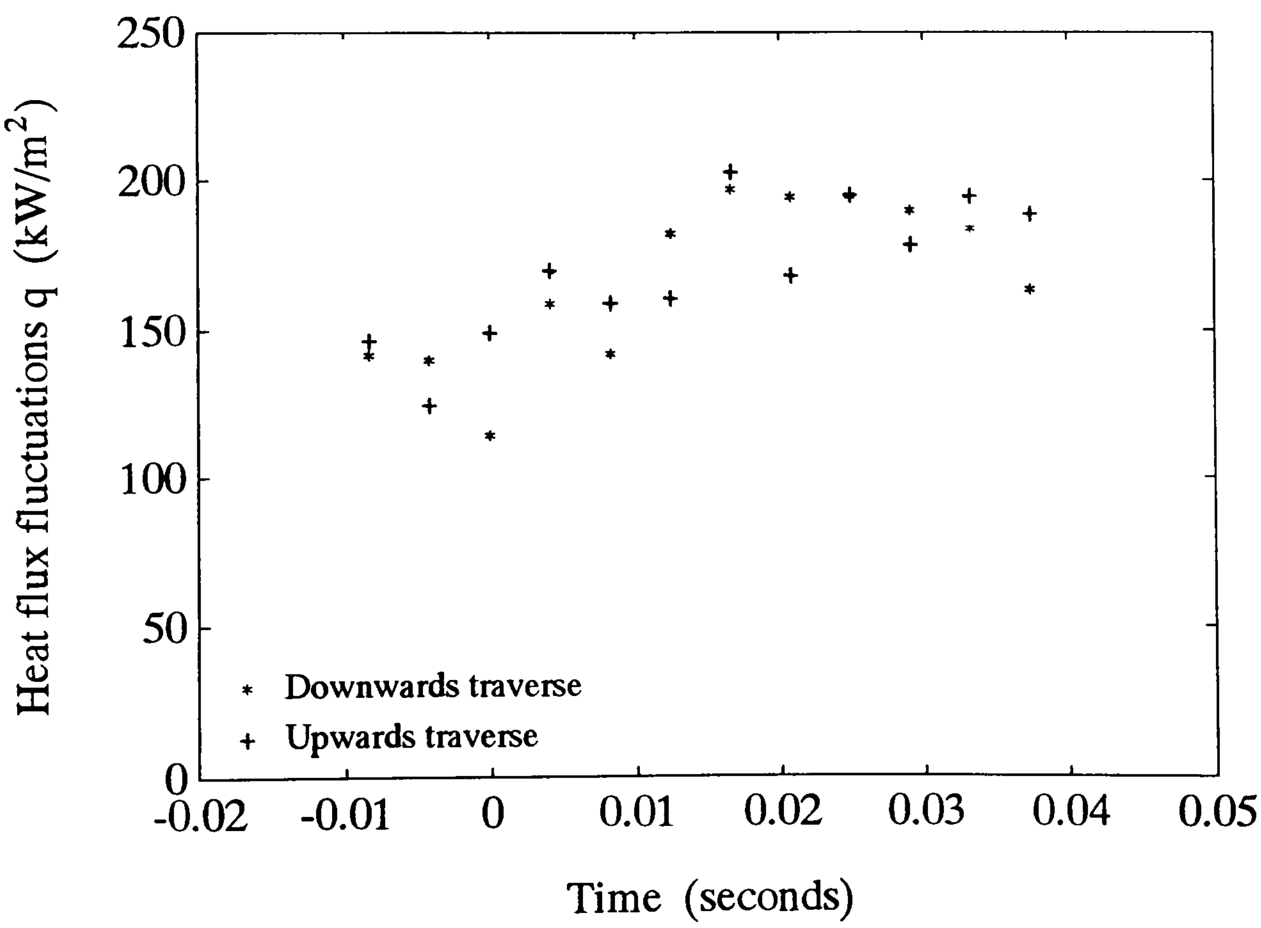

Figure A.3.6. Heat flux rms levels over $200 < k < 1200$.

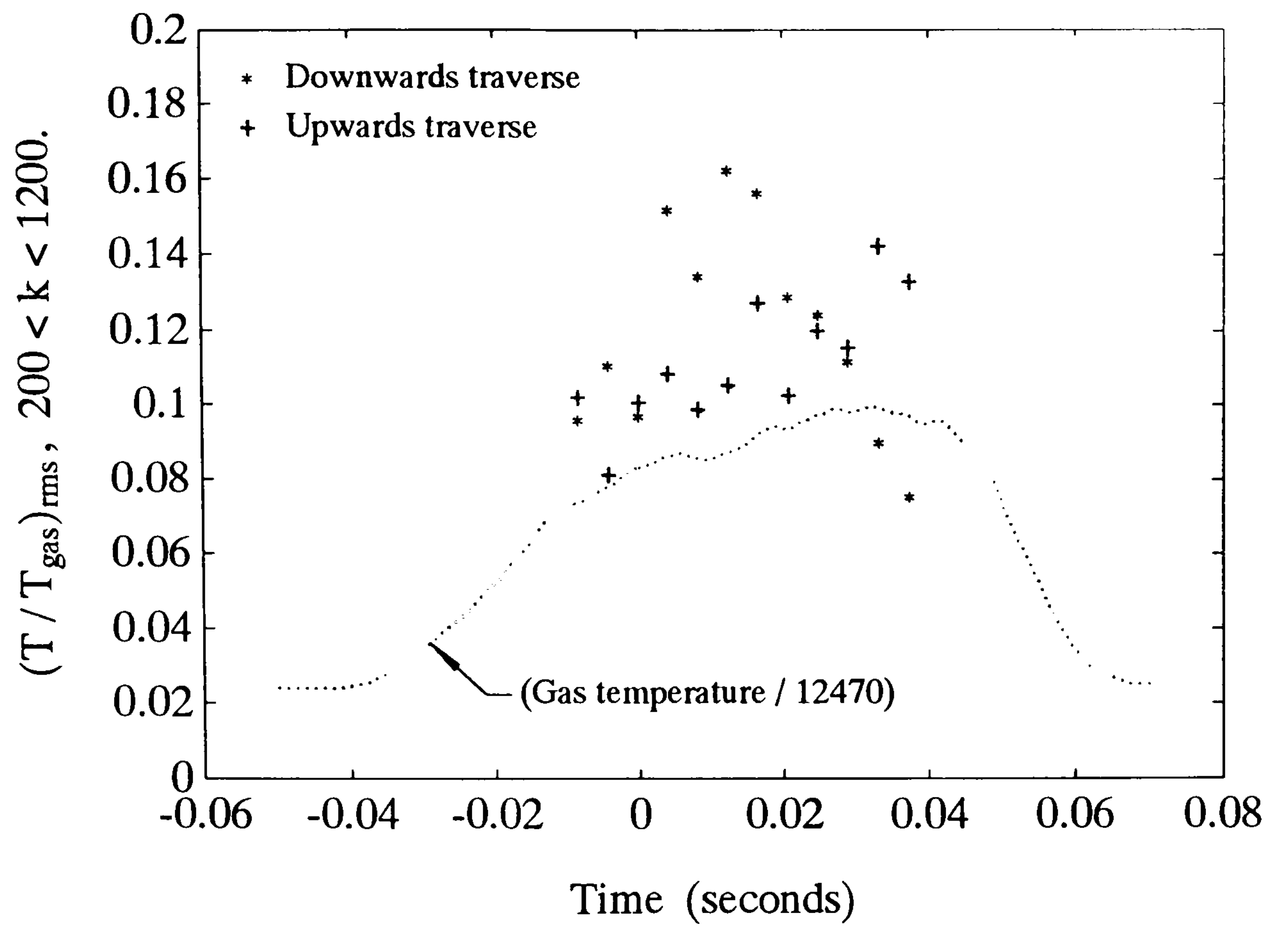

Figure A.3.7. Temperature fluctuations (rms) derived from equation 4.1 using data at wavenumbers from 200 to 1200 m^{-1}.

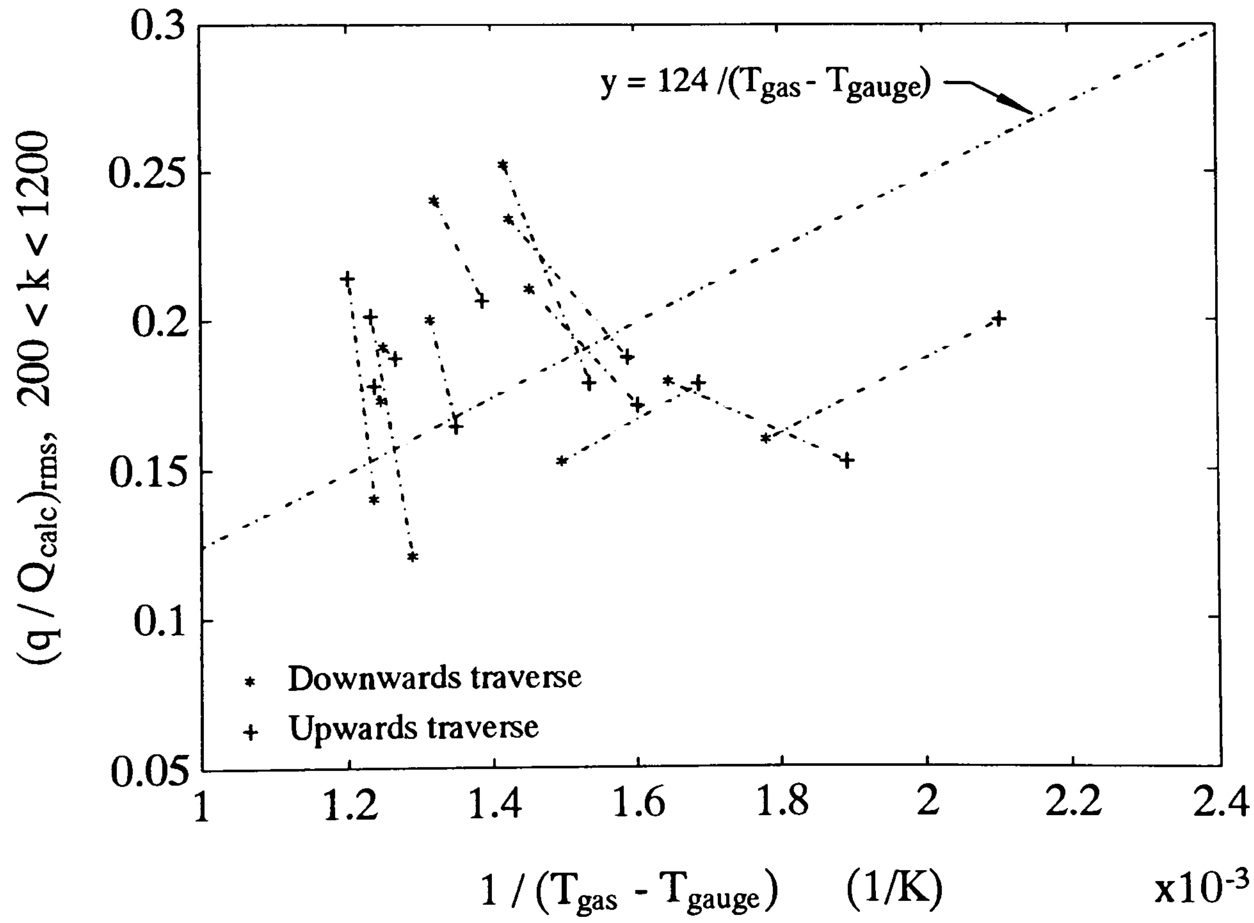

Figure A.3.8. Rms heat flux levels vs 1/driving temperature difference. The fact that these do not lie on a straight line suggests that the q' signal is not due to temperature fluctuations.